



# Collective spontaneous emission from dense ensembles of two-level atoms

Antoine Glicenstein

## ► To cite this version:

Antoine Glicenstein. Collective spontaneous emission from dense ensembles of two-level atoms. Optics [physics.optics]. Université Paris-Saclay, 2022. English. NNT : 2022UPASP001 . tel-03584259

**HAL Id: tel-03584259**

**<https://pastel.hal.science/tel-03584259>**

Submitted on 22 Feb 2022

**HAL** is a multi-disciplinary open access archive for the deposit and dissemination of scientific research documents, whether they are published or not. The documents may come from teaching and research institutions in France or abroad, or from public or private research centers.

L'archive ouverte pluridisciplinaire **HAL**, est destinée au dépôt et à la diffusion de documents scientifiques de niveau recherche, publiés ou non, émanant des établissements d'enseignement et de recherche français ou étrangers, des laboratoires publics ou privés.

Collective spontaneous emission from  
dense ensembles of two-level atoms  
*Emission spontanée collective par des ensembles denses  
d'atomes à deux niveaux*

**Thèse de doctorat de l'université Paris-Saclay**

École doctorale n°572 : ondes et matière (EDOM)

Spécialité de doctorat : physique

Graduate School : Physique, Référent : Institut d'Optique

Thèse préparée au Laboratoire Charles Fabry (Université Paris-Saclay, Institut d'Optique Graduate School, CNRS) sous la direction d'Antoine Browaeys, Directeur de recherche, et la co-direction d'Igor Ferrier-Barbut, Chargé de recherche.

**Thèse soutenue à Paris-Saclay, le 18 Janvier 2022, par**

**Antoine GLICENSTEIN**

**Composition du jury**

**Isabelle Bouchoule**

Directrice de recherche, Laboratoire Charles Fabry

**William Guerin**

Chargé de recherche, HDR, Institut de Physique de Nice

**Sebastian Hofferberth**

Professeur, Université de Bonn

**Alban Urvoy**

Maître de conférence, Laboratoire Kastler Brossel

**Antoine Browaeys**

Directeur de recherche, Laboratoire Charles Fabry

**Igor Ferrier-Barbut**

Chargé de recherche, Laboratoire Charles Fabry

**Sylvie Paolacci-Riera**

Tutrice AID

Présidente

Rapporteur

Rapporteur

Examineur

Directeur de thèse

Co-directeur de thèse

Invitée

**Titre :** Emission spontan  e collective par des ensembles denses d'atomes    deux niveaux

**Mots cl  s :** Diffusion de la lumi  re, Interaction dip  le-dip  le, Atomes froids, Emission spontan  e, Superradiance, Sousradiance.

**R  sum   :** On s'int  resse au probl  me de la diffusion de la lumi  re par un ensemble dense d'atomes froids dans le r  gime dit "de Dicke", dans lequel un grand nombre d'atomes est contenu dans un volume dont les dimensions sont plus petites que la longueur d'onde de la transition atomique. Quand le milieu est dense et que la fr  quence de la lumi  re est proche de celle d'une transition atomique, les dip  les induits par la lumi  re interagissent entre eux. Ces interactions r  sonantes entre les dip  les induits modifient la r  ponse collective de l'ensemble. En particulier, elles modifient le taux auquel l'ensemble se d  sexcite par   mission spontan  e. Une d  sexcitation plus rapide que celle d'un atome unique est appel  e super-radiance et une d  sexcitation plus lente est appel  e sous-radiance. Dans cette th  se, nous d  veloppons d'abord des m  thodes exp  rimentales pour l'  tude de ce pro-

bl  me, nous permettant de pr  parer, d'observer et de manipuler des nuages denses d'atomes    deux niveaux contenant plusieurs milliers d'atomes froids dans un r  gime proche du r  gime de Dicke. Nous   tudions ensuite les propri  t  s d'  mission collective de ces syst  mes lorsqu'ils sont soumis    de la lumi  re laser r  sonante, pendant et apr  s l'excitation. On observe les d  sexcitations super- et sous-radiantes pour la premi  re fois dans ce r  gime, et on montre qu'elles sont gouvern  es uniquement par le nombre d'atomes dans le nuage. Nous avons ensuite caract  ris   les oscillations de Rabi collectives des ensembles d'atomes pilot  s par laser. Enfin, nous d  montrons un protocole pour rel  cher    la demande des excitations stock  es dans des   tats sous-radiants, ce qui est un pr  requis pour des applications de stockage de la lumi  re.

**Title :** Collective spontaneous emission from dense ensembles of two-level atoms

**Keywords :** Light scattering, Dipole-Dipole interaction, Cold atoms, Spontaneous emission, Superradiance, Subradiance.

**Abstract :** We are interested in the problem of light scattering by dense ensembles of cold atoms in the so-called "Dicke regime", in which many atoms are trapped in a volume whose dimensions are smaller than the wavelength of the atomic transition. When the medium is dense and the frequency of the light is close to that of an atomic transition, the light-induced dipoles interact with each other. These resonant interactions between the dipoles modify the collective response of the ensemble. In particular they modify the rate at which the energy of the ensemble decays by spontaneous emission. A faster decay than that of a single atom is called superradiance and a slower one is called subradiance. In this thesis, we first develop experimental methods for the study

of this problem, allowing us to prepare, observe and manipulate dense clouds of two-level atoms containing several thousand cold atoms in a regime close to Dicke's regime. We then study the collective emission properties of these systems under resonant laser light, during and after driving. We observe super- and subradiant decay for the first time in this regime and show that they are governed uniquely by the number of atoms in the cloud. We have then characterized the collective Rabi oscillations of atomic ensembles under laser driving. Finally, we demonstrate a protocol for the on-demand release of excitations stored in subradiant states, which is a prerequisite for the realization of light storage.

Traditionnellement, écrire les remerciements est la dernière étape d'une thèse : le point final sur trois années de vie, dont le manuscrit ne rend compte que d'une infime partie. C'est l'occasion pour moi de dire merci à tous ceux qui ont permis ces travaux, de près ou de loin.

Tout d'abord, je tiens à remercier Antoine Browaeys, sans qui rien n'aurait été possible. Je te remercie Antoine de m'avoir fait très vite confiance, d'abord avec Yvan puis avec Igor. Avec Igor, vous avez été pour moi ce que l'on peut rêver de directeurs de thèse : présents et d'un formidable soutien tout au long de ma thèse, dans les moments simples mais surtout dans les moments les plus compliqués. Je remercie ensuite l'ensemble des membres du groupe Optique Quantique avec qui j'ai pu interagir pendant ces trois années. Bien sûr, je pense en particulier à Ludo, qui m'a accueilli puis donné les clés de la manip. Les moments que nous avons passé ensemble au labo avec Daniel à essayer de faire marcher la machine, même si nous ne nous en rendions pas compte alors, ont été primordiaux pour la suite de ma thèse et pour les résultats obtenus. Ensuite, je voudrais remercier Giovanni avec qui nous formons, je pense, une super équipe. Nous avons su affronter ensemble les nombreux défis qu'impose une expérience d'atomes froids, presque toujours dans la joie et la bonne humeur. Je suis très content de pouvoir prolonger un peu notre collaboration. Je remercie aussi la Team Photon, dont j'ai eu le privilège de faire partie à titre officieux.

Au-delà du travail, ces années ont été extraordinaires. J'ai pu compter sur le soutien et l'amour de mes proches, de ma famille, de ma compagne et de mes amis. Les concernés se reconnaîtront (et comme ça je ne risque pas d'oublier quelqu'un par mégarde). J'espère que vous êtes fiers du chemin parcouru, et le meilleur reste à venir !

*A mes parents.*

# Introduction

\*\*\*

The study of many-body systems is a very active field of research in physical, chemical and mathematical sciences and it is currently booming. As an example, almost 2,000 publications published in 2020 contain “many-body” in their title or abstract. Less than 1,000 were published in 2010 and less than 400 in 1990 <sup>1</sup>. This attractiveness could be explained by the incredible complexity of the problems in the presence of interactions, entanglement or complex dynamics just to cite a few examples (Amico et al. 2008; Bloch et al. 2008; Alet and Laflorencie 2018; Abanin et al. 2019). The development of new methods and approaches has allowed for a rapid progress in the past decade, and opened avenues for the study of new paradigms such as out-of equilibrium or driven-dissipative regimes. In this manuscript, we are particularly interested in how light interacts with driven-dissipative many-body atomic systems.

Light is indeed a formidable tool to probe matter: from microscopy (Lawlor 2019; Lichtman and Conchello 2005) to X-ray diffraction (Waseda et al. 2011) or ultra-fast lasers (Guo et al. 2019), it provides information about the structure of matter and how it works. The way light scatters on ensembles of particles can also explain a wide variety of everyday life situations, from the blue color of the sky to the opacity of milk.

The amazing progress of the toolbox offered by atomic physics platforms allows one to “shed new light” on this problem. The response of a classical single atom to resonant excitation with light is well known (Jackson 1999). Under the effect of the electric field, the atom polarizes and forms a driven dipole that emits light in turn. This dipole is characterized by its resonant frequency  $\omega_0$  and damping rate  $\Gamma$ . With several atoms, the light induced dipoles may interact with each other: each dipole is also driven by the fields radiated by the neighboring dipoles. They are thus coupled to each other. This interaction between the dipoles is called *resonant dipole-dipole interaction*, and we will see in the following that the strength of this interaction increases when the dipoles get closer, in particular when the distance between the dipoles becomes smaller than  $\lambda/2\pi$  (or equivalently when the peak density  $n_0$  is of the order or larger than  $k^3 = (\frac{2\pi}{\lambda})^3$ ). The interaction between the dipoles strongly modifies the response of the atoms to a resonant excitation. This response becomes collective rather than individual. This leads to a shift of the resonance frequency and a change in the decay rate. Light is thus used twice in our experiments: it is the basis of the interactions (because it induces dipoles), and the way it is scattered by the atoms informs us about the physical phenomena at play in the atomic ensemble.

---

<sup>1</sup>[www.scopus.com](http://www.scopus.com)

There are many motivations to understand the interaction between light and ensemble of atoms. To begin with, their potentially rich internal structure and external degrees of freedom (velocity, momentum, temperature) make them perfect models of complex emitters, both theoretically and experimentally (Foot 2005). Moreover, their resonance frequency can be in the visible or near-infrared range, allowing one to use high performance laser sources to manipulate and study them. Atoms are therefore of great interest for fundamental research. Let us add that there are many atom-like systems (or artificial atoms) such as semiconductor quantum dots (Solomon et al. 2001; Awschalom et al. 2002), diamond NV centers (Lenef and Rand 1996), plasmonic oscillators (Thijssen et al. 2013) and many other which benefit from the methods developed in atomic physics over many decades.

Then, the field also has implications for technological applications. For example in nanophotonics, if one wants to create an intense light source by combining many emitters. If these emitters are close enough (of the order of  $\lambda/2\pi$ ), it has been shown that the emissivity of such a system is strongly modified by the interaction between the emitters (Huang et al. 2010). Similarly, the coupling properties of quantum dots with light can be altered by the dipole-dipole interaction. These dots can be used as single photon sources, for example. Another application for which the study of interactions between dipoles is crucial is atomic sensors such as optical clocks (Ludlow et al. 2015). These are the reference for ultra-precise time measurement (they reach in 2018 a relative precision of  $1.5 \times 10^{-19}$  (Marti et al. 2018), which means that they deviate by less than 1s in 15 billion years). Such accuracy is used for testing fundamental theories (measurement of fundamental constants (Colaço et al. 2021), Einstein's general relativity (Jiang et al. 2021)) and in applications like GPS positioning (Mehlstäubler et al. 2018) or telecommunications (Riehle 2005). The principle of these clocks is to measure the frequency of an atomic transition, called a clock transition, by sending light onto ensemble of atoms usually trapped in optical lattices. It has been shown that the interactions between light-induced dipoles constitutes a fundamental limit to the precision achievable with the clocks, because this interaction introduces shifts of the resonance frequencies (Chang, Ye, et al. 2004; Bromley et al. 2016; Campbell et al. 2017).

Finally, the interaction between dipoles does not only hinder performances. Several works propose to use them to develop enhanced light-matter interfaces. It has for example been proposed (Bettles et al. 2016b; Perczel et al. 2017; Shahmoon et al. 2017), and experimentally demonstrated (Rui et al. 2020) that a 2D plane of atoms leads to a total reflection of light. It has also been proposed to use subradiant states, collective states in which excitations decay more slowly than for isolated atoms, as an efficient storage medium for quantum memories applications (Facchinetti, Jenkins, et al. 2016; Asenjo-Garcia et al. 2017).

Several types of experimental systems are adapted to the study of the interaction between light and atoms, allowing one to observe these interactions on a wide range of parameters such as the number of atoms, the density or the temperature of atoms for example. Among others, we find

- Extended and dilute clouds of cold atoms, for instance in the groups of Kaiser & Guerin (Guérin, Araújo, et al. 2016), Havey (Roof et al. 2016) or Wilkowski (Chalony et al. 2011).

In these systems, the low atomic density ( $n_0 \ll k^3$ ) is compensated by a large optical depth, which governs the collective effects (Guerin, Rouabah, et al. 2017).

- Thermal atomic vapors, for instance in the Adams group (Keaveney et al. 2012) and collaboration with Browaeys group (Peyrot, Y. R. Sortais, Browaeys, et al. 2018; Peyrot, Y. R. Sortais, Greffet, et al. 2019; Peyrot, Šibalić, et al. 2019). These systems can reach a very high density ( $n_0 \sim 100k^3$ ), but at the cost of phenomena that make the study more complex : important atomic motion leading to inhomogeneous Doppler broadening, collisions with walls...
- cold atomic clouds in microscopic traps. These systems permit to reach a sufficient density to observe collective effects due to the dipole-dipole interactions ( $n_0 \sim k^3$ ) while keeping the advantages of cold atoms: their internal and external degrees of freedom can be manipulated by laser, which offers a very fine and versatile control.

This last option has been chosen in the Quantum Optics group of the Laboratoire Charles Fabry. Microscopic traps are created by focusing a laser beam with a large numerical aperture aspheric lens placed under vacuum, a technique that has been developed and used for other experiments in the group (Y. R. P. Sortais, Marion, et al. 2007; Browaeys, Barredo, et al. 2016; Browaeys and Lahaye 2020). This method has made it possible to observe the response of gaussian clouds containing between 1 and 800 atoms, up to densities of  $n_0 = 3 \times 10^{14} \text{at.cm}^{-3} \sim 0.6k^3$ . Collective fluorescence (Pellegrino et al. 2014) and transmitted light (Jennewein, Y. R. P. Sortais, et al. 2016; Browaeys, Jennewein, et al. 2016) have been measured and compared to theoretical models, without reaching a better than qualitative agreement (Jenkins et al. 2016; Jennewein, Brossard, et al. 2018). Starting in 2016, a new generation of the experimental setup was built with the goals of improving the observation and manipulation of atomic clouds, as well as preparing structured ensembles (Brossard 2019). This was the status when I arrived in the group in 2018.

The manuscript is organized as follows. The first part, divided into four chapters, aims at describing the theoretical and experimental tools used and/or implemented during my work. In the first chapter, I recall the theoretical notions necessary to the understanding of the subject and we describe the different types of numerical simulations that I will use in the rest of the text. The second and third chapters are dedicated to the experimental system and the methods used to prepare, observe and manipulate our atomic ensembles. The fourth chapter is dedicated to the study of light scattering in an ordered system of atoms, the 1D chain, using the methods described in the previous chapters.

The second part of this manuscript, divided into four chapters, is devoted to the study of dense clouds. In a first chapter, I explain the protocol developed during my thesis for the loading of these clouds in optical traps. This protocol is an important contribution because it allowed us to observe effects never seen before with the previous generation of the experimental system. The following chapters contain an in-depth study of these effects. Chapter 6 is dedicated to superradiance, a phenomenon predicted by Dicke in the 1950's but for which we report observations close to the ideal conditions. In chapter 7, the collective response of dense clouds under a resonant laser excitation is observed and characterized. Finally, chapter 8 is dedicated to subradiance in our dense clouds. In particular, we demonstrate a

protocol for the on-demand release of excitations stored in subradiant states, which would be a prerequisite for the realization of light storage.

Finally, a synthesis of the obtained results is made and perspectives for future research are proposed.



# Contents

\*\*\*

<b>I</b>	<b>Tools for the study of light scattering in cold atomic ensembles</b>	<b>9</b>
<b>1</b>	<b>Theory background and simulations methods</b>	<b>13</b>
1	Theory of light-matter interaction in atomic ensembles . . . . .	14
1.1	Classical light-matter interaction . . . . .	14
1.2	Semi-classical treatment of light-matter interaction . . . . .	18
2	Numerical methods . . . . .	22
2.1	Coupled Dipoles Simulations . . . . .	22
2.2	Nonlinear Coupled Dipoles Simulations . . . . .	26
2.3	Fully quantum models . . . . .	27
3	Conclusion . . . . .	29
<b>2</b>	<b>Experimental setup</b>	<b>31</b>
1	Trapping and observing cold atoms . . . . .	32
1.1	Trapping cold atoms in an Optical Dipole Trap . . . . .	32
1.2	Brief overview of the setup . . . . .	34
1.3	The imaging systems . . . . .	37
1.4	The <i>OptoTelescope</i> . . . . .	43
2	Preparation and characterization of a 1D atomic chain . . . . .	48
2.1	Preparation of the chain . . . . .	48
2.2	Controllable length . . . . .	49
2.3	Oscillation frequencies . . . . .	49
2.4	Temperature and radial extension . . . . .	51
3	Control of the atomic internal state . . . . .	52
3.1	Compensation of the stray magnetic fields . . . . .	52
3.2	Preparing a two-level system . . . . .	55
4	Conclusion . . . . .	60
<b>3</b>	<b>Single atoms in optical tweezers using <math>\Lambda</math>-enhanced gray molasses</b>	<b>61</b>
1	Principles of $\Lambda$ -enhanced GM . . . . .	62
1.1	Dark states . . . . .	62
1.2	Cooling mechanism . . . . .	63
1.3	Use of GM to load optical tweezer with high efficiency . . . . .	64
2	Implementation . . . . .	65
2.1	Setup . . . . .	65
2.2	Temperature measurement . . . . .	66
3	Experimental results . . . . .	67

3.1	Single atom loading and temperature . . . . .	67
3.2	1D chain loading . . . . .	69
3.3	Many atoms in the tweezer . . . . .	69
4	Conclusion . . . . .	71
<b>4</b>	<b>Collective shift in a 1D atomic chain</b>	<b>73</b>
1	Motivations . . . . .	74
2	Collective resonance shift . . . . .	78
2.1	Local shift along the chain . . . . .	79
2.2	Shift reduction due to transverse disorder . . . . .	80
2.3	Shift reduction due to interatomic distance . . . . .	81
2.4	Beyond the low-intensity limit . . . . .	82
3	Conclusion . . . . .	84
<b>II</b>	<b>Super- and Subradiance in a dense cloud of two-level atoms near Dicke's regime</b>	<b>85</b>
<b>5</b>	<b>Preparation of dense clouds of 2-level atoms</b>	<b>89</b>
1	Preparation and characterization of a dense cloud. . . . .	90
1.1	Loading sequence . . . . .	90
1.2	Trapping frequencies . . . . .	91
1.3	In-situ size and temperature . . . . .	91
2	Density estimation using the cloud dynamics . . . . .	95
2.1	Inelastic collisions in the absence of light . . . . .	95
2.2	Temporal evolution of $N$ and $T$ . . . . .	97
2.3	Estimation of the density . . . . .	98
3	Control of the internal state . . . . .	100
3.1	Rabi Oscillations as a function of the driving intensity . . . . .	100
3.2	Optimization of the preparation of a 2 level system . . . . .	101
4	Control of the atom number . . . . .	103
5	Crossed dipole trap . . . . .	103
6	Conclusion . . . . .	106
<b>6</b>	<b>Superradiance in a dense ensemble of 2-level atoms</b>	<b>107</b>
1	Qualitative description of Dicke superradiance . . . . .	108
1.1	Collective spontaneous emission of $N$ two-level systems . . . . .	108
1.2	Dicke super- and subradiant states . . . . .	109
2	Observation of superradiant emission of an inverted atomic cloud . . . . .	113
2.1	Realization of a $\pi$ -pulse . . . . .	113
2.2	Superradiant flash . . . . .	116
3	Analysis of the superradiant decay . . . . .	117
3.1	Theoretical model . . . . .	118
3.2	Initial photon rate . . . . .	119
3.3	Peak of the photon emission . . . . .	119
3.4	Decay time . . . . .	120
3.5	Influence of the trap geometry . . . . .	120
4	Conclusion . . . . .	122

<b>7</b>	<b>Driven superradiance</b>	<b>123</b>
1	Laser driven collective oscillations . . . . .	124
1.1	Directionality . . . . .	124
1.2	Peak over Steady-state value . . . . .	124
2	Collective properties of the driven system . . . . .	127
2.1	Decay time . . . . .	127
2.2	Rabi frequency . . . . .	129
2.3	Photon rate in the early decay . . . . .	130
2.4	Influence of the internal structure . . . . .	130
3	Superradiance in steady-state . . . . .	132
3.1	Observation of the steady-state superradiance . . . . .	132
3.2	Directionality . . . . .	133
3.3	Cooperativity parameter . . . . .	135
4	Superradiance as a function of the probe intensity . . . . .	138
4.1	Peak over steady-state . . . . .	138
4.2	Decay time . . . . .	139
4.3	Steady-state fluorescence . . . . .	140
5	Conclusion . . . . .	140
<b>8</b>	<b>Storage and Release of subradiant excitations</b>	<b>141</b>
1	Observation of subradiance . . . . .	143
1.1	Directionality . . . . .	143
1.2	Nonlinear coupled dipoles (NLCD) simulations . . . . .	144
1.3	Detuning . . . . .	144
1.4	Polarization and internal structure . . . . .	146
2	Subradiance near Dicke's regime . . . . .	146
2.1	Tail ratio . . . . .	146
2.2	Cooperativity parameter . . . . .	147
2.3	Fitting procedure . . . . .	148
2.4	Subradiant lifetime . . . . .	149
3	Study of multiply-excited subradiant states . . . . .	150
3.1	Single mode approximation . . . . .	150
3.2	Limits of NLCD . . . . .	152
4	Release of subradiant excitations . . . . .	154
4.1	Release of light stored in subradiant excitations . . . . .	154
4.2	Two dipoles toy model . . . . .	154
4.3	Experimental demonstration . . . . .	155
4.4	Analysis using eigenmodes and NLCD simulations . . . . .	156
4.5	Role of internal structure and magnetic field . . . . .	157
5	Exploring the Dicke ladder : population of the long lived-states from the super-radiant states . . . . .	159
5.1	Decay time . . . . .	160
5.2	Photon in the late decay . . . . .	160
5.3	Master equation . . . . .	162
6	Conclusion . . . . .	164



## **Part I**

# **Tools for the study of light scattering in cold atomic ensembles**

**Numerical simulations, experimental setup and application to an  
1D atomic chain**



\*\*\*

The first part of this manuscript is dedicated to the presentation of the tools developed and used during my thesis.

- Chapter 1 presents the theoretical framework for the description of light-matter interaction performed in this thesis, and the numerical simulations methods that are used to solve the equations and predict our experimental results.
- In chapter 2, we present the experimental setup used to trap, manipulate and observe the atomic ensembles. We then explain how we isolate a closed two-level transition using magnetic fields and optical pumping.
- In chapter 3, we explain the principle of the gray molasses (GM) and their implementation on the experiment to load efficiently single atoms, highlighting that the low scattering rate of GM allows us to have many atoms in a microscopic dipole trap. In the second part of the manuscript, we will exploit this experimental tool to increase the number of trapped atoms by almost a factor of 10 compared to the previous generation of the experiment.
- In chapter 4, we use the tools presented in the previous chapters to prepare and perform experiments on a 1D atomic chain, demonstrating the interest of the 1D dimension to obtain enhanced collective effects and showing that controlling the geometrical arrangement of the sample allows us to shape its collective response.

---



# Theory background and simulations methods

\*\*\*

The systems we study are ensembles of atoms. The excitation by light induces dipoles which are then driven by all neighboring dipoles, coupling them the ones to the others. We thus obtain a complex many-body system. The purpose of this chapter is first to recall the theoretical notions necessary to describe the interaction between light and an atomic ensemble such as the one produced in our experiment. Second, we explain the principle of the different types of numerical simulations that can be performed in order to understand the physics involved and in order to make reliable predictions about our systems, even if the models are not analytically solvable.

## Contents

<b>1</b>	<b>Theory of light-matter interaction in atomic ensembles . . . . .</b>	<b>14</b>
1.1	Classical light-matter interaction . . . . .	14
1.2	Semi-classical treatment of light-matter interaction . . . . .	18
<b>2</b>	<b>Numerical methods . . . . .</b>	<b>22</b>
2.1	Coupled Dipoles Simulations . . . . .	22
2.2	Nonlinear Coupled Dipoles Simulations . . . . .	26
2.3	Fully quantum models . . . . .	27
<b>3</b>	<b>Conclusion . . . . .</b>	<b>29</b>

## 1 Theory of light-matter interaction in atomic ensembles

Most of the results presented here are textbook materials. We will first present this interaction in the framework of classical electromagnetism and then in the semi-classical approximation, in which atoms are described quantum mechanically while the light field is classical. This section also gives a first overview of the phenomena of superradiance and subradiance, which will be studied experimentally in the following chapters of this manuscript.

### 1.1 Classical light-matter interaction

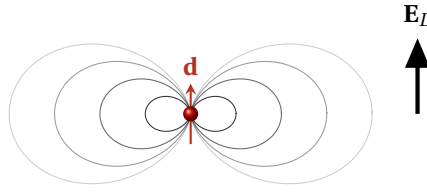


Figure 1.1: A dipole  $\mathbf{d}$  under the effect of the electric field  $\mathbf{E}_L$ .

Let us first consider an atom of mass  $m$ , consisting of a nucleus and an electron of charge  $q$  elastically bound with a harmonic potential of frequency  $\omega_0$ , at distance  $\mathbf{r}$  of the nucleus. If an electric field  $\mathbf{E}_L(\mathbf{r}, \omega)$  is shone, the equation of motion of the electron is

$$\ddot{\mathbf{r}} + \omega_0^2 \mathbf{r} + \Gamma_\omega \dot{\mathbf{r}} = q \frac{\mathbf{E}_L(\mathbf{r}, \omega)}{m} \quad (1.1)$$

where  $\Gamma_\omega$  is a dissipation term due to the radiative energy losses, calculated using the Larmor formula  $\Gamma_\omega = \frac{q^2 \omega^2}{6\pi\epsilon_0 mc^3}$  (Jackson 1999). The electron is a moving charged particle; leading to an electric dipole  $\mathbf{d} = q\mathbf{r}$ , as represented in figure 1.1. Let us write  $\mathbf{E}_L = \mathbf{e} \text{Re}[E_\omega e^{-i\omega t}]$  and  $\mathbf{d} = \mathbf{e} \text{Re}[d_\omega e^{-i\omega t}]$ . Here the dipole is parallel to the driving field and the dipole can thus be considered as a scalar amplitude  $d_\omega$ . In the quasi-resonant case  $\omega \simeq \omega_0$ , one can show that equation (1.1) implies that

$$\dot{d}_\omega = \left(i\Delta - \frac{\Gamma}{2}\right) d_\omega + i \frac{3\pi\epsilon_0\Gamma}{k_0^3} E_\omega \quad (1.2)$$

where  $k_0 = \omega_0/c$  and  $\Delta = \omega - \omega_0$  is the detuning of the laser with the resonance frequency and where  $\Gamma = \Gamma_{\omega_0} = \left(\frac{\omega_0}{\omega}\right)^2 \Gamma_\omega$ . One defines the complex polarizability  $\alpha(\omega) = \alpha'(\omega) + i\alpha''(\omega)$  which relates the steady-state atomic dipole to the driving field,  $d_\omega = \epsilon_0 \alpha(\omega) E_\omega$ . Taking (1.2) in steady state we get:

$$\alpha(\omega) = \frac{6\pi i}{k_0^3} \frac{1}{1 - \frac{2i\Delta}{\Gamma}}. \quad (1.3)$$

The energy transfer  $\Delta U$  between the field  $\mathbf{E}_L$  and the atom during a time  $\Delta t \gg 1/\omega_0, 1/\omega$ , is given by (Jackson 1999)

$$\Delta U = \frac{1}{\Delta t} \int_{\Delta t} q \mathbf{E} \cdot \dot{\mathbf{r}} = \frac{1}{\Delta t} \int_{\Delta t} \mathbf{E} \cdot \dot{\mathbf{d}} = \frac{\omega}{2} \text{Im}(d_\omega E_\omega^*) = \frac{\omega}{2} \alpha'' |\mathbf{E}_\omega|^2.$$

The transfer of energy is thus proportional to the imaginary part of the polarizability  $\alpha''$ . As  $\Delta U \propto \Gamma$ , there is an exchange of energy between the atom and the field only if the system is

dissipative.

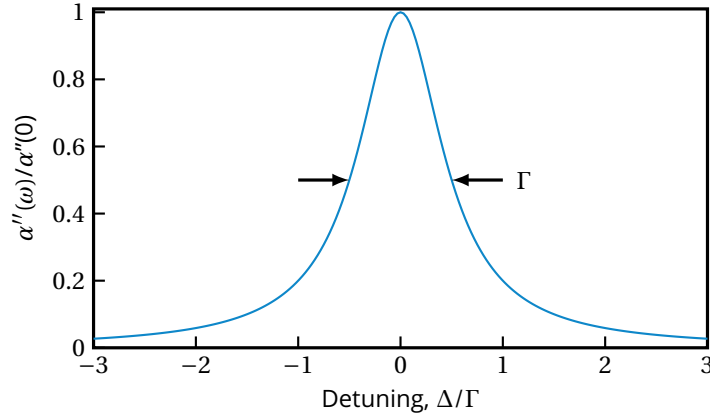


Figure 1.2: Imaginary part  $\alpha''$  of the susceptibility as a function of the detuning  $\Delta = \omega - \omega_0$  of the electric field with the potential frequency.

In the figure 1.2, we plot  $\alpha''$  as a function of detuning. This is a Lorentzian function centered on  $\Delta = 0$  with a width  $\Gamma$ . This means that the atom exchanges energy with the field only if its frequency is less than  $\Gamma$  away from the resonance.

### Two interacting classical dipoles

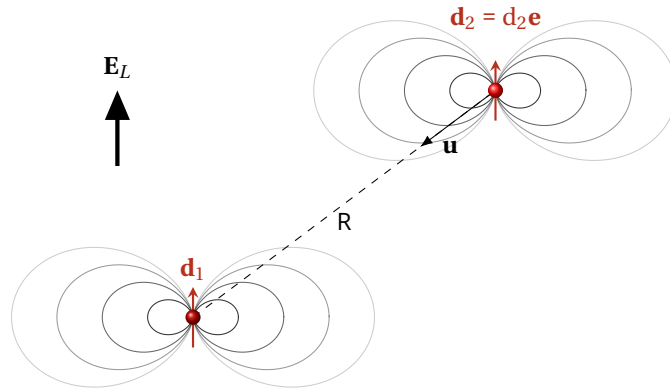


Figure 1.3:  $N=2$  coupled dipoles excited by the field  $\mathbf{E}_L$ .

Let us now consider the case of 2 dipoles illuminated by the laser field  $\mathbf{E}_L$ , as represented in the figure 1.3. The dipole  $\mathbf{d}_1$  located at  $\mathbf{r}_1$  sees the laser field and the field  $\mathbf{E}_2(\mathbf{r}_1)$  radiated by the dipole  $\mathbf{d}_2 = d_2 \mathbf{e}$  at the position of the first atom (Jackson 1999)

$$\mathbf{E}_2(\mathbf{r}_1) = \frac{k_0^3 d_2}{4\pi\epsilon_0} \frac{e^{ik_0 R}}{(k_0 R)^3} \left[ (3(\mathbf{u} \cdot \mathbf{e}) \mathbf{u} - \mathbf{e})(1 - ik_0 R) + (\mathbf{u} \times \mathbf{e}) \times \mathbf{u} (k_0 R)^2 \right], \quad (1.4)$$

where  $R = |\mathbf{r}_1 - \mathbf{r}_2|$  and  $\mathbf{u} = \frac{\mathbf{r}_1 - \mathbf{r}_2}{R}$ . The atoms are then coupled to each other via these radiated fields. Inserting this in (1.2), one obtains the so-called *coupled dipole equations* governing the evolution of the dipoles

$$\begin{cases} \dot{\mathbf{d}}_1 = \left(i\Delta - \frac{\Gamma}{2}\right) \mathbf{d}_1 + i \frac{3\pi\epsilon_0\Gamma}{k_0^3} [\mathbf{E}_L(\mathbf{r}_1) + \mathbf{E}_2(\mathbf{r}_1)] \\ \dot{\mathbf{d}}_2 = \left(i\Delta - \frac{\Gamma}{2}\right) \mathbf{d}_2 + i \frac{3\pi\epsilon_0\Gamma}{k_0^3} [\mathbf{E}_L(\mathbf{r}_2) + \mathbf{E}_1(\mathbf{r}_2)] \end{cases}.$$

We project this set of equations on the complex conjugate vector  $\mathbf{e}^*$  and find

$$\begin{cases} \dot{d}_1 = \left(i\Delta - \frac{\Gamma}{2}\right) d_1 + i \frac{3\pi\epsilon_0\Gamma}{k_0^3} \mathbf{E}_L(\mathbf{r}_1) \cdot \mathbf{e}^* - \frac{i}{\hbar} V_{21} d_2 \\ \dot{d}_2 = \left(i\Delta - \frac{\Gamma}{2}\right) d_2 + i \frac{3\pi\epsilon_0\Gamma}{k_0^3} \mathbf{E}_L(\mathbf{r}_2) \cdot \mathbf{e}^* - \frac{i}{\hbar} V_{12} d_1 \end{cases}$$

with  $V_{12} = V_{21} = V$  called *dipole-dipole interaction* term (see expression below). The previous system can be solved introducing the coupled basis  $d_{\pm} = (d_1 \pm d_2) / \sqrt{2}$ . By summing the two previous equations, one obtains

$$\begin{aligned} \dot{d}_{\pm} &= \left(i\Delta - \frac{\Gamma}{2}\right) d_{\pm} + i \frac{3\pi\epsilon_0\Gamma}{k_0^3} \frac{[\mathbf{E}_L(\mathbf{r}_1) \pm \mathbf{E}_L(\mathbf{r}_2)] \cdot \mathbf{e}^*}{\sqrt{2}} \mp \frac{i}{\hbar} V d_{\pm} \\ &= \left[i(\Delta - \omega_{\pm}) - \left(\frac{\Gamma}{2} - \frac{\Gamma_{\pm}}{2}\right)\right] d_{\pm} + i \frac{3\pi\epsilon_0\Gamma}{k_0^3} \frac{[\mathbf{E}_L(\mathbf{r}_1) \pm \mathbf{E}_L(\mathbf{r}_2)] \cdot \mathbf{e}^*}{\sqrt{2}} \end{aligned} \quad (1.5)$$

where we introduced  $\omega_{\pm} = \pm \frac{\text{Re}[V]}{\hbar}$  and  $\Gamma_{\pm} = \pm 2 \frac{\text{Im}[V]}{\hbar}$ . This shows that the coupling between the dipoles creates two modes (in phase or out of phase)  $d_{\pm}$  with their resonant frequencies shifted by a quantity  $\omega_{\pm}$  and their decay rates modified by a quantity  $\Gamma_{\pm}$  that depends respectively on the strength of the real and imaginary parts of the dipole-dipole interaction potential and thus of the inter-atomic distance  $R$ . In order to consider the importance of the coupling,  $\omega_{\pm}$  and  $\Gamma_{\pm}$  have to be compared to  $\Gamma$ . Indeed, we have seen that the interaction between the field and a dipole is important when  $|\Delta| < \Gamma$  (section 1.1) and that a non-interacting dipole is damped over a time  $1/\Gamma$ . We thus compare  $|V|$  to  $\hbar\Gamma$ . Using  $d^2 = \frac{3\pi\epsilon_0\hbar\Gamma}{k_0^3}$  and equation (1.4), we write

$$V = -\frac{3\hbar\Gamma}{4} e^{ik_0R} \left[ \left( \frac{1}{(k_0R)^3} - \frac{i}{(k_0R)^2} \right) (3\cos^2(\theta) - 1) + \frac{\sin^2(\theta)}{k_0R} \right] \quad (1.6)$$

where  $\theta$  is the angle between  $\mathbf{u}$  and  $\mathbf{e}$  (see Fig 1.3). The dipole-dipole interaction term is thus composed of terms proportional to  $1/k_0R$ ,  $1/(k_0R)^2$  and  $1/(k_0R)^3$ . In figure 1.4, we plot the real and imaginary part of  $V$  as a function of the interatomic distance, for two parallel dipoles.

Not surprisingly, we see that the terms in  $1/(k_0R)^2$  and  $1/(k_0R)^3$  of (1.6) cannot be neglected when  $R$  is of the order of  $\lambda_0 = \frac{2\pi}{k_0}$ . When  $R < \lambda = \lambda/2\pi$ , we have  $V_{dd} \sim \hbar\Gamma$ . The coupling between the light-induced dipoles becomes thus dominant over the response of independent dipoles to the driving field. The aim of our experiment is to explore this regime, where the interaction between the induced dipoles makes collective effects appear. The imaginary part, responsible of the dissipation, saturates at the value  $\hbar\Gamma$  when  $R$  goes to 0. This implies that  $\Gamma_+ = \Gamma = -\Gamma_-$  in this limit. The decay rate of  $d_+$  is thus  $2\Gamma$  and the decay rate of  $d_-$  is 0. As demonstrated later in this chapter, this result is the same as the one found using a quantum treatment of the problem, leading to phenomena of *superradiance* and *subradiance*.

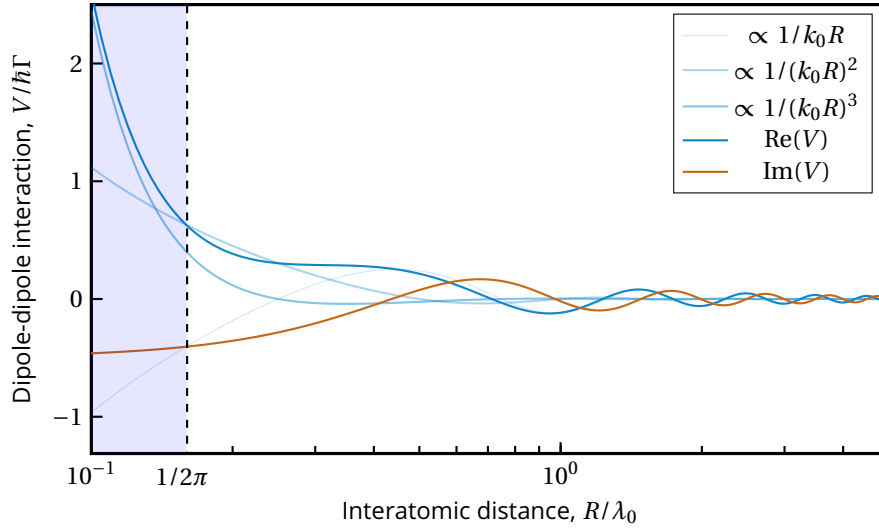


Figure 1.4: Real and imaginary part of  $V$  as a function of the interatomic distance  $R$ . The different terms of the real part are represented. The shaded region corresponds to the values of  $R$  for which the dipole-dipole coupling dominates over the single dipole response (see text).

### N atoms, Coupled Dipoles Equation

Let us generalize the previous reasoning to a  $N$ -atom ensemble. The dipole  $\mathbf{d}_m$  is driven by the field emitted by the laser  $\mathbf{E}_L$  and by all other dipoles, as represented in figure 1.5:

$$\mathbf{E}_{\text{driving}}(\mathbf{r}_m) = \mathbf{E}_L(\mathbf{r}_m) + \sum_{n \neq m} \mathbf{E}_n(\mathbf{r}_m).$$

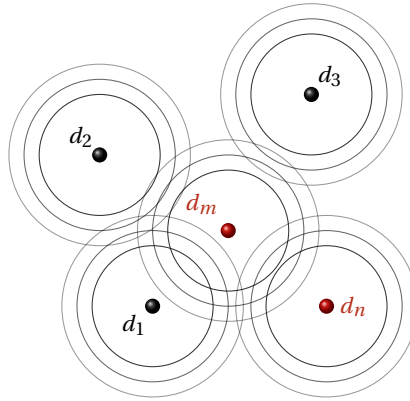


Figure 1.5: Schematic: each dipole receives the field emitted by the neighboring dipoles.

Using equation (1.2), one obtains

$$\dot{d}_m = \left( i\Delta - \frac{\Gamma}{2} \right) d_m + i \frac{3\pi\epsilon_0\Gamma}{k_0^3} \left[ \mathbf{E}_L(\mathbf{r}_m) + \sum_{n \neq m} G(\mathbf{r}_m - \mathbf{r}_n) \mathbf{d}_n \right] \quad (1.7)$$

where we have introduced  $G(\mathbf{r})$  the Green's function (Jackson 1999) such as  $G(\mathbf{r}_m - \mathbf{r}_n) \mathbf{d}_n =$

$\mathbf{E}_n(\mathbf{r}_m)$ , given by equation (1.4).  $G(\mathbf{r}_m - \mathbf{r}_n) \mathbf{d}_n$  is therefore by definition the field emitted by the dipole  $n$  seen at the position of the dipole  $m$ . Equation (1.7) is called the *Coupled Dipoles Equation*. It actually corresponds to a set of  $N$  equations that couple the dipoles together. Once solved, this system of equations allows to calculate the field radiated or transmitted by the assembly of atoms. This result is at the origin of the *Coupled Dipole simulations*, which will be presented in the second part of this chapter.

## 1.2 Semi-classical treatment of light-matter interaction

### Optical Bloch Equations

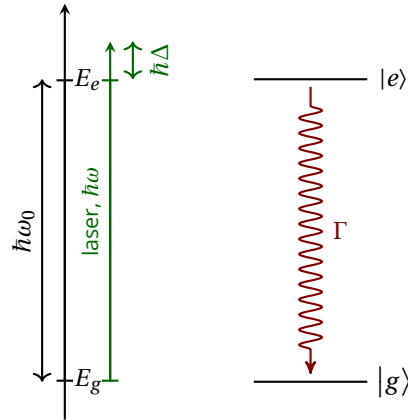


Figure 1.6: Schematic of the system: an atom has two levels  $|g\rangle$  and  $|e\rangle$  of energies  $E_g$  and  $E_e$  respectively. The excited state  $|e\rangle$  can be reached by using a laser at frequency  $\omega$ . The detuning is defined by  $\Delta = \omega - \omega_0$ . The atom decays via a radiative transition with rate  $\Gamma$  (in red).

The classical description of the dipole presented previously is not sufficient in the quantum regime, where saturation must be taken into account: an excited atom does not absorb any more photons. The simplest model for a quantum dipole is a two-level system. Let us consider the interaction of a two-level atom with a quasi-resonant electric field with Rabi frequency  $\Omega$ . The atom is described by its density matrix  $\rho$  and the field is a classical electromagnetic field. The equations that give the evolution of  $\rho$  in this case are the *Optical Bloch Equations* (OBE), derived for example in references (Grynberg, Aspect, et al. 2010) and (Allen and Eberly 1987).

By definition, the density matrix of a two-level atom written in the  $(|g\rangle, |e\rangle)$  basis is

$$\rho = \begin{pmatrix} \rho_{gg} & \rho_{ge} \\ \rho_{eg} & \rho_{ee} \end{pmatrix}$$

Let us write the OBEs in the rotating wave approximation (Grynberg, Aspect, et al. 2010),

for a closed system, with the parameters defined in the figure 1.6. We have

$$\begin{cases} \frac{d\rho_{ee}}{dt} = i\frac{\Omega}{2}(\rho_{eg} - \rho_{ge}) - \Gamma\rho_{ee} \\ \frac{d\rho_{eg}}{dt} = (i\Delta - \Gamma/2)\rho_{eg} + i\frac{\Omega}{2}(\rho_{ee} - \rho_{gg}) \\ \rho_{ge} = \rho_{eg}^* \\ \rho_{gg} + \rho_{ee} = 1. \end{cases} \quad (1.8)$$

In addition to the rotating wave approximation, these equations are true under the assumption that the relaxation of the atom is only realized by spontaneous emission. The last equation corresponds to the fact that the population is conserved. In the weak excitation case, where  $\frac{\Omega}{\Gamma} \ll 1$ , we can make the approximation that  $\rho_{ee} \simeq 0$ . We then recover equation (1.2) if we define  $d_\omega = 2d\rho_{eg}$  with  $d = |\langle g | \mathbf{D} | e \rangle| = \left( \frac{3\pi\epsilon_0\hbar\Gamma}{k_0^3} \right)^{1/2}$  and  $\Omega = \frac{dE}{\hbar}$ .

One can consider the stationary solutions and find that

$$\begin{aligned} \rho_{eg,st} &= \frac{\Omega}{2} \frac{\Delta - i\Gamma/2}{\Delta^2 + \frac{\Delta_\omega^2}{4}} \\ \rho_{ee,st} &= \frac{1}{2} \frac{\Omega^2}{\Delta^2 + \frac{\Delta_\omega^2}{4}}. \end{aligned} \quad (1.9)$$

The population of the excited state in steady state is  $\rho_{ee,st}$ . Its lineshape as a function of the driving frequency is a lorentzian function of central frequency  $\omega_0$  ( $\Delta = 0$ ) and with width  $\Delta_\omega = \sqrt{\Gamma^2 + 4\Omega^2}$ . This is called *power broadening* of the transition (Citron et al. 1977). As a matter of fact,  $\Omega^2 \propto |\mathbf{E}|^2 \propto I$ . This result is quite similar to the one obtained with the classical theory : the atom interacts strongly with the light if its frequency deviates from the resonance frequency by less than  $\Gamma$ .

Let us write  $\rho_{ee,st} = \frac{1}{2} \frac{s}{1+s}$ , defining  $s$  as the saturation parameter. This defines the saturation intensity  $I_{\text{sat}}$  in the same way,  $s = \frac{I}{I_{\text{sat}}} = 2\left(\frac{\Omega}{\Gamma}\right)^2$ . Recall that the number of photons emitted by a single atom per second is equal to  $R = \Gamma\rho_{ee}$ . On the figure 1.7, we plot the OBE (1.8) solutions for intensities  $s = (1, 5, 50)$ .

As a function of time,  $\rho_{ee}(t)$  starts to increase (we took  $\rho_{ee}(t=0) = 0$  as initial condition). For  $s > 2$  (or  $\Omega > \Gamma$ ), we then see *Rabi oscillations* : the population oscillates between the states  $|g\rangle$  and  $|e\rangle$  at the Rabi frequency  $\Omega$ . The amplitude of these oscillations depends on  $s$ , thus on  $\Omega$ . The Rabi oscillations are damped in a time of some  $1/\Gamma$ . At long times, the population of the excited state reaches a stationary regime which, according to the above, also depends on intensity. The OBEs also allow the calculation of the average dipole  $\langle \mathbf{D} \rangle$ :

$$\langle \mathbf{D} \rangle = \text{Tr}[\rho \mathbf{D}] = 2d\text{Re}(\rho_{eg}).$$

The evolution of the coherence as a function of the driving is plotted in figure 1.8.

When the driving is intense, the coherence of the quantum 2-level system saturates, departing from the linear dipole case. This means that the dipole is no longer proportional to the exciting field, but goes to 0. This observation validates the fact that to simulate the system when excited with an intense probe, the linear (classical) coupled dipole equations are not sufficient and require refinement to account for the saturation of the atoms. The principle of the *nonlinear* coupled dipole simulations will be explained later in this chapter.

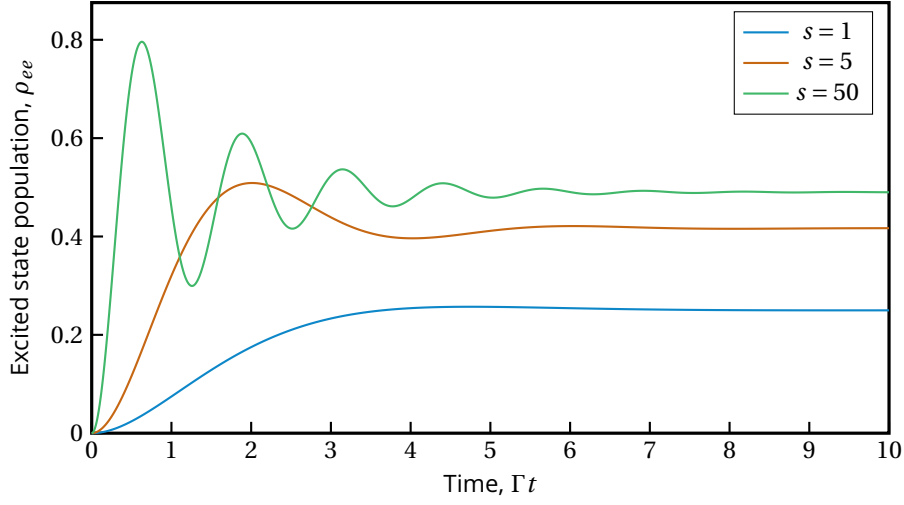


Figure 1.7:  $\rho_{ee}$  for various saturation parameter  $s$ . As a function of time, we see the so-called Rabi oscillations. For these calculations, we took  $\rho_{ee}(t=0) = 0$  and  $\Delta = 0$ .

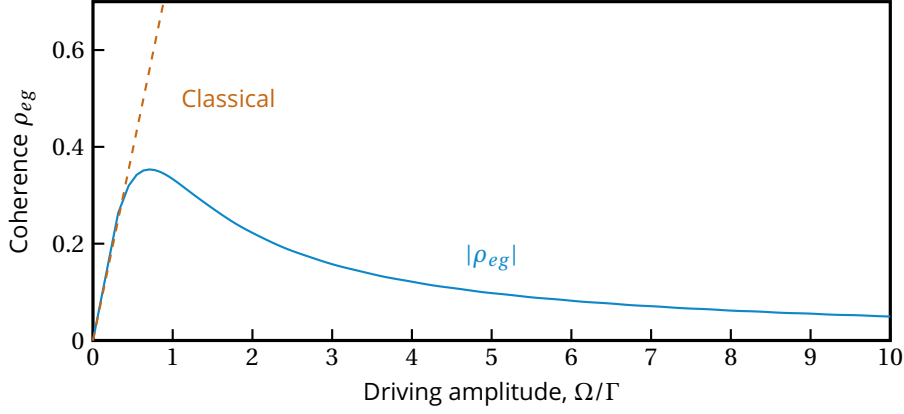


Figure 1.8:  $|\rho_{eg}|$  as a function of the driving amplitude (blue). When the driving is intense, the coherence is different from the classical dipole case, in dashed line. In particular, the coherence goes to zero at high intensity, while the population saturates.

### Two and more interacting atoms : subradiance and superradiance

For  $N$  atoms, the full quantum description is based on the density matrix formalism and the master equation. The system of  $N$  two-level atoms is represented by a density matrix  $\rho$  of size  $2^N \times 2^N$ . The dynamics is given by the master equation (Friedberg et al. 1973)

$$\frac{d\rho}{dt} = \sum_n \left[ \frac{1}{i\hbar} [H_n, \rho] + \mathcal{L}_n(\rho) \right] + \sum_n \sum_{m \neq n} \left[ \frac{1}{i\hbar} [H_{nm}, \rho] + \mathcal{L}_{nm}(\rho) \right]. \quad (1.10)$$

Here,  $H_n$  and  $\mathcal{L}_n$  are the one atom Hamiltonian and Lindblad operators,

$$H_n = \hbar \left( \frac{\Omega_n^+}{2} \sigma_n^+ + \frac{\Omega_n^-}{2} \sigma_n^- - \Delta_n e_n \right)$$

$$\mathcal{L}_n(\rho) = \frac{\Gamma}{2} (2\sigma_n^- \rho \sigma_n^+ - e_n \rho - \rho e_n)$$



where we define

$$\begin{aligned} e_n &= |e_n\rangle\langle e_n| \\ \sigma_n^- &= |g_n\rangle\langle e_n| \\ \sigma_n^+ &= |e_n\rangle\langle g_n| \end{aligned}$$

and  $\Omega_n^+ = (\Omega_n^-)^*$  is the complex Rabi frequency seen by the atom  $n$  and  $\Delta_n$  is the detuning of the transition for the atom  $n$ .  $H_{nm}$  and  $\mathcal{L}_{nm}$  are given by (Asenjo-Garcia et al. 2017)

$$H_{nm} = \hbar\Omega_{nm}\sigma_n^+\sigma_n^-$$

and

$$\mathcal{L}_{nm} = \frac{\Gamma_{nm}}{2} (2\sigma_n^-\rho\sigma_m^+ - \sigma_m^+\sigma_n^-\rho - \rho\sigma_m^+\sigma_n^-).$$

In the previous equations,  $\hbar\Omega_{nm}$  is the real part of the dipole-dipole interaction  $V_{nm}$  (eq. 1.6) and  $\Gamma_{nm}$  is the collective decay, two times the imaginary part of  $V$  (Krämer and Ritsch 2015; Do Espirito Santo et al. 2019). The Linblad operator describes a collective decay, characterized by the matrix  $\gamma$  made of  $\Gamma_{nm}$ . This matrix is not diagonal, so the decay channels are not independent. In the case of  $N = 2$  atoms separated by a distance  $R$ , the matrix is written

$$\gamma = \begin{pmatrix} \Gamma & \bar{\Gamma}(R) \\ \bar{\Gamma}(R) & \Gamma \end{pmatrix} \quad (1.11)$$

where  $\Gamma$  is the single atom decay rate and  $\bar{\Gamma}(R) = 2\text{Im}(V(R))/\hbar$ . This matrix has for eigenvectors  $|\pm\rangle = \frac{1}{\sqrt{2}}(|e_1g_2\rangle \pm |g_1e_2\rangle)$  with eigenvalues  $\Gamma \pm \bar{\Gamma}(R)$ . These states are also eigenstates of the Hamiltonian with the same eigenenergies than in the classical case. We find exactly the same results than using the classical model. Moreover, we find that for infinitely close atoms, ( $R = 0$ ),  $\Gamma_+ = 2\Gamma$  and  $\Gamma_- = 0$ .

The states  $|+\rangle$  and  $|-\rangle$  are respectively called *superradiant* state and *subradiant* state. This is due to their de-excitation rate, which is respectively faster and slower than that of an isolated atom. Note that this result is strictly true in the limit  $R \rightarrow 0$ . Otherwise, the states are shifted due to the distance dependent dipole-dipole interaction and their decay thus depends on  $R$  (Figure 1.4). For  $k_0R \geq 1$ , which is the case in most experiments with cold atoms or ions, we thus expect the decay rate to oscillate with  $R$ . Indeed,  $\text{Im}(V) \propto \frac{\sin k_0R}{k_0R}$ . Researchers have observed the variation of the decay rate as a function of the distance between 2 ions (Devoe and Brewer 1996). These properties of the  $|+\rangle$  and  $|-\rangle$  states are general and do not depend on the studied system. Superradiance and subradiance have been observed in a very wide range of systems, from hot atomic vapors (Pavolini et al. 1985) to cloud of cold atoms (Guerin, Araújo, et al. 2016), atoms in hollow core fiber (Okaba et al. 2019), nanofiber (Solano et al. 2017), Rydberg atoms (Wang et al. 2007), molecular systems (Hettich et al. 2002; McGuyer et al. 2015) and artificial atoms (Angerer et al. 2018) just to cite a few. This model allows one to understand superradiance and subradiance. A thorough experimental study of these phenomena was carried out during my thesis, and will be the subject of following chapters.

## 2 Numerical methods

The purpose of this second part is to explain the numerical simulations frameworks that are used to describe the collective interaction of light with the ensembles produced in our experiments. First, we will give detail about the simulations performed in the framework of the classical model. We will then see how to take into account the effects of saturation by realizing, in the mean field approximation, simulations of nonlinear coupled dipoles. Finally, we will discuss different possibilities to simulate problems beyond the mean field approximation.

### 2.1 Coupled Dipoles Simulations

This type of simulation is widely used to model linear systems of coupled dipoles, for which the amplitude of the dipoles is proportional to that of the exciting field. The model is often treated in the scalar case, for which the dipoles are parallel to the exciting field (see section 1.1). Otherwise, the model is said to be vectorial. Its general character allows it to be used in many publications to simulate atomic ensembles ((Do Espirito Santo et al. 2019; Meir et al. 2014; Bromley et al. 2016; Zhu et al. 2016; Kwong et al. 2019; Bienaimé et al. 2011; Chabé et al. 2014; Courteille et al. 2010; Sokolov and Guerin 2019), but also artificial atoms such as superconductors (Lin et al. 2019) or nanocavities (Dobbertin et al. 2020)..

The principle of the simulation is simply to numerically solve the coupled dipoles system (1.7). These equations can be rewritten

$$\dot{b}_m = \left( i\Delta - \frac{\Gamma}{2} \right) b_m + i \left( \Omega_m^L + \frac{3\Gamma}{4} \sum_{n \neq m} f_{mn} b_n \right) \quad (2.1)$$

with  $b_m = d_m / |D_0|$ ,  $\Omega_m^L = \frac{|D_0| E_L(\mathbf{r}_m)}{\hbar}$  and

$$f_{mn} = \frac{e^{ik_0 R_{mn}}}{(k_0 R_{mn})^3} [(3 \cos^2 \theta_{mn} - 1)(1 - ik_0 R) + \sin^2 \theta_{mn} (k_0 R)^2]$$

using the definitions of figure 1.3 and equation 1.6 with  $\mathbf{e} \cdot \mathbf{u} = \cos \theta_{mn}$ . Let us write these equations in matrix form

$$\frac{d}{dt} \mathbf{b}(t) = \mathbf{M} \mathbf{b}(t) + \mathbf{w} \quad (2.2)$$

with

$$M_{mn} = \delta_{mn} \left( i\Delta - \frac{\Gamma}{2} \right) + (1 - \delta_{mn}) i \frac{3\Gamma}{4} f_{mn}$$

and  $w_m = i\Omega_m^L$ . We deduce the dipoles from it in the steady-state solution

$$\mathbf{b}_s = -\mathbf{M}^{-1} \mathbf{w}. \quad (2.3)$$

#### Eigenvalues

Following for example (Bettles et al. 2016a), one shows that the eigenvalues  $\mu_l$  of  $\mathbf{M}^{-1}/i$  are related to the decay rate  $\Gamma_l$  and the shift  $\Delta\omega$  of the collective mode  $l$  of the dipole ensemble

$$\begin{aligned} \Delta\omega_l &= -\text{Re}[\mu_l] \\ \Gamma_l &= 2\text{Im}[\mu_l] \end{aligned}$$

To numerically compute the eigenmodes of a system, one simply computes the  $M$  matrix and inverts it. The number of emitters can be relatively large (typically up to a few thousand) as the inversion of  $M$  has a polynomial cost.

Let us calculate the eigenvalues for different typical systems that we will study experimentally in the following chapters. To begin, consider a pair of atoms placed at distances  $R$  ranging from almost 0 to  $\lambda_0$ . We plot in figure 1.9 these eigenvalues in the  $(\Delta\omega, \Gamma)$  plane. The eigenvalues spiral around the non-interacting case ( $\Delta\omega = 0, \Gamma = \Gamma_0$ ), approaching this point as  $R$  increases. There are 2 eigenvalues for a given  $R$ , depending of the relative phase of the dipole. The decay time of two branches of the spiral have for asymptotes  $\Gamma = 0$  and  $\Gamma = 2\Gamma_0$  respectively. They correspond to the decay of 2 infinitely close parallel dipoles. As the atoms are getting closer, the shift of the resonance diverges. We recover with this simulation the results obtained in Section 1.1 for the eigenvalues of  $d_{\pm}$ .

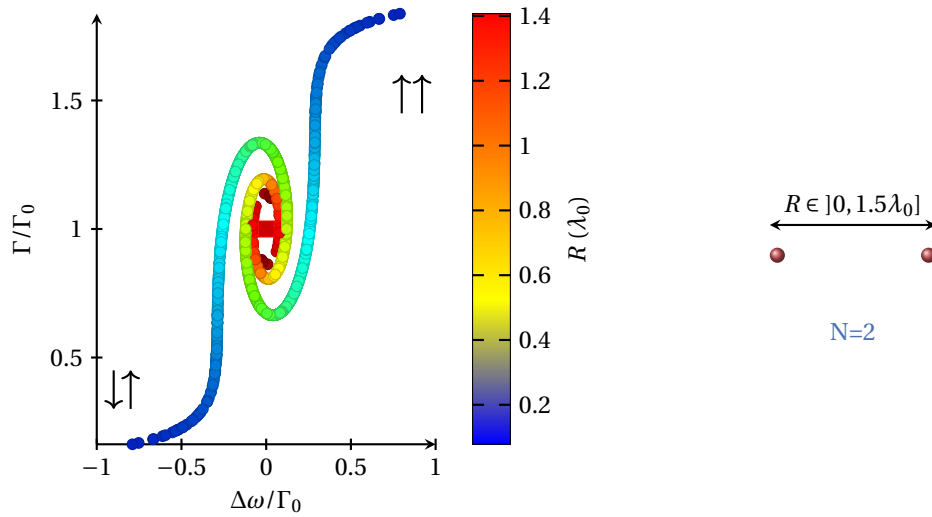


Figure 1.9: Collective decay and shift for a 2-atom pair for 1000 interatomic distances  $R$  smaller than  $1.5\lambda_0$ . The color code indicates the values of  $R$ . The red square corresponds to the single atom response.

The next example of interest is the 1D chain of dipoles equally spaced with a distance  $0.6\lambda_0$  as represented in the figure 1.10. There the eigenvalues are arranged along two branches that are not centered on the values without interactions. This would indicate an average shift in the resonance and a variation in the average decay rate due to the interactions when all modes are excited. We will verify this experimentally in the following chapters.

The last interesting example is a disordered gaussian cloud, figure 1.11. The eigenvalues are quite spread out in this case. We observe that the range of  $\Delta\omega$  is small with respect to the range of  $\Gamma$ .

The analysis of the modes gives information about the collective response of the system to an excitation, in particular the mean frequency shift and linewidth (Schilder et al. 2016; Goetschy and Skipetrov 2011; Skipetrov and Goetschy 2011). As the matrix  $M$  is not Hermitian but is complex symmetric, the eigenvectors  $\mathbf{m}_l$  are not orthogonal and they do not form a basis. Using reference (Ruostekoski and Javanainen 2017), we introduce the effective weight

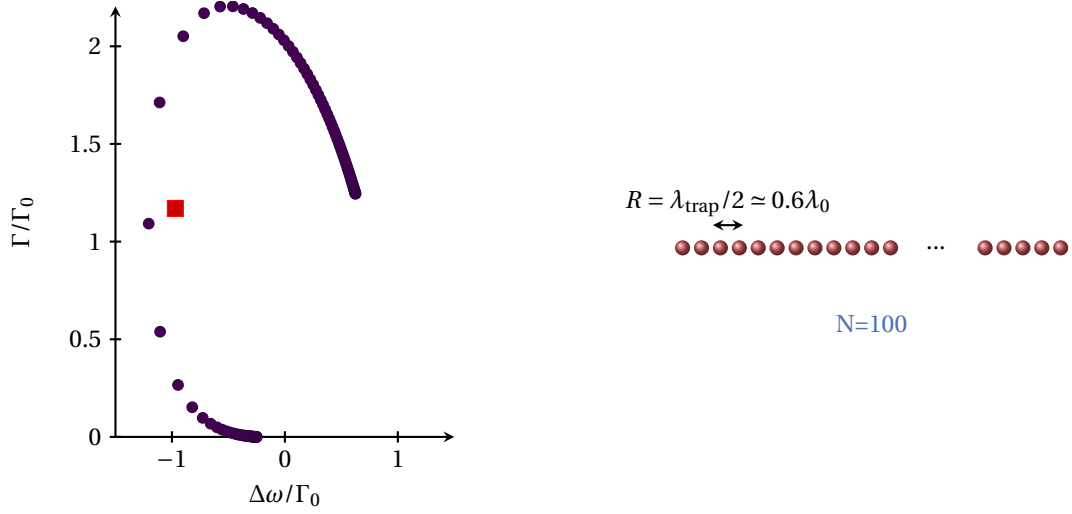


Figure 1.10: Collective decay and shift of a defect-free 1D chain of  $N = 100$  atoms with interatomic distance  $0.6\lambda_0$ . The red square corresponds to the weighted average response (see text below).

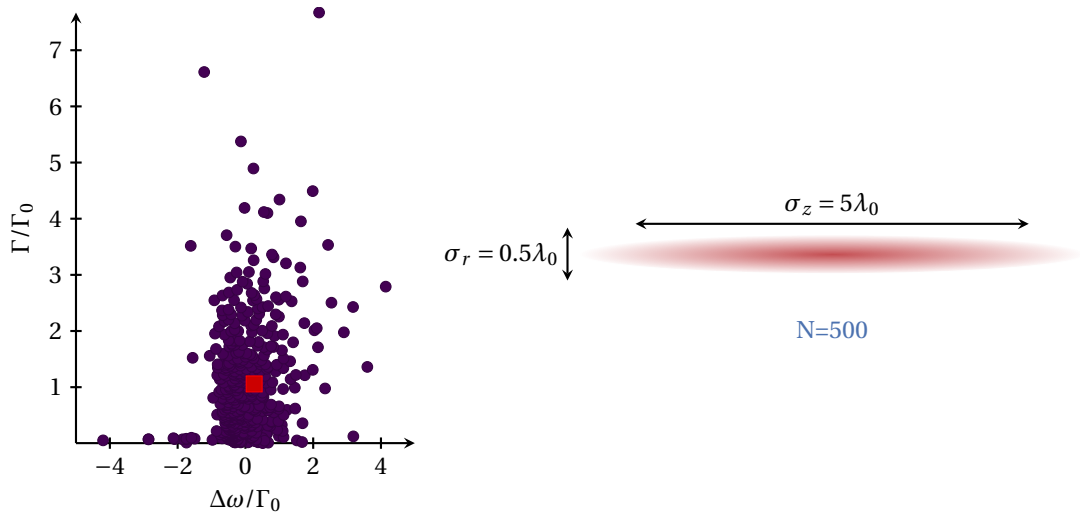


Figure 1.11: Collective decay and shift of a gaussian cloud of  $N = 500$  atoms with sizes  $\sigma_r$  and  $\sigma_z$ . The red square corresponds to the weighted average response (see text below).

of the eigenvector  $\mathbf{m}_l$  in the state  $\mathbf{b}$  as follows :

$$w_l = \frac{|\mathbf{m}_l^* \cdot \mathbf{b}|^2}{\sum_{l'} |\mathbf{m}_{l'}^* \cdot \mathbf{b}|^2}$$

We deduce a decomposition of the  $\mathbf{b}_s$  vectors as superpositions of the  $\mathbf{m}_l$ ,

$$\mathbf{b}_s = \sum_l w_l \mathbf{m}_l$$

This decomposition depends on the driving  $\mathbf{w}$  via  $\mathbf{b}_s$ . All modes are thus not necessarily excited. We therefore deduce the collective response (frequency shift and linewidth) of the

ensemble by calculating the average decay and the average shift of the resonance . For the examples above and considering a uniform excitation  $\mathbf{w}$ , the average collective response is plotted with a red square in the figures 1.9,1.10 and 1.11. In the case of the chain, this response is quite different than the non-interacting ( single atom) response, indicating that the collective effects are strong in this system.

### Time dependent scattered light intensity

From the dipoles, we calculate the light emitted by a cloud of any number of atoms and dimension in the low driving regime, where the dipoles can be described classically. Indeed, the electric field at a position  $\mathbf{r}$  from the cloud is in far field (Jackson 1999)

$$\mathbf{E}(\mathbf{r}, t) \propto \frac{e^{-i\omega_0(t-r/c)}}{r} \sum_{m=1}^N e^{-ik_0 \frac{\mathbf{r} \cdot \mathbf{r}_m}{r}} b_m(t)$$

where  $\mathbf{r}_m$  is the position of the atom  $m$  and  $b_m$  is the dipole. The scattered intensity is thus given by

$$I(\mathbf{r}, t) \propto \frac{1}{r^2} \left| \sum_{m=1}^N e^{-ik_0 \frac{\mathbf{r} \cdot \mathbf{r}_m}{r}} b_m(t) \right|^2$$

This formula allows us to calculate the angular- and time-dependent response during the driving ((Araújo, Guerin, et al. 2018)) and after. This allows us to simulate the collective decay of a cold atom ensemble (Zhu et al. 2016), showing for example the presence of subradiance (Guerin, Araújo, et al. 2016).

### Spectrum of the scattered light

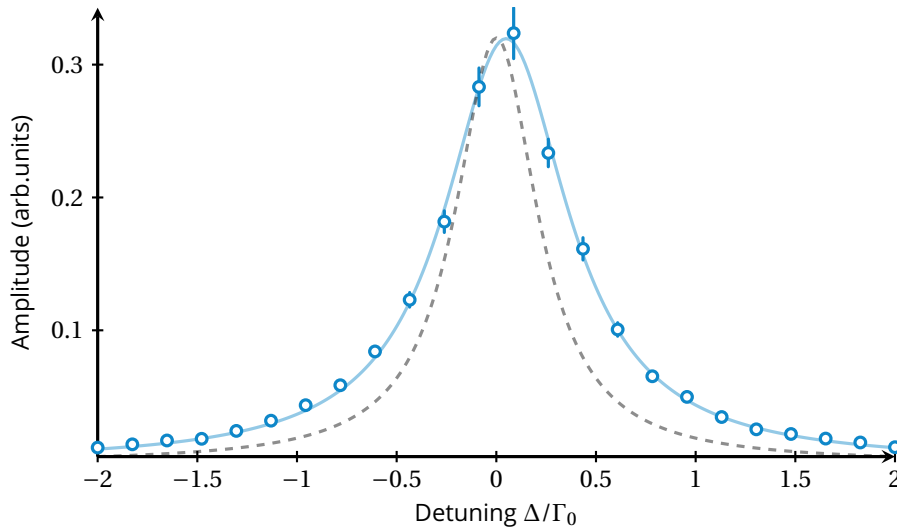


Figure 1.12: Fluorescence spectrum of a spherical gaussian cloud with density  $\rho = 0.1/k_0^3$  containing  $N = 100$  atoms illuminated with a plane wave perpendicularly to the direction of observation. The signal is averaged over 500 random atomic positions. The error bars correspond to the standard errors. The solid line is a lorentzian fit. We plot the fluorescence spectrum of a single atom with a dashed line.

In this manuscript, the spectrum of the emitted light corresponds to the total scattered intensity as a function of the frequency of the driving. In particular, this is not the frequency of the scattered light. In the figure 1.12, we plot the spectrum of a spherical gaussian cloud. Even if in this case the cloud is dilute (density  $\rho = 0.1/k_0^3$ ), we have to average over 500 times to reduce the effect of the close pairs of atoms. Indeed, their interaction is large and the numerics are very sensitive to their exact value. Some works use an exclusion volume in the simulations to avoid this effect (Araújo, Guerin, et al. 2018). In the figure 1.12, we see that the fluorescence spectrum of the cloud is shifted compared to the single atom case and its width is larger due to the interactions. The shape is still a lorentzian in this case but this is not necessarily the case. In other situation, when the density and thus the interactions increase, the shape evolves and becomes asymmetric. In the same way, one evaluates the field transmitted by the cloud: the total field is then the sum of the fields radiated by the dipoles and the driving field.

The coupled dipole predictions, while correct in dilute ensembles for which the interactions are weak, become largely incompatible with experiments in dense clouds, even when  $s \ll 1$  (Jennewein, Y. R. P. Sortais, et al. 2016; Browaeys, Jennewein, et al. 2016). The disagreement remains even when one refines the model by taking into account the internal structure of the atoms (12 levels for the D2 transition of rubidium, (Jennewein, Brossard, et al. 2018)) and the atomic motion due to the non-zero temperature of the atoms.

In the simulations described above, we did not take into account the saturation effects which appear when  $s$  is no longer negligible with respect to 1. To account for the saturation, we use for this the *nonlinear coupled dipoles equations* (NLCD).

## 2.2 Nonlinear Coupled Dipoles Simulations

The principle of this method is to include the coupled dipoles into the Optical Bloch Equations (see section 1.2). For the dipole  $m$ , they are

$$\begin{cases} \frac{d\rho_{ee,m}}{dt} = -\Gamma\rho_{ee,m} + i\rho_{eg,m}\frac{\Omega_m}{2} - i\rho_{ge,m}\frac{\Omega_m^*}{2} \\ \frac{d\rho_{eg,m}}{dt} = (i\Delta - \Gamma/2)\rho_{eg,m} + i\frac{\Omega_m}{2}(\rho_{ee,m} - \rho_{gg,m}) \end{cases} \quad (2.4)$$

where  $\Omega_m$  is now the Rabi frequency due to the total field experienced by the atom  $m$ ,

$$\frac{\Omega_m}{2} = d_m \cdot \left[ \mathbf{E}_L(\mathbf{r}_m) + \sum_{n \neq m} G(\mathbf{r}_m - \mathbf{r}_n) \mathbf{d}_n \right]$$

where we have introduced  $G(\mathbf{r})$  the Green's function as in section 1.1 and  $d_m$  is the dipole  $m$ . We define the population inversion  $z_m = \rho_{ee,m} - \rho_{gg,m}$ , following (Glicenstein, Ferioli, Šibalić, et al. 2020), and  $d_m = 2|D_0|\rho_{eg,m} = b_m|D_0|$  with  $|D_0|$  the dipole matrix element between  $|e\rangle_m$  and  $|g\rangle_m$ . From the equations above, we obtain the following equations

$$\begin{cases} \frac{dz_m}{dt} = -\Gamma(1 + z_m) + i\text{Im}[b_m\Omega_m^*] \\ \frac{db_m}{dt} = i(\Delta - \Gamma/2)b_m - iz_m\Omega_m \end{cases} \quad (2.5)$$

The first equation is thus about the population, and the second about the dipole. In steady state, solving (2.5) is equivalent to solve the coupled system

$$\mathbf{d}_m = \alpha_{\text{NL}} \left( \mathbf{E}(\mathbf{r}_m) + \sum_{n \neq m} G(\mathbf{r}_m - \mathbf{r}_n) \mathbf{d}_n \right)$$

where

$$\alpha_{\text{NL}}(\Delta, \Omega) = \frac{6\pi i}{k_0^3} \frac{1 + 2i\Delta/\Gamma}{1 + \left(\frac{2\Delta}{\Gamma}\right)^2 + \frac{2\Omega^2}{\Gamma^2}}$$

is the nonlinear expression of the atomic polarizability (Grynberg, Aspect, et al. 2010) given by the solution of the optical Bloch Equations (1.8).

If we neglect the population of the excited state,  $\rho_{ee,m} \ll 1$ , then  $z = -1$ , we recover the (classical) coupled dipoles equation (1.7). NLCD allow the simulation of coupled dipoles driven with  $s > 1$ , taking into account the saturation of the dipoles. However, we will see in the next section that this model contains a mean-field approximation that does not account for the quantum correlations between atoms. For this, a quantum treatment of the problem is required.

### 2.3 Fully quantum models

The full quantum description, described in section 1.2, is generally not solvable analytically and is numerically limited to a small number of atoms. Because of the  $2^N$  size of the Hilbert space, a full time-dependent resolution of these equations is indeed computationally hard and limited to a small number of atoms (Daley 2014). The numerical resolution based on a quantum Monte carlo (QMC), (Carmichael 1993) allows one to reduce the number of operation to calculate, but remains very demanding. There are efficient numerical frameworks to compute the solutions, for example in the *MATLAB* programming language (Tan 1999) or open source, coded in *Python* (Johansson et al. 2012). One can recover the NLCD from the full density matrix using a mean-field product state ansatz (Do Espirito Santo et al. 2019)

$$\rho = \bigotimes_m \rho_m$$

where the  $\rho_m$  is the local density matrix of the atom  $m$ . Taking the partial trace, we obtain the governing equations for all  $\rho_m$

$$\frac{d\rho_m}{dt} = \text{Tr}_{n \neq m} \left( \frac{d\rho}{dt} \right)$$

Following (Do Espirito Santo et al. 2019), we can recover the equations (2.5) by defining  $b_m = \langle \sigma_m^- \rangle$ ,  $z_m = \langle \sigma_m^+ \sigma_m^- - \sigma_m^- \sigma_m^+ \rangle$  and using

$$\rho_m = (\mathbb{1} + 2b_m^* \sigma_m^- + 2b_m \sigma_m^+ + z_m \sigma_m^z).$$

The mean-field approximation mean physically that two-particle expectations can be factorized, that is for an observable  $O$  and two atoms  $n$  and  $m$ ,

$$\langle O_m O_m \rangle \simeq \langle O_m \rangle \langle O_m \rangle. \quad (2.6)$$

This approximation gives good results when the interparticle interactions are weak (Krämer and Ritsch 2015). As an example, we show on figure 1.13 the results of NLCD and QMC done by Nikola Šibalić for a half-filled 1D chain with interatomic distance  $0.6\lambda_0$ . The two simulations are in reasonable agreement. As explained before, this comparison is only possible for a small atom number, here  $N = 6$ .

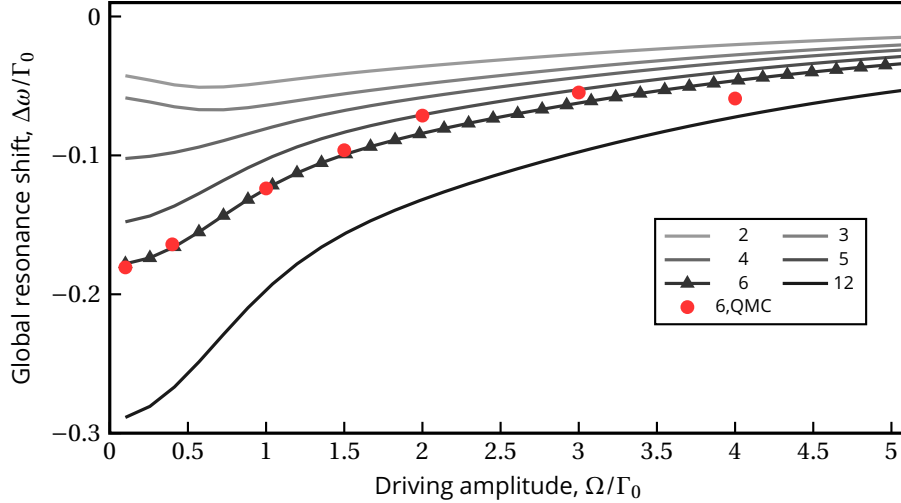


Figure 1.13: Global resonance shift as a function of the driving for a  $N$ -atoms chain (see text). Comparison between nonlinear coupled dipoles (NLCD) and Quantum Monte Carlo (QMC).

However, the mean-field approximation is not sufficient to calculate pair correlations. It can be extended to higher order of correlations using the so-called *cumulants method*.

### Cumulant method

The main idea is to still perform approximations but including the expectation values of one operator (standard mean-field), two operators, three operators... This is understood as a "higher order mean-field". At each step, the level of accuracy increases, but the computational cost increases rapidly. The number of operations necessary to compute the mean-field is  $N^2$  according to equation (2.6). We can calculate the higher order particle correlations using the cumulant expansion (Kubo 1962). The joint cumulant of a product of  $n$  operators is by definition (Plankensteiner, Hotter, et al. 2021)

$$\langle O_1 O_2 \dots O_n \rangle_c = \sum_{p \in P(I)} (|p| - 1)! (-1)^{|p|-1} \prod_{B \in p} \left\langle \prod_{i \in B} O_i \right\rangle. \quad (2.7)$$

where  $I = \{1, 2, \dots, n\}$ ,  $P(I)$  is the set of all partitions of  $I$  and  $|p|$  is the length of partition  $p$ . As an example, let us consider  $n = 3$ ,

$$\langle O_1 O_2 O_3 \rangle_c = \langle O_1 O_2 O_3 \rangle - \langle O_1 O_2 \rangle \langle O_3 \rangle - \langle O_1 O_3 \rangle \langle O_2 \rangle - \langle O_1 \rangle \langle O_2 O_3 \rangle + 2 \langle O_1 \rangle \langle O_2 \rangle \langle O_3 \rangle.$$

Importantly the cumulant of order  $n$  is composed of averages of order  $n$  or lower. The key argument of the cumulant method is a theorem (Kubo 1962) that says that the cumulant is equal to zero if any one of the operator that is inside is statistically independent of the others.



The principle of the calculations is thus to assume that the cumulant of a given order  $n$  is zero. The averages of order  $n$  can thus be expanded in terms of only lower order averages. It is clear that assuming this for  $n = 2$  in equation (2.7) gives  $\langle O_1 O_2 \rangle = \langle O_1 \rangle \langle O_2 \rangle$ , that is the usual mean-field hypothesis. Depending of the complexity of the problem, one can increase the order  $n$ . This method has been used at the third order for example to simulate the dynamics of an open spin ensemble (Krämer and Ritsch 2015) or the superradiance in inverted multi-level atomic clouds (Sutherland and Robicheaux 2017). Some cases where the third order is not sufficient, for example to calculate the intensity correlation function  $g^2(\tau)$ , are detailed in (Robicheaux and Suresh 2021). Recently a *Julia* framework was developed to calculate the cumulant expansion (Plankensteiner, Hotter, et al. 2021).

### 3 Conclusion

In this chapter, we have first recall the theoretical notions necessary to describe the interaction between light and an atomic ensemble. In the second part, we have explained the different types of numerical simulations that can be performed to make reliable predictions about our systems, even if the models are not analytically solvable.



# Experimental setup

\*\*\*

In this chapter, we first explain how to optically trap cold atoms. The experimental setup is then described in its main parts. In the last section, we present how a closed two-level transition is isolated using optical pumping and magnetic fields.

## Contents

<b>1</b>	<b>Trapping and observing cold atoms</b>	<b>32</b>
1.1	Trapping cold atoms in an Optical Dipole Trap	32
1.2	Brief overview of the setup	34
1.3	The imaging systems	37
1.4	The <i>OptoTelescope</i>	43
<b>2</b>	<b>Preparation and characterization of a 1D atomic chain</b>	<b>48</b>
2.1	Preparation of the chain	48
2.2	Controllable length	49
2.3	Oscillation frequencies	49
2.4	Temperature and radial extension	51
<b>3</b>	<b>Control of the atomic internal state</b>	<b>52</b>
3.1	Compensation of the stray magnetic fields	52
3.2	Preparing a two-level system	55
<b>4</b>	<b>Conclusion</b>	<b>60</b>

## 1 Trapping and observing cold atoms

### 1.1 Trapping cold atoms in an Optical Dipole Trap

#### Dipolar potential

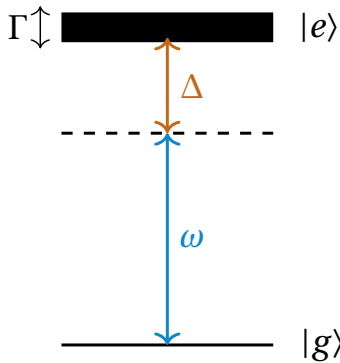


Figure 2.1: Parameters of the problem. The 2-level atom is driven by an electric field of frequency  $\omega$  with detuning  $\Delta$ .

As seen in the first chapter, an electric field  $\mathbf{E}$  with frequency  $\omega$  applied on an atom induces an atomic dipole

$$\mathbf{d} = \alpha \mathbf{E}(\omega)$$

where  $\alpha$  is the complex polarizability. The interaction potential of the induced dipole moment in the driving field is given by the time average

$$U_{\text{dip}} = -\frac{1}{2} \langle \mathbf{d} \cdot \mathbf{E} \rangle = -\frac{1}{2} \text{Re}(\alpha) |\langle \mathbf{E} \rangle|^2 \simeq \frac{\hbar \Omega^2}{4\Delta}$$

where we have introduced the Rabi frequency  $\Omega = |\mathbf{d} \cdot \mathbf{E}| / \hbar$ , used the expression of the polarizability (eq. (1.3)) and  $\Delta$  the detuning, as represented in figure 2.1. The formula above is valid under the assumption of low saturation and large detuning  $\Delta \gg \Gamma$ .

The saturation intensity  $I_{\text{sat}}$  is defined by

$$\frac{I}{I_{\text{sat}}} = 2 \left( \frac{\Omega}{\Gamma} \right)^2.$$

For the  $D_2$  line of  $^{87}\text{Rb}$ ,  $I_{\text{sat}} = 1.67 \text{ mW cm}^{-2}$ . One writes the potential as a function of the field intensity,

$$U_{\text{dip}} = \frac{\hbar \Gamma^2}{8\Delta} \frac{I}{I_{\text{sat}}}.$$

Considering the D1 and D2 lines of  $^{87}\text{Rb}$ , one notices that  $\Gamma_{D1} = 2\pi \times 5.7 \text{ MHz} \simeq \Gamma_{D2} = 2\pi \times 6.1 \text{ MHz}$ , and that  $I_{\text{sat}}^{D1} \simeq I_{\text{sat}}^{D2}$ . We write  $\Delta_1$  the detuning to the excited state ( $5P_{1/2}$ ) and  $\Delta_2$  the detuning to the excited state ( $5P_{3/2}$ ), as represented in figure 2.2. With the appropriate Clebsch-Gordan coefficients, for a  $\pi$ -polarized electric field, one shows that

$$U_{\text{dip}} = \frac{\hbar \Gamma^2}{8} \frac{I}{I_{\text{sat}}} \left( \frac{1}{3\Delta_1} + \frac{2}{3\Delta_2} \right). \quad (1.1)$$

A more detailed description of the potential for arbitrary light polarization is given in the thesis (Fuhrmanek 2011).

From the expressions above, it appears that light can be used to create a potential whose depth is proportional to the intensity of the light. Experimentally, the focused laser beams used to create optical traps are Gaussian beams. Their intensity dependence will determine the trapping potential landscape. The following part proposes some reminders on such traps, as in (Brossard 2019).

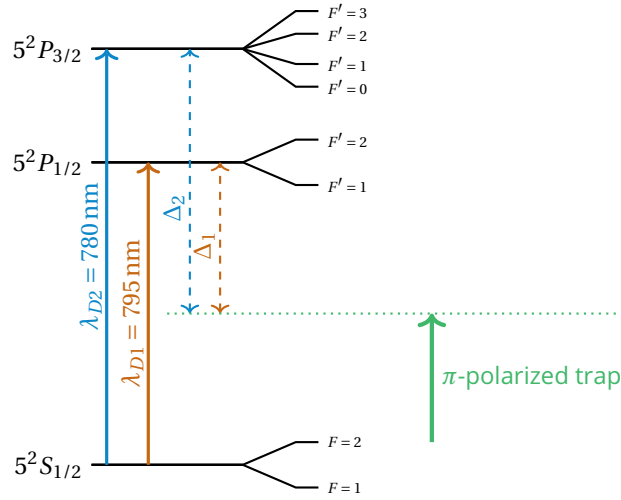


Figure 2.2: Hyperfine structure and transitions considered for the  $D1$  and  $D2$  lines. The laser light (polarization  $\pi$ ) can coupled different Zeeman sublevels with each other. We call  $\Delta_1$  and  $\Delta_2$  the detuning with respect to the  $D1$  and  $D2$  line, respectively.

### Gaussian traps

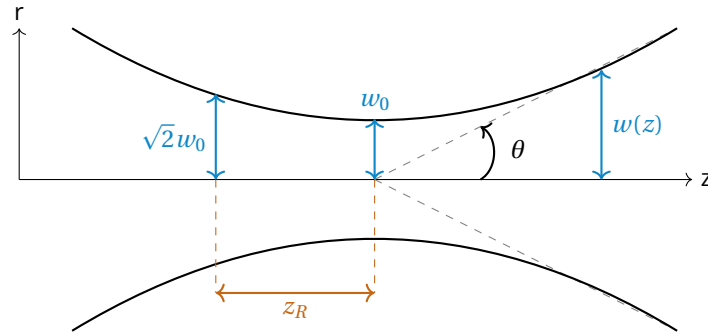


Figure 2.3: Parameters of a Gaussian beam.

The electric field of a Gaussian beam  $\mathbf{E}(\mathbf{r}, z)$  (under the paraxial approximation) has for expression, assuming a polarization in the  $x$ -direction and a propagation along the  $z$ -direction,

$$\mathbf{E}(r, z) = E_0 \frac{w_0}{w(z)} \exp\left(\frac{-r^2}{w(z)^2}\right) \exp\left(-ikz - ik\frac{r^2}{2R(z)} + i\psi(z)\right) \mathbf{e}_x.$$

In the expression above,  $r$  is the radial distance from the center axis of the beam,  $z$  is the axial distance from the focus,  $k = 2\pi/\lambda$ ,  $E_0$  is the electric field amplitude. We define the waist  $w$ , the radius of curvature  $R$  and the Gouy phase  $\psi$  by

$$\begin{aligned}
w(z) &= w_0 \sqrt{1 + \left(\frac{z}{z_R}\right)^2}, \\
R(z) &= z \left[ 1 + \left(\frac{z_R}{z}\right)^2 \right], \\
\psi(z) &= \arctan\left(\frac{z}{z_R}\right),
\end{aligned}$$

as represented in the figure 2.3.  $w_0$  is the radius of the beam at the focus and  $z_R = \frac{\pi w_0^2}{\lambda}$  is the Rayleigh range. The light intensity can be computed from this, using  $I = \frac{1}{2} \epsilon_0 c |\mathbf{E}|^2$ . It gives

$$I(r, z) = \frac{I_0}{1 + (z/z_R)^2} \exp\left(-\frac{2r^2}{w(z)^2}\right).$$

The intensity at focus  $I_0$  is related to the beam power  $P$  by  $I_0 = \frac{2P}{\pi w_0^2}$ . Using equation (1.1), the trapping potential has the same shape than the beam:

$$U(r, z) = -\frac{U_0}{1 + (z/z_R)^2} \exp\left(-\frac{2r^2}{w(z)^2}\right). \quad (1.2)$$

where  $U_0 = -\frac{\hbar \Gamma^2}{8\Delta} \frac{I_0}{I_{\text{sat}}} > 0$  when  $\Delta < 0$ . Given expression (1.2), the potential is attractive (repulsive) for a red- (blue-) detuned trapping laser. When  $\Gamma \ll \Delta$ , the spontaneous emission is negligible and the potential is conservative, creating an *optical dipole trap*. In the attractive case, near the trap center, the potential is approximated by a harmonic potential whose radial and axial oscillation frequencies are

$$\begin{aligned}
\omega_r &= \sqrt{\frac{4U_0}{m w_0^2}} \\
\omega_z &= \sqrt{\frac{2U_0}{m z_R^2}}.
\end{aligned} \quad (1.3)$$

Using the equipartition theorem, one determines the size of the cloud of the temperature  $T$  inside the trap as a function of the trap parameters,

$$\begin{aligned}
\sigma_r &= w_0 \sqrt{\frac{k_B T}{4U_0}} \\
\sigma_z &= z_R \sqrt{\frac{k_B T}{2U_0}}.
\end{aligned} \quad (1.4)$$

In most of the current experiments using cold atoms, they are first cooled (Phillips and Metcalf 1982; Joffe et al. 1993) and trapped in a magneto-optical trap (Lett et al. 1988; Helmerston et al. 1992). This trap is then used as a reservoir of atom to load dipole traps (Grimm et al. 2000; Kuppens et al. 2000). Let us now present the experimental system in its broad outline.

## 1.2 Brief overview of the setup

The general architecture of the experiment is relatively usual for a cold atom experiment. The principle of the different parts necessary for the cooling of a rubidium vapor: oven, Zee-

man slower, magneto-optical trap (MOT) can be found for example in (Foot 2005) and is not detailed here. This part aims at showing briefly the layout of the experiment and its specificities. In the experiment, the MOT is made of three perpendicular pairs of counter-propagating maser beams with diameter 1 cm and a magnetic gradient created by a pair of vertical coils in anti-Helmholtz configuration. The cold atoms, slowed down at the oven exit by a Zeeman slower, are captured by the MOT. The MOT is then used as a reservoir of atoms to load the dipole trap, which is created by strongly focusing an off-resonant laser via aspheric lenses.

### In-vacuum system

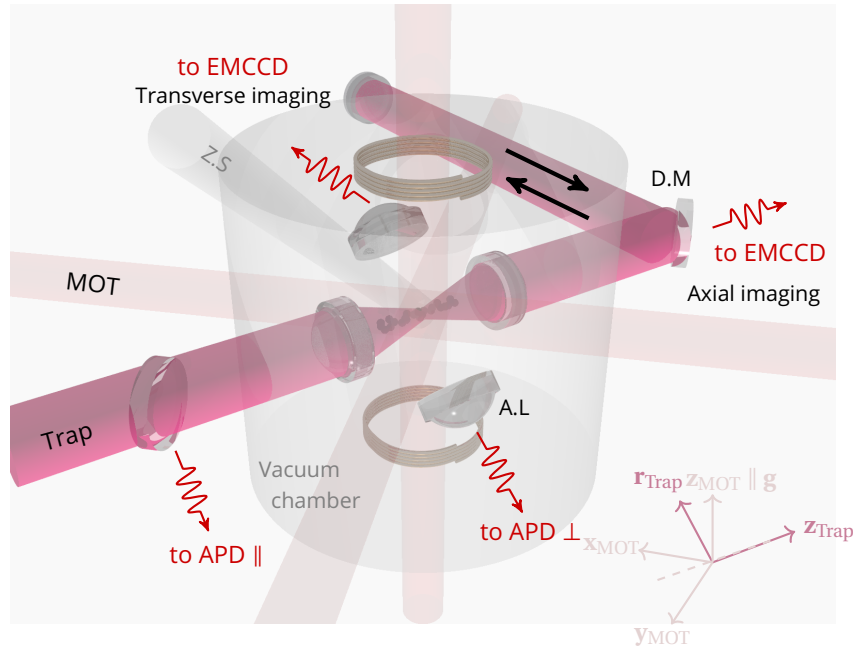


Figure 2.4: Schematic of the experimental setup. See description in the text. A.L stands for aspherical lens, D.M for dichroic mirror and Z.S for Zeeman slower. The plane that contains  $x_{MOT}$ ,  $y_{MOT}$  and  $z_{Trap}$  is horizontal, therefore perpendicular to gravity  $\mathbf{g}$ .  $z_{MOT}$  is parallel to  $\mathbf{g}$  and the axis formed by the last 2 aspherical lenses  $\mathbf{r}_{Trap}$  is at  $45^\circ$  from the horizontal and the vertical.

As shown in figure 2.4, our experimental system is composed of four aspherical lenses in the "maltese cross" configuration (Bruno et al. 2019). This configuration consists of two pairs of confocal lenses whose axes intersect at  $90^\circ$ . These lenses are placed under vacuum so as to be as close as possible to the atoms and to avoid optical aberrations that would be introduced by the viewports (Y. R. P. Sortais, Marion, et al. 2007). The high numerical aperture diffraction-limited lenses ( $NA = 0.44$ ) allows us to focus the trap beams on diameters of a few micrometers (Glicenstein, Ferioli, Brossard, et al. 2021) in order to realize tight optical tweezers. The performances of the optics have been carefully tested and the results are detailed in the thesis (Brossard 2019). The lenses are manufactured by Asphericon<sup>®1</sup>. Their diameter is 2 cm, making the working distance (15 mm) sufficient for the horizontal beams of the

<sup>1</sup>part number AHL25-20-S-U

magneto-optical trap to cross at  $90^\circ$  (see figure 2.4). The purpose of this configuration is to facilitate the alignment and stability of the MOT, while limiting the amount of stray light scattered by the elements inside the chamber: lenses, lens holders, coils, RF antenna, etc. even using beams with a diameter of 1 cm. In the other experiments based on two confocal aspheric lenses operated by our group, past (Fuhrmanek 2011) and present (Béguin 2014; K.-N. Schymik et al. 2021), the horizontal MOT beams cross each other with an angle of about  $50^\circ$  and have a much smaller diameter, less than 5 mm, making the alignment more tedious and less stable. Contrary to these setups, we almost never have to re-align the MOT beams, and the position of the MOT is only controlled via the power balance between the different beams and the bias magnetic field, tuned by the compensation coils (not represented in fig.2.4).

The vacuum chamber, manufactured by *Kimball Physics* is a truncated sphere of diameter 20 cm and height approximately 15 cm which comprises 9 CF40 viewports and one 20 cm horizontal window on top, offering high optical access for trap, MOT and Zeeman slower beams (Brossard 2019).

The system also contains a pair of in-vacuum coils whose axis is parallel to the vertical axis of the MOT. The purpose of these coils is to generate the magnetic field gradient of the MOT but also to be able to generate a homogeneous magnetic field strong enough to lift the degeneracy of the Zeeman structure of the atoms and to place them in a regime where they can be considered as two-level atoms, according to a method that will be explained later in this chapter. The advantage of placing the coils in vacuum is to reduce their inductance, allowing them to commute as fast as possible between Helmholtz and anti-Helmholtz configurations. However, heating induced by the high current (typically 20 A) leads to possible displacements of the lens supports due to the change of temperature, which would cause a defocus of the aspherical lenses. The characterization of the coils is in (Brossard 2019).

Finally, the vacuum chamber is also equipped with a microwave antenna<sup>1</sup>. This antenna is intended to address more efficiently the atomic hyperfine transitions than if it were outside the chamber. Indeed, placing it inside reduces the distance to the atoms and avoid possible shielding by the metallic chamber and lens holder.

The ultra-high vacuum environment, under a pressure of some  $5 \times 10^{-11}$  mbar, is maintained by one ion pump and a titanium sublimator.

## Laser intensities

The experimental system requires several lasers of different power and wavelength. The goal of this part is to give orders of magnitude of the laser powers necessary for our experiment. Lasers are first needed for atom cooling and magneto-optical trapping.

The cooling beams come from a tapered-amplifier laser<sup>2</sup> whose frequency is controlled by saturated absorption on the D2 transition of wavelength  $\lambda_0 = 780$  nm. The exact frequency of the different beams is adjusted using acousto-optical modulators. The pumping beams come from a laser diode<sup>3</sup>, whose frequency is also fixed on the D2 transition. The cooling and pumping beams are then coupled into fibers before being fed into the science chamber. After shaping the beams, their diameters and polarizations, the typical intensities of the (1 cm) beams when they arrive on the atoms are :

<sup>1</sup> Allectra® 380-SMA-MX-500

<sup>2</sup> Toptica® TA pro

<sup>3</sup> Toptica® DL100



	MOT/beam	Zeeman
Cooling (mW)	2	6
$I/I_{\text{sat}}$	3	10
Repumper (mW)	0.7	3
$I/I_{\text{sat}}$	1	5

An extra laser diode<sup>1</sup> of wavelength  $\lambda_0$  is used to probe (drive) the system for light scattering experiments. Depending on the configuration, in particular whether this beam is strongly focused through an aspherical lens or not, saturation parameters up to several thousand are obtainable. Unlike the other diodes in our experiment, one arm of the saturated absorption spectroscopy is modulated via an AOM. This allows us to operate with a reduced spectral width from about 1 MHz to 100 kHz with respect to the case where the current of the laser is modulated. The light used for saturated absorption is shifted by a double-pass AOM (offset-lock) allowing to tune the laser frequency on tens of MHz without power variation. A last diode with a wavelength of 795 nm, on the D1 transition, is used for optical pumping and grey molasses (see chapter 3). In summary, cooling and trapping atoms in the MOT, while it requires several lasers, does not require laser power higher than a few mW.

Now that the experimental setup is outlined, we will then look in detail at two of its main parts: the high-resolution imaging system and the trapping system, whose size is dynamically variable.

### 1.3 The imaging systems

As explained in the previous section, the atomic ensembles are observed along two perpendicular axes noted  $\mathbf{z}_{\text{Trap}}$  and  $\mathbf{r}_{\text{Trap}}$  in figure 2.4. These axes correspond to four possible directions of observation thanks to the 4 aspheric lenses. Among these directions, we choose to use for each axis one direction for spatial imaging, using a camera, and the opposite direction to align an avalanche photodiode (APD), allowing to record the time dependence of fluorescence from the atoms. The two different APDs are noted  $APD \parallel$  and  $APD \perp$  according to whether it is placed along the trapping axis or at 90°. The fluorescence lights collected along the two axis are combined for both axes on the same CCD camera<sup>2</sup>. This camera is an electron-multiplying CCD (EMCCD) whose high gain and low noise ensures single photon sensitivity. The fluorescence emitted by the atoms is separated from the dipole trap light (along the  $\mathbf{z}_{\text{Trap}}$  axis) by means of dichroic mirrors. A standard CCD camera is also available for the observation of the MOT through the top window.

Let us now discuss in more detail the imaging systems. These are designed to observe single atoms in both directions. Indeed, a tool often used by our group for nearly 20 years is the trapping of single neutral atoms (Schlosser et al. 2001) in dipole traps and their use to characterize these traps (Y. R. P. Sortais, Marion, et al. 2007; Tuchendler et al. 2008).

#### Trapping single atoms using light-assisted collisions

Near-resonant light shone on atoms trapped in an optical tweezer induces an interaction and collisions, which lead to the loss of the trapped atoms. Let us first consider two atoms in their internal ground state. As represented in figure 2.5, their interaction potential as a function of

---

<sup>1</sup>Toptica® DL100

<sup>2</sup>Andor® iXonEM+ 897 (back-illuminated)

the interatomic distance is given by  $U(R) = U_{\text{IA}}(R) + U_{\text{CB}}(R)$  where  $U_{\text{IA}}(R)$  is the interatomic Lennard-Joes potential, composed of a repulsive hard-core potential plus an attractive longer range van-der-Walls contribution (Cohen-Tannoudji et al. 2012),  $U_{\text{IA}}(R) = C_{12}/r^{12} - C_6/r^6$ .  $U_{\text{CB}}(R) = \frac{\hbar^2 l(l+1)}{2mR^2}$  is the centrifugal barrier. For  $l > 0$ , this barrier prevents the atoms from colliding.

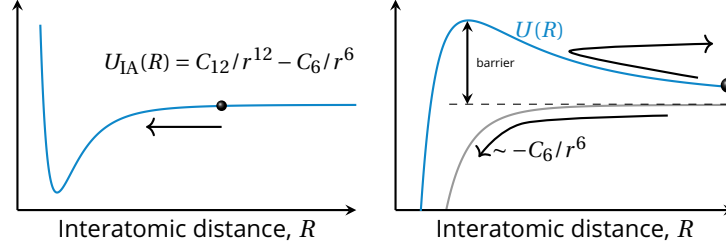


Figure 2.5: Left pannel : interatomic potential  $U_{\text{IA}}(R)$  as a function of  $R$ . This potential has bound states. Right pannel : an atom with  $l > 0$  does not collide with another atom if its kinetic energy is lower than the centrifugal barrier.

The atoms trapped in our dipole traps have a temperature below 1 mK. In this regime, the *s-wave* collisions, for which  $l = 0$ , are dominant (represented on the left panel of the previous figure). However, as we will see when we are interested in our densest clouds, *d-wave* scattering must also be taken into account (Buggle et al. 2004). Let us now consider collisions in the presence of quasi-resonant light, following (Gallagher and Pritchard 1989; Fung et al. 2016). The scattering potential between two atoms in their ground state ( $S + S$ )  $5^2S_{1/2}$  is  $U_g(R) \simeq -C_6/R^6$ . In the presence of light, the pair can absorb a photon and we must consider the first excited molecular state  $5^2S_{1/2} + 5^2P_{3/2}$  ( $D_2$  line), denoted  $S + P$ . In that case, the potential is  $U_e(R) \simeq \hbar\omega_0 \pm C_3/R^3$ , where  $\hbar\omega_0$  is the energy of the transition and  $C_R$  is a constant that quantifies the resonant dipole interaction (Fuhrmanek 2011). This potential can therefore be repulsive or attractive depending on the relative phase of the two dipoles. When the driving light is red-detuned ( $\Delta = \omega - \omega_0 < 0$ ), the pair is thus resonantly excited towards the attractive potential, see figure 2.6.

When the interatomic distance  $R$  approaches the Condon point  $R_c = \left(\frac{C_3}{\hbar\Delta}\right)^{1/3}$ , the driving light is resonant with the transition, step 1) in figure 2.6. The two atoms then accelerate towards each other due to the attractive potential (step 2)). At position  $R_s$ , a spontaneous emission occurs, resulting in a gain in kinetic energy  $\Delta E$  (step 3). If the gain  $\Delta E$  is larger than the trap depth, the atoms are expelled from the trap. This effect is known as *radiative escape*. The collision loss rate can be large and is not adjustable. Indeed, the energy gain depends on the difference  $R_c - R_s$  (see figure 2.6), which is random as it is dictated by spontaneous emission. Our group has quantified the light-assisted two-body losses, finding a two-body losses coefficient  $\beta = 3 \times 10^{-8} \text{ cm}^3 \text{ s}^{-1}$ . The high losses due to light assisted collisions lead to the phenomenon of *collisional blockade* in micro-meter scale optical tweezers (Schlosser et al. 2001; Y. R. P. Sortais, Fuhrmanek, et al. 2012). By this process, in a trap of volume  $V \sim 1 \mu\text{m}^3$ , on average  $\tau = \frac{1}{n\beta} \sim 100 \mu\text{s}$  after a second trapped atoms enters a trap that is already occupied, the atoms experience an inelastic collision whose energy gain ejects both out of the trap.  $\tau \ll 20 \text{ ms}$ , which is the typical time needed to acquire enough fluorescence signal to determine if one atom is trapped or not ( see next section). An optical tweezer thus contains either 1, or zero atoms. The loading efficiency of a single atom in the tweezer is thus limited to 50%.

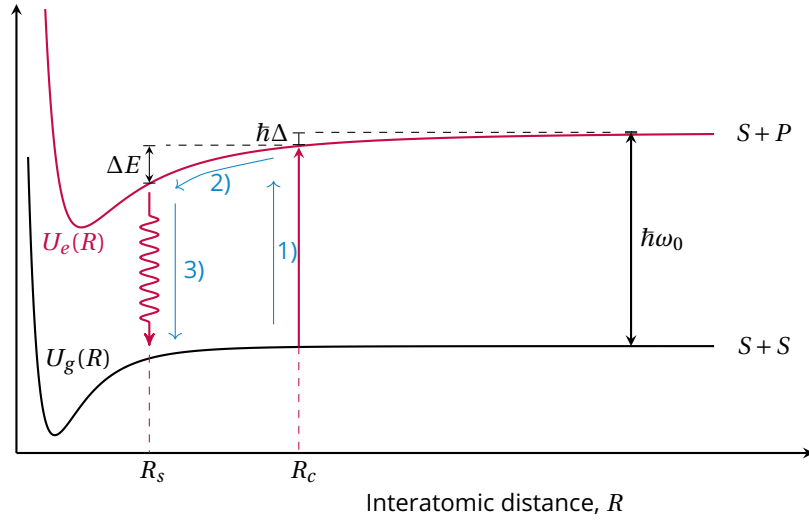


Figure 2.6: Light-assisted collision for the attractive part of the excited state potential. A photon may be absorbed when the interatomic distance is  $R_c$  (1). The atoms are then attracted each other due to the potential (2), before the photon is spontaneously emitted at  $R = R_s$  (3). The kinetic energy gain  $\Delta E$  can be sufficient to expel the two atoms from the trap.

### Observing single atoms along 2 directions

Being able to observe a single atom requires a proper design of the imaging system (Y. R. P. Sortais, Fuhrmanek, et al. 2012), with a large numerical aperture to collect the maximum number of photons. The system must act (in *photometric* terms) as a flux collector, i.e. all the photons collected must arrive on the same pixel of the camera. Indeed, this does not dilute the flux on several pixels and therefore maximizes the signal to noise ratio, the noise being essentially identical for all pixels (mainly due to the read-out noise of the EMCCD). Assuming that the system is limited by diffraction, the radius of the Airy spot imposed by the finite aperture of the lenses is

$$r_{\text{Airy}} = \frac{1.22\lambda_0}{2NA} \sim 1\mu\text{m}$$

using  $\lambda_0 = 780\text{nm}$  and  $ON = 0.44$ . One typically fixes as starting criterion that the image of one Airy spot in the plane of the atoms is conjugated with one pixel (size  $p^2 = 16\mu\text{m} \times 16\mu\text{m}$ ). The transverse resolution of the imaging system will thus be  $2dy' \simeq 1\mu\text{m}$ .

This resolution is satisfactory, but experience shows that to find the atomic signal in the first place, it is easier to observe a slightly larger field on each pixel, say  $2dy' = 2.5\mu\text{m}$ . We choose this resolution on the horizontal axis and a resolution of  $1\mu\text{m}$  on the transverse axis (see figure 2.4).

We therefore choose the magnifications  $g_y = p/dy'$  along the two axes where  $p$  is the pixel size and  $2dy'$  is the image of one pixel on the atom's plane. Actually, one pixel receives the light from  $2dy'$  and the light coming from the small distance  $d\epsilon$ , as represented in figure 2.7. This corresponds to the *depth of field* of the imaging system. It is clear that

$$\tan(\alpha') = \tan(0.44) = \frac{dy'}{d\epsilon}.$$

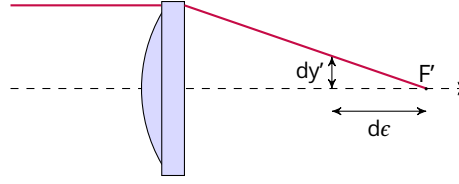


Figure 2.7: Schematic representation of the relation between resolution  $dy'$  and depth of field  $d\epsilon$ .

It gives

	Axial	Transverse
Magnification $g_y$	6.4	16
Resolution $2dy' (\mu\text{m})$	2.5	1
Depth of field $d\epsilon (\mu\text{m})$	2.7	1.1

In the rest of this manuscript, the "axial" and "transverse" axes correspond to the axes along  $\mathbf{z}_{\text{Trap}}$  and  $\mathbf{r}_{\text{Trap}}$  respectively. To verify the magnification values, calibrated pinholes placed in a plane conjugate to that of the atoms are used (the atoms being inaccessible because inside the vacuum chamber). The values obtained are then compared to those predicted by the design and an error of 6% is found.

Another test performed is to measure the relative displacement of the horizontal axis with respect to the transverse axis. The same atom is thus observed in both directions. By moving the trap, one measures the relative displacement of one imaging axis with respect to the other. This measurement is plotted in figure 2.8. A linear fit yields a slope of 3 instead of 2.5, which corresponds to an error of 20%. We do not take into account here the optical aberrations related to the limited fields of the two imaging systems.

The measurement above requires to trap single atoms, to be sure that the same object is observed on the two directions. In order to verify that one atom and one atom only is in the trap, the fluorescence emitted by this atom is collected. Typically, we distinguish this signal from the noise, which is mostly due to the light of the MOT beams scattered in the science chamber and to the atoms trapped in the MOT, when illuminating the atom with the MOT beams, detuned by  $-3\Gamma$  with respect to the transition, during 20 to 50 ms.

Over time, the received signal has the form of a "square" wave. An example is given in figure 2.9, panel a). A high signal indicates that an atom is trapped. When the level is low, the background is measured (there is no atom in the trap). If one plots the histogram of the data (panel b), one sees the two levels and can determine a threshold, represented in dotted lines, above which an atom is trapped. As expected in the blockade regime, there are never two atoms trapped at the same time, which translates into the absence of a second level on the histogram. So it is known at any time if an atom is in the trap. This is done along both axes. We verify that the signals are correlated. Measuring the fluorescence along both axes, the same atom is thus observed in both directions.

### Atom number calibration

An important parameter for our experiments with many atoms is the number of atoms  $N$  in the trap. For a cloud with  $N > 2$ , it becomes complicated to use histograms as explained previously. The method we rather use is that we divide the fluorescence of the

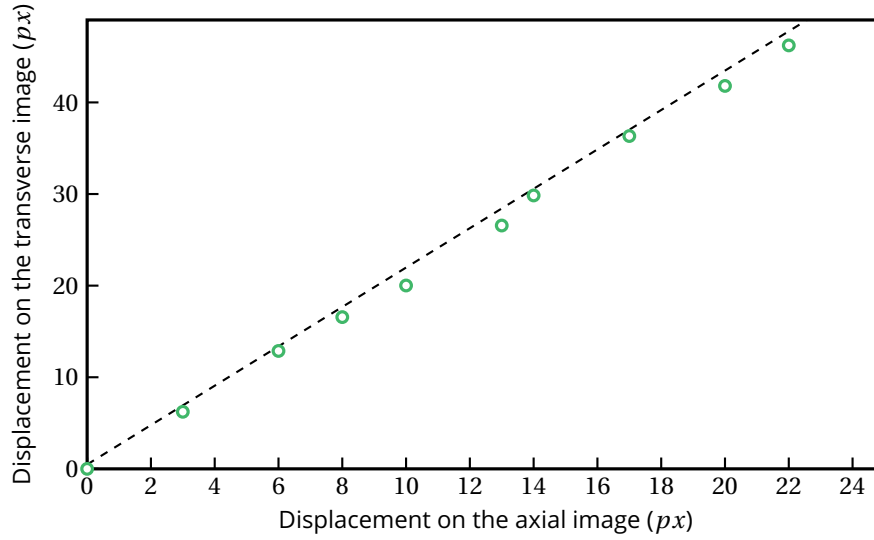


Figure 2.8: Measurement of the relative displacement of the imaging systems. This gives the ratio of the magnifications. By fitting with a line, we find  $\frac{g_{\text{transverse}}}{g_{\text{axial}}} = 3$ , which is close to the theoretical value of 2.5.

cloud by the fluorescence signal of a single atom. A precise measurement relies on a precise calibration of the signal emitted by an atom, as we will now explain. Moreover, in the general case, the fluorescence emitted by an atomic cloud containing  $N$  atoms is not equal to the sum of the fluorescence emitted by  $N$  independent atoms. If the cloud has a high optical density, the effect of the absorption in the cloud cannot be neglected. When the cloud is dense, as is the case for the systems we study, the atoms interact by dipole-dipole interaction. This leads to a shift in the frequency of the resonance, and a strong suppression of the scattered light (Pellegrino et al. 2014; Jenkins et al. 2016).

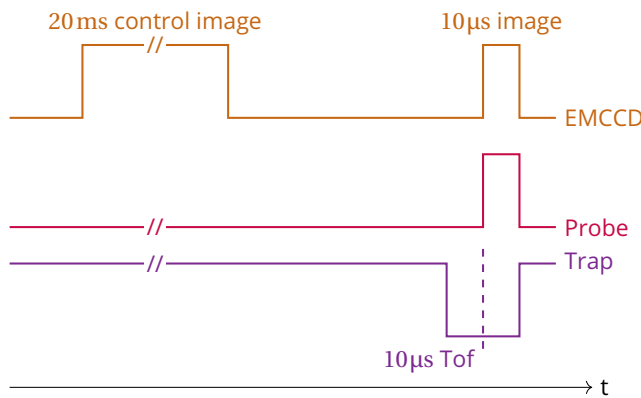


Figure 2.10: Chronogram of the calibration from the atom number measurement, using the fluorescence of a single atom. The MOT beams, used for the control image, are not represented.

To count the number of atoms, one must therefore ensure the atomic cloud is very dilute to avoid these systematic effects. This is done by letting the cloud spread in free flight, without a trap. A *time-of-flight* (Tof) of  $10\mu\text{s}$  is chosen, which ensures both that the cloud is sufficiently dilute. Starting from our densest cloud containing 2500 atoms at a temperature of  $700\mu\text{K}$ , with peak density  $n_0/k_0^3 \sim 2$  (see chapter 5), the density drops by one order of magnitude and we have verified that the obtained atom number is the same as the one obtained with a five-time-longer time

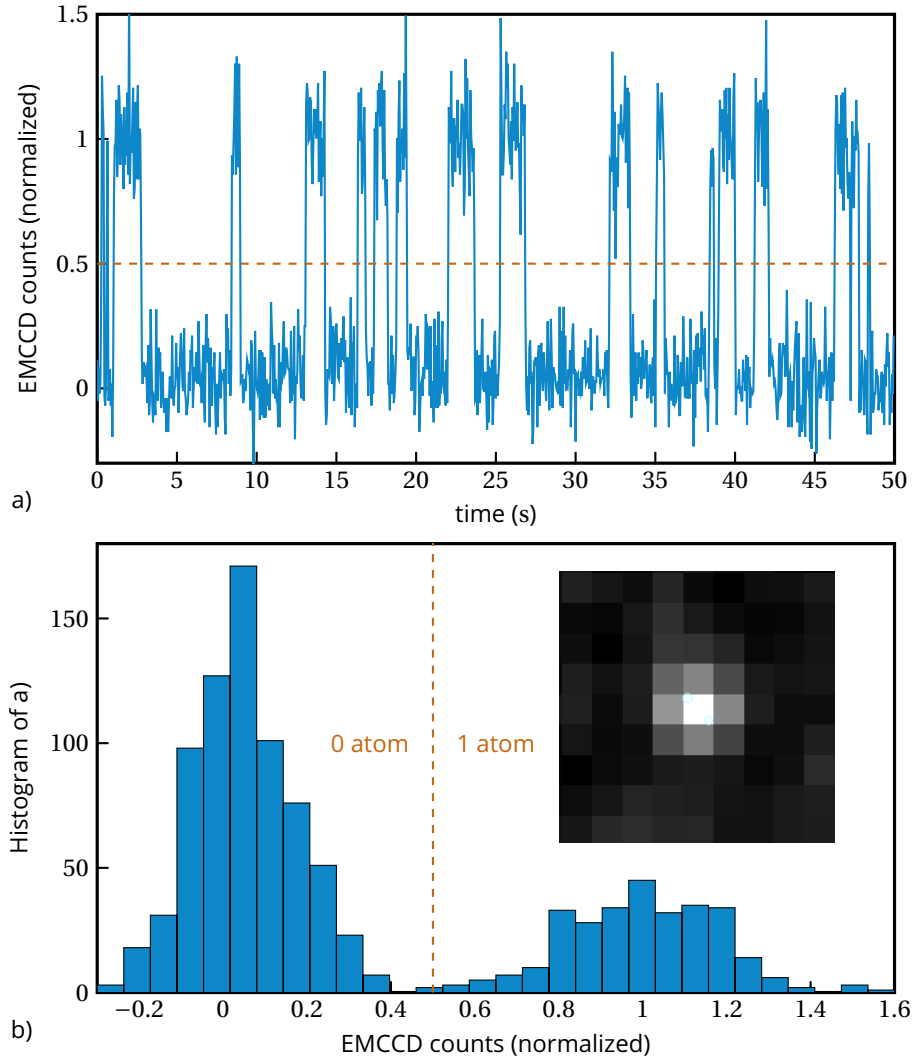


Figure 2.9: a) Fluorescence from a single atom collected on the horizontal axis as a function of time with the EMCCD. All light emitted by the atom arrives on the same pixel (insert). b) Histogram of the data from panel a). In both panel, the threshold to determine the presence of a single atom is plotted as a dashed line.

of flight, after which the cloud is even more dilute ( $n_0/k_0^3 \ll 1$ ). In  $10\mu\text{s}$ , the cloud has spread by less than  $3\mu\text{m}$ , which ensures it remains in the field of view of the imaging systems.

The collection efficiency of our entire imaging system is calibrated using the fluorescence of a single atom. Using experimental signal as the one shown in figure 2.9, the sequence starts when an atom is in the trap (the signal is then above the threshold). The MOT cooling beams and magnetic gradient are then turned off. We then take a "control" image by turning on only the MOT beams for  $20\text{ms}$  (see Fig.2.10). This image is used to post-select the sequences in which an atom was trapped (despite the triggering on the atomic signal, it may be lost before being used in the sequence). Resonant light for  $10\mu\text{s}$  is then sent, trap off, after  $10\mu\text{s}$  of free flight and record the image. This sequence is repeated many times ( more than 10000 times), until, keeping only the sequences where an atom was actually present in the trap, a

standard error of 10% on the signal is obtained. We find that the signal of an atom observed along the horizontal axis with the protocol described above is 175 counts on the EMCCD. This corresponds, according to the camera specs, to 5 photons received during  $\Delta t = 10\mu\text{s}$ . A strong and resonant probe is used, the number of emitted photons is thus

$$n_{\text{phot}} = \frac{\Gamma}{2} \Delta t \approx 188.$$

This corresponds to a collection efficiency of about 2.5%. The efficiency of the transverse axis is a bit lower, around 2%. This number is well explained by the collection angle of aspherical lenses

$$\frac{d\Omega}{4\pi} = \frac{1 - \cos(NA)}{2} \sim 5\%,$$

the quantum efficiency of the EMCCD (85% at  $\lambda_0$ ) and the transmission of the optical elements: mirrors, lenses, dichroic mirrors, interferometric filters, etc.

To conclude, the originality of our imaging system is the possibility to observe in two perpendicular directions, and thus to perform in-situ measurements of the size of our atomic ensembles. This will be used in the next chapters of this manuscript.

## 1.4 The OptoTelescope

The dipole trap is realized using a titanium-sapphire laser <sup>1</sup> pumped by a Verdi <sup>2</sup> of maximum power 18W at a wavelength of 532nm. The chosen wavelength is  $\lambda_{\text{Trap}} = 940\text{nm}$  in order to limit the Raman scattering by the trap photons (Brossard 2019). The output power of the laser is about 1W, and about 280mW on the atoms. Using the results of Section 1.1 and taking a waist at focus  $w_0 = 1.8\mu\text{m}$ , this results in traps with a maximum depth

$$U_0 \simeq k_B \times 12\text{mK} \simeq h \times 270\text{MHz}$$

This depth is high enough to capture relatively hot atoms with a limited laser power. We will see that the temperature of our densest clouds is about 700 $\mu\text{K}$ . As a comparison, the temperature of the single atoms trapped from the MOT is about 100 $\mu\text{K}$ , requiring trap depths around 1mK.

Our experimental setup includes a telescope with a controllable magnification in the dipole trap beam path, that we name in the following OptoTelescope (OT) (Glicenstein, Ferioli, Brossard, et al. 2021). This telescope is composed of two 1-in. lenses whose focal length is controlled by a current. The lenses are manufactured by OptoTune<sup>®3</sup>. This telescope is used to dynamically change the waist of dipole traps (Léonard et al. 2014). To do this, we change the size of the incident beam on the aspherical lens, which serves to focus it and form the trap. At the input, a beam of diameter about 1mm is used, which allows us to limit the aberrations in the OT. The lenses are subjected to gravity as they consist of a container which is filled with an optical fluid and sealed off with an elastic polymer membrane. The deflection of the lens is proportional to the pressure in the fluid, controlled by an electromagnetic actuator. The aberrations due to gravity are minimized by placing the lenses vertically. The OT is designed to allow varying magnification between 1 and 3.5.

---

<sup>1</sup> Coherent<sup>®</sup> MBR

<sup>2</sup> Coherent<sup>®</sup> G18

<sup>3</sup> Part No. EL-10-30 Series

This choice results from a compromise between a high dynamical range of magnification, and trying to have the smallest possible trap waist. The OT is followed by a  $4\times$ -telescope to obtain the correct beam sizes at the input of the asphere. We measure a total transmission of 75% at  $\lambda_{\text{Trap}} = 940\text{nm}$  (measured up to 700mW in input). The focal length of the lenses can be controlled via a driver, which includes a temperature correction. The variation of the focal length as a function of temperature is pre-calibrated by the manufacturer over a range from 10 to 50°C, which allows us to compensate for the heating of the laser and the control power.

### OT characterization using trap depth measurement

As seen in equation (1.1), the depth of an optical trap scales as  $U_0 \propto P/w_0^2$ . This means that one can measure the waist by measuring the trap depth. A trapped atom is used for this purpose. For a given power of the trapping beam, we measure the shift of the atomic transition compared to the case without trap. The transition from  $(5S_{1/2}, F=2, m_F=+2)$  to  $(5P_{3/2}, F'=3, m_F=+3)$  is used because it can be shown that in this case, the excited level is not light-shifted by a  $\pi$ -polarized trap. The measured shift is therefore directly the trap depth. To measure the frequency of the resonance, the sequence represented in figure 2.11 is applied. It starts with a trapped atom and ramp the trap power to a low value. This ensures that atoms are easily lost from the trap when excited with resonant light. A probe whose frequency is controlled is then sent. When the probe is resonant with the atom in the trap, the atom is pushed out of the trap. An image is then taken to measure the probability of keeping the atom in the trap, called "recapture probability", as a function of the push-out beam frequency. As seen in figure 2.12 a), we find that this probability is well fitted by a Lorentzian function, centered on the frequency of the shifted resonance. This sequence is repeated 50 times for each frequency.

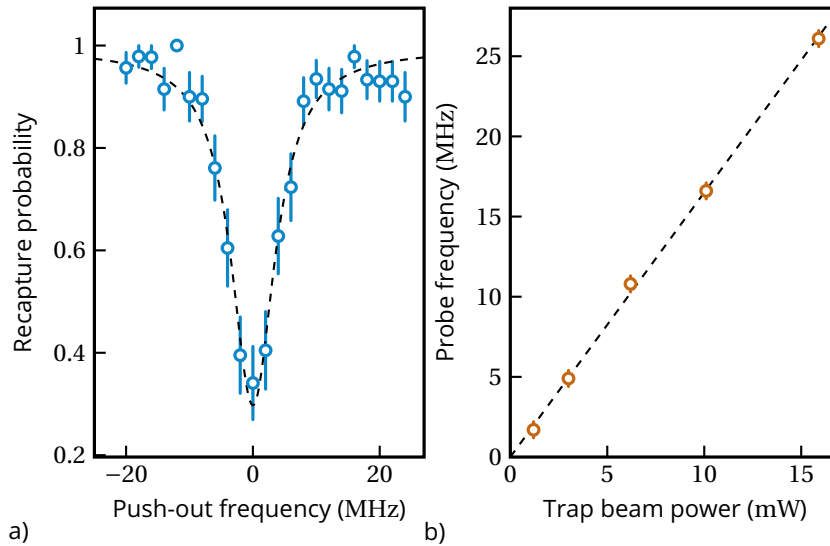


Figure 2.12: a) Loss spectrum for a given trap beam power, with a Lorentzian fit of the data. b) Shift of the resonance as a function of the trap beam power, with a linear fit of the data.



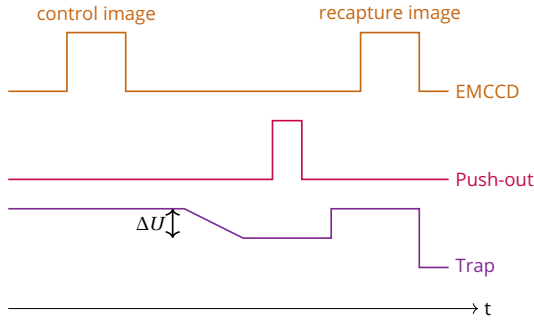


Figure 2.11: Chronogram of the trap depth measurement. The control and recapture images are done using the MOT beams for 20ms.

Using equation (2.7), we have

$$U_0 = \frac{\hbar \Gamma^2}{8} \frac{2P}{\pi w_0^2 I_{\text{sat}}} \left( \frac{1}{3\Delta_1} + \frac{2}{3\Delta_2} \right) \propto P. \quad (1.5)$$

By fitting the resonance shift as a function of the beam power, 2.12 b) with a linear function, one can thus determine the waist  $w_0$ . The obtained value can be confirmed by the measurement of the radial oscillation frequency,  $\omega_r$ . Indeed, we have (1.3)

$$w_0 = \sqrt{\frac{4U_0}{m\omega_r^2}}.$$

The principle of this measurement is explained in (Brossard 2019). The described method is used to measure the waist of the trap as a function of the OT magnification, as shown in figure 2.13.

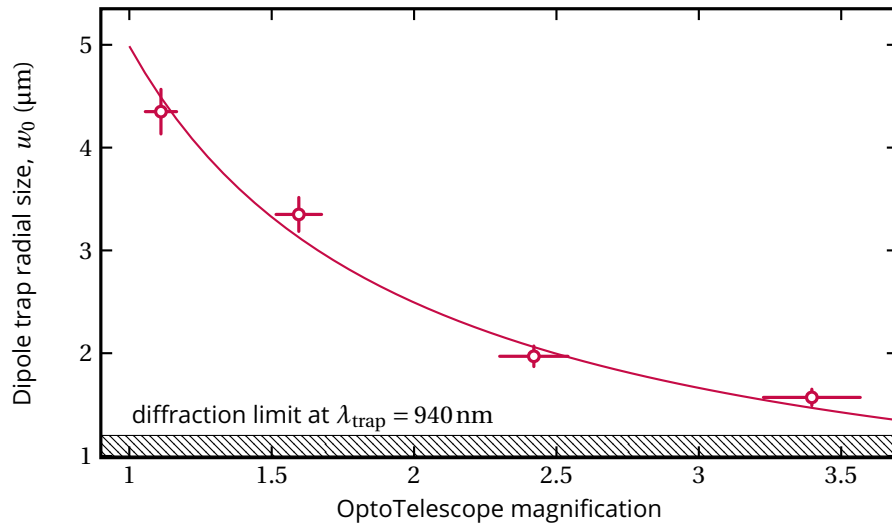


Figure 2.13: Dipole trap waist as a function of the OT magnification. The diffraction limit  $1.22\lambda_{\text{Trap}}/2NA \approx 1.15\mu\text{m}$  is indicated as the smallest trap achievable with the apparatus. The solid line corresponds to the expected size.

We are thus able to dynamically change the size of our trap between from  $1.6\mu\text{m}$  to about  $4.3\mu\text{m}$ , in agreement with the theoretical values calculated using gaussian optics. Figure 2.13 is replotted from (Glicenstein, Ferioli, Brossard, et al. 2021).

### Limitations

One limitation of the OT comes from the step response of the lenses. Depending on the step amplitude, this time is between 2 and 4ms, and it takes about 15ms for the lens to be

stabilized. We plot in figure 2.14 the values given by the manufacturer<sup>1</sup>.

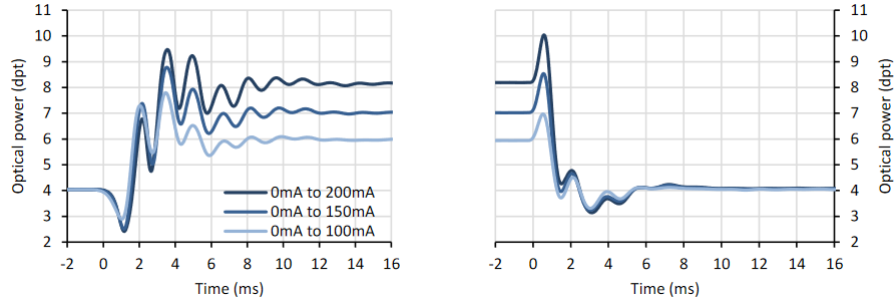


Figure 2.14: Typical optical response of the EL-10-30 a current step, from OptoTune® website.

This requires to be careful with the choice of steps when trying to dynamically change the size of the trap with atoms in it. The number of steps and their amplitude result from a compromise between speed ( to minimize the losses due to collisions, see chapter 5) and smoothness ( to limit losses due to the overshoots of the step response, see figure 2.14).

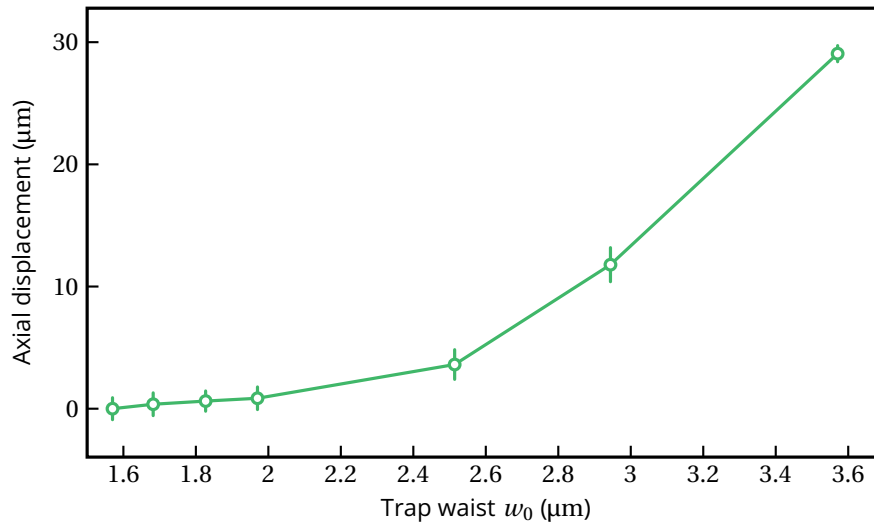


Figure 2.15: Axial displacement of the center of the trap as a function of the OT magnification.

Another important limitation is the longitudinal displacement induced by the change of magnification. Indeed, the output beam of the OT is not perfectly collimated for all the magnifications. That implies that the position of the waist after the aspherical lens is not exactly in the focal plane resulting into a longitudinal displacement. Figure 2.15 shows the displacement of the center of the trap measured using the transverse imaging system described in section 1.3. This might be corrected for by adaptating slightly the focal length of the second OT lens to adjust the beam divergence. When compressing the beam dynamically to load

<sup>1</sup><https://www.optotune.com/el-10-30-tc-lens>

dense traps, as explained in chapter 5, we don't use waists larger than  $2.5\mu\text{m}$  to avoid significant heating and thus atom losses due to the trap displacement.

## 2 Preparation and characterization of a 1D atomic chain

In chapter 4, we will study the collective interferences in a 1D atomic chain. This section is devoted to the preparation and the characterization of this chain.

### 2.1 Preparation of the chain

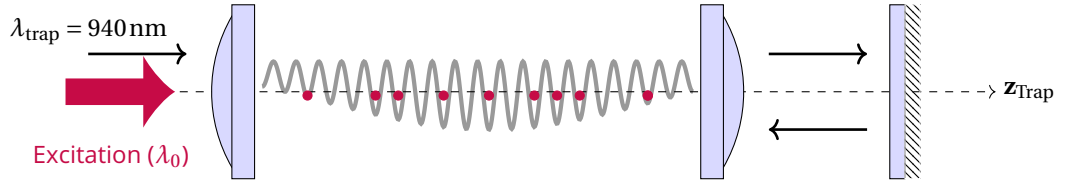


Figure 2.16: Schematic of the experimental setup. The 1D optical lattice is produced by retroreflecting the trapping beam. The light at wavelength  $\lambda_0 = 780 \text{ nm}$  is separated from the light at wavelength  $\lambda_{\text{trap}}$  using a dichroic mirror, and is therefore not retroreflected. The axis  $z_{\text{Trap}}$  refers to figure 2.4.

To prepare a chain, a 1D optical lattice is produced by retroreflecting a trapping beam ( $\lambda_{\text{Trap}} = 940 \text{ nm}$ ) using the second aspherical lens of the same axis (see figure 2.16). The obtained lattice has an intersite spacing  $\lambda_{\text{trap}}/2 = 470 \text{ nm}$ . The radial confinement is ensured by the tight focusing of the beams ( $w_0 \sim 3 \mu\text{m}$ ). The mirror used for the retroreflection is placed in a plane conjugated to the waist of the incoming beam such that the two beams focus at the same position. The retroreflected beam intensity is 50% of the intensity of the forward propagating beam due to the transmission of optical elements. It creates an optical lattice with an inhomogeneous depth, as represented in figure 2.16.



Figure 2.17: Average image of the fluorescence collected by the transverse imaging axis.

The chain is loaded from a 3D MOT superimposed to the lattice and then using a 200 ms pulse of  $\Lambda$ -enhanced gray molasses on the D1 line (see Chapter 3), the MOT beams and magnetic gradient being switched off. At this stage, the lattice is filled with more than one atom per trap. We then switch back on the MOT beams for 5 ms to induce light-assisted collisions. After this step, one or zero atom remains in each site. This also ejects the atoms out of the shallowest traps. At the end of the loading sequence (at most) the 200 central lattice sites are loaded, with an average filling  $\eta = 0.5 \pm 0.1$  measured by comparing the fluorescence of the chain with that of a single atom (section 1.3). The interatomic distance is thus on average  $\langle r_{mn} \rangle \simeq \lambda_{\text{trap}} \simeq 1.2\lambda_0$  with  $\lambda_0 = 780 \text{ nm}$ . The atoms are then optically pumped in the ( $5S_{1/2}, F = 2, m_F$ ) state (section 3.2) with the quantization axis aligned with the chain with an efficiency larger than 99%. The quantization axis is set by a 0.5 G magnetic field. This value is much smaller than the 50 G used for the 3D study (section 3.2), but is however large enough to isolate the two level transition in the 1D geometry.

We find that the loading efficiency is improved compared to the direct loading from the MOT ( $\sim 0.25$ ), as explained in chapter 3, section 1. The loading is also more robust to mis-

alignment and daily fluctuations than when using the MOT. The fluorescence emitted by the chain under a 20ms excitation of the MOT beams is collected using an aspherical lens in the transverse direction,  $\mathbf{r}_{\text{Trap}}$  in figure 2.4. A typical example of atomic chain is shown figure 2.17. In this figure, 50 images have been summed to average over the random filling. As the resolution of the imaging system is  $\sim 1\mu\text{m} > \lambda_{\text{trap}}/2$  (see section 1.3), the individual sites are not resolved.

## 2.2 Controllable length

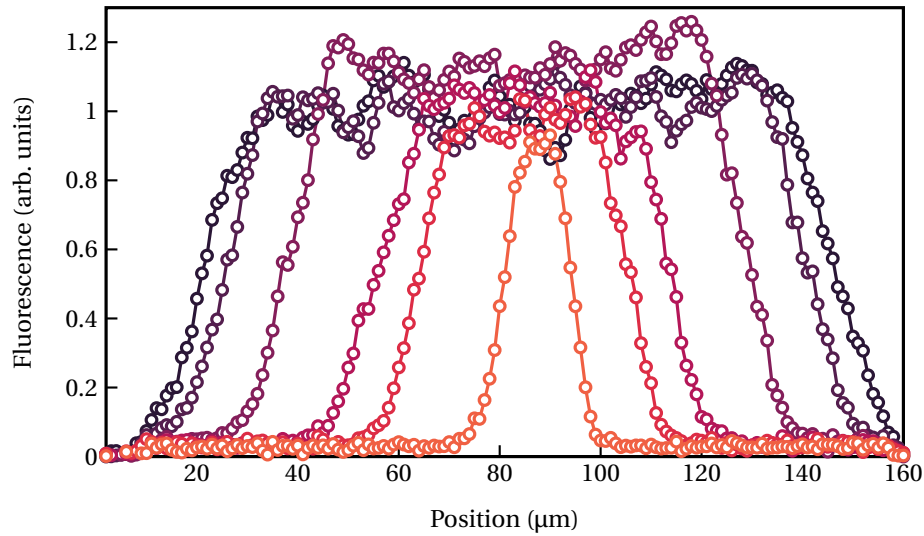


Figure 2.18: Cuts of fluorescence along the chain, for various chain lengths (for various  $w_0$ ).

The length of the chain is set by the Rayleigh range  $z_R = \pi w_0^2 / \lambda_{\text{trap}}$ , which is the range where the beam intensity is large enough to trap atoms. As shown in Section 1.4, we are able to vary  $w_0$  using the OptoTelescope. This leads to chains with different lengths and atom number. The trapping beam power is adapted to keep the depth at the center of the chain at  $U_0/k_B \sim 1\text{mK}$ . In figure 2.18 are shown cuts of fluorescence along the chain for various lengths, the longest having length of  $\sim 100\mu\text{m}$ , corresponding to  $\sim 200$  sites.

## 2.3 Oscillation frequencies

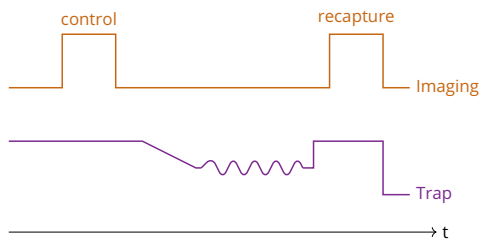


Figure 2.19: Chronogram of the oscillation frequencies measurement. The control and recapture images are done using the MOT beams for 20ms.

To characterize the chain, radial and longitudinal trapping frequencies  $\omega_r$  and  $\omega_z$  are measured using parametric heating. The sequence is represented figure 2.19. Starting with a filled chain, the trapping beam intensity is modulated with a relative amplitude of 5% during 100ms using an arbitrary waveform generator. When the frequency of the modulation is equal to  $2\omega_r$  or  $2\omega_z$ , losses are induced. Since the waist varies along the chain, the oscillations frequencies depend on

the position. Two fluorescence images are taken (one before modulating and the second after) to estimate the losses. For each modulation frequency, this sequence is repeated 50 times to average over the chain filling. The atomic losses as a function of the modulation frequency are shown figure 2.20. The oscillations frequencies can be calculated using the

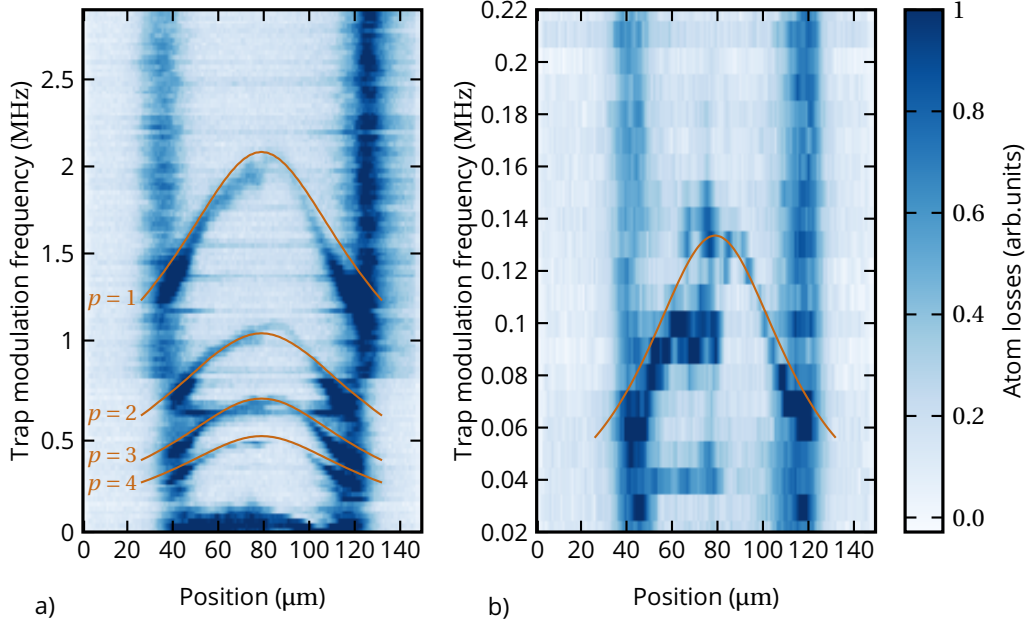


Figure 2.20: Parametric losses along the chain, exciting the axial oscillation  $\omega_z$  (a) and the radial oscillation  $\omega_r$  (b). The solid lines are the calculated values using the experimental parameters (see text).

experimental parameters: the trap beam has a power  $P = 140\text{ mW}$  (the retroreflected beam thus has a power  $P = 70\text{ mW}$ ) and its waist is  $w_0 = 3.3\text{ }\mu\text{m}$ . The trap depth at the center of the chain is given by  $U_0 = -\frac{\hbar^2}{8\Delta_{\text{Trap}}} \frac{I_0}{I_{\text{sat}}}$  with  $I_0 = \frac{2P}{\pi w_0^2}$  and  $\Delta_{\text{Trap}} = 2\pi c \left( \frac{1}{\lambda_0} - \frac{1}{\lambda_{\text{Trap}}} \right)$  (section 1.1). With these parameters, one expects

$$\omega_z = \frac{2}{\hbar} \sqrt{U_0 E_R} \simeq 2\pi \times 1\text{ MHz}$$

where  $E_R = \frac{\hbar^2 k^2}{2m}$  is the recoil energy and

$$\omega_r = \sqrt{\frac{4U_0}{mw_0^2}} \simeq 2\pi \times 70\text{ kHz}$$

at the center of the chain. The trap depth is then calculated for every position  $z$  using equation (1.2) and the oscillation frequencies using equations (1.3). The results are plotted figure 2.20 and are in very good agreement with the measured values.

The different lines reported in panel a) are given by  $2\omega_z/p$  with  $p$  integer. Losses are observed at these frequencies since the amplitude modulation is not perfectly sinusoidal and thus contains higher-order harmonics at  $\omega, 2\omega, \dots, p\omega$ . One thus observes parametric losses when  $p\omega = 2\omega_z$ . The losses on the chain edges (where the trap is the shallowest) are due to the imaging light during the first image, which expel the atoms.

The perfect agreement between calculations and measurements shows that the prepared system is well controlled. The radial confinement (waist) and the trap depths are in particular well-known along the chain.

## 2.4 Temperature and radial extension

The temperature  $T$  of the atoms is obtained by time-of-flight. One obtains  $T = 80(20)\mu\text{K}$ , yielding a transverse width  $\sigma_{r,0} \approx 300\text{nm} \approx 0.38\lambda_0$ . During the sequences, atoms are released

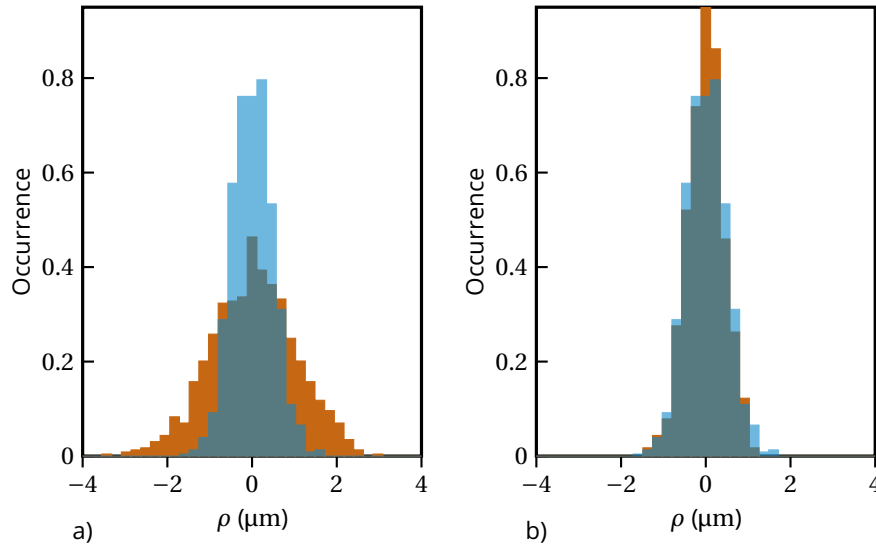


Figure 2.21: Effect of pulsing on the radial distribution a) using a single  $10\mu\text{s}$  pulse in free flight b) using the  $50 \times 200\text{ns}$  release and recapture sequence. The initial distribution is plotted in blue.

in free flight for imaging and then recaptured. We typically apply 50 pulses of  $200\text{ns}$  between which we recapture the atoms for  $200\text{ns}$  by switching the trapping beams on. This ensures to collect a sufficient signal and that the chain does not expand significantly. The effect of the pulsing on the radial size of the cloud is investigated by running simulations of the atomic motion during the sequence.

In the simulations we consider only the release and recapture of the atoms, not the heating induced by the resonant light. Indeed, the total recoil heating during  $\Delta t = 10\mu\text{s}$  is

$$\Delta T = \frac{\Gamma}{2} \frac{s}{1+s} T_r \Delta t \sim 2\mu\text{K} \ll T$$

using  $s = 0.3$  and the recoil temperature  $T_r = \frac{\hbar^2 k^2}{mk_B}$ .

For the simulations, we first chose randomly the position and velocity of an atom according to a thermal distribution of temperature  $T = 80\mu\text{K}$  in a harmonic trap of depth  $2.5\text{mK}$  and with trapping frequencies  $\omega_z$  and  $\omega_r$ . In the first case, we let the atom in free flight for  $10\mu\text{s}$  and record its position. The sequence is repeated 1000 times to obtain the distribution shown in figure 2.21a). In a second case, we simulate the sequence of 50 times  $200\text{ns}$  pulses. During the pulses, the atom is released in free flight. Between each pulse, the atom is recaptured (the displacement of the atoms during the free-flight is about  $20\text{nm}$ , thus much smaller

than  $w_0 = 3.3\mu\text{m}$ , so they are all recaptured at each pulse) and it oscillates in the trap during 200ns. By repeating this sequence 1000 times, one obtains the distribution figure 2.21b).

We see that the radial distribution of the cloud doesn't vary over the usual release and recapture sequence, contrary to the 10 $\mu\text{s}$  continuous sequence. The parametric heating induced by the pulse train is negligible (less than 5% of atom lost) thanks to its high frequency.

### 3 Control of the atomic internal state

Once the atoms are trapped, we are interested in controlling their internal state, for instance to isolate a closed two-level transition. This control is realized by applying an external magnetic field, and carefully setting the light polarization. The Zeeman effect lifts the degeneracy of magnetic sublevels (Foot 2005). The objective is to isolate an optical transition between two Zeeman levels.

#### 3.1 Compensation of the stray magnetic fields

The first thing to do to precisely control the magnetic field on the atoms is to cancel the static stray fields, mainly due to the Earth magnetic field.

##### Microwave Rabi oscillations

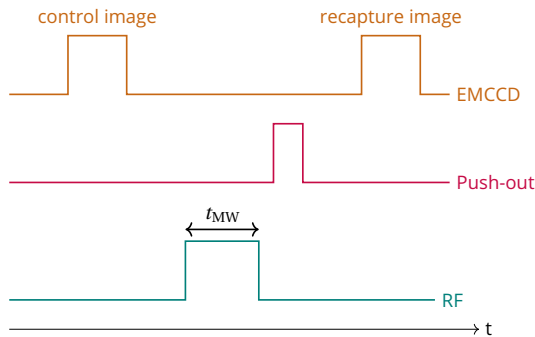


Figure 2.22: Chronogram of the MW Rabi oscillations. The control and recapture images are done using the MOT beams for 20ms. The push-out beam is optimized to eject an atom in the  $F=2$  state from the trap while an atom in  $F=1$  remains unchanged.

The in-vacuum microwave antenna (Section 1.2) is used to drive microwave transitions between hyperfine levels of the ground state  $5S_{1/2}$ ,  $F=1$  and  $F=2$ . The goal is then to use these transitions, which are sensitive to magnetic fields, to measure and cancel the residual fields. To determine the hyperfine state of a trapped atom, a recapture sequence is performed based on the use of an intense push-out beam in resonance with the  $(5S_{1/2}, F=2)$  to  $(5P_{3/2}, F'=3)$  transition. If the atom is in the  $F=2$  state, it is ejected from the trap when the push-out beam is switched on. If the atom is in the  $F=1$  state, the beam is far detuned and the atom is not perturbed. We then take an image with the MOT beams (cooling and repumper beam) to determine if the atom is still present (atom in  $F=1$ ) or not (in  $F=2$ ).

To prepare an atom in  $F=1$ , we shine the cooling MOT beams without a repumper. The atoms are pumped in  $F=1$  in a few ms. If the MOT repumping beams only are turned on, the atom is found in  $F=2$ . The antenna is then used to induce microwave transitions. The coupling between an atom and the field radiated by the antenna is measured by performing Rabi oscillations (see fig.2.22). An atom is loaded in the tweezer, then placed in the  $F=1$  state as explained above. The antenna is



then switched on for a time  $t_{\text{MW}}$ . We send the maximum power available at the desired frequency,  $\nu_0 \approx 6.834\text{GHz}$ , equal to the energy splitting between the two ground state levels (Steck 2001). This power is provided by a RF generator and by a 2W amplifier. The exact microwave power on the atoms is hard to estimate because the emission pattern inside the science chamber is complex and impedance matching of the amplifier with the antenna is not fulfilled. The probability of finding the atom in  $F = 1$  as a function of time with the microwave on  $t_{\text{MW}}$  is shown in figure 2.23, and shows the expected Rabi oscillations between the Zeeman sublevels ( $F = 1, m_F = 0$ ) and ( $F = 2, m_F = 0$ ).

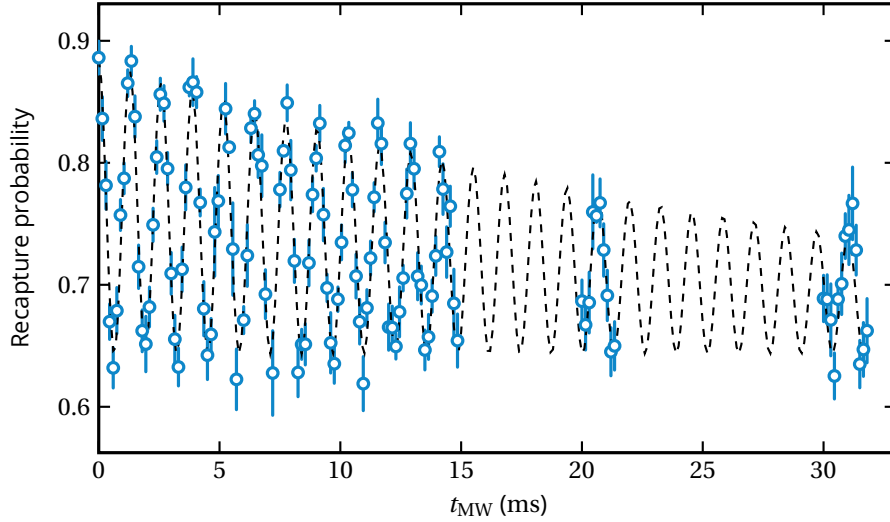


Figure 2.23: Recapture probability, proportional to the probability of finding the atom in  $F = 1$  as a function of the microwave duration. The data are fitted by a cosine square and an exponential decay in order to determine the Rabi frequency.

The data are fitted by the phenomenological function

$$Ae^{-t/\tau} \cos^2 \left( 2\pi \frac{f_{\text{Rabi}}}{2} t + \phi \right) \quad (3.1)$$

to extract the Rabi frequency  $f_{\text{Rabi}} = 774\text{Hz}$  and the decay time  $\tau = 29\text{ms}$ , indicating a quality factor  $Q = \tau f_{\text{Rabi}} = 22$ . The Rabi frequency corresponds to the coupling between the RF field and the atom. The decrease is due to the loss of coherence coming from the fluctuations of the magnetic field. The contrast is reduced by the detection efficiency and by the loss of atoms during the control and recapture images. To conclude, this measurement shows that we are able to perform good hyperfine spectroscopy.

### Compensation of the stray magnetic fields

Three pairs of "compensation" coils are placed around the science chamber to cancel out stray magnetic fields. They allow us to create static bias homogeneous fields in all directions. Let us showcase the optimization for the  $z$  direction, using spectroscopy on the hyperfine ground states with microwaves transitions. The shift of the energy states depends on the magnetic field amplitude, in particular, there is a minimum shift when the field is at minimum. For a given current  $I_Z$  in the coil, the "loss spectrum" when scanning the MW frequency is

measured using the recapture sequence. During this sequence, the field is applied for a fixed time  $t_{\text{MW}}$  so that the recapture probability is minimal at resonance to optimize the contrast. We obtain a set of spectra, figure 2.24 a). If we plot the position of the resonance as a function of the current applied in the coil, we obtain the curve figure 2.24 b).

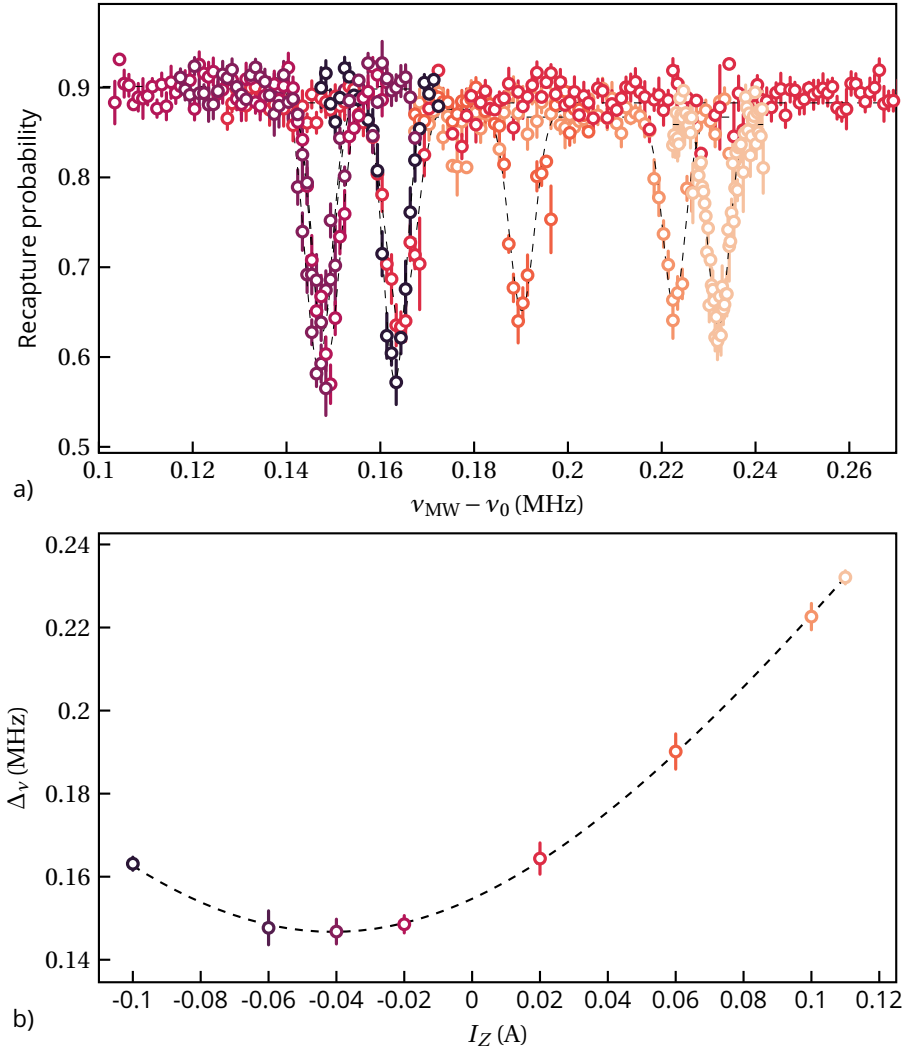


Figure 2.24: a) Loss spectra for different values of the bias field along  $\mathbf{z}$ , with lorentzian fits (dashed lines). b) Shift of the resonance frequency  $\Delta\nu$  as a function of the current in the bias coil, with a parabolic fit (dashed line) to determine the minimum.

The current to be applied to compensate for the stray fields is thus deduced. By doing the same with the other two directions ( optimization of  $I_X$  and  $I_Y$ ), the stray magnetic field is minimized. However, we have experimentally found that it is not possible to cancel it completely. Based on the shift from the resonance (fig 2.25), we deduce a residual field of about  $B \simeq 100\text{mG}$  of unknown origin, maybe due to magnetization of an element in vacuum.

### 3.2 Preparing a two-level system

Once the magnetic environment is controlled, a 2-level system is prepared by applying a homogeneous magnetic field and optically pumping the atoms to the Zeeman sub-level of interest in the ground state. The states of interest and the closed transition are represented Figure 2.25.

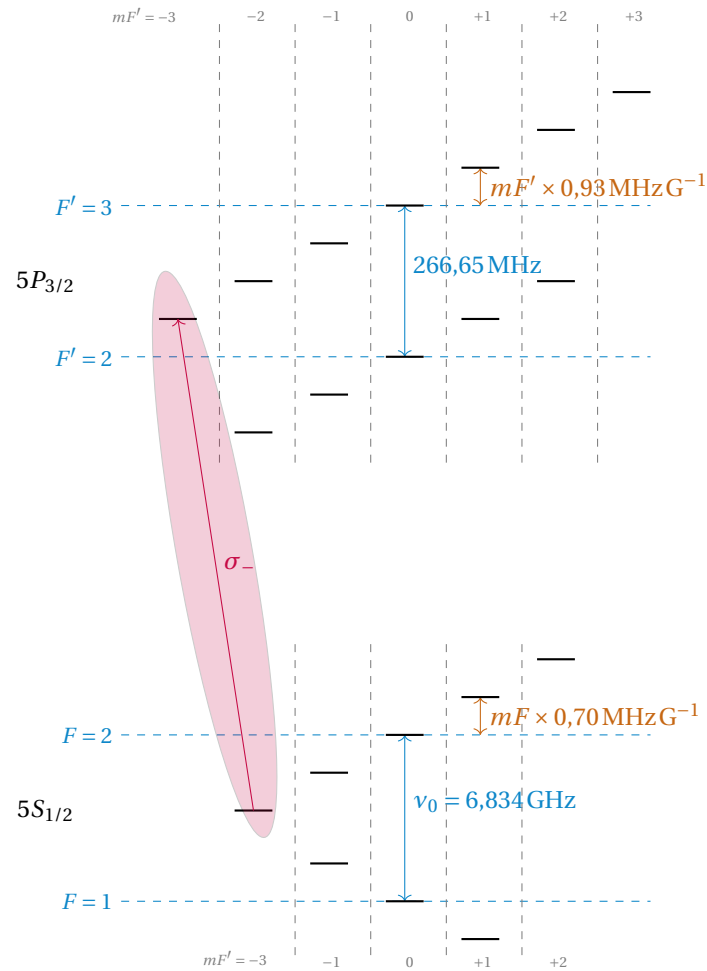


Figure 2.25: Zeeman structure and splitting due to magnetic field. The combination of large magnetic field a  $\sigma_-$  polarization allows one to isolate a closed two-level transition.

#### Optical pumping

We first want as many atoms as possible in the Zeeman sublevel ( $5S_{1/2}, F=2, m_F = -2$ ) (see figure 2.25). The optical pumping is two-fold, it repumps atoms from  $F=1$  to  $F=2$  (hyperfine pumping), and pumps into  $F=2, m_F = -2$  (Zeeman pumping). Zeeman pumping is performed with a beam resonant with the D1 transition. The repumping beam is on the D2 transition (figure 2.26). Both beams are coupled in the same optical fiber and have the same polarization. We typically use  $I = 10I_{\text{sat}}$  for the pumping beam and  $I = 5I_{\text{sat}}$  for the repumper.

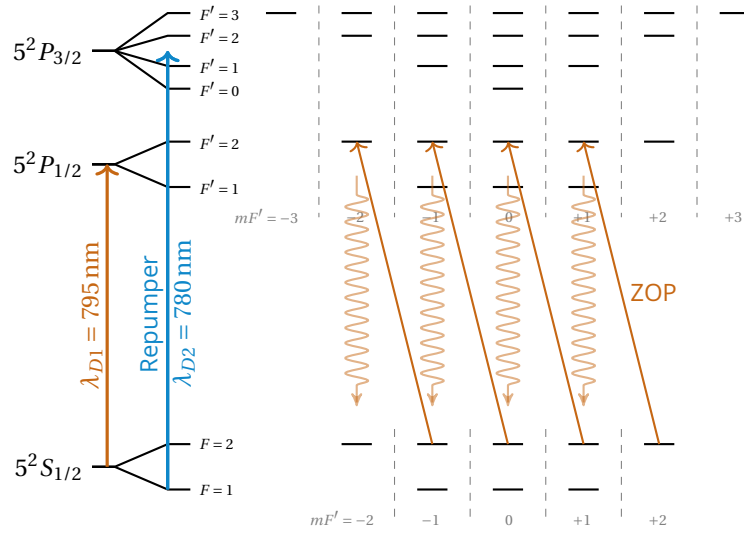


Figure 2.26: States and transitions used for the optical pumping to ( $5S_{1/2}, F=2, m_F=-2$ ). The solid arrows correspond to the stimulated  $\sigma_-$  transitions. The curved ones correspond to the other transitions. ZOP : Zeeman Optical Pumping

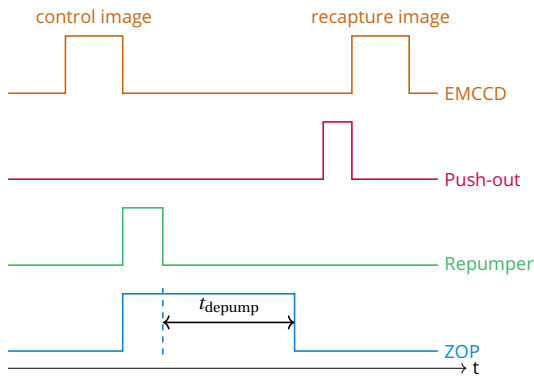


Figure 2.27: Chronogram of the optimization of the optical pumping.

The efficiency of optical pumping depends strongly on the purity of the polarization, the power of the different beams and the magnetic field. Here will be presented the general method for optimizing these parameters. For more clarity, the beam tuned on the transition  $F=2$  to  $F'=2$ , in other words the pumping beam, is called in the following the Zeeman optical pumping beam (ZOP). The other beam is called the repumping beam. The optimization sequence is the following (fig 2.27). After loading one or more atoms into the optical tweezer, we try to bring them into the desired state by varying a set of parameters. For this the two beams are used, ZOP and repumper. The re-

pumper is then turned off and the ZOP is kept for a time  $t_{\text{depump}}$ . During this time, there are two possibilities. If the process is perfectly optimized, the atoms are in the desired ( $5S_{1/2}, F=2, m_F=-2$ ) state which is a dark state for the ZOP, whose polarization is thus perfectly  $\sigma_-$ . They remain in this state. If the process is not perfect, for example if the polarization of the ZOP is not perfectly  $\sigma_-$ , the atoms are not in a dark state and after a certain time, they end up in  $F=1$ , where they stay since the repumping is turned off. The measurement of the time it takes for the atoms to fall into  $F=1$  under the effect of the ZOP alone thus tells us about the quality of the pumping and the polarization. We measure if the atom is in  $F=1$  using the push-out beam described in the previous paragraphs.

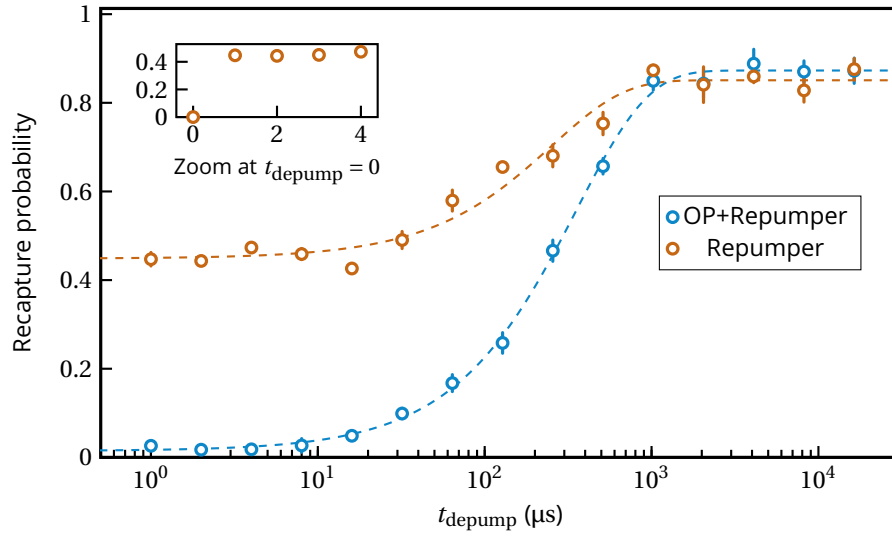


Figure 2.28: Recapture probability, proportional to the probability of finding the atom in  $F = 1$  as a function of  $t_{\text{depump}}$  for the case of the atoms are optically pumped in ( $5S_{1/2}, F = 2, m_F = -2$ ) using OP+repumper and the case of all the levels of  $F = 2$  are equally filled, using the repumper only. The dashed lines are phenomenological fits used to determine the pumping efficiency (see text).

In figure 2.28 is plotted in two cases the recapture probability after the push-out, which is proportional to the ratio of atoms in  $F = 1$ . In one case, both the repumper and the ZOP are used and we observe that all the atoms are initially in  $F = 2$  and that it is necessary to apply the ZOP for more than  $350\mu\text{s}$  to depump half of them. This means that the atoms are in fact in a very dark state. In the case where only the repumper is used in the preparation, the atoms are uniformly distributed in all  $m_F$  states. We observe that when the ZOP is applied, half of them are quickly depumped, in less than  $1\mu\text{s}$  (see inset). The other half is depumped over a much longer time, these are atoms that are initially in or pumped into  $m_F = -2$  by the ZOP.

The optical pumping is modeled by the evolution of the population  $P$  of the desired state (Walker and Saffman 2012),

$$\frac{dP}{dt} = R_{\text{op}}(1 - P) - R_{\text{depump}}P.$$

The final population is thus given by

$$P_{\infty} = \frac{R_{\text{op}}}{R_{\text{op}} + R_{\text{depump}}} = \frac{\tau_{\text{depump}}}{\tau_{\text{depump}} + \tau_{\text{op}}}$$

defining  $\tau_{\text{depump}} = 1/R_{\text{depump}}$  and  $\tau_{\text{op}} = 1/R_{\text{op}}$ . To quantify the efficiency of pumping, we measure the time it takes to pump,  $\tau_{\text{op}}$ , and the time it takes to depump,  $\tau_{\text{depump}}$ . The first is less than  $10\mu\text{s}$  for the used beam intensities. It is limited by the time needed to repump the atoms from  $F = 1$ . The second is the time extracted from the figure 2.28 by fitting the data with a phenomenological function. Indeed, these measurements correspond to the time it takes to depump the atoms in the absence of the repumper beam. We find  $\tau_{\text{depump}} \approx 350\mu\text{s}$ . We thus have a very good quality pumping with an efficiency of more than 97%. The pumping is performed with a homogeneous field of 50 G. We observed that the pumping efficiency could

be better by using lower fields, but this field is necessary to isolate the two levels. The quality of the pumping is satisfactory.

### Bias magnetic field

As shown in Figure 2.25), two Zeeman sublevels can be isolated by applying a bias magnetic field. In the experiment, it is in the  $\mathbf{z}_{\text{MOT}}$  direction, which gives the quantization axis (see figure 2.4). To isolate a transition, the frequency of this transition must be sufficiently detuned from other transitions. The criterion that we take is that the transition must be at least  $10 \Gamma = 2\pi \times 6\text{MHz}$  away from all other transitions to be sure to neglect the effects of dipole-dipole interaction and of the power broadening (Brossard 2019; Jennewein 2017).

Ignoring the quadratic effect to gain an intuition, the Hamiltonian for the interaction between an atom and an external field  $\mathbf{B}$  is

$$H = g_F \mu_B \mathbf{F} \cdot \mathbf{B}$$

where

$$g_F = \frac{F(F+1) + J(J+1) - I(I+1)}{2F(F+1)} g_J.$$

and  $\mu_B \simeq h \times 1.4\text{MHzG}^{-1}$  is the Bohr magneton and  $g_J$  is the fine structure Landé g-factor (Foot 2005). The Zeeman energy is thus

$$E = g_F \mu_B B m_F. \quad (3.2)$$

We deduce the energy splitting given on figure 2.25 for the states of interest  $F' = 3$  ( $g_{F'} =$

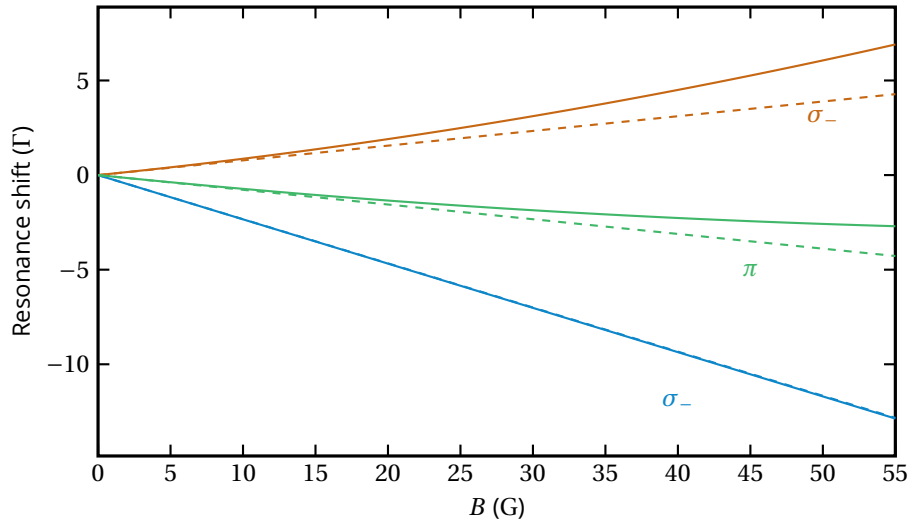


Figure 2.29: Resonance shift from the transitions  $\sigma_-$ ,  $\pi$  and  $\sigma_+$  starting from the state  $(5S_{1/2}, F=2, m_F=-2)$ . The dotted lines are the weak field model (see text), the solid lines are the full calculation.

$2/3)$  and  $F = 2$  ( $g_F = 1/2$ ). The transition that we want to isolate is the  $\sigma_-$  transition from  $(5S_{1/2}, F=2, m_F=-2)$  to  $(5P_{3/2}, F'=3, m_F=-3)$ , as represented in figure 2.25. We thus calculate the energy shifts starting from these states, for the three types of transitions  $\sigma_-$ ,  $\pi$  and

$\sigma_+$ , figure 2.29. The transitions starting from the other  $m_F$  are avoided by preparing the system in the correct state using optical pumping. Equation (3.2) gives  $\Delta E = \frac{5}{6}\mu_B B$  between the transitions  $\sigma_-$  and  $\pi$  (which are the closest). The condition  $\Delta E > 10\Gamma$  gives roughly  $B \geq 50\text{G}$ . In figure 2.29 are shown the results described above with dashed lines and the result of the full diagonalization of the interaction Hamiltonian with solid lines (Foot 2005). They are identical for the  $\sigma_-$  transition and quite close for the other two, the real shift being slightly larger. We see that for a field  $B = 50\text{G}$ , the  $\sigma_-$  transition is detuned by more than  $10\Gamma$  compared to the  $\pi$  transition. To verify that we isolate a closed two-level system, we measure the shift of the resonance of fluorescence spectra as a function of the current applied in the coil. This measurement is performed in a dilute cloud containing a few hundred atoms.

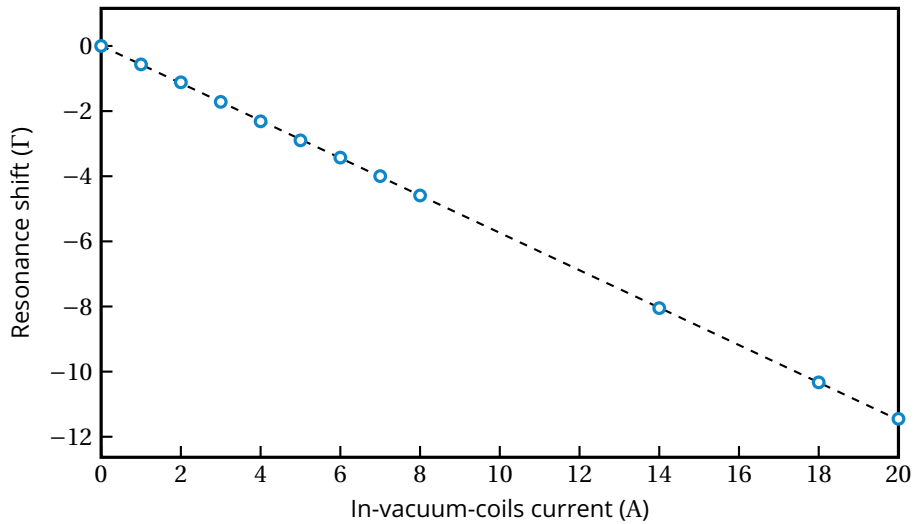


Figure 2.30: Resonance shift of the fluorescence spectrum as a function of the in-vacuum coil current. The dashed line is a linear fit of the data.

Figure 2.30 shows that the resonance varies linearly with the current in the coils  $I$ , as expected. From this, we obtain the calibration

$$B(\text{G}) = 2.5I(\text{A}),$$

as expected knowing the number of coils and its dimensions. We therefore circulate a current of 20A to create the desired field of 50G. This is large and leads to a heating of the vacuum chamber and to a vacuum pressure increase. As an example, we observe that the pressure increases from  $5 \times 10^{-11}\text{ mbar}$  to  $1 \times 10^{-10}\text{ mbar}$  after a few hours of continuous current. We thus opted for a solution where the current is increased only when needed. Moreover, we use the same coils to create the magnetic field gradient of the MOT. We therefore switch the coils from anti-Helmoltz configuration to the Helmholtz configuration during the sequence, by changing the direction of the current in one of the coils.

## **4 Conclusion**

In this chapter, we have given a brief overview of the experimental setup and explained how we trap and observe atomic clouds. In the last part, we have presented how to isolate a closed two-level transition using magnetic fields and optical pumping.



# Single atoms in optical tweezers using $\Lambda$ -enhanced gray molasses

\*\*\*

Gray-molasses (GM) are used for more than 20 years to achieve sub-Doppler cooling of atoms (Weidemüller et al. 1994; Grynberg and Courtois 1994; Esslinger et al. 1996; Boiron et al. 1995). Recently, C. Regal’s group at JILA (Brown et al. 2019) has explored the loading single atoms in optical tweezers from a GM-cooled sample, and reported a single atom loading probability as high as 89%, much higher than the usual 50% obtained by collisional blockade with red-detuned laser cooling. GM should allow to explore higher loading probability of single atoms, which is a key point for the experiments of our group (Browaeys and Lahaye 2020; K. N. Schymik et al. 2020). Moreover, the loaded atoms should be cooler than when loaded from the MOT. This technique has however never been implemented in the team.

In GM, light assisted collisions are partially suppressed. Thus, the density of atomic ensembles that can be achieved in a dipole trap is increased with respect to the direct loading from the MOT. The number of trapped atoms is in our case ten times larger than when using previous techniques, for similar traps (Bourgain et al. 2013). This will be described in the last part of this chapter.

## Contents

<b>1</b>	<b>Principles of <math>\Lambda</math>-enhanced GM</b>	<b>62</b>
1.1	Dark states	62
1.2	Cooling mechanism	63
1.3	Use of GM to load optical tweezer with high efficiency	64
<b>2</b>	<b>Implementation</b>	<b>65</b>
2.1	Setup	65
2.2	Temperature measurement	66
<b>3</b>	<b>Experimental results</b>	<b>67</b>
3.1	Single atom loading and temperature	67
3.2	1D chain loading	69
3.3	Many atoms in the tweezer	69
<b>4</b>	<b>Conclusion</b>	<b>71</b>

## 1 Principles of $\Lambda$ -enhanced GM

$\Lambda$ -enhanced gray molasses (Grier et al. 2013) are the combination of a gray molasses cooling scheme on a  $F \rightarrow F' = F$  transition and a phase coherent addressing of the  $F - 1 \rightarrow F'$  transition, creating velocity-selective coherent population trapping (VSCPT)-like dark states .

### 1.1 Dark states

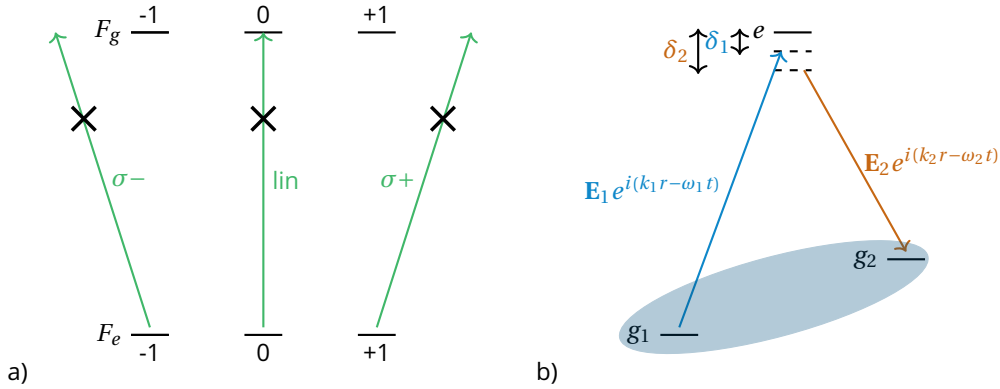


Figure 3.1: a) The atom interacts with  $\sigma^+$ ,  $\sigma^-$  and  $\pi$  polarized light. In each case, there exists a state that can not be excited by the light. For the  $0 \rightarrow 0$  transition, the Clebsch-Gordan coefficient is zero. b) Dark state in a  $\Lambda$ -type atomic system. An additional dark exists when the Raman condition  $\delta = \delta_2 - \delta_1 = 0$  is fulfilled.

Dark states exist on any  $F \rightarrow F' \leq F$  transition. For simplicity, we consider as an example the transition  $1 \rightarrow 1$  in one dimension. For each polarization, it exists a state that can not be excited by the light, as represented figure 3.1 a). For the  $0 \rightarrow 0$  transition, the Clebsch-Gordan coefficient is zero. These states are called *dark states*.

#### Dark state in a $\Lambda$ -type atomic system

To show the existence of a dark state in a  $\Lambda$ -type atomic system, one starts by writing the Hamiltonian  $H_t$  of the system submitted to a phase coherent field  $\mathbf{E} = \mathbf{E}_1 e^{i(k_1 r - \omega_1 t)} + \mathbf{E}_2 e^{i(k_2 r - \omega_2 t)}$  in the  $(e, g_1, g_2)$  basis, using notations of figure 3.1 b). One writes  $\hbar\omega_e$ ,  $\hbar\omega_{g_1}$  and  $\hbar\omega_{g_2}$  the energies associated to the states and  $\Omega_i = \frac{d_i E_i}{\hbar}$  the Rabi frequency associated to the transition  $g_i \rightarrow e$ .

$$H_t = \begin{pmatrix} \omega_e & \frac{\Omega_1}{2} e^{-i\omega_1 t} + \text{c.c} & \frac{\Omega_2}{2} e^{-i\omega_2 t} + \text{c.c} \\ \frac{\Omega_1}{2} e^{i\omega_1 t} + \text{c.c} & \omega_{g_1} & 0 \\ \frac{\Omega_2}{2} e^{i\omega_2 t} + \text{c.c} & 0 & \omega_{g_2} \end{pmatrix}.$$

In the rotating wave approximation (Grynberg, Aspect, et al. 2010), one does the change of basis ( $g_1 \rightarrow e^{-i\omega_1 t} g_1$ ,  $g_2 \rightarrow e^{-i\omega_2 t} g_2$ ,  $e \rightarrow e$ ) and obtains the time independent Hamiltonian  $H$ ,

$$H = \begin{pmatrix} 0 & \frac{\Omega_1}{2} & \frac{\Omega_2}{2} \\ \frac{\Omega_1}{2} & \delta_1 & 0 \\ \frac{\Omega_2}{2} & 0 & \delta_2 \end{pmatrix},$$

where  $\delta_i = \omega_{gi} + \omega_i - \omega_e$ . We write  $\Omega = \sqrt{\Omega_1^2 + \Omega_2^2}$  and define the states

$$|D\rangle = \frac{1}{\Omega} (\Omega_2 |g_1\rangle - \Omega_1 |g_2\rangle) \quad (1.1)$$

and

$$|B\rangle = \frac{1}{\Omega} (\Omega_2 |g_1\rangle + \Omega_1 |g_2\rangle). \quad (1.2)$$

One easily express  $H$  in the  $(e, B, D)$  basis:

$$H_{db} = \begin{pmatrix} 0 & \frac{\Omega}{2} & 0 \\ \frac{\Omega_1^2 \delta_1 + \Omega_2^2 \delta_2}{\Omega^2} & \omega_{g1} & \frac{\Omega_1 \Omega_2}{2\Omega^2} (\delta_1 - \delta_2) \\ 0 & \frac{\Omega_1 \Omega_2}{2\Omega^2} (\delta_1 - \delta_2) & \frac{\Omega_1^2 \delta_1 + \Omega_2^2 \delta_2}{2\Omega^2} \end{pmatrix}. \quad (1.3)$$

Using equation (1.1), one sees that the state  $|D\rangle$  is not coupled to the light field  $\mathbf{E}$  due to destructive interference between the transition amplitudes. It does not depend on the polarization. One sees in equation (1.3) that  $|D\rangle$  and  $|B\rangle$  are decoupled if  $\delta_1 = \delta_2$ , that is when the Raman transition is fulfilled (fig. 3.1 b). The electric fields  $\mathbf{E}_1$  and  $\mathbf{E}_2$  must be coherent. In practice, the same laser is used to create the two beams.  $\mathbf{E}_2$  is created from  $\mathbf{E}_1$  and its frequency is shifted using an electro-optical modulator. The  $\Lambda$  configuration enhances the cooling efficiency by a factor 3 compared to the standard GM scheme (Grier et al. 2013). In the following, GM will stand for  $\Lambda$ -enhanced gray molasses.

## 1.2 Cooling mechanism

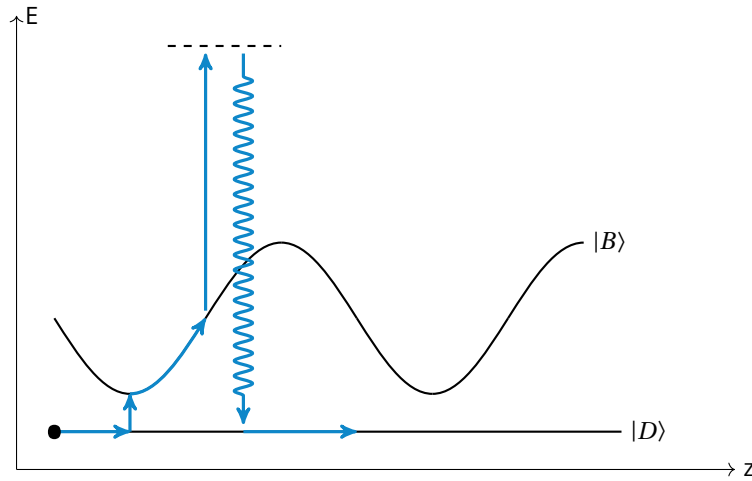


Figure 3.2: Gray-molasses scheme. On a  $F \rightarrow F' \leq F$  transition with positive detuning, the ground state splits into a dark state  $|D\rangle$  and a bright state  $|B\rangle$ . The bright state energy is spatially modulated in presence of a polarization gradient. From (Rio Fernandes et al. 2012).

Let us consider an atom with two ground states, a dark state  $|D\rangle$  and a bright state  $|B\rangle$  propagating in a one dimensional lin $\perp$ lin configuration. If the incident light is blue detuned,  $\Delta = \omega - \omega_0 > 0$  where  $\omega$  is the laser frequency and  $\omega_0$  is the transition frequency, the bright state energy is light-shifted at higher energy and depends on the position, as represented

figure 3.2. As in Sisyphus cooling (Foot 2005), energy is lost when an atom in  $|B\rangle$  climbs a potential hill before being pumped back to the dark state. The pumping out of the bright states occurs mostly at intensity maxima. Motional (non adiabatic) coupling and optical excitation to off-resonant hyperfine states complete the cooling cycle (figure 3.2), most likely at the bottom of the potential hills where the energy difference between the states is the smallest. This process results in a sub-Doppler cooling.

GM have to main features :

- they are based on blue detuned light
- atoms are in dark states, so the scattering rate is low.

We will see that the first feature may lead to loading optical tweezers with high efficiency. The second feature leads to the possibility of significantly increasing the density compared to a cloud of atoms loaded from bright molasses. This will be discussed in the last part of this chapter.

### 1.3 Use of GM to load optical tweezer with high efficiency

Let us consider the case of light-assisted collisions described in section 1.3 but for a blue-detuned driving light ( $\Delta = \omega - \omega_0 > 0$ ) where  $\omega$  is the laser frequency and  $\omega_0$  is the transition frequency. In this case, the cooling laser excites the atoms to a state with a repulsive inter-atomic potential (fig. 3.3). The atoms then repel each other. By going down the potential hill, they gain an energy  $\hbar\Delta$ , assuming the excited state lifetime is long enough.

The light frequency can thus be tuned such that the energy gain is large enough for one atom to leave the trap (depth  $U_0$ ), but not for two of them:  $U_0 < \hbar\Delta < 2U_0$ . Only one atom of the pair is then expelled from the trap (Fung et al. 2016). The Andersen group in New Zealand reported a loading efficiency of more than 90% by adding an intense blue-detuned laser beam to the red-detuned molasses (Grünzweig et al. 2010).

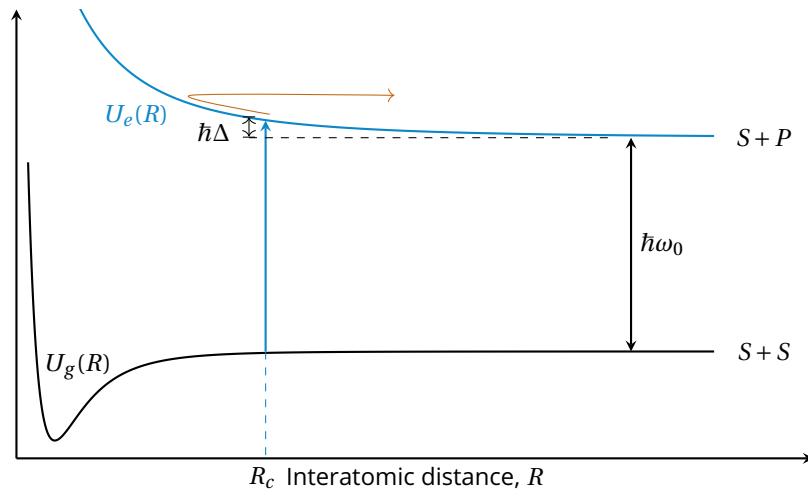


Figure 3.3: Light assisted collision for the repulsive part of the excite potential. A photon may be absorbed when the interatomic distance is  $R_c$ . The collision may be inelastic, resulting in an energy gain  $\hbar\Delta$ .

One limitation of this method is that it requires deep traps, about 3 mK against 1 mK for traps loaded with red detuned beams (Grünzweig et al. 2010). Another limitation is that it still

requires red-detuned light for cooling. The strategy developed in the Regal group is based on  $\Lambda$ -enhanced gray molasses to do both cooling and single atom loading, in shallower traps (red-detuned molasses are used only after this stage, to image the atoms). The principle is the following. The collisional energy gain is  $\hbar\Delta$ . If  $\hbar\Delta \ll 2U_0$ , losses due to GM are weak, likely leading to  $N \gg 1$  atoms in the trap, but then there will be light-assisted collision during the imaging and one recovers the 50% loading probability of red-detuned light-induced collisions (see section 1.3). If  $\hbar\Delta \gg 2U_0$ , two-body losses will occur during the GM phase, but the released energy is high enough to expel both atoms, leading to 50% loading efficiency. At the transition  $\hbar\Delta \approx 2U_0$ , only one atom will be lost during the GM pulse and the imaging pulse will not expel the remaining atom. As noticed in (Brown et al. 2019), the transition is at  $\hbar\Delta < 2U_0$  because of the finite atomic temperature.

## 2 Implementation

### 2.1 Setup

First we chose for simplicity to implement GM on the D2 line, using the same laser as the one used for the MOT. It has indeed been shown recently that the D2 line of  $^{87}\text{Rb}$  results in similar cooling performances in free space as obtained with the D1 line (Rosi et al. 2018), even though a blue detuned beam from for the  $F = 2$  to  $F' = 2$  transition is automatically red-detuned from the  $F = 2$  to  $F' = 3$  transition, leading to light-induced collisions.

The cooling beam is blue-detuned from the  $(5S_{1/2}, F = 2)$  to  $(5P_{3/2}, F' = 2)$  transition and is superimposed on the 6 MOT beams. The intensity per beam is  $I \sim I_{\text{sat}} = 1.67 \text{ mW cm}^{-2}$ . The intensity balance between the beams is tuned using half-wave plates and polarization beam splitters. The coherent repumper is created from the same laser using an electro-optical modulator <sup>1</sup> with frequency  $\nu = 6834.68 \text{ MHz}$ , equal to the ground state hyperfine splitting. The intensity of the repumper is  $I \sim I_{\text{sat}}/10$ , given by the sideband amplitude. The RF signal is generated by a RF generator <sup>2</sup> and a 3W-amplifier.

The goal of the study is to find the best parameters to optimize both the loading probability and the temperature of the atoms. The temperature of a single atom is measured using the *release and recapture* method (Tuchendler et al. 2008), described below.

---

<sup>1</sup>Qubig<sup>®</sup> PM - Rb 6.8

<sup>2</sup>Anritsu<sup>®</sup> MG3691A

## 2.2 Temperature measurement

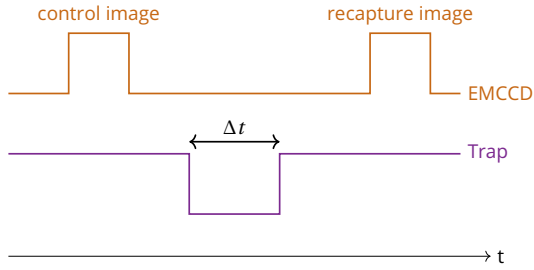


Figure 3.4: Chronogram of the single atom temperature measurement. The control and recapture images are done using the MOT beams for 20 ms.

The concept of temperature defined for ensembles of particles is here extended to a single atom. Repeated experiments on single laser cooled atoms yield an energy distribution given by a Maxwell-Boltzmann law with a well defined temperature. The chronogram of the experimental sequence used to measure this temperature is represented in figure 3.4. The sequence starts with a single trapped atom. The trap is then switched off during a finite time  $\Delta t$  (*release*) and then turned back on to determine if the atom has been *recaptured*.

The effect of the release and recapture is described in figure 3.5. When  $\Delta t = 0$ , the atom is always trapped. The characteristic size of the trap is given by its waist  $w_0$ , in dashed line. When  $\Delta t > 0$ , the atom is released in free-flight. The distance  $\sigma(\Delta t)$  that the atom travels during the free flight depends on its thermal velocity  $v_T$ :

$$\sigma(\Delta t) = v_T \Delta t = \sqrt{\frac{k_B T}{m}} \Delta t.$$

When the trap is switched back on, the atom is recaptured if it remained in the trap region during the flight:  $\sigma < w_0$ . Otherwise, the atom is lost (represented in black figure 3.5).

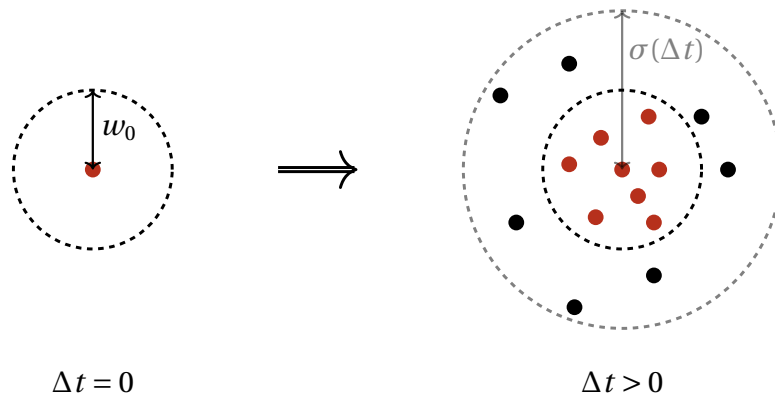


Figure 3.5: Principle of the *release and recapture* method. The various positions at  $\Delta t > 0$  correspond to repetitions of the experiment for the same atom.

To illustrate the method, we show the recapture probability of a single atom loaded from the MOT in a dipole trap of waist  $w_0 = 2\mu\text{m}$  and of depth  $U_0/k_B \sim 1\text{mK}$  as a function of the release time, figure 3.6. As expected, the atom is always recaptured when  $\Delta t < w_0/v_T$ . Data are then compared with Monte-Carlo simulations in order to estimate the temperature. In the case of figure 3.6,. These simulations are done for several temperatures, each averaged over 2000 trials.

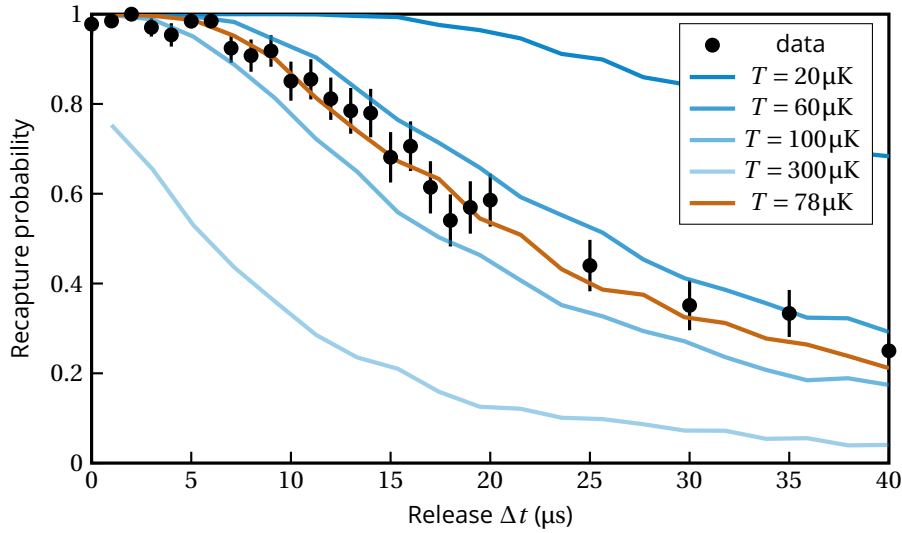


Figure 3.6: Temperature estimation by comparison with Monte-Carlo simulations. The temperature that minimizes the  $\chi^2$  test is plotted in orange ( $T = 78 \mu\text{K}$ ).

The temperature and its uncertainty are extracted by a  $\chi^2$  test (Bevington et al. 1993). In the case of figure 3.6, we obtain  $T_0 = 78(7) \mu\text{K}$ , which is typically the temperature of a single atom in our  $\sim 1 \text{ mK}$  dipole trap loaded from the MOT.

### 3 Experimental results

#### 3.1 Single atom loading and temperature

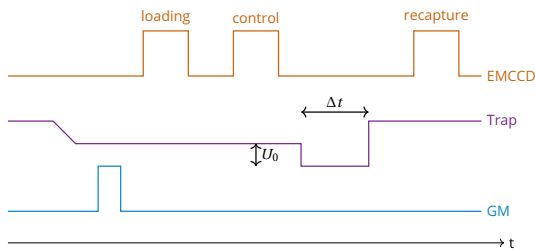


Figure 3.7: Chronogram of the GM optimization. A GM pulse is applied. A first image is taken to estimate the trap loading. The temperature is then measured using the sequence of figure 3.4. All images are done using the MOT beams for 20 ms

Having described how  $T$  is measured, we can now turn into the optimization of the loading probability and the temperature of the atoms as a function of two key parameters: the trap depth at focus  $U_0$  (with a fixed waist  $w_0 = 1.6 \mu\text{m}$ ) and the detuning  $\Delta$  of the GM with respect to the  $(5S_{1/2}, F=2)$  to  $(5P_{3/2}, F'=2)$  transition. The other parameters (beam powers, duration etc.) are optimized in the same way. From section 1, we expect to find an optimal loading for  $2U_0 = \hbar\Delta$ .

The experimental sequence is represented in figure 3.7. After loading the MOT, the magnetic field gradient and MOT beams are switched off. A cooling pulse with the GM is then applied, for a duration of 200 ms. An

image is then taken with the (red detuned) MOT beams, to determine whether an atom is loaded in the trap. The number of trapped atoms after this image is necessarily 0 or 1 because of red-detuned light induced collisions. The method described in section 2.2 is then

used to measure the atom temperature. The temperature as a function of  $\Delta$  and  $U_0$  is plotted figure 3.8.

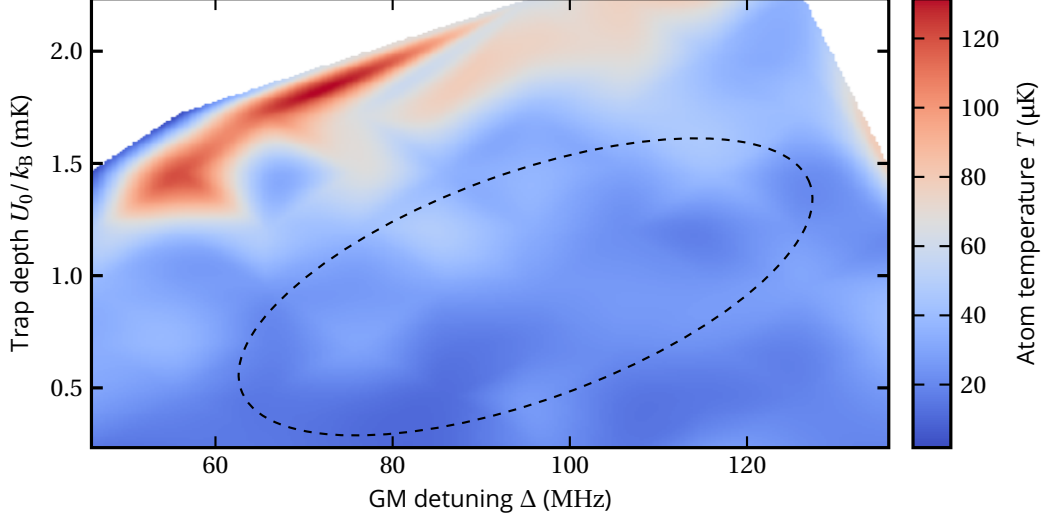


Figure 3.8: Temperature of the atom as a function of the trap depth  $U_0$  and of the GM detuning  $\Delta$ . The colorbar indicates the temperature. The dashed ellipse indicates a large sweet spot of parameters that give the same temperature.

We find that using the GM results in atoms cooler than using the MOT,  $\sim 20\mu\text{K}$  instead of  $80\mu\text{K}$ . The parameters used do not change the temperature over a large range, represented by a dashed ellipse in figure 3.8. The cooling by GM appears to be very robust over a broad range of parameters. When the cooling laser becomes resonant with the  $(5S_{1/2}, F=2)$  to  $(5P_{3/2}, F'=2)$  transition, the atom is heated up. This is the case either when the GM frequency is reduced, or when the trap power is increased, light-shifting the transition. This is what we observe in the regions  $\Delta < 80\text{MHz}$ , or  $U_0/k_B > 1\text{mK}$ . The loading efficiency measured in the same conditions is plotted in figure 3.9.

We succeed in trapping atoms in traps with depth  $U_0/k_B \sim 200\mu\text{K}$ , which is in itself an improvement over direct loading from the MOT ( $U_0/k_B \sim 1\text{mK}$ ). However, there is no significant improvement over 50% over the entire range of parameters explored. There is in particular no improvement in the region ( $\hbar\Delta \simeq 2U_0$ ). This might be due to the fact that the blue-detuned beam on the  $(5S_{1/2}, F=2)$  to  $(5P_{3/2}, F'=2)$  transition is detuned to the red of the  $(5S_{1/2}, F=2)$  to  $(5P_{3/2}, F'=3)$  transition. This transition is 267MHz above in energy and may cause red-detuned light-induced collision.

Hoping to improve these results and reproduce the performances claimed in (Brown et al. 2019) of  $>50\%$  loading rates, we implemented gray molasses on the D1 line to avoid this effect. In contrast to (Brown et al. 2019), we were not able to obtain individual atoms with a probability larger than 50%. This result might be explained by the fact that the volume of our trap is more than 10 times larger, reducing the collision rate. This loss rate might be too low to induce the selective losses during the time of the cooling pulse (200ms). Another group has recently tried to use GM to load optical tweezers, without reaching the 90% (Ang'ong'a et al. 2021).



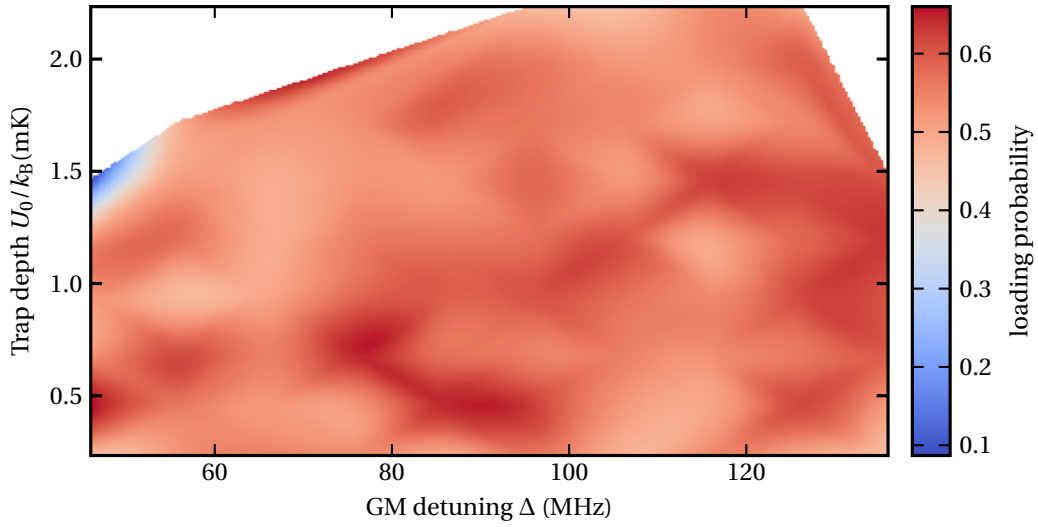


Figure 3.9: Single-atom loading probability as a function of the trap depth  $U_0$  and of the GM detuning  $\Delta$ .

### 3.2 1D chain loading

As we have explained in the previous chapter, we can prepare a chain of atoms in an 1D optical lattice. The volume of individual sites can be smaller than for a single optical tweezer because the axial dimension is now given by  $\lambda_{\text{trap}}/2 = 470 \text{ nm}$ . We perform the same experiments than above, varying the trapping depth at the center of the chain  $U_0$  and the detuning  $\Delta$  of the GM. Exploiting the high resolution transverse imaging system, we can observe the average filling along the chain. Figure 3.10 shows the obtained loading probability as a function of  $U_0$  and  $\Delta$  for two positions in the chain : at the center, where the traps are the deepest and smallest because the radial confinement is the strongest, and at one side of the chain, where the traps are shallower.

In the figure above, we show with a dashed line the light shift  $\Delta_{\text{trap}}$  at the center of the chain, to show the limit where GM are indeed blue detuned. In the same figure, we plot  $\Delta_{\text{trap}} + \frac{2}{U_0} h$ . We observe an enhanced loading around this line, showing a strong effect of the GM. The loading efficiency is not significantly larger than 50%, but this is an improvement compared to the direct loading obtained from the MOT (  $\sim 25\%$ ). The loading of atoms in the chain is still not totally understood. In the right panel, we consider the side of the chain, where the traps are less confined radially. The loading here is quite similar to that of a single optical tweezer and does not depend on the parameters.

We have found that the loading is also more robust to misalignment and daily fluctuations than when using the MOT.

### 3.3 Many atoms in the tweezer

Results of the previous section suggest that the low scattering rate of the GM, preventing light assisted collisions, allows us to have much more than one atom in the trap. At first sign, we compare the absolute fluorescence after loading using the GM on the D1 line with the after direct loading from the MOT, in the collisional blockage regime. In the case of the MOT loading, when sending near-resonant light for imaging (during 20 ms), two clear fluorescence

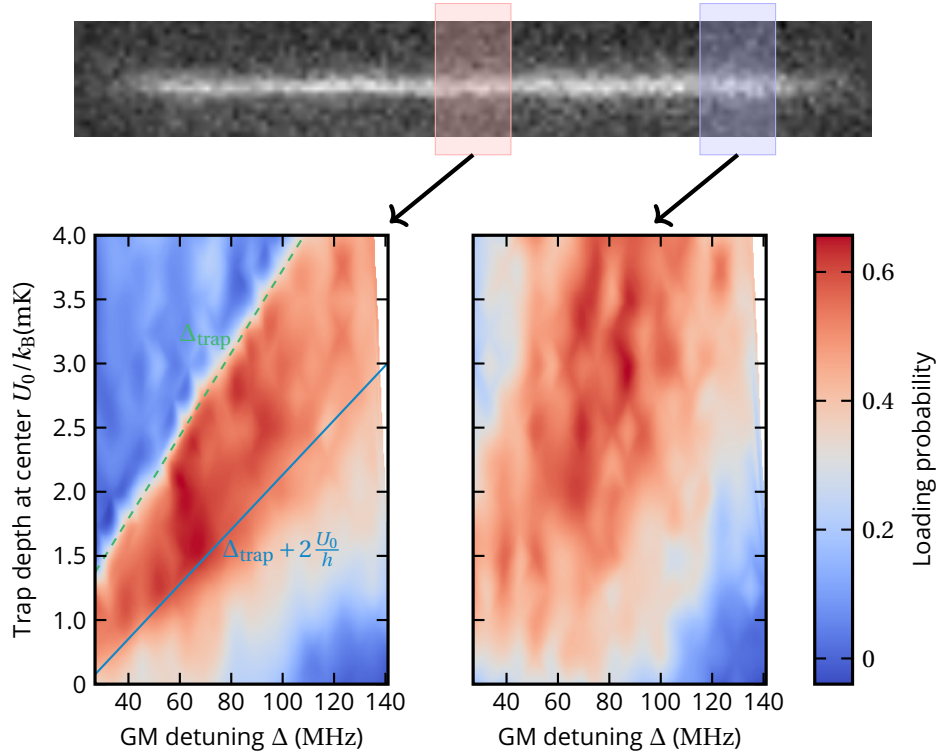


Figure 3.10: Single-atom loading probability as a function of the trap depth  $U_0$  and of the GM detuning  $\Delta$  at the center of the chain (left) and at one side of the chain (right).

levels are observed corresponding to either zero or one atoms in the trap (see figure 2.9 and section 1.3). In the other case, a 200 ms GM pulse is applied to load the trap, and then an image is taken as before. A broad fluorescence histogram is observed, as shown in figure 3.11. This is a signature of the presence of many atoms in the trap.

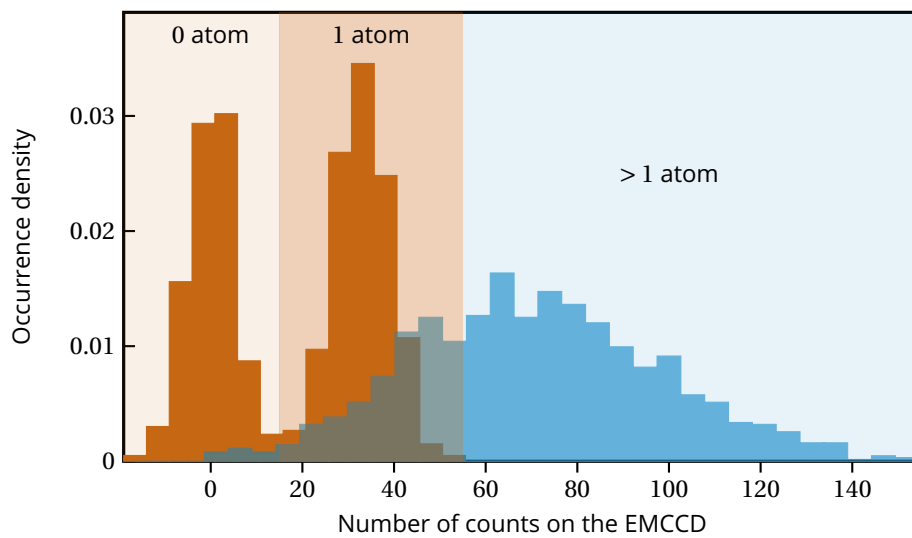


Figure 3.11: Histogram of the collected fluorescence of atoms in a trap loaded with the GM (blue) in comparison with a trap loaded with a single atom (orange).

The imaging light induces collisions and thus strong losses during the 20 ms, so that the atoms fluoresce in a much shorter (uncontrolled) time. Atoms thus cannot be counted in this measurement. We will see in chapter 5 that GM allows us to load more than 6000 atoms in a micrometric trap, reaching peak densities  $n_0/k_0^3 > 1$ .

## 4 Conclusion

In this chapter, we have briefly explained the principle of the gray molasses and their implementation on the experiment to load efficiently single atoms. In contrast to (Brown et al. 2019), we were not able to obtain individual atoms with a probability larger than 50%. In the last part, we have observed that the low scattering rate of GM allows us to have many atoms in a microscopic dipole trap. This feature will be exploited in chapter 5 to reach high peak densities. During my thesis, we increased the number of trapped atoms by almost a factor of 10 compared to the previous generation of the experiment (Bourgain et al. 2013), for similar dipole traps, exploiting GM. Reaching this number of atoms has allowed us to observe previously elusive effects, in particular subradiance and superradiance, which will be studied in the next chapters.



# Collective shift in a 1D atomic chain

\*\*\*

In an ensemble of atoms, the excitation by light induces dipoles which are then driven by the fields radiated by all neighboring dipoles. In a disordered ensemble containing many emitters, the random relative phases of the radiated fields lead to destructive interferences suppressing the effect of interactions. Structuring the sample could instead enhance the interactions by forcing the radiated field to interfere constructively, and provide strong light-matter coupling .

For example, it has been recently predicted (Bettles et al. 2016b; Shahmoon et al. 2017; Facchinetti and Ruostekoski 2018) and demonstrated (Rui et al. 2020) that interactions can lead to an enhanced reflectivity for single atomic layer. This subject has also been very active in recent years in 1D systems, theoretically (Plankensteiner, Ostermann, et al. 2015; Chui et al. 2015; Asenjo-Garcia et al. 2017; Needham et al. 2019) and experimentally. It has been studied in various systems: with atoms trapped near nano-photonic waveguides (Yu et al. 2014; Corzo et al. 2019), nanofibers (Vetsch et al. 2010; Solano et al. 2017; Prasad et al. 2019) and with a small chain of ions (Meir et al. 2014).

This chapter presents the experimental realization of a 1D atomic chain (Glicenstein, Ferioli, Brossard, et al. 2021) and the observation of collective interferences in resonant dipole-dipole interaction in this chain (Glicenstein, Ferioli, Šibalić, et al. 2020). This system is disordered but the 1D dimensionality strongly enhances the interactions.

## Contents

<b>1</b>	<b>Motivations . . . . .</b>	<b>74</b>
<b>2</b>	<b>Collective resonance shift . . . . .</b>	<b>78</b>
2.1	Local shift along the chain . . . . .	79
2.2	Shift reduction due to transverse disorder . . . . .	80
2.3	Shift reduction due to interatomic distance . . . . .	81
2.4	Beyond the low-intensity limit . . . . .	82
<b>3</b>	<b>Conclusion . . . . .</b>	<b>84</b>

## 1 Motivations

Let us first illustrate how the dimensionality of the ensemble may enhance the interactions between the emitters. Consider a disordered 1D chain of atoms excited by a plane wave propagating along the chain axis  $z$  with frequency  $\omega = kc = \frac{2\pi}{\lambda}c$ , as represented in figure 4.1.

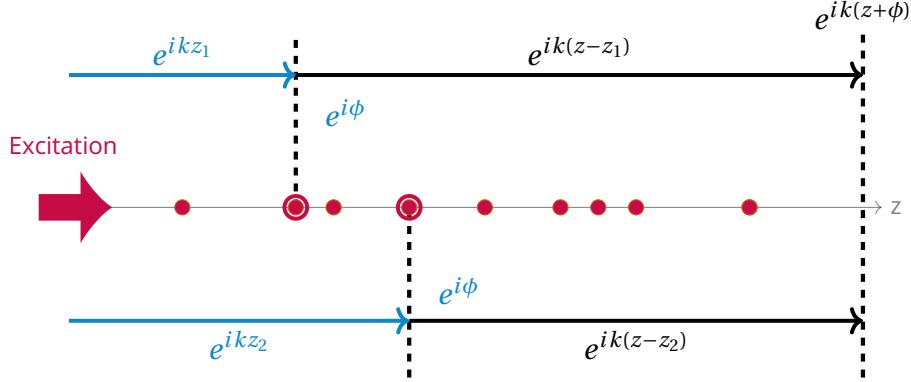


Figure 4.1: Schematic of an atomic chain under axial excitation. The total phase accumulated by propagation and a single scattering event is the same in the forward direction, irrespective of the atomic positions.

By propagating along  $z$ , the driving field accumulates a phase  $kz_n$  on atom  $n$  (position  $z_n$ ). Under a weak excitation, the induced dipoles scatter a field with an amplitude proportional to the amplitude of the driving field and with a phase shifted by  $\phi = \text{Arg}(\alpha)$  (Aljunid et al. 2009), where  $\alpha$  is the atomic polarizability (see Section 1.1). Atom  $n$  also sees the field scattered by other atoms. The scattered field then accumulates a phase  $k|z - z_n|$  by propagation. For simplicity, we first consider that the field is scattered once. Therefore, as represented in figure 4.1, the phase at position  $z$  accumulated by a scattered field propagating in the forward direction ( $z > z_n$ ),  $k(z - z_n) + kz_n = kz$ , is independent of the atomic position  $z_n$ . At this first order (with a single scattering event), the fields scattered in the forward direction thus interfere constructively. This argument is only valid if the atoms are aligned along the propagation axis of the driving field. Otherwise, the accumulated phase is random (because it depends on the random position of the atoms) and does not lead to constructive interference. In particular, this is also the case if the driving field propagates perpendicularly to the chain. In general, the fields scattered in the backward direction are also not constructive.

Due to the 1D dimensionality, one thus expects an enhancement of the interactions. Note that the equal spacing of the atoms is not necessary here.

### Growth of the excitation along a chain

Following (Sutherland and Robicheaux 2016) and (Brossard 2019), let us detail the case of a defect-free ordered 1D chain, with interatomic distance  $a$ . For a weak driving, the dipoles induced by a field  $E_L(\mathbf{r}_m) = E_0 e^{ikr_m}$  propagating along the chain are treated classically (section 2.2) and are modeled by the coupled dipole equation (1.7). In steady state, this equation for atom  $m$  is, in the scalar approximation,

$$0 = (2i\delta - 1) E_m - E_L(\mathbf{r}_m) - \sum_{n \neq m} G(\mathbf{r}_n - \mathbf{r}_m) E_n \quad (1.1)$$

where  $E_m = b_m \frac{\hbar \Gamma}{2id}$  is the field scattered by atom  $m$  ( $d$  being the dipole matrix element and  $b_m$  the induced dipole),  $\delta = \Delta/\Gamma$  is the normalized detuning of the laser with the resonance frequency and  $G(\mathbf{r})$  is the Green function (see section 1.1). We consider a perfectly ordered chain such that  $r_m = ma$ , the Green function becomes

$$G(\mathbf{r}_n - \mathbf{r}_m) = \frac{3e^{ika|n-m|}}{2ika|n-m|} \left[ 1 + \frac{i}{ka|n-m|} - \frac{1}{(ka|n-m|)^2} \right] = \frac{3e^{ika|n-m|}}{2ika|n-m|} f_{n-m}$$

and equation (1.1) becomes

$$(2i\delta - 1)E_m = E_0 e^{ikma} + \sum_{n \neq m} \frac{3e^{ika|n-m|}}{2ika|n-m|} f_{n-m} E_n. \quad (1.2)$$

Assuming that  $ka \gg 1$  (large interparticle distance), one can solve perturbatively equation (1.2) and finds at zeroth order (corresponding to no interaction),

$$E_m^{(0)} = \frac{E_0 e^{ikma}}{2i\delta - 1}$$

and at first order (one scattering)

$$E_m^{(1)} = \frac{E_0 e^{ikma}}{2i\delta - 1} + \sum_{n \neq m} \frac{3e^{ika|n-m|}}{2ika|n-m|} f_{n-m} \frac{E_0 e^{ikna}}{2i\delta - 1}.$$

Factorizing the global phase  $e^{ikma}$  and splitting the sum into two parts leads to

$$E_m^{(1)} = \frac{E_0 e^{ikma}}{2i\delta - 1} \left\{ 1 + \frac{3}{2i(2i\delta - 1)} \left[ \underbrace{\sum_{n < m} \frac{f_{n-m}}{ka(m-n)}}_{\text{forward scattering}} + \underbrace{\sum_{n > m} \frac{f_{n-m}}{ka(n-m)} e^{2ika(n-m)}}_{\text{backward scattering}} \right] \right\} \quad (1.3)$$

Equation (1.3) shows that all forward scattering terms add constructively at long distance because they have the same phase factor. This comes from the fact that the atoms are aligned along the chain axis (as we saw above, the fact that they are equally spaced does not play a role here). The backward scattering does not build constructively at long range because of this phase factor if  $a \neq j\frac{\lambda}{2}$ , where  $j \in \mathbb{N}$ .

We consider the case  $a \neq j\frac{\lambda}{2}$ . Keeping only the forward scattering term and assuming  $f_{n-m} = 1$  for simplicity, the field intensity at atom  $m$  is thus given by

$$|E_m^{(1)}|^2 = \frac{|E_0|^2}{1 + 4\delta^2} \left| 1 + \frac{3}{2i(2i\delta - 1)} \sum_{n < m} \frac{1}{ka(m-n)} \right|^2$$

which gives at lowest order in  $\frac{1}{ka}$ ,

$$|E_m^{(1)}|^2 = \frac{|E_0|^2}{1 + 4\delta^2} \left\{ 1 - \frac{6\delta}{1 + 4\delta^2} \sum_{n < m} \frac{1}{ka(m-n)} \right\}. \quad (1.4)$$

This result shows that, depending on the sign of  $\delta$ , the scattered field intensity increases ( $\delta < 0$ ) or decreases ( $\delta > 0$ ) along the chain. The excitation probability is  $P_m = |d_m^{(1)}(\delta)|^2 \propto |E_m^{(1)}|^2 / [1 + 4\delta^2]$ . Using  $|d_m|^2 = \frac{4d^2}{\hbar^2 \Gamma^2} |E_m|^2$ , one obtains (Sutherland and Robicieux 2016) with  $p = m - n$ ,

$$P_m = \frac{(dE_0/\hbar\Gamma)^2}{\delta^2 + 1/4} \left\{ 1 - \frac{3\delta}{2ka(\delta^2 + 1/4)} \sum_{p=1}^{n-1} \frac{1}{p} \right\}. \quad (1.5)$$

The excitation probability is plotted figure 4.2 for  $\Delta = \pm\Gamma$  and  $a = 1.2\lambda$ . The excitation probability increases (decreases) for a red (blue) detuned excitation, with a logarithmic behavior. This is a signature of the enhancement of the interactions, that add coherently along the chain even at large interatomic distance.

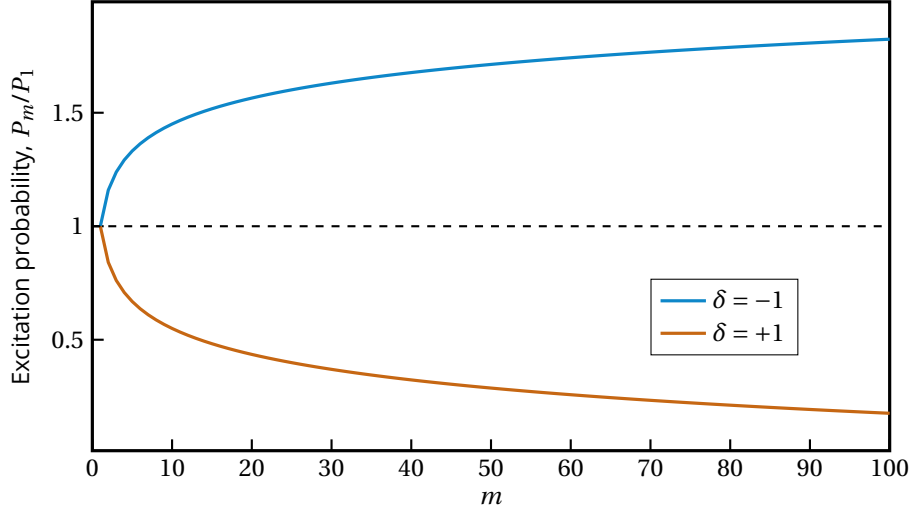


Figure 4.2: Probability of excitation of atom  $m$  divided by the single atom excitation probability for  $\delta = \pm 1$  and  $a = 1.2\lambda$ .

We compare the analytic solution (1.5) with the full numerical calculation (1.1). As shown in figure 4.3, the model is only accurate in the regime  $ka \gg 1$  (which is the approximation done). Otherwise, the agreement is only qualitative. The oscillations in the full numerical solution are due to reflections at the end of the chain.

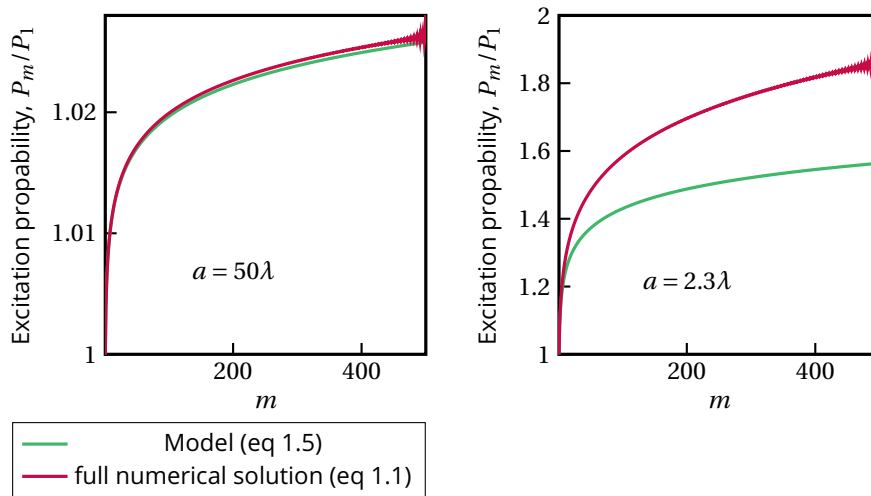


Figure 4.3: Comparison between the analytic solution (green) and the full numerical solution (red), for  $\delta = -1$ .



The description above holds only for values of  $a \neq j\frac{\lambda}{2}$ . When  $a = j\frac{\lambda}{2}$ , the backward scattered fields also add constructively and  $P_m$  has a mirror symmetry (Sutherland and Robicheaux 2016). Moreover, equation (1.5) is based on the approximation of large interparticle distance ( $ka \gg 1$ ) and are not valid for  $a < \lambda/2$ , where the behavior of the system may be dominated by subradiant modes.

The increase of the excitation probability is spectrally translated by a shift of the resonance frequency. Using equation (1.5), we see that this shift is towards the red. We calculate the shift using the full numerical solution for a perfect 100 atom-chain with interatomic spacing  $a = 1.2\lambda$ . Figure 4.4 shows this (local) shift of the resonance as a function of the atom position in the chain. One sees that, as expected, the shift increases along the chain. The global (mean) resonance frequency over the chain is also shifted, as described using the numerical methods in the first chapter (figure 1.10). As seen in chapter 1, the frequency is much more shifted for a (disordered) chain than in 3D systems, which reflects the importance of interactions in the chain.

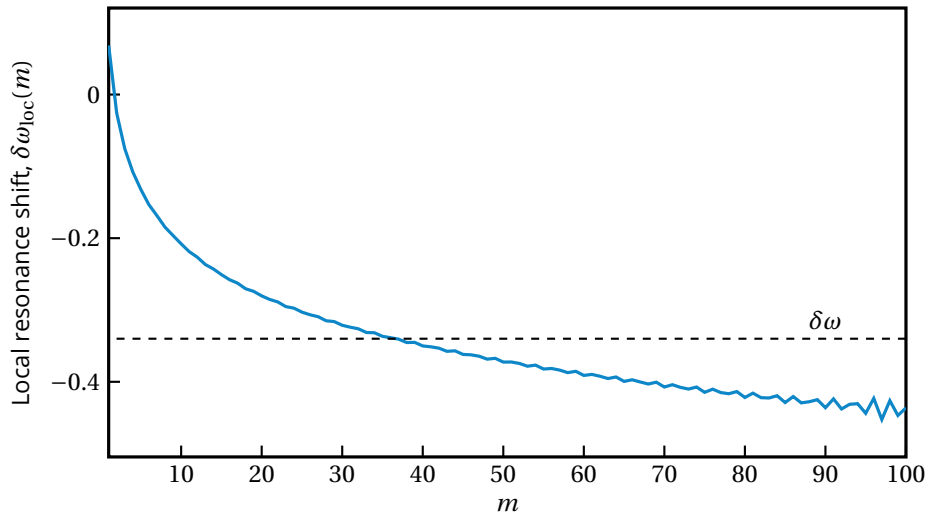


Figure 4.4: Local resonance shift  $\delta\omega_{\text{loc}}(m)$  as a function of the position in the chain. The global (mean) shift  $\delta\omega$  is plotted as a dashed line.

The resonance shifts are the experimental observables that we will measure to study the collective effects.

## Conclusion

Due to this spectacular enhancement, the 1D chain is a good candidate to observe collective effects even at large interatomic distance (larger than the light wavelength). The rest of the chapter is dedicated to the experimental study of this system.

## 2 Collective resonance shift

The goal of this section is to observe the collective shift predicted in the first part of this chapter, compared to that of a single atom.

As explained in chapter 2 (section 44), we prepare a 1D chain of 100 atoms in a 1D optical lattice. The average filling  $\eta = 0.5 \pm 0.1$  of the lattice, exploiting  $\Lambda$ -enhanced Gray molasses (chapter 3), results in an interatomic distance  $\langle r_{mn} \rangle = 1.2\lambda_0$  where  $\lambda_0 = 780\text{nm}$ . The atoms are then optically pumped in the  $(5S_{1/2}, F=2, m_F)$  state (section 3.2) with the quantization axis aligned with the chain with an efficiency larger than 99%.

The temperature  $T$  of the atoms is obtained by time-of-flight. One obtains  $T = 80(20)\mu\text{K}$ , yielding a transverse width  $\sigma_{r,0} \approx 300\text{nm} \approx 0.38\lambda_0$ . The transverse confinement is ensured by a tight focusing of the trapping beam ( $w_0 = 3.3\mu\text{m}$ ). The atoms are excited along the chain axis by applying 200ns pulses of a  $\sigma_+$ -polarized probe (at wavelength  $\lambda_0 = 780\text{nm}$ ) in free space with an intensity  $I/I_{\text{sat}} = 0.3$ . The probe waist is  $w_{\text{probe}} = 20\mu\text{m}$  (Rayleigh range  $z_R = 1.6\text{mm}$ ) such that it approximates a plane wave. 50 pulses are sent, between which atoms are recaptured by switching the trap beams on (see section 2.4). We vary the probe detuning in order to measure fluorescence spectra. For a given probe detuning, the sequence is repeated over 300 samples to obtain sufficient statistics.

The scattered light is collected perpendicularly to the chain, as in figure 2.17. The intensity spectrum is extracted by repeating this measurement at different detunings between  $\Delta = -3\Gamma$  and  $3\Gamma$ , where  $\Gamma = 2\pi \times 6.1\text{MHz}$  is the natural linewidth of the D2 line. The profiles are fitted by a Lorentzian function, from which the global (mean) shifts  $\delta\omega$  of the resonance are extracted. Note that there is no distortion of the spectra, which remains Lorentzian for all parameters tested. This is numerically predicted by the coupled dipoles simulations for interatomic distances larger than  $\lambda_0$ . We show examples of shifted spectra in figure 4.5.

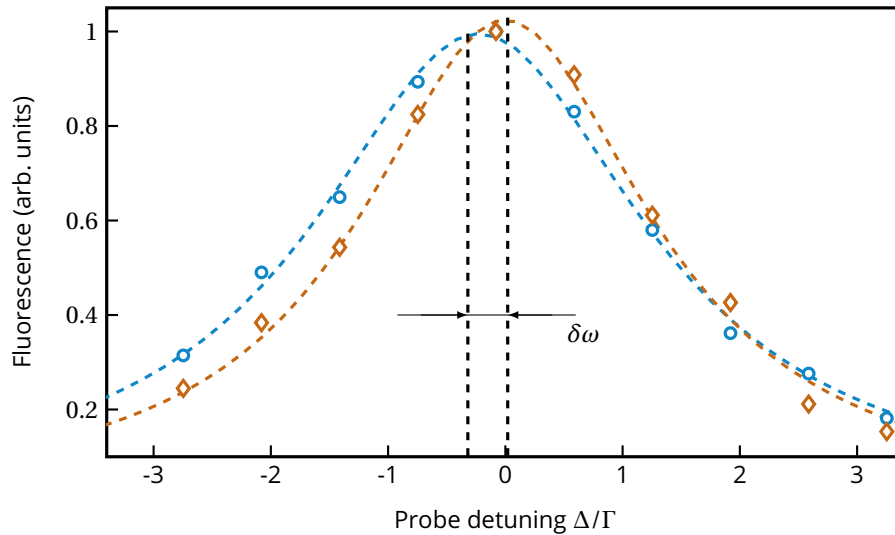


Figure 4.5: Example of shift measurement using fluorescence spectra. Data are fitted by Lorentzian function (dashed lines). These spectra are used in figure 4.8 using the same colors, see text.

In figure 4.5, one sees that the width of the spectra is larger than the natural linewidth  $\Gamma$ . This is due to the Fourier width of the 200ns probe pulses.

### Reference of the shifts

In figure 4.5 and following, the reference of the measured shifts is given by the resonance of non interacting atoms ( $\Delta = 0$ ). It is measured using a dilute 3D cloud, so that the interactions are negligible.

### 2.1 Local shift along the chain

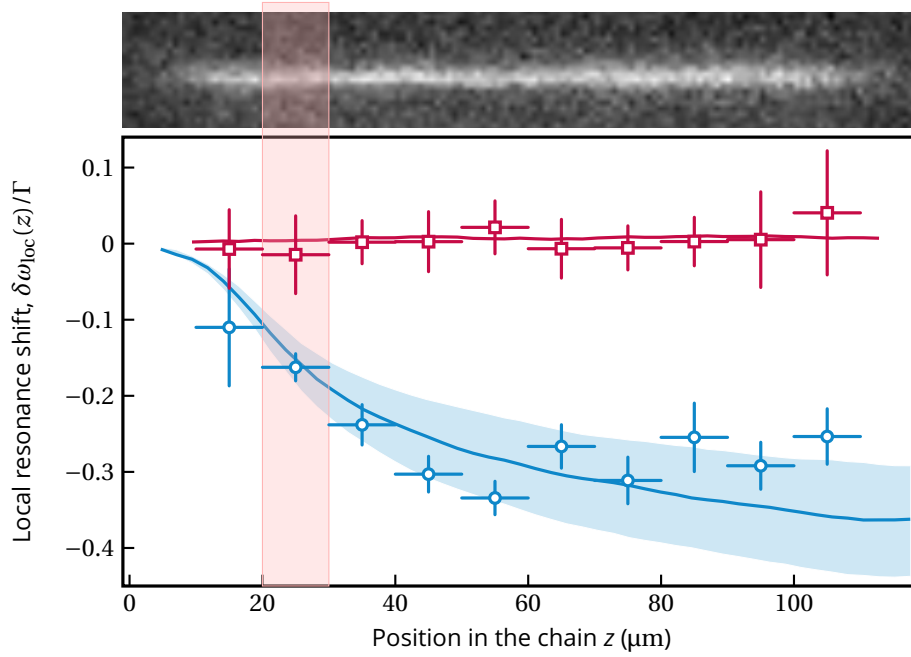


Figure 4.6: Local shift  $\delta\omega_{\text{loc}}(z)$  as a function of the position along the chain. The blue circles (red squares) correspond to the axial (transverse) excitation. Each data point is the resonance frequency of a  $10\mu\text{m}$  segment around  $z$ . The vertical error bars are from the fits. The results are compared to coupled dipoles simulations (solid lines), the shaded area corresponding to the experimental uncertainty in chain filling (see text).

Figure 4.5 shows a global collective shift, but we showed in the first part of this chapter that it is due to the enhancement of the interactions along the chain. To observe it, we divide the chain into  $10\mu\text{m}$  segments, as represented in figure 4.6. On each of these segments, the intensity spectrum is fitted by a lorentzian function, allowing to determine a *local* shift of the resonance  $\delta\omega_{\text{loc}}(z)$ , shown figure 4.6.

One sees in figure 4.6 that the resonance is redshifted compared to the single-atom resonance. This can be understood using equation (1.4). For red detunings ( $\Delta < 0$ ), the scattered fields and the driving field are in phase such that constructive interferences increase the total field intensity. For blue detunings ( $\Delta > 0$ ), destructive interferences reduce the field. The local shift increases along the chain for an axial excitation (blue circles), indicating a buildup of the interactions. The resonance is shifted by more than  $\Gamma/4$ . Such a shift has been obtained in disordered 2D and 3D samples but for ten times smaller interatomic distances (Jennewein, Y. R. P. Sortais, et al. 2016; Corman et al. 2017). This confirms that the collective response is strongly enhanced, as explained section 1.

To demonstrate the cumulative effect, we perform a second experiment where we apply an identical excitation procedure but with a plane wave probe sent perpendicularly to the chain ( $w_{\text{probe}\perp} \simeq 1.5\text{mm}$ ). The result is plotted figure 4.6 (red squares). We do not observe any shift, in agreement with the discussion section 1 (and fig. 4.1). In this case, the scattered fields have a random phase relation along the chain, leading to no cumulative effect. We thus obtain the response of independent atoms.

While the perturbative model allows for an intuitive picture, the results are compared to coupled dipoles simulations (section 2.1) including all experimental parameters. We take into account the random filling and the atomic motion is negligible during the excitation pulse. Simulations give spectra which are well fitted by a lorentzian line shape, allowing to extract a resonance shift. The results are plotted as solid lines figure 4.6, for fillings  $\eta = 0.5 \pm 0.1$ . We obtain a good agreement between the data and the model, without any adjustable parameter.

## 2.2 Shift reduction due to transverse disorder

As explained in introduction of this chapter, the collective enhancement relies on the 1D geometry and thus should be reduced by adding transverse disorder. To quantify the reduction due to transverse disorder, consider an atom at distance  $\rho_n$  from the chain axis, as represented in figure 4.7. The phase factor of the field scattered by this atom at position  $\mathbf{r}$ , ( $\rho = 0$ ) is

$$k|\mathbf{r} - \mathbf{r}_n| \simeq k|z - z_n| + \frac{k\rho_n^2}{2|z - z_n|}$$

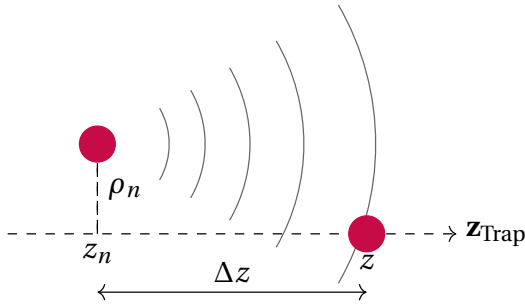


Figure 4.7: Schematic : condition to have constructive interferences away from 1D.

assuming that the atom is slightly off axis ( $\rho_n \ll |z - z_n|$ ). To have interferences with the field scattered by an atom on the axis at a distance  $\Delta z$ , one must have  $k\rho_n^2/2\Delta z \ll 2\pi$  that is  $\rho_n^2/\lambda_0\Delta z \ll 1$ . This shows that when  $\sigma_r/\lambda_0 \gg 1$ , where  $\sigma_r$  is the radial extent of the chain, interferences should disappear thus the shift.

We verify this prediction experimentally by changing the radial size of the atomic distribution. The radial size of the cloud is directly measured using the transverse imaging system (section 1.3) by a 2D gaussian fit of the fluorescence image. To change the radial distribution, we let the cloud expand in free flight during a time  $t_{\text{of}}$ . The radial size is then given by

$$\sigma_r(t_{\text{of}}) = \sqrt{\sigma_{r,0}^2 + \frac{k_B T}{m} t_{\text{of}}^2}.$$

As  $\sigma_{z,0} \gg \frac{k_B T}{m} t_{\text{of}}^2$ , the axial size of the chain does not change during the free flight. For a given time-of-flight, a fluorescence spectrum is measured sending a near-resonant probe pulse for  $10\mu\text{s}$  for detunings between  $-3\Gamma$  and  $3\Gamma$ . The global resonance shift is then extracted using a lorentzian fit of the data. The shift as a function of  $\sigma_r$  is shown figure 4.8. As expected, we observe that the shift vanishes when the atoms are not in 1D geometry ( $\frac{\sigma_r}{\lambda_0} \gtrsim 1$ ). The

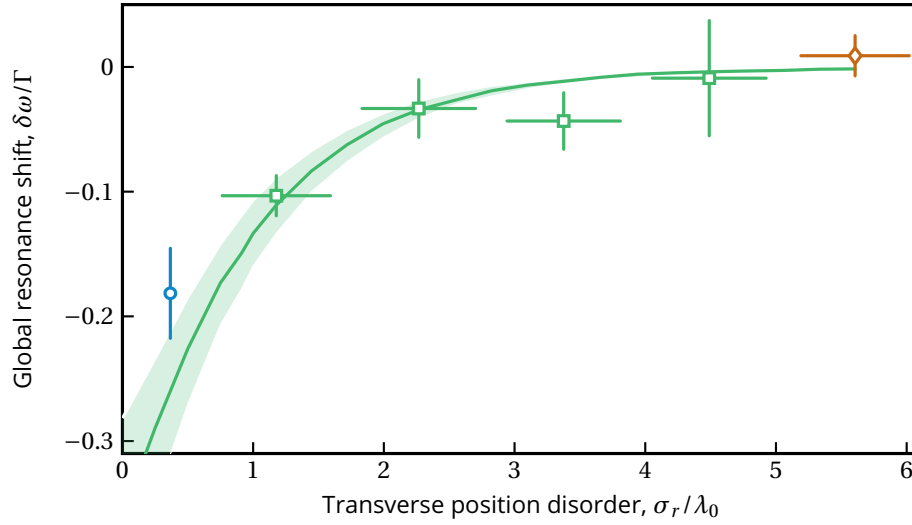


Figure 4.8: Global shift  $\delta\omega$  as a function of the radial size  $\sigma_r$  of the cloud after a time of flight. The vertical error bars correspond to the fit standard errors, the horizontal error bars correspond to the size variation during the probe pulse. Data are compared to coupled dipoles simulations (solid line). The reference of the shifts is given by the diamond point, corresponding to the resonance frequency of non-interacting atoms.

solid line corresponds to coupled dipoles simulations, which are in good agreement with the experimental data. In figure 4.8, the blue circle and the orange diamond correspond to the resonances extracted from the spectra of figure 4.5, with the same color code.

### 2.3 Shift reduction due to interatomic distance

In this part, we demonstrate the importance of the 1D geometry. We increase the interatomic distance while keeping the 1D geometry. This distance is changed by tuning the filling fraction, using the following method. A chain is first loaded as before. A fraction of the atoms are then optically pumped in ( $5S_{1/2}, F=2$ ) before being ejected from the trap using a state-selective push out beam. The number of remaining atoms is thus controlled by tuning the duration of the optical pumping pulse. The remaining atoms are assumed to form a uniformly filled chain with reduced density. The filling is measured by comparing the fluorescence of the chain with that of a single atom. The global shift as a function of the filling  $\eta$  is shown figure 4.9, together with coupled dipoles simulations. A reduction of the shift is observed in agreement with the simulations, but not a clear linear dependence as predicted in the simulations. The horizontal error bars are quite large. They are provided by the (single shot) filling measured using a 5 ms image with the MOT beams. The discrepancy between the data and the simulations could also be enhanced by a non-uniform filling along the chain.

To compare the 1D and 1D+transverse disorder situations, we plot the two datasets of figures 4.8 and 4.9 as a function of the interatomic nearest-neighbour distance  $k\langle r_{nn} \rangle$  in figure 4.10. For the disordered measurement of figure 4.8, the average distance is simulated by choosing randomly the atomic positions uniformly along the chain and with a gaussian law with variance  $\sigma_r$  in the radial direction.

The results shown in figure 4.10, confirm that the shift (so the interactions) is much stronger for a 1D sample, at a given  $k\langle r_{nn} \rangle$ . By plotting (dashed line) the result measured in

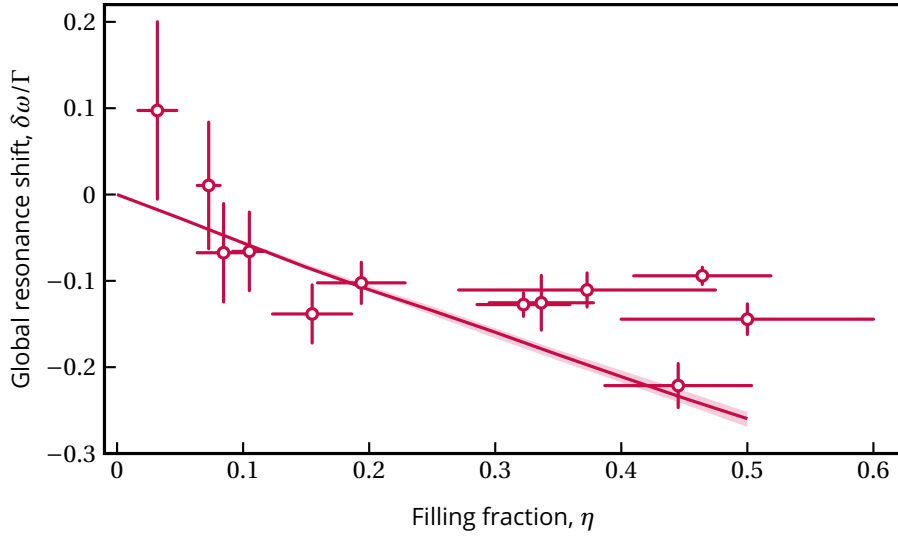


Figure 4.9: Global shift  $\delta\omega$  as a function of the filling fraction  $\eta$ . Data are compared to coupled dipoles simulations (solid line), with the error area accounting for the uncertainty in temperature. The reference of the shifts is the intercept of a linear fit of the data.

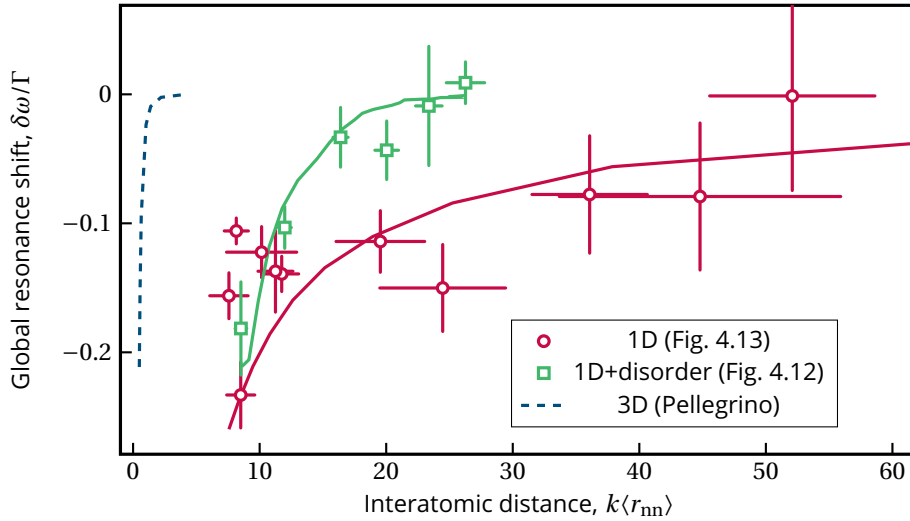


Figure 4.10: Comparison of data from fig. 4.8 and 4.9 as a function of the nearest-neighbor distance. The dashed line corresponds to the result of (Pellegrino et al. 2014) in a 3D gaussian cloud.

a 3D gaussian cloud (Pellegrino et al. 2014), one sees that the interactions are much stronger in the chain. Indeed, the same shift is obtained for interatomic distances that are ten times smaller.

## 2.4 Beyond the low-intensity limit

We finally explore beyond the regime beyond the low-intensity excitation, where the saturation effects appear and the data must be modelled by the nonlinear coupled dipoles equations (section 2.2). The intensity of the driving field is increased up to  $I \sim 20I_{\text{sat}}$  ( $\Omega_L/\Gamma \approx 3.1$ ),

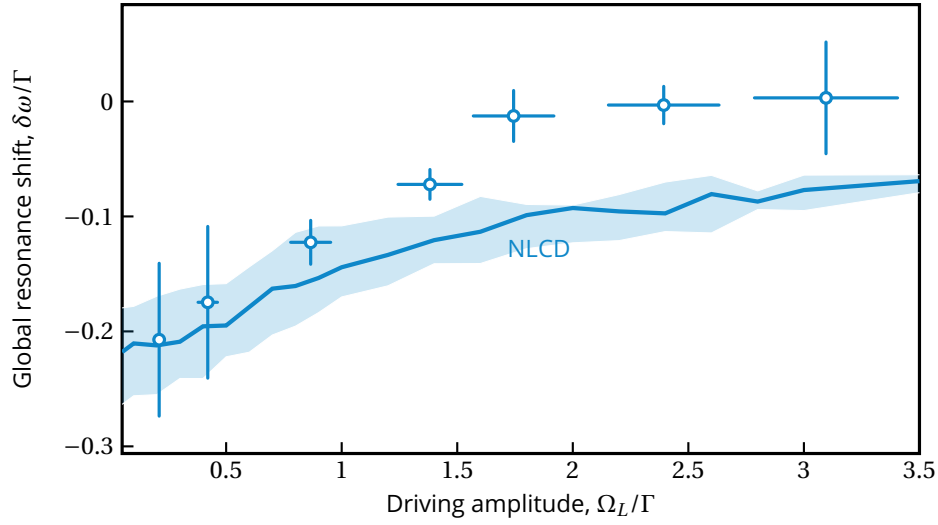


Figure 4.11: Global resonance shift  $\delta\omega$  as a function of the laser Rabi frequency  $\Omega_L$ . Vertical error bars are from the fits and the horizontal error bars correspond to the 10% uncertainty on the probe intensity. Data are compared to Nonlinear Coupled Dipoles simulations (solid lines) done by N.Šibalić including the experimental parameters.

while ensuring that it does not lead to extra atom losses and heating. When increasing the intensity, we observe a shift of the resonance frequency, as shown figure 4.11. This can be understood by the fact that the dipole vanishes when increasing the driving intensity (the coherence  $\rho_{eg}$  goes to zero, as shown in the first chapter section 1.2). The simulations are in good agreement with the experiment but predict a more gradual reduction of the resonance shift, due to saturation of individual quantum emitters. This might be explained by some mechanisms that pump atoms out of the two-level system for strong driving fields.

### 3 Conclusion

In this chapter, we have prepared and characterized a 1D atomic chain. Experiments have then been performed on this chain and have demonstrated the interest of the 1D dimension to obtain enhanced collective effects. The measurements presented here show that controlling the geometrical arrangement of the sample allows us to shape its collective response.

The studied chain has an average interatomic distance of  $1.2\lambda_0$ , which makes the interactions between the induced dipoles weak. An extension of this work will be to realize a chain with a smaller intersite spacing, for example by using a laser at wavelength 532 nm (the intersite spacing would be 532 nm assuming a filling fraction of 0.5).

Another promising perspective is the prospect of a tunable distance atomic 'Fabry Perot'. Indeed, in the motivations given section 1, we have only considered the case where the intersite distance  $a$  is not a multiple of  $\lambda/2$ . On the other case, the probability of excitation has a mirror symmetry (instead of only increase along the chain), as shown figure 4.12. The chain thus act as an atomic 'cavity' (Sutherland and Robicheaux 2016).

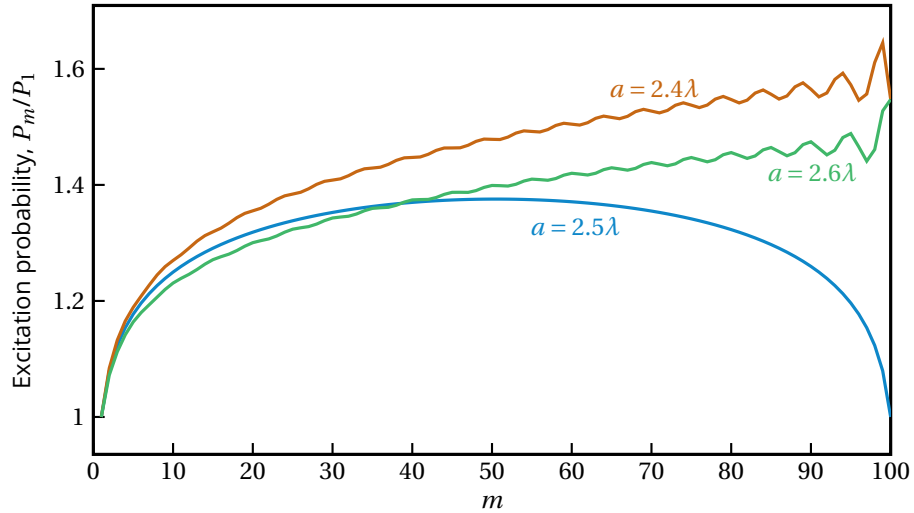


Figure 4.12: Probability of excitation of atom  $m$  divided by the single atom excitation probability for  $\delta = -1$  and  $a = 2.5\lambda$ ,  $a = 2.4\lambda$  and  $a = 2.6\lambda$ .

By varying the distance between the atoms around multiples of  $\lambda/2$ , one could thus change the behavior of the chain to a resonant excitation.



## **Part II**

# **Super- and Subradiance in a dense cloud of two-level atoms near Dicke's regime**



\*\*\*

In 1954, Dicke predicted that the radiation emitted by a dense ensemble of atoms should be dramatically different from the emission from independent atoms (Dicke 1954). In particular, he predicted the presence of collective states whose decay is faster than that of an isolated atom (*superradiance*), and others whose decay is slower or even zero (*subradiance*). The subject has been intensively studied since the 1970s both theoretically and experimentally (Gross and Haroche 1982; Scully, Fry, et al. 2006; Scully and Svidzinsky 2009). Due to the general character of the subject, it attracted a broad interest and has been investigated on many platforms ranging from hot atomic vapors (Pavolini et al. 1985) to cloud of cold atoms (Guerin, Araújo, et al. 2016; Roof et al. 2016), atoms in hollow core fiber (Okaba et al. 2019), nanofiber (Solano et al. 2017), Rydberg atoms (Wang et al. 2007), molecular systems (Hettich et al. 2002; McGuyer et al. 2015) and artificial atoms (Angerer et al. 2018; Mlynek et al. 2014) just to cite a few but also in the context of relativity and astrophysics (Brito et al. 2020).

Recently, the subject has regained interest in the context of quantum technologies. Indeed, it has been proposed for example to use sub-radiant states as a storage medium (Facchinetti, Jenkins, et al. 2016; H. H. Jen et al. 2020; Asenjo-Garcia et al. 2017) or as a tool for quantum information processing (Shahmoon et al. 2017) and for metrology (Plankensteiner, Ostermann, et al. 2015; Krämer, Ostermann, et al. 2016).

The second part of this manuscript is dedicated to the experimental study of superradiance and subradiance in a dense ensemble of two-level atoms in a regime close to Dicke's regime, in which the emitters are much closer than the wavelength of the emitted light.

- Chapter 5 is devoted to the description of the preparation and characterization of a dense cloud of two-level atoms.
- In chapter 6, a qualitative analysis of superradiance and of its main features is presented, before describing their experimental observation.
- In chapter 7, we extend our study of superradiance to the driven regime, during Rabi oscillations and in the steady state.
- Chapter 8 is devoted to the study of subradiance in our system. In particular, we demonstrate a protocol for the storage and release of subradiant excitations.

In the next chapters, the following experimental setup is used for the observation of super- and subradiance.

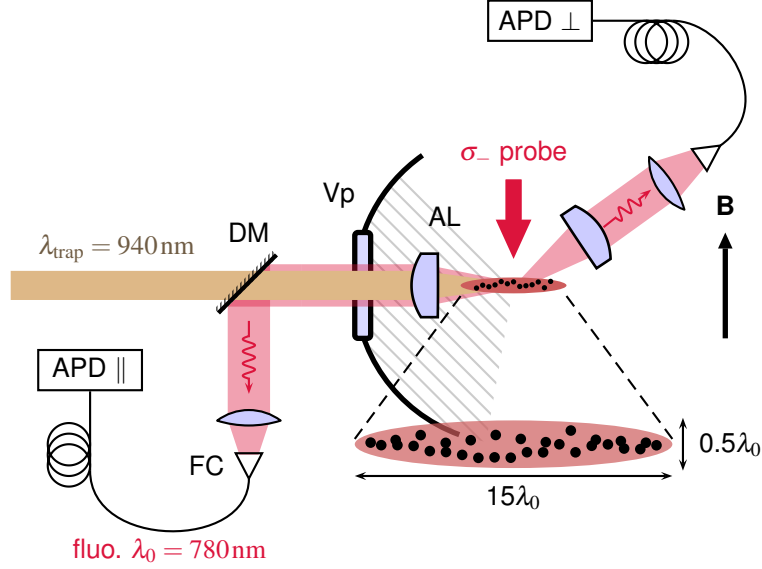


Figure 1: Experimental setup for the observation of super- and subradiance in chapters 6 to 8. AL : Aspheric Lens, Vp: CF40 Viewport, DM: Dichroic Mirror, FC: Fiber Coupler, APD: Avalanche PhotoDiode.

As it will be explained in chapter 5, a dense cloud is loaded in a dipole trap. In chapters 6 to 8, unless explicitly stated, this atomic cloud is excited using a resonant probe along the quantization axis given by the magnetic field  $\mathbf{B}$ , perpendicular to the long axis of the cloud, as represented in Figure 1. The probe has a  $\sigma-$  polarization in order to isolate a two-level transition, as explained in Chapter 2 (section 3). The fluorescence emitted by the cloud is then collected along the cloud's main axis, thus perpendicularly to the excitation direction (APD ||) or radially (APD  $\perp$ ). This direction is not parallel to the probe direction, but at  $45^\circ$ , as represented figure 2.4. It is detected by a fiber-coupled avalanche photodiode<sup>1</sup> (APD) and then counted digitally with a counting module<sup>2</sup>.

<sup>1</sup>Perkin Elmer® SPCM-AQRH

<sup>2</sup>Swabian Instruments® Time Tagger 20

# Preparation of dense clouds of 2-level atoms

\*\*\*

As seen in the first chapter, collective effects due to the light-induced dipole-dipole interaction appear when the interatomic distance is of the order of the light wavelength  $\lambda_0$ . The purpose of this chapter is to present how we prepare and characterize atomic clouds containing thousands of atoms with a peak density  $n_0/k^3 \sim 1$  where  $k = \frac{2\pi}{\lambda_0}$ .

Contents

1	<b>Preparation and characterization of a dense cloud.</b>	<b>90</b>
1.1	Loading sequence	90
1.2	Trapping frequencies	91
1.3	In-situ size and temperature	91
2	<b>Density estimation using the cloud dynamics</b>	<b>95</b>
2.1	Inelastic collisions in the absence of light	95
2.2	Temporal evolution of $N$ and $T$	97
2.3	Estimation of the density	98
3	<b>Control of the internal state</b>	<b>100</b>
3.1	Rabi Oscillations as a function of the driving intensity	100
3.2	Optimization of the preparation of a 2 level system	101
4	<b>Control of the atom number</b>	<b>103</b>
5	<b>Crossed dipole trap</b>	<b>103</b>
6	<b>Conclusion</b>	<b>106</b>

## 1 Preparation and characterization of a dense cloud.

### 1.1 Loading sequence

In order to obtain the highest atomic density, the main idea is to load as many atoms as possible into a large dipole trap using  $\Lambda$ -enhanced gray molasses (GM, see chapter 3), and, similarly to (Kinoshita et al. 2005), compress the cloud by dynamically reducing the beam waist, using the OptoTelescope (OT, see section 1.4). The loading sequence is shown figure 5.1.

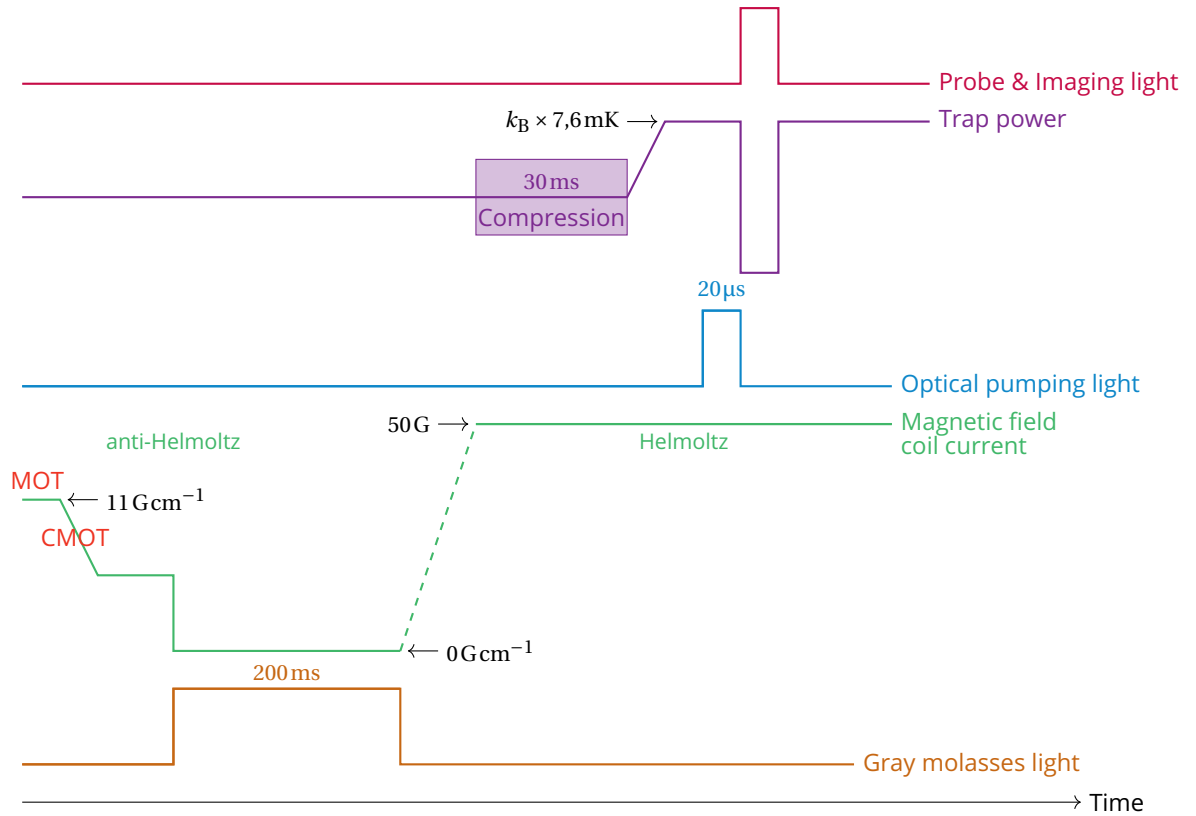


Figure 5.1: Chronogram of the sequence to load dense clouds.

We start from a 3D MOT (with magnetic gradient  $11 \text{ Gcm}^{-1}$ ), which is compressed in 15 ms by red-detuning the MOT beams from  $-3\Gamma$  to  $-5\Gamma$ , where  $\Gamma = 6.1 \text{ MHz}$  is the line width of the  $^{87}\text{Rb}$  D2 transition. The magnetic field gradient is then decreased by 50% from  $11 \text{ Gcm}^{-1}$  to  $5.5 \text{ Gcm}^{-1}$ . The MOT beams and magnetic field are then switched off and GM are applied for 200 ms. The dipole trap is kept on during all these steps. Its depth is  $U_0/k_B \simeq 4.2 \text{ mK}$  and its waist is  $w_0 \simeq 2.5 \mu\text{m}$ . In this configuration, up to 6000 atoms can be trapped at a temperature of  $625 \mu\text{K}$ , corresponding to a peak density  $n_0 \simeq 1.6 \times 10^{14} \text{ at/cm}^3 \simeq 0.3 k^3$ , assuming a gaussian thermal distribution of the positions. Using GM instead of directly loading from the MOT allows us to trap much more atoms. We typically gain a factor 5 in the atom number. The procedure to measure the atom number is given section 1.3.

Following the loading, the in-vacuum coils (see fig. 2.4) are changed to the Helmholtz configuration to create a homogenous magnetic field  $B = 50 \text{ G}$  in 10 ms.

The trap is then compressed to a waist  $w_0 = 1.8 \mu\text{m}$  by changing the magnification of

the OT, keeping the power constant. After that, the trap depth is increased up to 7.6 mK in 10 ms. The duration of the compression has been optimized to be short enough to minimize the three-body losses (see next section) but long enough compared to the response time of the OT (see section 1.4). The atoms are finally optically pumped in the  $(5S_{1/2}, F=2, m_F=-2)$  state in 20  $\mu$ s (section 3.2) in presence of a strong magnetic field to avoid depumping by the scattered fields. This step is realized less than 1  $\mu$ s before sending the resonant light on the system in order to minimize the depumping due to collisions. After this stage, we obtain a cloud of about 2500 atoms in the trap at temperature of 700  $\mu$ K, which corresponds to a cloud peak density  $n_0 \approx 1 \times 10^{15}$  at/cm<sup>3</sup> or equivalently  $n_0/k^3 = 1.7 \pm 0.3$  (Glicenstein, Ferioli, Brossard, et al. 2021). This density is three times larger than the one reported with our previous apparatus, using a large dipole trap as a reservoir for a small tweezer (Bourgain et al. 2013; Pellegrino et al. 2014).

The repetition rate of the experiment is about 2 Hz, limited by the MOT loading time.

### Peak density

The peak density of the cloud is

$$n_0 = \frac{N}{V_{\text{th}}} \quad (1.1)$$

where  $N$  is the atom number and

$$V_{\text{th}} = \left( \frac{2\pi k_B T}{m \bar{\omega}^2} \right)^{3/2}$$

is the thermal volume, assuming a harmonic trap. In this equation,  $\bar{\omega} = (\omega_r^2 \omega_z)^{1/3}$  is the mean oscillation frequency of the trap. A precise measurement of the density thus relies on a precise measurement of the atom number (explained in section 1.3), of the cloud temperature  $T$  and of its trapping frequencies, which I now present.

## 1.2 Trapping frequencies

This measurement has been described in chapter 4 to characterize the atomic chain (section 2.3). It is based on the parametric heating induced by the modulation of the trap beam intensity. Figure 5.2 shows as an example the evolution of the radial trapping frequency  $\omega_r$  as a function of the trap power for two different trap waist ( $w_0 = 1.8 \mu\text{m}$  and  $w_0 = 3.2 \mu\text{m}$ ). These measurements are used either to determine the value of  $w_0$ , using equation 1.3, or to use directly the measured values of  $\omega_r$  and  $\omega_z$ .

## 1.3 In-situ size and temperature

### In-situ size & radiation pressure explosion

Using equations (1.4), equation (1.1) can be written (here using time-dependent variables)

$$n_0(t) = \frac{N}{(2\pi)^{3/2} \sigma_r^2(t) \sigma_z(t)} \quad (1.2)$$

where  $\sigma_r(t)$  and  $\sigma_z(t)$  are the radial and axial size of the cloud (we assume here a cigar-shaped cloud). To estimate the density, one can thus directly measure the cloud size in the

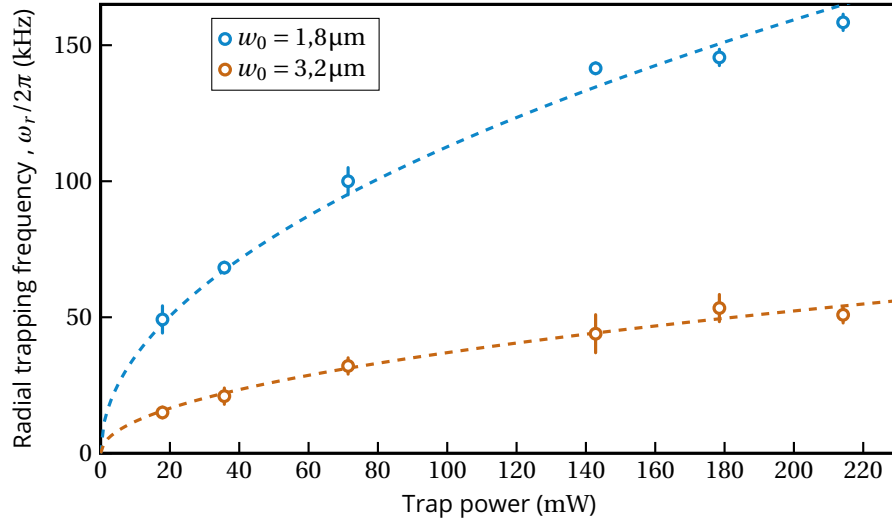


Figure 5.2: Radial trapping frequency  $\omega_r$  as a function of the trap beam power, for two trapping beam waists. The dashed lines correspond to fits based on equation 1.3 to determine  $w_0$  knowing the trap power. The error bars are from the fits used to determine the resonances.

trap, using imaging. For the compressed cloud,  $\sigma_r = 280 \text{ nm}$  and  $\sigma_z = 2.3 \mu\text{m}$ . The radial size is thus smaller than the resolution of the imaging system ( $\sim 1 \mu\text{m}$ ) but not the axial size. It should thus be measurable.

In a dense cloud ( $n_0/k^3 \sim 1$ ), the radiation pressure due to the probe pulse increases significantly the size of the cloud, making the measurement of the in-situ size difficult. One obtains physical intuition by considering the atomic equations of motion. For saturating resonant light, the (radial) force acting on atom  $j$  is given by (Steane et al. 1992)

$$\nabla F_j(r) = \hbar k \frac{\Gamma}{2} \sigma_R n(r)$$

where

$$n(r) = n_0 e^{\frac{-m(\omega_r^2 r^2 + \omega_z^2 z^2)}{2k_B T}}$$

is the atomic density and  $\sigma_R \sim \frac{3\lambda^2}{2\pi} \frac{1}{1+s}$  is the light absorption cross-section.

We solve the equation of motion using Monte-Carlo simulations. Let us consider a cloud of  $N = 2500$  atoms at temperature  $700 \mu\text{K}$  with a peak density  $n_0 = 1.7 k^3$ . To make the discussion simpler, we assume that the cloud is spherical. To model it, we assign to each atom a position  $\mathbf{r}_j$  according to a gaussian distribution with width  $\sigma_0 = \frac{1}{\sqrt{2\pi}} \left( \frac{N}{n_0} \right)^{1/3} \simeq 560 \text{ nm}$  and a velocity  $\mathbf{v}_j$  according to Maxwell-Boltzmann distribution. The simulation is then performed using time steps of  $10 \text{ ns}$ . At each step, the new values of the force, atomic positions and velocities are computed. The distribution of the atomic radial positions is then fitted by a gaussian function, from which the width  $\sigma(t)$  is extracted. Simulations are averaged over 100 clouds. In figure 5.3 we show  $\sigma(t)$  as a function of the probe pulse time, for a probe intensity  $s = 1$ .

As a comparison, we plot in figure 5.3 the calculated cloud size neglecting the radiation pressure force ( $F = 0$ , in free flight) and calculated neglecting the thermal motion of the cloud ( $T = 1 \text{ nK}$ ). As seen in the figure, the cloud is almost two times bigger when sending resonant



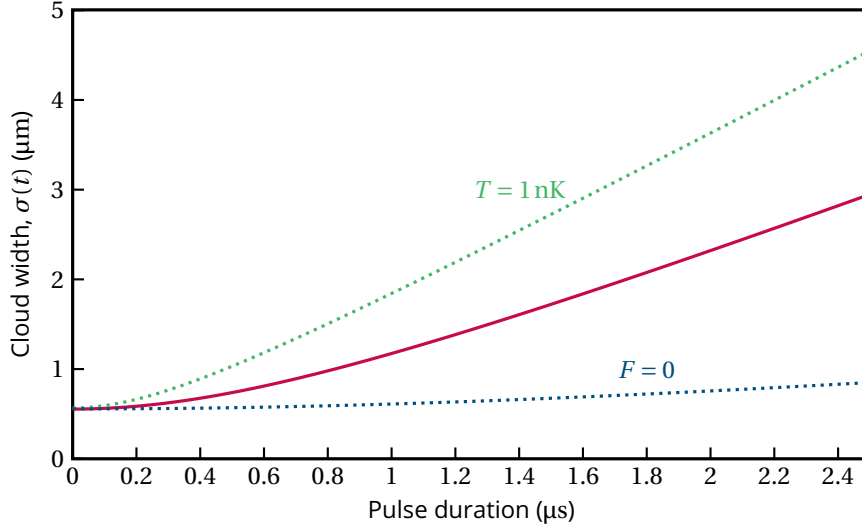


Figure 5.3: Cloud width as a function of the time (sending resonant light). The "realistic" case is compared to the case neglecting the radiation pressure ( $F = 0$ ) and to the case neglecting the thermal motion ( $T = 1$  nK).

light for  $1\mu\text{s}$  than in free-flight. Radiation pressure acts mostly at early times of the probe pulse, triggering an explosion, after which the expansion is ballistic. The thermal expansion ( $T \neq 0$ ) leads to a reduction of the density at initial times, thus reducing the radiation pressure.

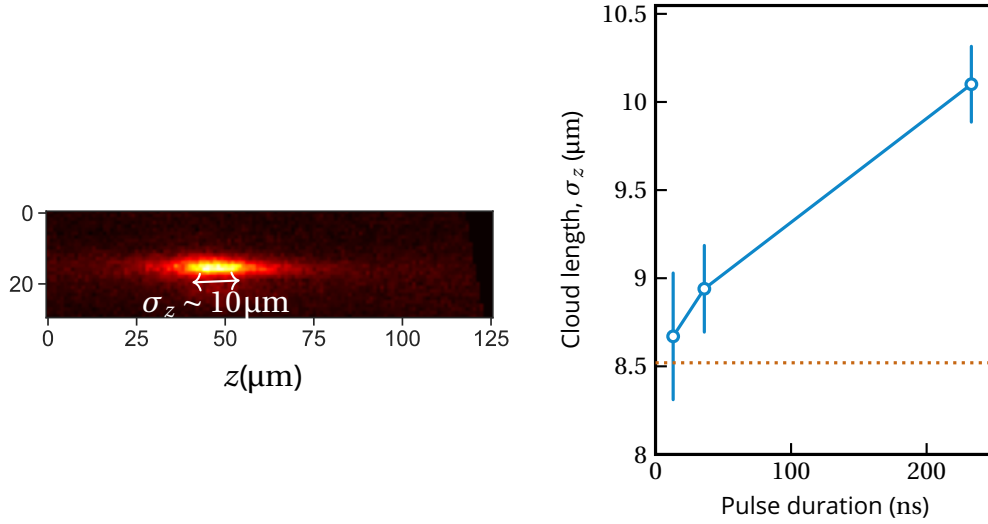


Figure 5.4: Left : Experimental average *in-situ* image of the cloud under 230ns of resonant light (averaged over 20 images). Right:  $\sigma_z$  for various pulse duration, showing the effect of radiation pressure. The orange dotted line represents the length extracted from an image using a far off-resonant light . The error bars are from the fits.

We measure the in-situ size of a cigar-shaped cloud for various probe pulse duration using resonant light. The cloud contains 2500 atoms and has a peak density of  $n_0 = 1.7k^3$  (extracted independently). The experimental images, averaged over 20 repetitions of the sequence, are fitted using a 2D gaussian fit. The radial size of the cloud does not show a significant variation

as it is smaller than the resolution of the imaging system. The measured value of the length  $\sigma_z$  are shown figure 5.4. We observe that the size increases strongly with the pulse duration, as expected from the simulations figure 5.3. We perform the same measurement using far detuned light (we use the repumper beam, detuned by 6.8 GHz). We observe that in that case the size is smaller than using the resonant light, because the radiation pressure force is much smaller. However, the measured value is still about three times larger than the expected size from a thermal cloud in a harmonic trap with our trapping frequencies. This might be due to some imperfections of the trapping beam. Moreover, we have neglected in this study the effects of the light-induced collisions on the cloud size.

### Temperature

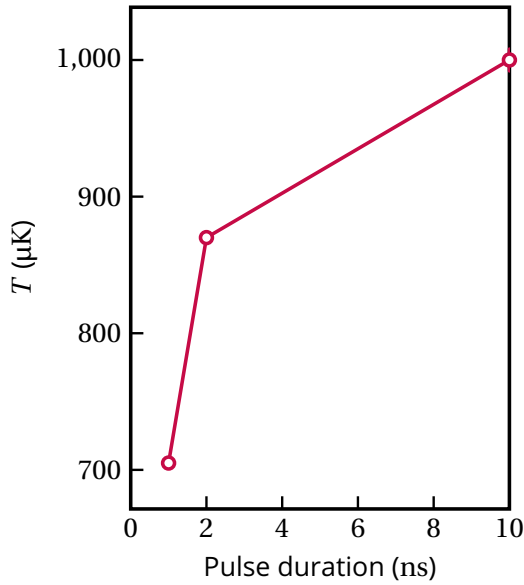


Figure 5.5:  $T$  as a function of the used pulse duration, showing the effect of the radiation pressure in the dense cloud.

The temperature of the atoms is measured using the *time-of-flight* method. The cloud with initial size  $\sigma_0$  is released in free-flight during a time  $t_{\text{of}}$ . After this time, the size is

$$\sigma(t_{\text{of}}) = \sqrt{\sigma_0^2 + v_{\text{th}}^2 t_{\text{of}}^2} \quad (1.3)$$

with  $v_{\text{th}} = \sqrt{\frac{k_B T}{m}}$ .

One thus obtains the temperature  $T$  by repeating the measurement of  $\sigma$  for different  $t_{\text{of}}$ . We assume that the atoms move only due to their temperature. As seen in the previous section, this is not the case when sending resonant light in a dense cloud. However, the probe light cannot be far from resonance because the scattered signal is too weak when the time of flight becomes large. We must therefore use a pulse as short as possible (as shown in figure 5.5).

In figure 5.6, we show the measured  $\sigma_z$  for the two clouds described in section 1.1, for various  $t_{\text{of}}$ , using 1  $\mu\text{s}$  pulses of resonant light. This duration is a compromise between minimizing the radiation pressure effect and maximizing the signal. Data are fitted using a linear function, as  $\sigma^2 \propto T t_{\text{of}}^2$  to determine the temperature.

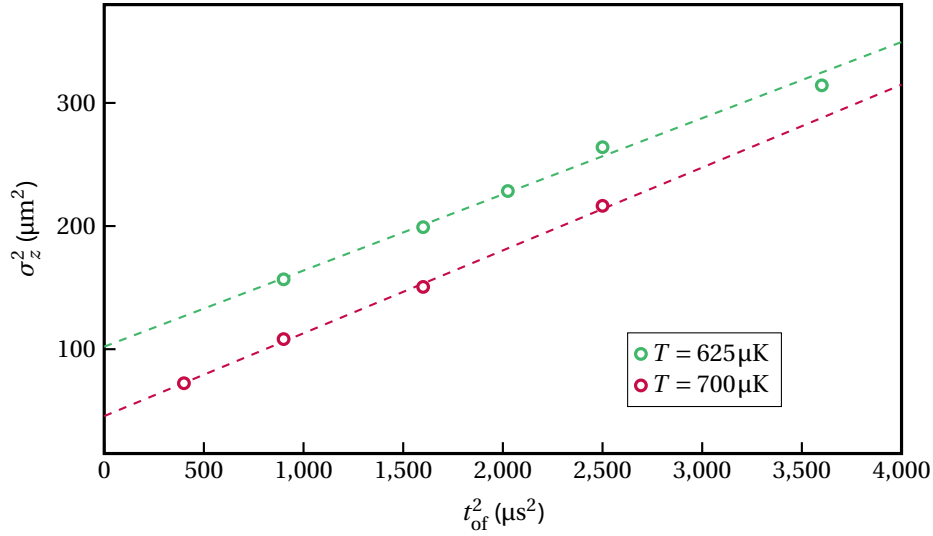


Figure 5.6: Cloud size (along  $z$ ) as a function of  $t_{\text{of}}$  before and after compression (section 1.1). Data are fitted by a linear function to extract the temperature (dashed lines).

## 2 Density estimation using the cloud dynamics

As seen in the previous section, a precise estimation of the density is difficult because it is based on the measurement of the cloud size, which is biased by the effects described above. In this section, we confirm the value that we have extracted from the previous measurements by studying the cloud dynamics. Indeed, such a high density results in large one-, two- and three-body losses and high collision rates, which offer a probe for estimating the density of the cloud.

### 2.1 Inelastic collisions in the absence of light

The relevant loss process in our experimental conditions are the inelastic losses due to one-, two- and three-body collisions. They lead to a decrease of the local density  $n$  as a function of time given by

$$\frac{dn}{dt} = -\gamma n - \beta n^2 - L_3 n^3 \quad (2.1)$$

with  $\gamma, \beta$  and  $L_3$  the coefficients for the one-, two- and three-body losses (inelastic collisions) respectively.

One-body losses do not depend on the number of atoms trapped. Indeed, they are mainly due to collisions with the residual atoms in the science chamber. This chamber is under ultra-high vacuum ( $P \sim 5 \times 10^{-11}$  mbar) but it contains hydrogen molecules at room temperature  $T = 300\text{K}$  or atoms which are outside the trap. These collisions limit the lifetime  $\tau$  of a single atom in the trap when all beams except for the laser used to trap are turned off. The precise measurement of this lifetime varies with the exact pressure and temperature of the oven but we find  $\tau \approx 20\text{s}$  which corresponds to  $\gamma = 5 \times 10^{-2}\text{s}^{-1}$ . The principle of this measurement is detailed in the thesis (Brossard 2019). Other effects that can limit the lifetime, such as fluctuations in the intensity of the trapping beam or heating due to the absorption of photons from the trap are estimated to be negligible. The duration of a typical experimental sequence

is shorter than 1 s, so one-body losses are not a limitation.

Two-body losses depend on the number of atoms in the trap. In the absence of resonant light, these losses are mainly due to hyperfine-changing collisions (Gensemer et al. 1997). In order to explain this, let us briefly recall the hyperfine structure of rubidium  $^{87}\text{Rb}$ . The  $5^2S_{1/2}$  ground state has two hyperfine levels  $F = 1$  and  $F = 2$ , separated by 6.8 GHz. During a collision, a spin-flip can occur and an atom in the  $5^2S_{1/2}F = 2$  level finds itself in the  $5^2S_{1/2}F = 1$  level. The energy released is very large compared to the typical depth of our traps, which is a few  $k_B \times \text{mK}$  or equivalently a few tens of  $h \times \text{MHz}$ . Atoms that experience this type of collision are therefore ejected from the dipole trap. The  $\beta$  rate for our clouds is of the order of  $1 \times 10^{-11} \text{ cm}^3 \text{ s}^{-1}$  (Gensemer et al. 1997). This rate can be strongly reduced by preparing all atoms in the  $F = 1$  manifold or in the  $F = 2$  manifold. In this case, the collisions involve only the spin-dipolar mechanism and have rate coefficients on the order of  $\beta = 1 \times 10^{-15} \text{ cm}^3 \text{ s}^{-1}$  (Julienne et al. 1997). In our experiment, we optical pump all the atoms in the  $(F = 2, m_F = -2)$  state.

The three-body losses are due to recombination of three atoms into a dimer and one free atom. Two-body collisions can not result in the production of a dimer since it can not conserve both the energy and the momentum. It is possible for a three-body collision, where the binding energy is transferred into kinetic energy to the dimer and to the third atom. This large energy gain leads to the loss of the three atoms. Three body losses become dominant when the density reaches values on the order of  $n \sim 1 \times 10^{15} \text{ cm}^{-3}$ . This also corresponds to  $n \sim 1/k_0^3$  for the  $^{87}\text{Rb}$   $D_2$  line, which is the regime we want to explore to study the effects of the interaction between light-induced dipoles (see section 1.1). Typical  $L_3$  rates of three-body losses for rubidium are on the order of  $L_3 \sim 1 \times 10^{-29} \text{ cm}^6/\text{s}$  (Söding et al. 1999; Burt et al. 2008).

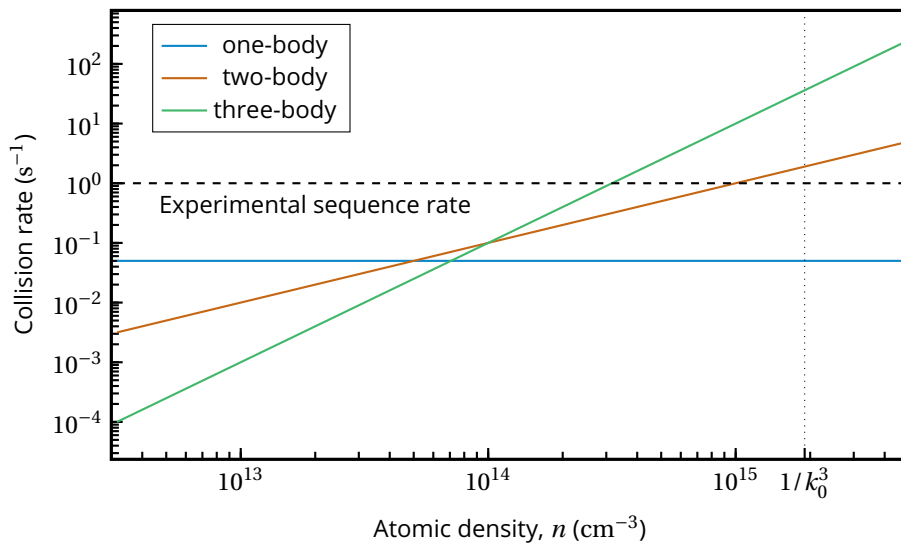


Figure 5.7: Collision rate as a function of the atomic density  $n$ , for the one-, two- and three-body losses, in the density range typically reached in our dipole traps. The one-body losses (rate  $\gamma$ ) can be neglected for the duration of the sequence ( $\sim 0.5\text{s}$ ), drawn with the dotted line. When the density approaches  $n \sim 1 \times 10^{15} \text{ cm}^{-3}$ , the 3-body losses dominant over the other types of collisions.

We plot the different collisions rates as a function of density in figure 5.7. We observe

that 3-body losses dominate when the density is important. They constitute a limitation on the achievable densities in our optical tweezers. We will use them to confirm our density measurements in the dense traps.

## 2.2 Temporal evolution of $N$ and $T$

We will measure the cloud atom number  $N$  and the temperature of the atoms  $T$  after the loading. The temporal evolution of these quantities are given by (Luiten et al. 1996; Eismann et al. 2016)

$$\dot{N} = -\gamma_3 \frac{N^3}{T^5} - \gamma_2(\sigma(T), T) \frac{N^2}{T} \quad (2.2)$$

$$\dot{T} = \frac{T}{3} \left[ \frac{5}{3} \gamma_3 \frac{N^2}{T^5} - \tilde{\gamma}_2(\sigma(T), T) \frac{N}{T} \right] \quad (2.3)$$

where  $\gamma_3$  depends on the trap geometry and is proportional to the three-body losses coefficient  $L_3$ . The coefficients  $\gamma_2$  and  $\tilde{\gamma}_2$  depend on the temperature, the trap geometry, and on the two-body elastic cross section  $\sigma(T)$ , whose temperature dependence takes into account the d-wave resonance at  $350\mu\text{K}$ . For the temperature of our cloud, the correction is significant (a factor 3, as shown in figure 5.8). We use data of (Buggle et al. 2004), figure 5.8, to find a functional form of  $\sigma(T)$ .

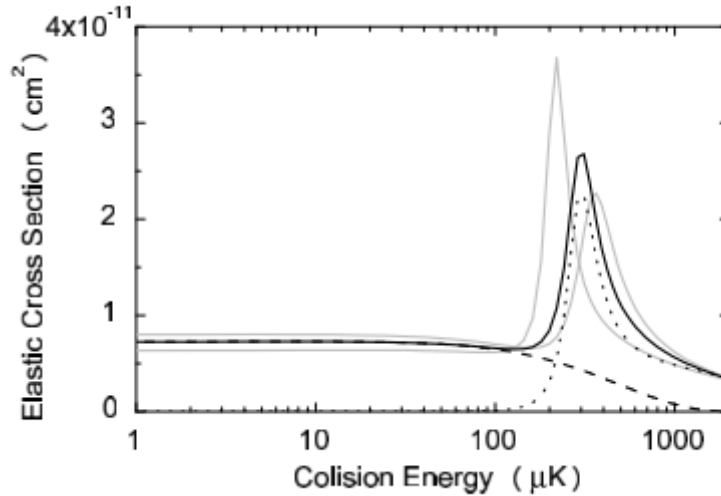


Figure 5.8: s-wave (dashed line), d-wave (dotted line) and total (full black line) elastic cross sections as a function of collision energy. From (Buggle et al. 2004).

The atom number is measured as a function of the time, after the end of the loading sequence (section 1.1). The result is shown figure 5.9. The decay of the atom number is fitted using equations (2.2) and (2.3), with  $L_3$  as a free parameter. We obtain  $L_3 = 4(1) \times 10^{-28} \text{ cm}^6/\text{s}$ . In the literature, one finds the value  $L_3 = 1.8(10) \times 10^{-29} \text{ cm}^6/\text{s}$  (Söding et al. 1999). It was measured for a Bose-Einstein condensate, for which the losses are reduced by a factor 6. The value that we have obtained is still too large. However, there exists no prediction for the effect of the d-wave resonance on the three-body losses and the literature values are measured only in the s-wave regime (Burt et al. 2008).

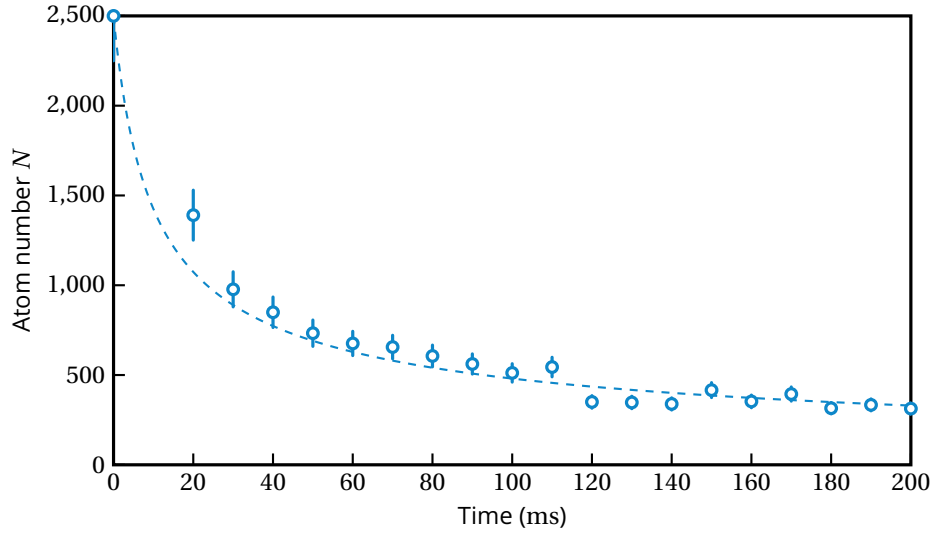


Figure 5.9: Time evolution of the atom number in the dense cloud. The dashed line corresponds to a fit using equations (2.2) and (2.3).

The solution from equations (2.2) and (2.3) extracted from the fit of the data of figure 5.9 predicts the evolution of the temperature. We therefore measure the temperature as a function of time and compare it to the predictions in figure 5.10 without any fit, showing a reasonable agreement and therefore indicating the consistency of our model.

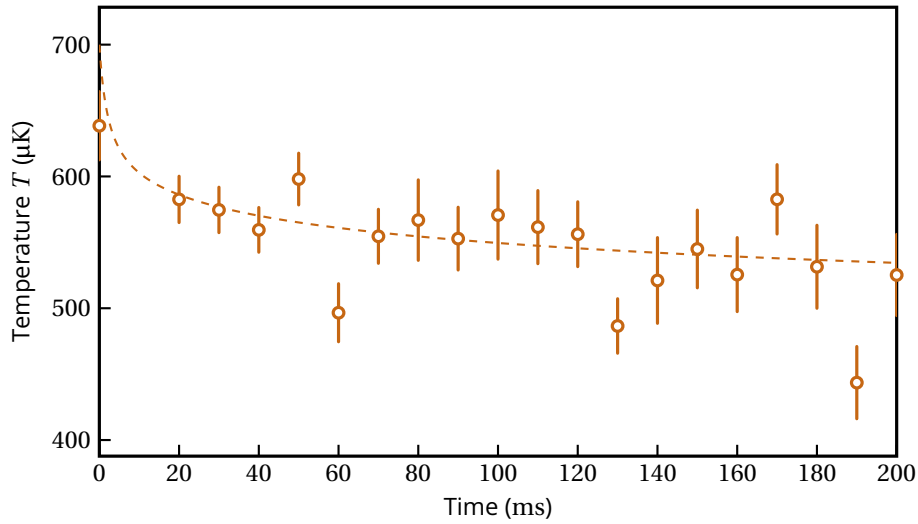


Figure 5.10: Time evolution of the temperature in the dense cloud. The dashed line corresponds to the prediction made using the fit figure 5.9 and equation (2.3).

### 2.3 Estimation of the density

We now combine the measurements of figure 5.9 and 5.10 to estimate the density, using equation (1.1). Its evolution is plotted figure 5.11.

We are thus able to produce cloud containing up to a few thousand atoms at densities

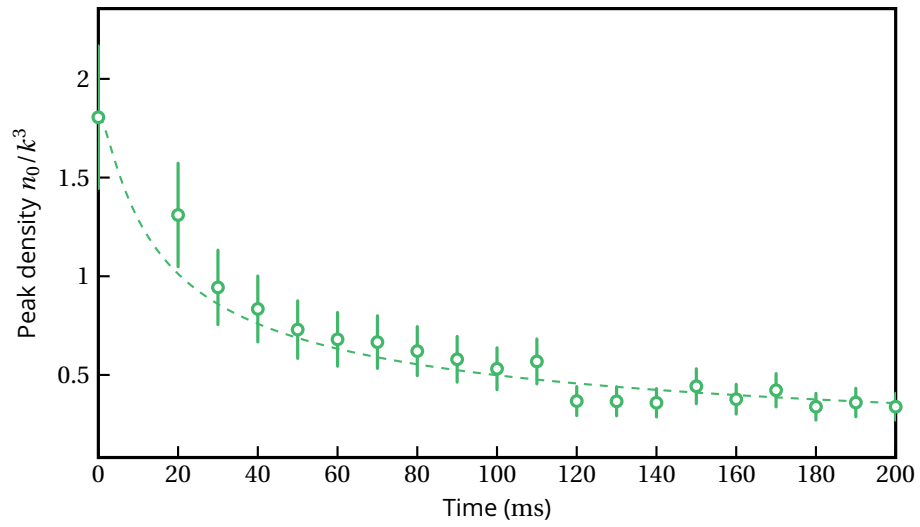


Figure 5.11: Time evolution of the density in the dense cloud. The dashed line corresponds to a fit using equations (2.2) and (2.3).

$n_0 \sim k^3$ . The dynamics of the evolution confirms the extracted value of the density.

### 3 Control of the internal state

The purpose of this section is to illustrate the manipulation of the internal state of the cloud. To avoid the collective effects that will be studied in the following chapters and to first characterize the single atom response, we now consider a dilute cloud ( $n_0/k^3 < 1$ ). It can be for example loaded directly from the MOT or reducing the atom number of a dense cloud (see section 3).

The cloud is excited using 20 pulses of high intensity resonant light along the quantization axis, with polarization  $\sigma_-$ . As we have isolated a closed two-level transition (see section 3.2), we observe Rabi oscillations (section 1.2) in the fluorescence collected using an avalanche photodiode (APD), as shown figure 5.12.

For all the data shown in this section, light is collected along the long axis of the cloud, thus perpendicularly to the direction of the driving pulse. We have checked that the single atom response is independent of the driving and observation directions (APD  $\parallel$  and APD  $\perp$  in figure 1. We repeat each measurement on 1000 clouds to acquire enough statistics.

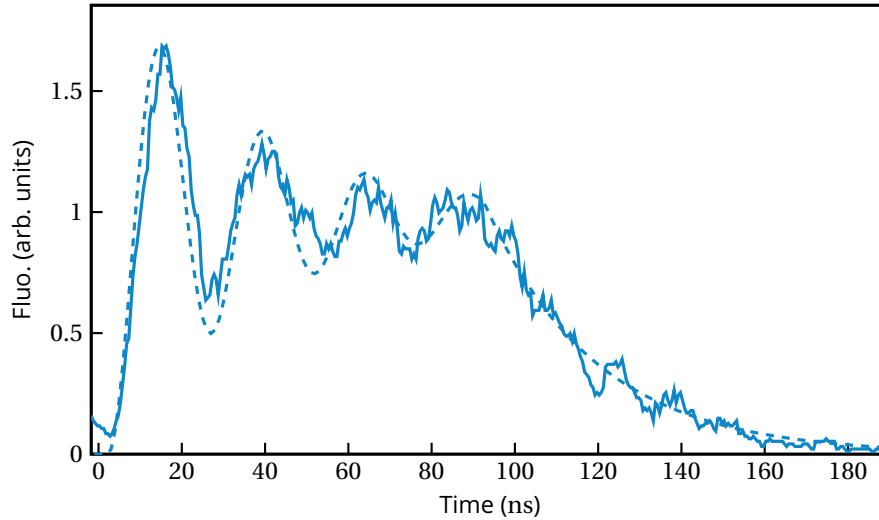


Figure 5.12: Fluorescence collected on an APD during resonant excitation of the cloud. The signal is fitted using the Optical Bloch Equations (dashed line).

Data of figure 5.12 are well fitted by a solution of the Optical Bloch Equations: this is a signature of the single atom response.

#### 3.1 Rabi Oscillations as a function of the driving intensity

We first confirm the dependence of the Rabi frequency  $\Omega$  as a function of the driving light intensity. To determine  $\Omega$ , we calculate the Fourier transform of the measured signal, during the oscillations. Figure 5.13 shows the result of this Fourier transform, each column corresponding to a fixed intensity  $I/I_{\text{sat}}$ .

We observe a good agreement between the obtained spectra and the theoretical value  $\Omega = \Gamma \sqrt{\frac{s}{2}}$  (section 1.2) where  $s = \frac{I}{I_{\text{sat}}}$ . For this particular measurement,  $s$  is determined independently using the atomic fluorescence in steady-state. In the following, we use the fit with solutions of the OBE to determine the light intensity on the atoms.



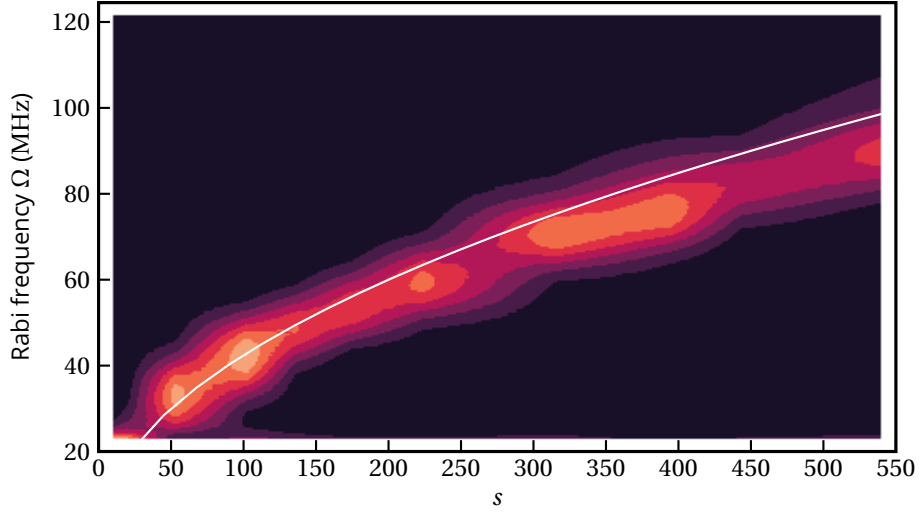


Figure 5.13: Rabi frequency  $\Omega$  as a function of the driving light intensity  $s = \frac{I}{I_{\text{sat}}}$ . Each column is the Fourier transform of the fluorescence trace for the corresponding intensity. The solid line corresponds to the theoretical value  $\Omega = \Gamma\sqrt{\frac{s}{2}}$ .

## 3.2 Optimization of the preparation of a 2 level system

### Magnetic field

Isolating a two-level system is necessary to observe a good contrast in Rabi oscillations. If it is not the case, multiple transitions are possible, leading to different Rabi frequencies, which blurs the oscillations. In this section, the goal is thus to optimize the magnetic field used to isolate the two-level transition, optimizing the contrast of the oscillations. We measure the fluorescence collected during the pulse in the case where the optical pumping was applied (see section 3.2) and in the case without optical pumping, as shown figure 5.14, left panel. In the latter, the system is thus prepared as mixture of Zeeman levels. As expected, we observe that the oscillations are quickly damped because of the frequency shift between the different possible transitions. Isolating two levels allows us to improve the contrast of the Rabi oscillations, and thus the control of the internal state of the atoms.

We calculate the fourier transform of the measured signal during the oscillations. In the case of the 2-level system, we observe a large peak. In the other case, the peak disappears: we cannot distinguish any oscillation. We are then interested in the evolution of the amplitude of the peak as a function of the magnetic field during the pumping. On figure 5.14, we show that the amplitude of the peak increases for  $B < 20\text{G}$  and then saturates. This result is consistent with the observed fact that the pumping efficiency increases until about 20 G and then saturates (see chapter 2). We don't observe any variation on  $\Omega$  as a function of the magnetic field.

### Polarization

We then study the effect of the polarization of the optical pumping beams and of the probe on the Rabi oscillations, using a bias magnetic field  $B = 50\text{G}$ . The two beams use the same optical path. Their polarization is tuned by rotating a  $\lambda/4$  waveplate. We have shown that when the polarization is  $\sigma-$ , we isolate a closed 2-level system. In that case, we should observe highly

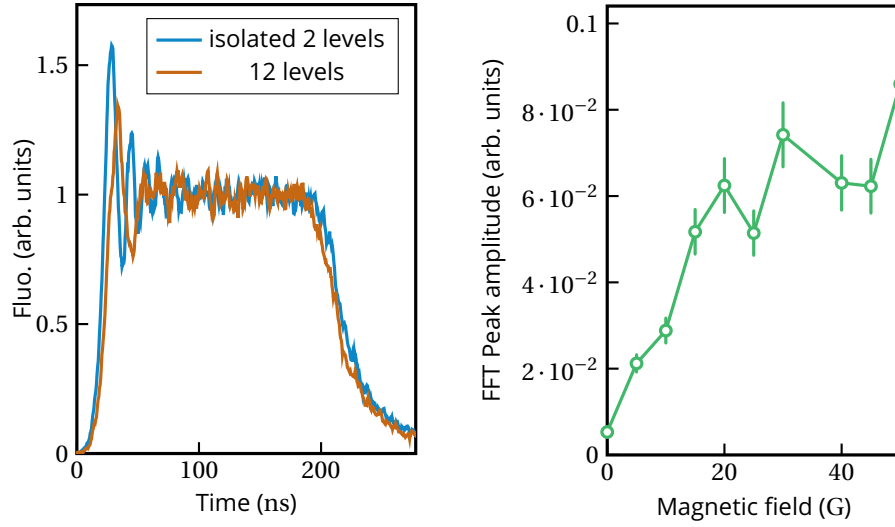


Figure 5.14: Left : Fluorescence collected on an APD during a resonant excitation of the cloud, using the two-level transition and without isolating the transition, using a 2 ns moving average. Right: FFT peak amplitude as a function of the magnetic field applied during the optical pumping. The error bars correspond to the uncertainty on the peak position.

contrasted Rabi oscillations. This is characterized by calculating the Fourier transform of the fluorescence signal during the probe pulse, as before, for various angles of the polarization plate (with an arbitrary origin).

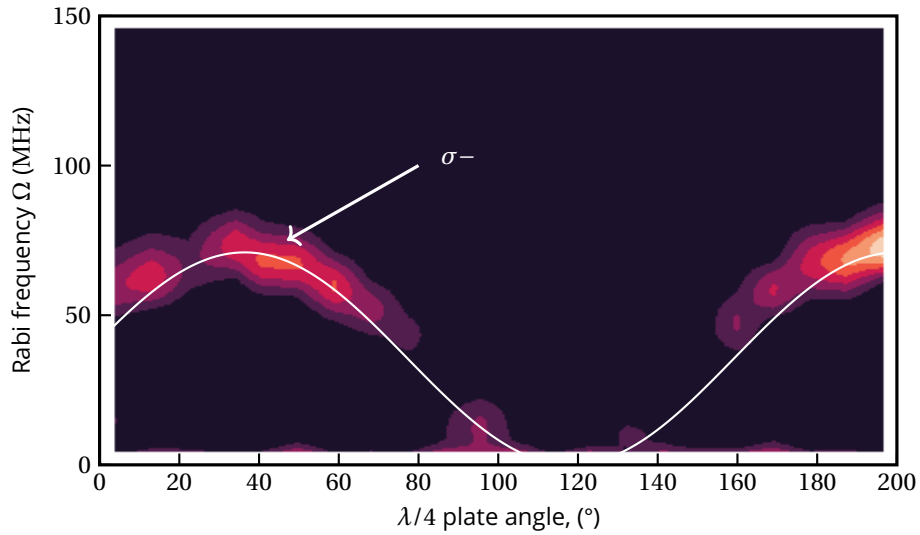


Figure 5.15: Rabi frequency  $\Omega$  as a function of the angle of the polarization waveplate. Each column is the Fourier transform of the fluorescence signal for a given angle of the waveplate. The origin of the angles on x-axis is arbitrary. The white solid line is a guide for the eyes.

In Figure 5.15, we show that for a waveplate angle of about  $50^\circ$ , the contrast of the Rabi oscillations is good. The contrast then decreases as the polarization of the optical pumping

beams and the probe becomes different from  $\sigma-$ , highlighting the crucial importance of finely tune the polarization to isolate a two-level transition.

The observation of the Rabi oscillations is a confirmation that we are able to prepare a closed 2-level system, and to manipulate the internal state of the atoms.

## 4 Control of the atom number

To study dense clouds, one must control both the number of atoms and the volume of the cloud (thus its temperature). We have set up an empirical protocol to vary the number of atoms without significantly changing their temperature.

To adjust the atom number  $N$ , we first load a dense cloud as explained section 1.1. The cloud is then released from the trap and recaptured after a variable time. The number of atoms as a function of the release time is calibrated at least every day, to take into account daily fluctuations. One example is shown figure 5.16.

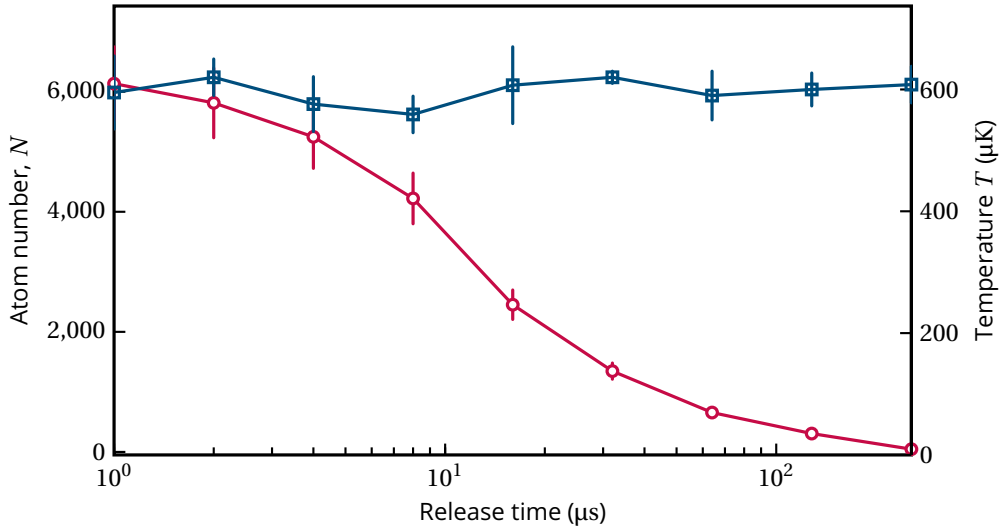


Figure 5.16: Atom number (dots) and temperature (squares) as a function of the release time.

We estimate the temperature as done in section 1.3, using 1  $\mu$ s pulse of resonant light. In figure 5.16, we show that the release and recapture protocol does not change significantly the cloud's temperature. It seems that the cloud quickly thermalizes with possibly some evaporation.

Releasing the cloud is thus an experimental knob to change the density only by changing the atom number. The size of the cloud, given by its temperature and by the trapping parameters, is not modified during the protocol.

## 5 Crossed dipole trap

Up to now, we have only considered "cigar" shaped traps, formed by focusing of a single laser beam. Now, we are interested in the implementation of a spherical trap, based on two

crossed traps. For this, we use the two high resolution axes formed by the aspherical lenses, as represented figure 5.17.

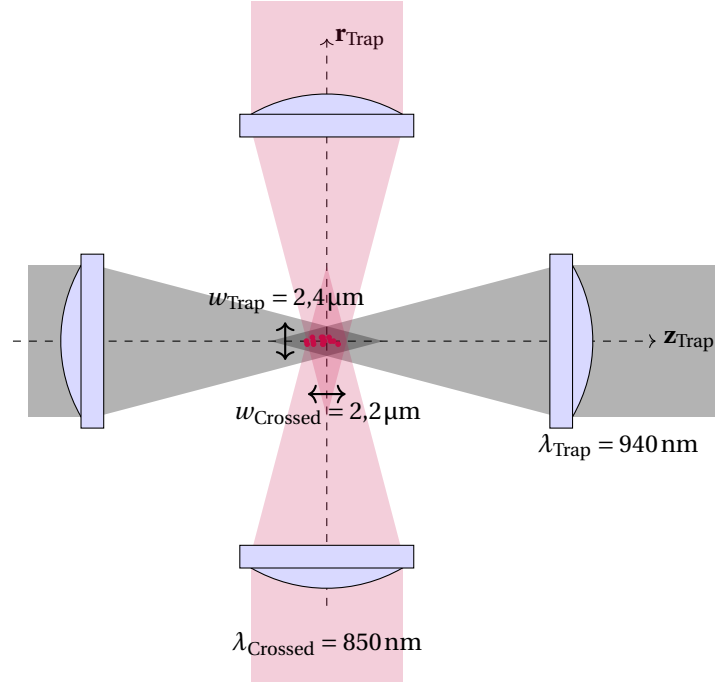


Figure 5.17: Schematic of the setup of the crossed dipole trap. The axes are defined in figure 2.4.

One of the traps is formed by focusing a laser beam at a wavelength 940nm along the  $\mathbf{z}_{\text{Trap}}$ -axis (called *horizontal trap*) with a waist of 2.4μm, the other using a laser at a wavelength of 850nm along the  $\mathbf{r}_{\text{Trap}}$ -axis with a waist of 2.2μm, called *transverse trap*.

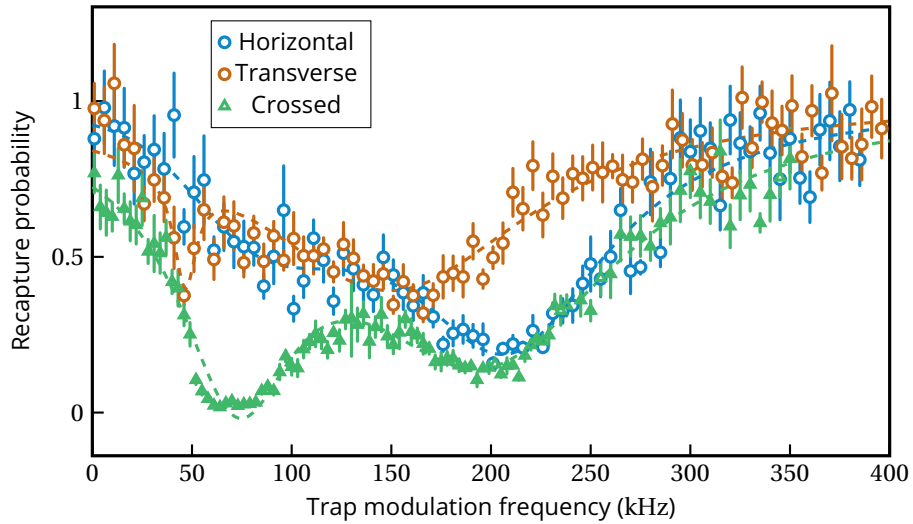


Figure 5.18: Radial oscillation: Recapture probability as a function of the trap modulation frequency for the horizontal trap, for the transverse trap and for the crossed trap . Data are fitted by the sum of two gaussian functions (dashed lines).

To characterize the trap thus formed, we measure the oscillation frequencies. As in chapter 4 (section 2.3), we modulate the intensity of the laser beams with a relative amplitude of 5% during 100ms once atoms are loaded in the trap. We then measure the probability of keeping the atoms in the trap as a function of the modulation frequency. This measurement is made for the horizontal trap alone, the transverse trap alone and then for the crossed trap, as shown figure 5.18 for the radial oscillation frequencies. Data are fitted by the sum of two Gaussian functions to account for resonances at  $2\omega_z/p$ , where  $p$  is an integer. In Figure 5.18, one of the oscillation frequencies of the cross trap is measured. It is however difficult to deduce its value from those of the individual traps.

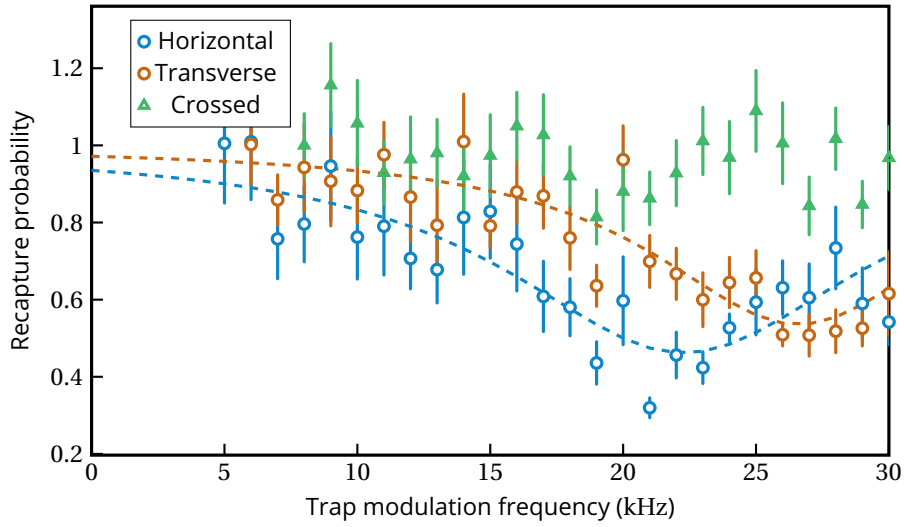


Figure 5.19: Axial oscillation: Recapture probability as a function of the trap modulation frequency for the horizontal trap, for the transverse trap and for the crossed trap. Data are fitted by the sum of two gaussian functions (dashed lines).

We then consider the axial trapping frequencies. We observe that the resonances present for the single traps have disappeared for the crossed trap. This is an indication of a much tighter axial trapping thanks to the transverse trap.

We measure the in-situ size of a cloud in the crossed trap. Based on the analysis in Section 1.3, a  $2\mu\text{s}$  pulse is used to limit the effect of radiation pressure. We collect the fluorescence along the transverse axis and fit the obtained images to deduce the cloud's size. By increasing the power in the beam of the transverse trap, we observe that the axial dimension (according to  $z_{\text{Trap}}$ -axis) decreases, as shown figure 5.20. We are thus creating a more spherical trap. The other dimension is not changed (measurement limited by diffraction). We have not reached a perfect isotropic trapping. This is probably due to the fact that the radial trap is not deep enough such that atoms can still explore a relatively large region axially.

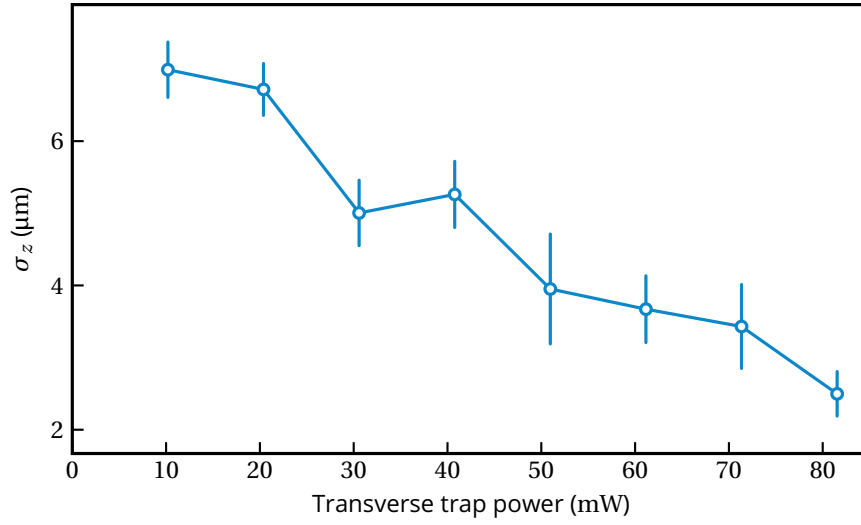


Figure 5.20: In situ size of the cloud along the axis  $z_{\text{Trap}}$  as a function of the power in the transverse trap beam.

## 6 Conclusion

In this chapter, we have shown how we prepare and characterize dense clouds of atoms, with density reaching  $n_0/k^3 \sim 1$ . In a second part, we have used Rabi oscillations to control the cloud's internal state. The last part was devoted to the experimental realization of a crossed dipole trap. In addition to the density, these clouds have the particular feature of containing several thousand atoms, which is a crucial improvement compare to the previous generations of the experiment. We will show in the following chapters that this ability to load high atom number has allowed us to observe super- and subradiance with our system.

# Superradiance in a dense ensemble of 2-level atoms

\*\*\*

Superradiance as described by Dicke is the collective spontaneous emission of photons from a fully excited atomic ensemble with dimensions smaller than the light wavelength (Dicke 1954). This emission happens in a much shorter time than the natural lifetime of a single atom  $\tau$ . One can gain a qualitative interpretation of the phenomenon using the following classical picture. Consider each atom as an antenna which emits light: if all antennas radiate in phase, the total electromagnetic field is proportional to  $N$ , thus the intensity is proportional to  $N^2$ . To conserve the energy, atoms must radiate  $N$  times faster than for incoherent emission ( $N$  time faster than independent atoms), the superradiant lifetime is thus given by  $\tau_s = \tau/N$ .

This simple picture is not complete because it predicts an exponential decay, but Dicke's theory, which describes the decay to the ground state of atoms that are all excited, predicts a *flash*: the photon emission rates increases even if the driving is switched off. Moreover, the initial total dipole of the system is zero and there is no phase relation between the dipoles. The complexity of the phenomenon lies in the phasing of the dipoles during the spontaneous decay of the system. This paradoxical situation where atomic dipole get progressively phased is at the origin of the interest in the phenomena.

In this chapter, we will first present a qualitative description of superradiance and its features and we will introduce Dicke's classification of the Hilbert space. This will allow us to show, in a second time, how we experimentally observe Dicke superradiance.

## Contents

<b>1</b>	<b>Qualitative description of Dicke superradiance . . . . .</b>	<b>108</b>
1.1	Collective spontaneous emission of $N$ two-level systems . . . . .	108
1.2	Dicke super- and subradiant states . . . . .	109
<b>2</b>	<b>Observation of superradiant emission of an inverted atomic cloud .</b>	<b>113</b>
2.1	Realization of a $\pi$ -pulse . . . . .	113
2.2	Superradiant flash . . . . .	116
<b>3</b>	<b>Analysis of the superradiant decay . . . . .</b>	<b>117</b>
3.1	Theoretical model . . . . .	118
3.2	Initial photon rate . . . . .	119
3.3	Peak of the photon emission . . . . .	119
3.4	Decay time . . . . .	120
3.5	Influence of the trap geometry . . . . .	120

## 1 Qualitative description of Dicke superradiance

### 1.1 Collective spontaneous emission of $N$ two-level systems

#### Case $N = 1$

Let us start the reasoning with the spontaneous emission from a single two-level atom. The ground  $|g\rangle$  and excited  $|e\rangle$  states are coupled via a dipolar transition. If initially in the state  $|e\rangle$ , the atom de-excites spontaneously in a characteristic time  $\tau = 1/\Gamma$ , where  $\Gamma$  is the natural linewidth of the transition  $|g\rangle \rightarrow |e\rangle$ . During all the process, the mean value of the dipole operator  $\mathbf{D}_+ = \mathbf{D}_x + i\mathbf{D}_y = (\mathbf{D}_-)^{\dagger}$  is equal to zero :

$$\langle \mathbf{D}_+ \rangle = 0.$$

The intuitive picture is that the vacuum induced dipole has a random phase, thus the average dipole vanishes. The mean value of the intensity  $\langle I \rangle$  is proportional to  $\langle \mathbf{D}^2 \rangle = \langle \mathbf{D}_+ \mathbf{D}_- \rangle$ , which is different from zero:

$$\langle I(t) \rangle \propto e^{-\Gamma t}.$$

$\langle I(t) \rangle$  is thus maximal at  $t = 0$  and decays exponentially in a characteristic time  $\tau$ .

#### Case $N = 2$

Following (Gross 2006), let us now consider two identical excited atoms at a distance  $|x_{12}| \ll \lambda_0$ . The mean radiated intensity at  $t = 0$  is

$$\langle I(t=0) \rangle \propto \langle \mathbf{D}^2 \rangle = \langle (\mathbf{D}_1 + \mathbf{D}_2)^2 \rangle = \langle \mathbf{D}_1^2 \rangle + \langle \mathbf{D}_2^2 \rangle$$

because the correlations between the two atoms are equal to zero at  $t = 0$ . The spontaneous emission starts as if the two atoms were independent, with a characteristic time  $\tau$ .

After the emission of one photon, since the atoms are at a distance much shorter than  $\lambda_0$ , it is impossible to determine which atom emitted the photon, even by measuring it. The system thus remains in a state invariant under the permutation of the two atoms. The state  $|\psi\rangle$  of the system is thus the symmetric superposition

$$|\psi\rangle = \frac{1}{\sqrt{2}} (|e_1 g_2\rangle + |g_1 e_2\rangle).$$

The correlations between the dipoles are then

$$\langle \psi | \mathbf{D}_1 \mathbf{D}_2 | \psi \rangle = \langle e_1 | \mathbf{D}_1 | g_1 \rangle \langle e_2 | \mathbf{D}_2 | g_2 \rangle \neq 0.$$

The square of the total dipole,  $\langle \mathbf{D}^2 \rangle = \langle \mathbf{D}_1^2 \rangle + \langle \mathbf{D}_2^2 \rangle + 2\langle \mathbf{D}_1 \mathbf{D}_2 \rangle$  is larger than the one of uncorrelated atoms. Light emission is thus stronger:

$$\langle I \rangle > \langle I_1 \rangle + \langle I_2 \rangle.$$

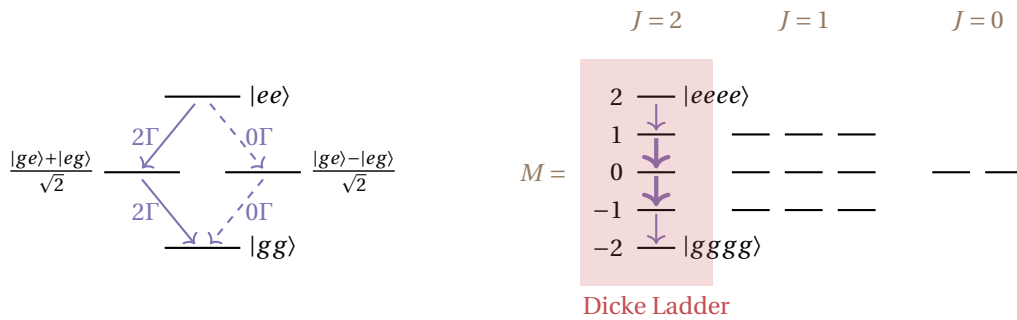


These equations mean that even if the two dipoles have individually a random phase,  $\langle \mathbf{D}_1 \rangle = \langle \mathbf{D}_2 \rangle = 0$ , the decay has created a phase relation between them. Superradiance results from constructive interference between the fields radiated by the correlated dipoles. It should also be noted that the total dipole of the system is still equal to zero, which is true for all Dicke states as we will discuss later. Let us now look at the Hilbert space of Dicke states in order to describe some features of superradiance.

## 1.2 Dicke super- and subradiant states

With an analogy to spin 1/2 quantum system, superradiance is described in terms of *Dicke ladder* states (Dicke 1954). The states can be written using their total angular momentum  $J$  ( $0 \leq J \leq N/2$ , where  $N$  is the atom number) and the magnetic moment ( $-J \leq M \leq J$ ), which are good quantum numbers and common eigenstates of the operators  $\mathbf{J}_z$  and  $\mathbf{J}^2$  (Cohen-Tannoudji et al. 2012).

We first classify the states by their value of  $M$ . For a given  $M$ , the energy ( $= M\hbar\omega_0$ ) has a degeneracy  $\frac{N!}{(N/2+M)!(N/2-M)!}$ . We then classify the states by their  $J$ . As examples, we represent in figure 6.1 the classified states for  $N = 2$  and  $N = 4$ . States for which  $J = N/2$  are symmetrical by permutations of the atoms. These states form the *Dicke ladder*. For other  $J$ , there is no particular symmetry.



a)  $N = 2$

b)  $N = 4$

Figure 6.1: Dicke Hilbert space for a)  $N = 2$  and b)  $N = 4$ . States are order by total angular momenta  $J$  and magnetic moments  $M$ . Dicke ladder of symmetric states,  $J = N/2$ , are identified for the case b). Decay from  $M = 0$  to  $M = 1$  in this ladder leads to the most superradiant emission.

The rate of photoemission  $\Gamma_{JM}$  from the state  $|JM\rangle$  is proportional to  $\langle \mathbf{J}_+ \mathbf{J}_- \rangle$  where  $\mathbf{J}_\pm = \mathbf{J}_x \pm i\mathbf{J}_y$ . One obtains

$$\Gamma_{JM} \propto \langle J, M | \mathbf{J}_+ \mathbf{J}_- | J, M \rangle \propto (J+M)(J-M+1)$$

This gives a maximal rate  $N^2/4$  for  $J = N/2$  and  $M = 0$  (if  $N \gg 1$ ). The decay from the fully excited state is a cascade of the ladder down to the ground state and does not involve the other states (Dicke 1954). Qualitatively, as explained for the  $N = 2$  case, since the atoms are at a distance much shorter than  $\lambda_0$ , it is impossible to determine which atom has emitted the photon, even by measuring it. The systems thus remains in a permutationally symmetric state during the decay of the excitation. The  $N^2$  enhancement of the light intensity is one of the main features of superradiance.

To illustrate the superradiant emission, we calculate the time evolution of the population  $\Pi_M$  of the Dicke Ladder states  $|J = N/2, M\rangle$ . This time evolution is given by

$$\dot{\Pi}_M = \begin{cases} \Gamma_{M+1}\Pi_{M+1} - \Gamma_M\Pi_M & \text{if } -\frac{N}{2} < M < \frac{N}{2} \\ -\Gamma_M\Pi_M & \text{if } M = \frac{N}{2} \\ \Gamma_{M+1}\Pi_{M+1} & \text{if } M = -\frac{N}{2} \end{cases}$$

where  $\Gamma_M = \Gamma \left( \frac{N}{2} + M \right) \left( \frac{N}{2} - M \right)$ . Starting from a fully inverted system ( $\Pi_{N/2} = 1, \Pi_{M \neq N/2} = 0$ ) and following (Gross and Haroche 1982), we then compute the rate of photon emission per atom

$$W_N = \frac{1}{N} \sum \Gamma_M \Pi_M.$$

The rate for two atoms ( $W_2$ ) and for four atoms ( $W_4$ ) are shown figure 6.2 and compared to the decay of independent atoms ( $W_1$ ).

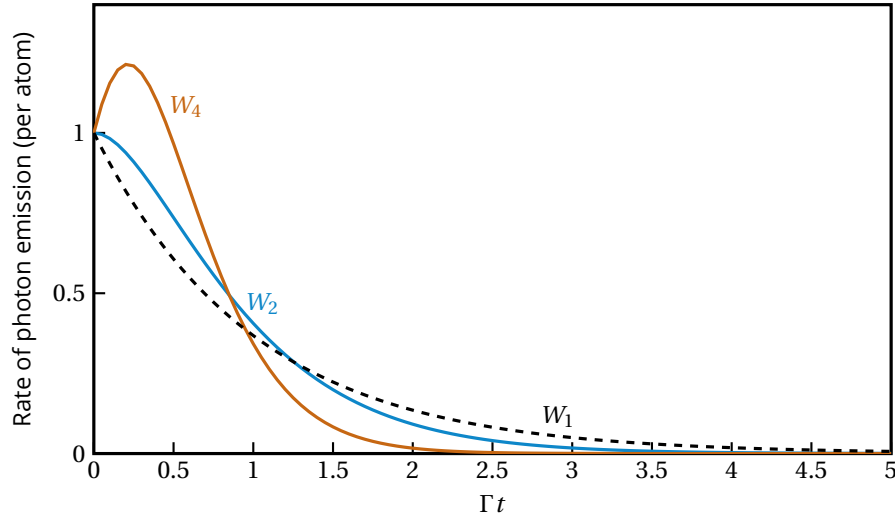


Figure 6.2: Photon emission rate per atom as a function of the time for two-atom superradiance ( $W_2$ ), four atom superradiance ( $W_4$ ) and for independent atoms ( $W_1$ , dashed line).

In figure 6.2, one sees the typical features of superradiance. First, the number of photons emitted per atom is larger than for a single atom ( $W_4, W_2 > W_1$ ) and the initial slope of the photon rate is positive in the decay. Then, a peak is observed with an amplitude proportional to  $N^2$ . Finally, the photon emission rate decays faster than the decay rate of a single atom  $W_1$ . This decay is inversely proportional to the atom number.

Dicke states are the symmetrical states with momentum  $J = N/2$ . One can show (H.-H. Jen 2020) that these states are highly correlated and that their collective dipole moment  $\langle \mathbf{J}_+ \rangle$  vanishes. Superradiance is thus related to the quantum coherences in the system. On the contrary, a product state of  $N$  coherent quantum emitters,

$$|\psi\rangle = \left( \frac{|g\rangle + |e\rangle}{\sqrt{2}} \right)^{\otimes N}$$

also presents an enhanced emission rate but has a large dipole moment. This product state does not show entanglement and it behaves more classically. Some authors distinguish its decay, calling it *superfluorescence* (Mandel and Wolf 1995).

We generalize Dicke's theory to a system whose dimensions are larger than the wavelength, in order to get closer to the conditions of our experiment.

### Generalization to a cylinder of finite size and superradiant threshold

Dicke's original theory takes place in a cloud with dimensions smaller than the light wavelength. To make it applicable in our experimental system, we generalize the previous paragraph in the case of  $N$  atoms in a cylindrical cloud with an axial dimension larger than the wavelength, following (Gross 2006), and we will show that it implies a threshold in the minimal atom number to observe superradiance (the radial dimension is smaller than the wavelength). After the emission of the first photons, the system is in the superposition of the states  $|e\rangle_m$  and  $e^{-i\mathbf{k}_0\mathbf{r}_m}|g\rangle_n$  where  $\mathbf{k}_0$  is the mean wavevector of the emitted photons and  $\mathbf{r}_m$  is the position of atom  $m$ . This leads to correlations between the dipoles:

$$\langle \mathbf{D}_m \mathbf{D}_n \rangle \propto d^2 e^{-i\mathbf{k}_0(\mathbf{r}_m - \mathbf{r}_n)}$$

where  $d = |\langle e|\mathbf{D}|g\rangle|$ .

The light emitted by the system is thus the sum of an isotropic incoherent part  $I_{\text{incoh}} \propto \sum_m \langle \mathbf{D}_m \rangle^2$  and a coherent part due to the interference between the fields emitted by different atoms :

$$I_{\text{coh}} \propto \sum_{m \neq n} \langle \mathbf{D}_m \mathbf{D}_n \rangle e^{-i\mathbf{k}_0(\mathbf{r}_m - \mathbf{r}_n)}. \quad (1.1)$$

The general theory of superradiance involves a summation over all atoms and all electromagnetic field modes. These sums are not independent because according to the laws of diffraction, the modes to which the atoms are coupled depend on the size and geometry of the cloud. Light emitted by the cloud in the direction  $\mathbf{k}_0$  is proportional to  $|S_N(\mathbf{k}_0)|^2$  where

$$S_N(\mathbf{k}_0) = \frac{1}{N} \sum_{m=1}^N e^{-i\mathbf{k}_0 \cdot \mathbf{r}_m}$$

is the structure factor of the atomic cloud. We approximate this sum by

$$S_N(\mathbf{k}_0) \sim \frac{1}{N} \int n(\mathbf{r}) e^{-i\mathbf{k}_0 \cdot \mathbf{r}} d\mathbf{r}$$

where  $n(\mathbf{r})$  is the atomic density. Assuming an ellipsoidal gaussian density

$$n(\mathbf{r}) = n_0 e^{-\frac{x^2+y^2}{2\sigma_r^2} - \frac{z^2}{2\sigma_z^2}},$$

one obtains for  $N \rightarrow \infty$  (Courteille et al. 2010), in spherical coordinates

$$S_\infty(k_0, \theta, \phi) = e^{-k_0^2 \sigma_r^2 [\sin^2(\theta) + \eta^2 (\cos(\theta) - 1)^2] / 2}$$

where  $\eta = \sigma_z / \sigma_r$  is the aspect ratio of the cloud. This means that the intensity is mostly emitted in a small angle  $\theta_g = 1/\eta = \sigma_r / \sigma_z \approx 0.03 \text{ rad}$ . To calculate the radiated intensity, we

therefore perform the summation only on the modes contained in a solid angle  $\Delta\Omega$  around the cylinder axis, for which the fields interfere constructively. It is given by

$$\Delta\Omega = 2 \times 2\pi (1 - \cos(\theta_g))$$

where the factor 2 comes from not favoring a direction along the axis of the cylinder.

In the case of the cylindrical cloud that we consider, the radiated fields vary essentially along the axis of the cylinder and negligibly in the radial direction. Following (Gross and Haroche 1982), the description of superradiance depends of the Fresnel number:

$$F = \frac{\pi\sigma_r^2}{\lambda\sigma_z}$$

In our case,  $F \simeq 0.05$ , so the emission occurs in a single mode. The counterpart is that this mode strongly diverges with a diffraction angle  $\theta_d = \lambda/\sigma_r = 2\text{ rad}$ , but the coupling mode is actually reduced by the geometry of the cloud to the angle  $\theta_g$ . Experimentally, this allows us to observe superradiance using our large NA lenses, as represented figure 6.3.

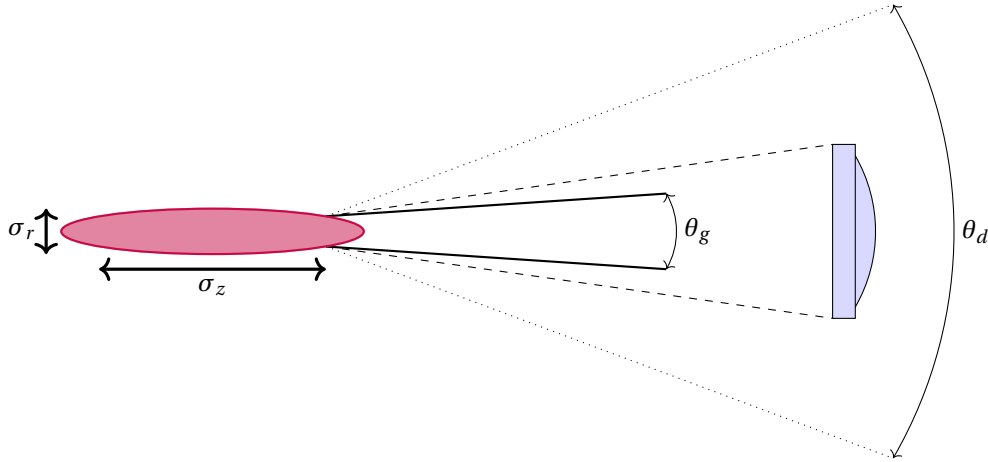


Figure 6.3: Schematic representation of the geometry. Because of the Fresnel number  $F \ll 1$ , a single mode is sustained by the emission (angle  $\theta_d$ ). It is limited by the geometrical angle  $\theta_g$ , with is smaller than the field of view of the detection system (NA=0.5).

One obtains

$$I_{\text{coh}} \propto N^2 \Delta\Omega$$

and

$$I_{\text{incoh}} \propto 4\pi N.$$

The superradiant emission is thus larger than the emission of independent atoms if  $N > \frac{4\pi}{\Delta\Omega}$ . This geometrical condition is often written

$$N\mu > 1 \tag{1.2}$$

where  $\mu = \frac{\Delta\Omega}{4\pi}$ . The physical interpretation of the geometrical factor  $\mu$  is given in (Gross and Haroche 1982). The spontaneous emission rate  $\Gamma$  is reduced to  $\Gamma\mu$  and only the photons in the diffraction solid angle (proportional to  $\mu$ ) are "useful" for the superradiant emission process.

With our experimental parameters,  $\mu \simeq 1/1800$ . We thus expect superradiance to dominate for  $N > 1800$ .

### Conclusion

Superradiance is a phenomenon described by classical theory in the sense that it results from the constructive interference between fields emitted by dipoles. However, quantum theory is necessary to explain the initial phasing of atomic dipoles, starting from a totally inverted system. Superradiance depends on the geometry of the system and the number of emitters via the threshold condition  $N\mu > 1$  (assuming that there is no other source of dephasing between the dipoles than the geometry of the system).

The rest of this chapter is dedicated to the experimental observation of superradiance.

## 2 Observation of superradiant emission of an inverted atomic cloud

As explained in the beginning of this part, all the measurements presented in this chapter have been obtained on the experimental setup represented figure 1.

### 2.1 Realization of a $\pi$ -pulse

#### Pulse shape

To observe superradiance, one first needs to invert the atomic system, that is to prepare the  $N$ -atom state  $|ee\dots e\rangle$ . As we have seen in chapter 5 (section 3), we are able to perform Rabi oscillations to control the internal state of the cloud. To obtain an inverted system, one must control the driving pulse after a duration  $\pi/\Omega$ , where  $\Omega$  is the Rabi frequency (assuming a square driving pulse). Experimentally, the pulse is shaped using two acousto-optical modulators (AOM) in series and a fiber electro-optical modulator (EOM). The EOM has a rising and falling time shorter than 1 ns, but its extinction is only of the order of  $10^{-2}$ . We use light intensities corresponding to saturation parameters  $s = I/I_{\text{sat}} \sim 85$ . Because of this high intensity, AOMs are thus needed to ensure a sufficient extinction. One of the AOM is in double-pass configuration and the other is in single pass configuration.

In figure 6.4 a), we show the pulse measured using an APD, for different pulse durations. We observe first a slow start ( $\sim 50$  ns), controlled by the AOMs. This relatively long time results from favouring a good extinction ratio over speed. At  $t = 0$ , the EOM is switched on in a time shorter than 1 ns. At the end of the pulse, the EOM is first switched off faster than 1 ns, but it takes about 20 ns to switch off the AOMs. As shown in panel b), we observe a rebound in the extinction of the pulse, after a time that depends on the duration of the pulse. This is due to the transient response of the EOM. By optimizing the delays between the AOMs and the EOM, we minimize this bounce as much as possible without distorting the pulse. Delays are controlled using a delay generator<sup>1</sup> with an accuracy of 1 ns. We obtain an extinction of  $10^{-3}$  in less than 5 ns, which is enough to make the residual driving negligible after the end of pulse for the study of superradiance.

---

<sup>1</sup>Stanford Research System<sup>®</sup> DG645

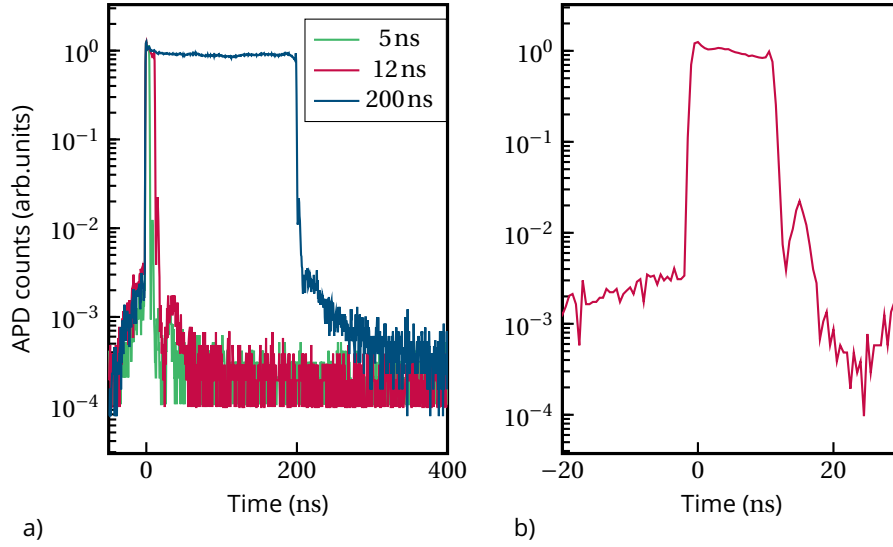


Figure 6.4: Excitation pulses of various durations, measured using an Avalanche photodiode (APD). b) Zoom on the 12 ns pulse used for the experiments.

The high extinction of the drive at longer times allows us to also study subradiance in the same experimental sequence. To the best of our knowledge, this has never been done before. This will be detailed in chapter 8.

The optimal (minimal) pulse duration is limited by the rising and falling times of the AOMs. With our experimental apparatus, this duration is  $\tau_{\text{opt}} = 12 \text{ ns}$ . For durations shorter than this, the shape of the pulse is distorted and the pulse intensity varies over time because of thermal effects. The shape of this pulse does not depend on the intensity within the range we explored ( $s \leq 100$ ).

### Intensity optimization

We want to apply a pulse as intense as possible and as short as possible, allowing an efficient population inversion before decoherence occurs. We therefore would use  $\Omega_{\text{opt}} = \pi/\tau_{\text{opt}}$  such as the shortest (12 ns) pulse realises a  $\pi$  pulse. However, it is difficult to calculate precisely the intensity actually applied on the atoms during the real pulse because the pulse is not a perfect square function. We thus find experimentally the optimal Rabi frequency using the following protocol.

There are two conditions to be fulfilled: the maximum of the population in the excited state must be as high as possible ( $P_e(\Omega)$  maximum for a pulse of fixed duration  $\tau_{\text{opt}}$ ) and this maximum must be reached at  $t = \tau_{\text{opt}}$ . In order to explain the method, we calculate the solutions of the single atom optical Bloch equations for several values of  $\Omega$ , as shown in figure 6.5. The photon rate is proportional to the population of the excited state  $\rho_{ee}$ . We want to find experimentally the intensity of the light that gives us the curve in black, which verifies the conditions above.

Using these curves, we deduce the population inversion at  $\tau_{\text{opt}}$ , shown in figure 6.6 panel a). For  $\tau_{\text{opt}} = 12 \text{ ns}$ , we obtain  $\rho_{ee,\text{max}} \approx 0.85$  at the end of the pulse. This value could be larger for higher probe intensity (but we cannot realize the pulse experimentally) and is smaller for lower intensities. The maximum for any pulse duration is represented by the dashed line.

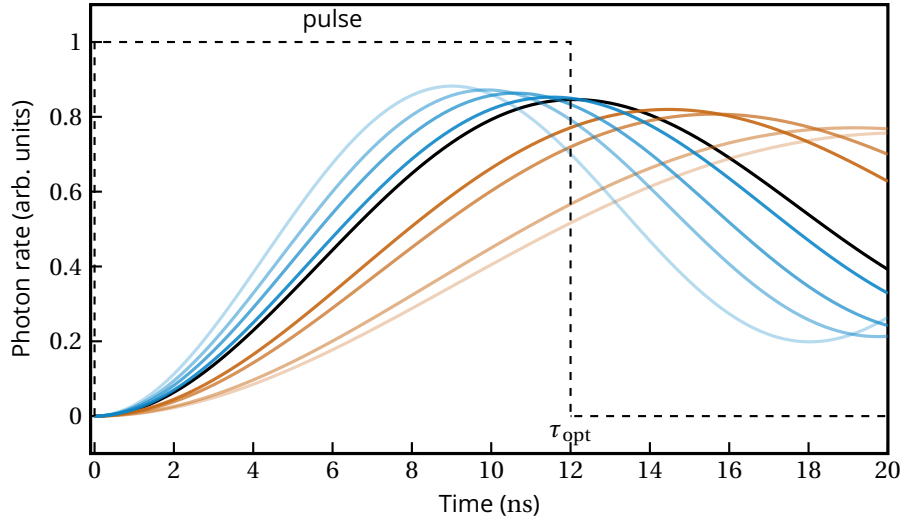


Figure 6.5: Calculated photon rates as a function of the time, for various Rabi frequencies around  $\Omega_{\text{opt}}$ . The shortest pulse (duration  $\tau_{\text{opt}} = 12\text{ ns}$ ) is shown with a dashed line.

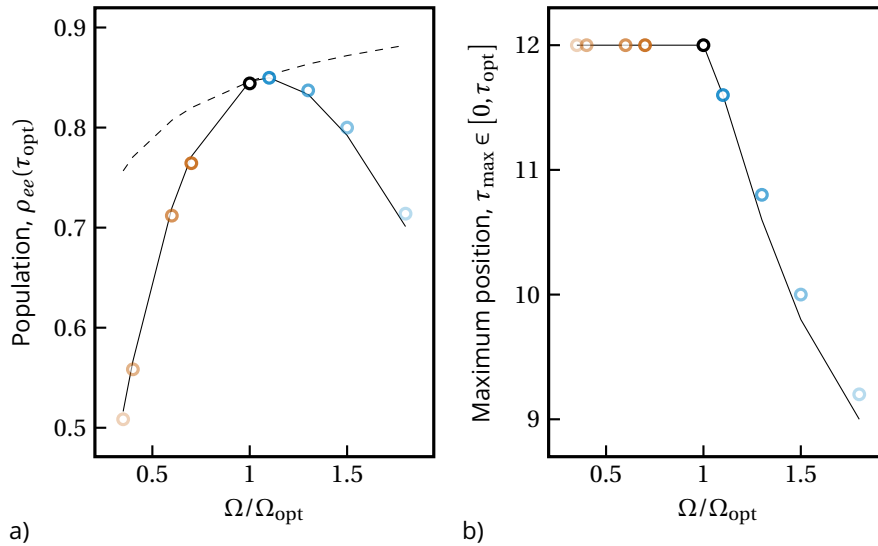


Figure 6.6: a) Population of the excited state at the end of the pulse as a function of the Rabi frequency. The maximum for any pulse duration is represented by the dashed line. b) Position of the maximum of the emission rate for  $t < \tau_{\text{opt}}$  as a function of the Rabi frequency. The colors are the same than in figure 6.5.

In panel b), we plot the position of the population maximum for  $t \in [0, \tau_{\text{opt}}]$ . This curve can be explained in the following way. If  $\Omega > \Omega_{\text{opt}}$ , the first peak of the oscillations is before  $\tau_{\text{opt}}$ , so  $\tau_{\text{max}} < 12\text{ ns}$ . If  $\Omega < \Omega_{\text{opt}}$ , the first peak is after  $\tau_{\text{opt}}$ , so the maximum on the considered interval (before the end of the pulse) is in  $\tau_{\text{max}} = \tau_{\text{opt}}$ . The Rabi frequency obtained at the intersection of the two asymptotes is the optimal frequency  $\Omega_{\text{opt}}$ .

We perform this measurement on a dilute cloud ( $n_0/k^3 \ll 1$ , to avoid any effect of the interactions) for pulses of duration  $\tau_{\text{opt}}$ . We also checked the method with an arbitrary pulse duration  $\tau_{\text{opt}} + 10 = 22\text{ ns}$ , as shown figure 6.7.

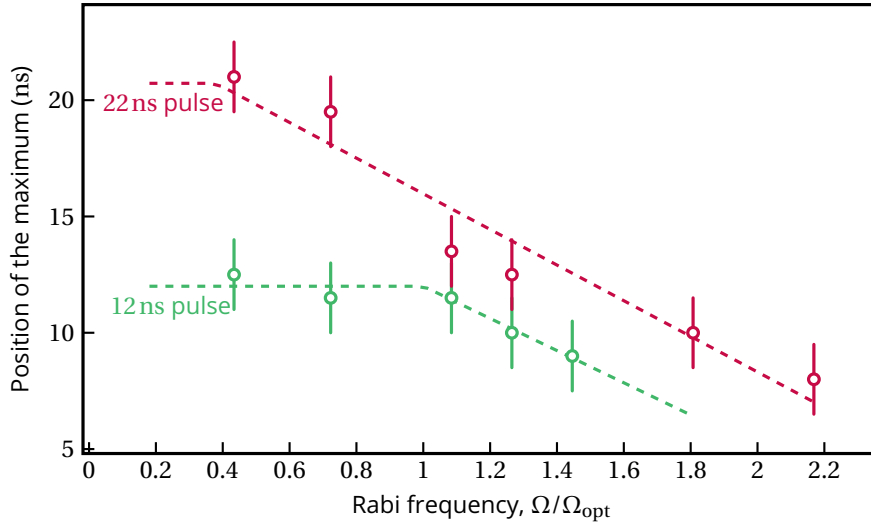


Figure 6.7: Measured maximum position of the photon emission for pulses of duration  $\tau_{\text{opt}}$  and 22 ns as a function of the Rabi frequency of the driving pulse. Rabi frequencies are normalized by the value  $\Omega_{\text{opt}}$  found with a fit of the data.

In figure 6.7, we observe the expected behaviour as a function of  $\Omega$ . By fitting the data for the pulse of duration  $\tau_{\text{opt}}$ , one obtains the value of  $\Omega_{\text{opt}}$ .

We use a long (200 ns) pulse to estimate the value of Rabi frequency  $\Omega_{\text{opt}}$  using a fit of the collected fluorescence by the solution of the optical Bloch equations, as done in chapter 5 (section 3). Expressed in terms of saturation parameter, we obtain  $s_{\text{opt}} \approx 85$ . If we had assumed a square pulse, we would have obtained  $s = 93$ . The above protocol therefore allows for a more accurate  $\pi$  pulse by taking into account the exact shape of the pulse.

The solution of the Bloch equations knowing the excitation pulse also allows to deduce the population of the excited state. With our experimental parameters, we find that about  $\rho_{ee,\text{max}} \approx 0.85$ , which means that 85% of the atoms are in their excited state at the end of the  $\pi$ -pulse.

## 2.2 Superradiant flash

We now apply a  $\pi$ -pulse in a dense cloud in order to observe the superradiant flash in photon emission. In the Dicke model, the cloud is smaller than the light wavelength and the good parameter to describe the effects is the atom number  $N$ . In order to increase  $N\mu$ , as explained in section 1.2, we load as many atoms as possible in a tight cloud. To do so, we apply the protocol explained in chapter 5 (section 1.1). The dimensions of the resulting cloud are radially  $0.5\lambda_0$  and  $15\lambda_0$  along the axis of the trap with  $\lambda_0 = 780 \text{ nm}$ . The cloud is excited perpendicularly to its long axis with a probe resonant with the two-level atoms transition, with polarization  $\sigma_-$  and a power of  $s = 85$ , realizing a  $\pi$ -pulse as described in the previous section. The probe has a diameter of about  $500 \mu\text{m}$  so that the cloud is excited homogeneously: the Rabi frequency is the same for all atoms.

We collect the fluorescence emitted by the cloud along the cloud axis with an APD. We apply the same excitation 20 times on the same cloud (less than 10% of the atoms are lost during these pulses). We repeat this sequence on 3000 different clouds to acquire enough signal. We then consider the histogram of arrival times, using 1 ns bins.



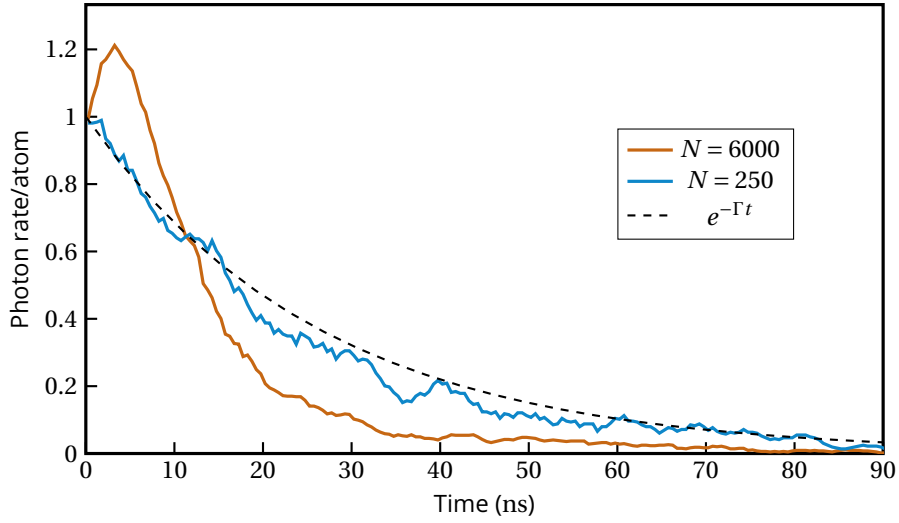


Figure 6.8: Normalized photon rate as a function of time. For  $N = 250$ , the decay rate per atom is similar to the decay of a single atom, as shown with a dashed line ( $e^{-\Gamma t}$ ). For  $N = 6000$ , a superradiant flash is observed.

The result strongly depends on the atom number. For a small atom number (we will explain in the following what ‘small’ means), the decay of the cloud matches the decay of independent atoms. In figure 6.8, we plot the number of photons emitted per atom from a cloud containing  $N = 250$  atoms normalized to the initial fluorescence. It is very well fitted by  $e^{-\Gamma t}$ , where  $1/\Gamma = 26.4 \text{ ns}$  is the natural decay time of the rubidium D2 line.

For  $N = 6000$  (‘large’ atom number regime), we observe a superradiant flash. The number of photons first increases until a maximum. It then decays faster than for independent atoms. This is the typical behaviour of superradiance, as described in the first section of this chapter (figure 6.2).

Let us now describe quantitatively the superradiant decay.

### 3 Analysis of the superradiant decay

In this section, we analyse the features of the observed superradiance, following (Ferioli, Glicenstein, Robicheaux, et al. 2021). These features depend of the number of atoms in the trap. The excitation scheme is the same as in the previous section, and we vary the atom number in the trap (see section 4). Fluorescence photons are collected along the cloud’s main axis, as represented in figure 1. Examples of experimental traces are shown figure 6.9, normalized by the atom number  $N$  so that we plot the fluorescence per atom.

We observe that the photon emission rate switches from an exponential decay to a short burst as  $N$  increases. In the ideal Dicke scenario, the intensity emitted per atom at the end of the pulse should be independent of  $N$ . This would be the case if the  $\pi$ -pulse was much faster than the superradiant emission. In our case, superradiance starts before the end of the excitation pulse. However, we still observe that the emission increases after the end of the pulse (flash). This effect increases as  $N$  increases. It is also clear that the timescale  $\tau_s$  decreases as  $N$  increases.

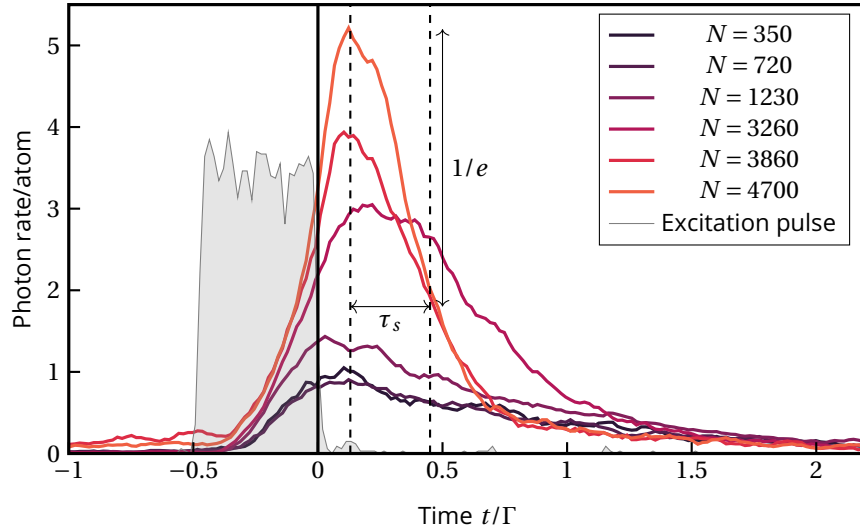


Figure 6.9: Examples of photon rates, normalized by the atom number  $N$ . The superradiant decay time  $\tau_s$  is defined as the time required for the emission rate to be reduced to  $1/e$  of its maximum, as represented. The end of the excitation pulse (gray are) is located at  $t = 0$ .

### 3.1 Theoretical model

Despite knowing the microscopic details of our clouds, the application of exact numerics is not possible due to the large number of atoms. Our data will be compared to simulations based on a truncated treatment of the problem (Robicheaux and Suresh 2021). As explained in the first chapter (section 2.3), it consists in replacing the third order operator expectations by products of one and two operator expectations, assuming that the cumulants for the three operators are zero (Kubo 1962).

These simulations, called *mean-field 2* (MF2), are performed by F. Robicheaux and R. Sutherland and account for dipole-dipole interactions between emitters. This approach differs from "traditional" treatments of the problem in that it does not impose any a priori coherence in the many-body wavefunction, as opposed to, in particular, (Allen and Eberly 1987).

The simulations are solved for fixed positions of the atoms in a thermal cloud with the same size as the clouds produced in the experiment. They are averaged up to 1000 times over random configurations.

F. Robicheaux has verified for a small number of atoms ( $<80$ ) that the emission rate calculated with MF2 differs by less than 5% compared to the rate calculated with MF3 (truncation of the cumulants to the higher order). The CPU and memory requirement of MF3 are too large to estimate the error induced by the MF2 in our experimental conditions. The number of operations for one time step of MF2 is proportional to  $3^2 N^3$ , and is proportional to  $3^3 N^4$  for MF3 (Robicheaux and Suresh 2021).

MF2 simulations are ab-initio simulations, without any free parameters. They are only based on measured values, such as the cloud's size and depth, the atom number and the temperature.

### 3.2 Initial photon rate

In this section, we study the evolution of the initial slope of the photon rate as a function of the atom number. The initial emission rate is extracted using a linear fit in a 5 ns window after the end of the pulse. We show the results in figure 6.10, compared to the single atom case (shown with a dashed line) and to the MF2 simulations.

At low atom number ( $N \leq 1350$ ), we observe a normal exponential decay (negative initial slope, equal to  $-\Gamma$ ). For  $N \geq 1350$ , the initial slope of the photon emission rate is positive, meaning that the number of photon emitted increases even if the driving is switched off : this is the superradiant flash. The slope increases with the atom number. Simulations results agree qualitatively with the data.

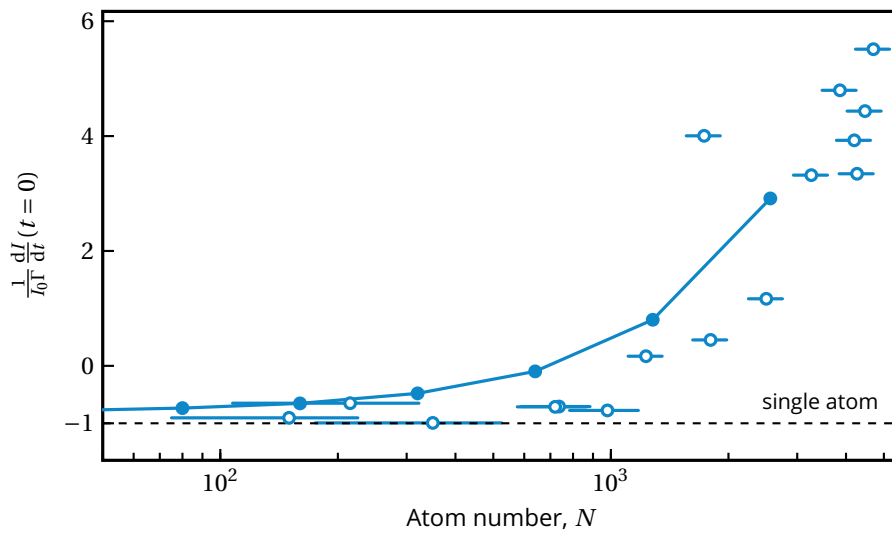


Figure 6.10: Initial slope of the photon emission rate as a function of the atom number  $N$ . The rates are compared to that of a single atom (dashed line) and to ab-initio MF2 simulations (filled dots), as explained in the text. The horizontal error bars correspond to the calibration of the atom number. The vertical error bars are from the fit of the initial slope.

In the figure above, we see a threshold above which superradiance is observed. As explained qualitatively section 1.2, the threshold is due to the fact that the axial size of the cloud is larger than the wavelength. The value of the threshold depends on the cloud geometry and is quite well reproduced by the simulations. The threshold value is also quite close to the one found qualitatively in section 1.2, which shows that the picture works.

### 3.3 Peak of the photon emission

We now investigate the scaling law of the peak amplitude of the photon emission rate as a function of the atom number. The result is shown figure 6.11.

In figure 6.11, we see that the peak intensity is constant for  $N \gtrsim N_t = 1350$  and then increases linearly. This means that the light emitted along the main axis of the cloud scales as  $N^2$  for large  $N$ , which is a feature of superradiance. Data are compared to ab-initio MF2 simulations, and show again a good qualitative agreement without any free parameter. This

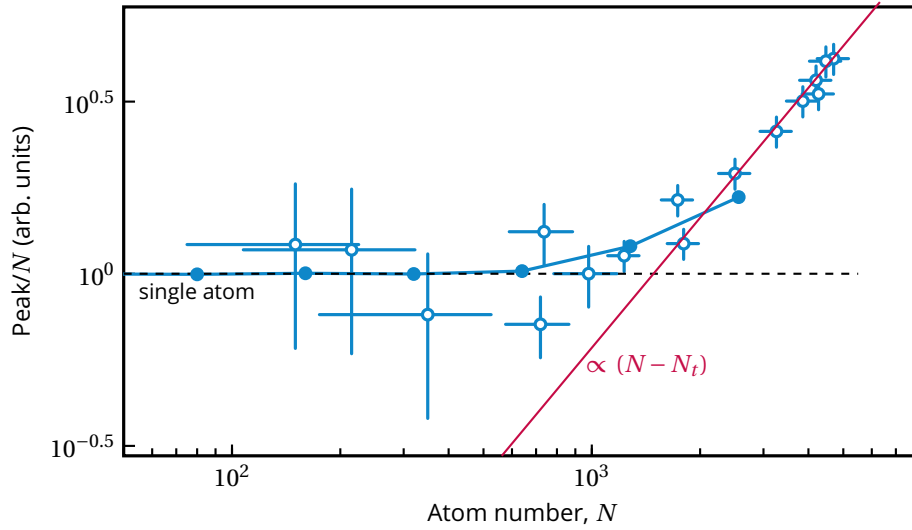


Figure 6.11: Peak photon emission in the axial direction normalized by  $N$ . The horizontal error bars correspond to the calibration of the atom number. The vertical error bars are calculated from the error on the peak position and the error on  $N$ . The dashed line shows the single atom behaviour and the solid red line shows as a guide the  $N^2$  scaling of the emission above the threshold  $N_t$ . Data are compared to MF2 simulations (filled dots).

result can be compared to those obtained by (Norcia et al. 2016) with laser-cooled Sr in a high-finesse cavity. They also have observed a  $N^2$  scaling of the peak of the photon emission rate above a minimum atom number. They found a threshold of 33,000, much higher than the one we obtained in free space. This shows that the collective enhancement of the emission rate is more important in our system, although the cavity allows them to force the electromagnetic mode of the photons.

### 3.4 Decay time

The  $N^2$  scaling of the peak intensity implies that the decay occurs in a duration shorter by a factor  $N$  compared to a single atom. The superradiant decay time  $\tau_s$  is defined as the time required for the emission rate to be reduced to  $1/e$  of its maximum. In figure 6.12, we plot  $\tau_s$  as a function of  $N$ . In the figure above, one sees the expected behaviour. Below the threshold  $N_t$ , the system acts as an ensemble of independent atoms. Above the threshold, we observe that the decay scales as  $1/(N - N_t)$ .

The observed scaling, as well as the existence of the threshold are typical features of Dicke superradiance.

### 3.5 Influence of the trap geometry

The measurements above report the superradiant emission from an elongated cloud ( $\sigma_z = 15\lambda_0$ ) with radial dimension smaller than the emission wavelength ( $\sigma_r = 0.5\lambda_0$ ), as depicted figure 1.

Without making a quantitative study of the evolution of the threshold as a function of the cloud geometry, we perform the same measurements as before in the crossed dipole trap

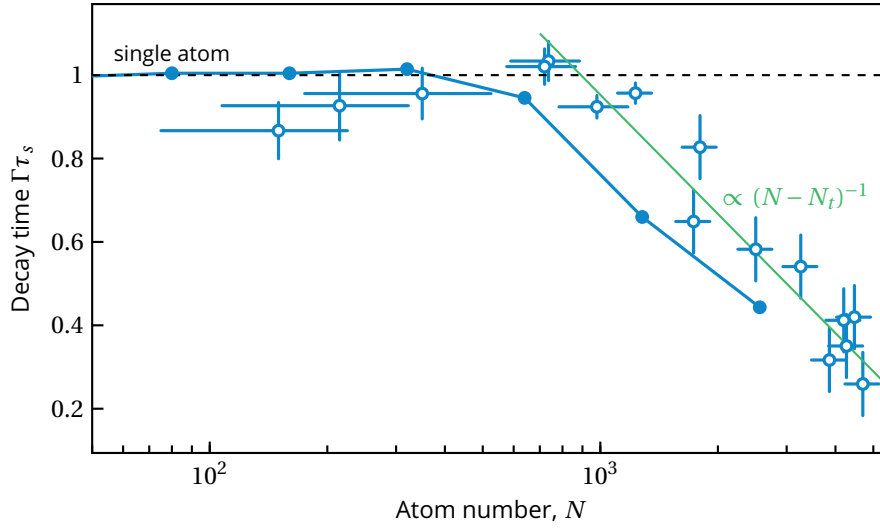


Figure 6.12: Decay time  $\tau_s$  as a function of the atom number. The horizontal error bars correspond to the calibration of the atom number. The vertical error bars are given by the resolution of the detector. The dashed line shows the single atom behaviour and the solid green line shows as a guide the  $N$  scaling of the decay above the threshold. Data are compared to MF2 simulations (filled dots).

presented in chapter 5 (section 5). The radial dimension is still  $\sigma_r$  but the new axial extension is  $\sigma_z \sim 2\lambda_0$  (figure 5.20). The peak amplitude obtained is shown figure 6.13.

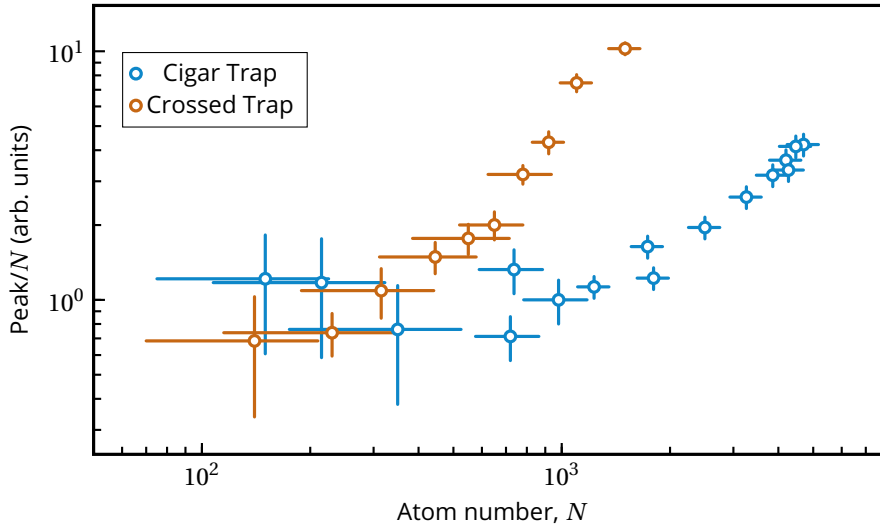


Figure 6.13: Peak photon emission in the axial direction normalized by  $N$  for the elongated cloud and for the crossed trap. The horizontal error bars correspond to the calibration of the atom number. The vertical error bars are calculated from the error on the peak position and the error on  $N$ .

In figure 6.13, one sees that the threshold for superradiance is reduced in the crossed trap. This can be understood by the fact that the cloud is now more spherical, so the emission (diffraction) angle  $\Delta\Omega$  is increases. Using the qualitative argument of section 1.2 and equation

(1.2), the threshold is thus reduced. Note that the slope above the threshold is also different for the two traps. It also depends on the geometry of the cloud.

## 4 Conclusion

In this chapter, we have first given a qualitative description of Dicke superradiance and of its features. In the second part, we have explained how we excite the system, realizing a  $\pi$ -pulse. We finally observe the typical features of Dicke superradiance in our disordered cloud of two-level atoms, allowed by the experimental progress on the number of trapped atoms. MF2 ab-initio simulations have been performed by our collaborators F. Robicheaux and R.T. Sutherland and show a good agreement with the experimental data without any free parameter.

The next chapter will be devoted to a more in-depth study of superradiance while our system is driven, as well as when the population steady state is reached.

# Driven superradiance

\*\*\*

In the previous chapter, we have studied the collective decay of an initially (almost) fully inverted system, showing Dicke superradiance. The purpose of this chapter is to investigate the presence of superradiance while the system is externally laser driven. We will first investigate the influence of superradiance on collective Rabi oscillations. In a second part, we will focus on superradiance when the steady-state under driving is reached, that is when the system is prepared in a mixed state.

Unless explicitly stated, each measurement presented in this chapter was performed using the configuration shown in Figure 1.

## Contents

<b>1</b>	<b>Laser driven collective oscillations</b>	<b>124</b>
1.1	Directionality	124
1.2	Peak over Steady-state value	124
<b>2</b>	<b>Collective properties of the driven system</b>	<b>127</b>
2.1	Decay time	127
2.2	Rabi frequency	129
2.3	Photon rate in the early decay	130
2.4	Influence of the internal structure	130
<b>3</b>	<b>Superradiance in steady-state</b>	<b>132</b>
3.1	Observation of the steady-state superradiance	132
3.2	Directionality	133
3.3	Cooperativity parameter	135
<b>4</b>	<b>Superradiance as a function of the probe intensity</b>	<b>138</b>
4.1	Peak over steady-state	138
4.2	Decay time	139
4.3	Steady-state fluorescence	140
<b>5</b>	<b>Conclusion</b>	<b>140</b>

## 1 Laser driven collective oscillations

We first investigate the influence of superradiance on Rabi oscillations. For this, we excite the cloud with a longer pulse than in the previous chapter. We chose a duration of  $150\text{ ns} \approx 6/\Gamma$ , which is sufficiently long to reach the steady state, and an intensity  $I/I_{\text{sat}} \approx 85$ .

As shown in the previous chapter, in the low atom regime (below a threshold of  $N \approx 1350$ ), the cloud behaves as an ensemble of independent atoms, and the dynamics is well described by the optical Bloch equations (OBE). As  $N$  increases, we observe two different behaviors depending on the direction of observation.

### 1.1 Directionality

For this particular measurement, we measure the fluorescence emitted *axially* (along the main axis of the cloud,  $\text{APD} \parallel$ ) and *radially* (perpendicularly to the long axis of the cloud,  $\text{APD} \perp$ ) exploiting the two high resolution imaging axes (chapter 2, section 1.3).

In the low atom number regime, the time dependence of the fluorescence is independent of the direction of observation. The cloud behaves as an ensemble of independent atoms, and its response is well modeled by the OBE, as shown in figure 7.1. In this figure, we show only the data collected along the axis because the collection efficiency is much higher on this axis (we choose a large field of view of about  $20\mu\text{m}$  on the transverse axis to collect the light emitted by the whole cloud, at the expense of a lower collection).

When increasing the atom number in the cloud, we observe two different regimes depending on the observation direction. Radially, we observe a response similar to that of a single atom (the dynamics follows accurately the prediction of the OBEs). Along the main axis however, we observe very large peaks at the maxima of the Rabi oscillations.

To explain these peaks, we compare data to ab-initio MF2 calculations (see previous chapter, section 3.1), shown with solid line in figure 7.1. These simulations have been done by F. Robicheaux using the experimental parameters, and show a good agreement with the data without any free parameter. The mismatch might be due to a concatenation of various factors that individually would be negligible, including a non-perfect knowledge of the density distribution of the cloud, depumping effects, effects of the atomic motion, atomic losses during the excitation protocol, and fluctuations in the intensity of the driving field (Ferioli, Glicenstein, Robicheaux, et al. 2021).

### 1.2 Peak over Steady-state value

As shown in figure 7.2, the interplay between superradiance and driving enhances the emission peaks during the Rabi oscillations only in the axial direction. In the radial direction, the clouds acts as an assembly of independent atoms (described by the OBEs) : the amplitude of the first peak of the oscillations is independent of  $N$ . MF2 simulations also qualitatively predict these two different behaviours. It is important to note that a standard mean-field treatment of the problem, neglecting two-atoms correlations, is unable to reproduce our data even qualitatively. Higher-order MF2 simulations are thus needed.

To explain the observed behaviours, we specify the quantity measured experimentally by the APD: the (scaled) rate of photon emission in a given direction  $\mathbf{k}$  (Allen and Eberly 1987):

$$\bar{\gamma}(t, \mathbf{k}) = \frac{1}{N} \sum_n \left[ \langle \hat{e}_n \rangle(t) + \sum_{m \neq n} e^{i\mathbf{k} \cdot (\mathbf{R}_m - \mathbf{R}_n)} \langle \hat{\sigma}_m^+ \hat{\sigma}_n^- \rangle(t) \right] \quad (1.1)$$



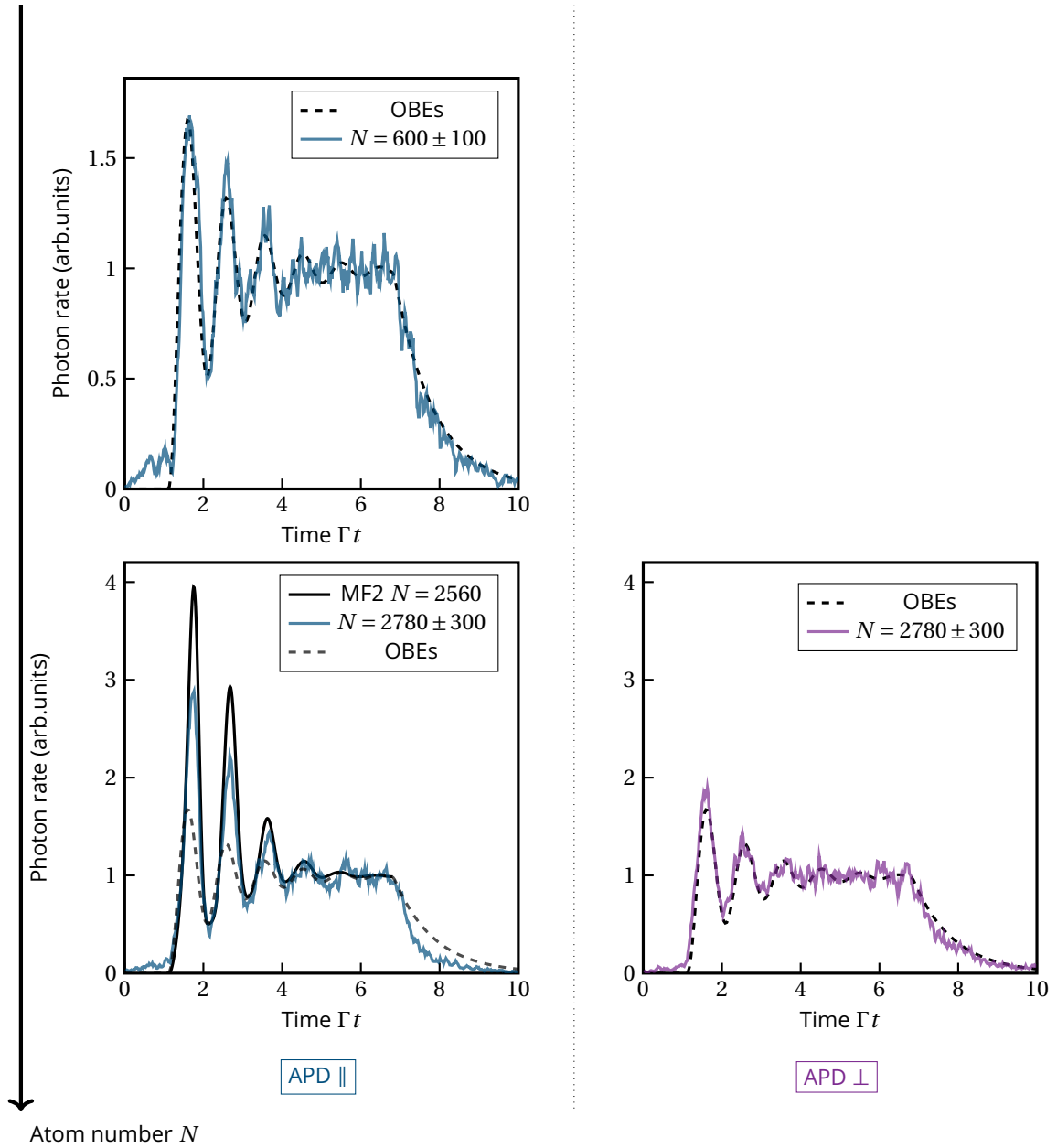


Figure 7.1: Photon rate as a function of time, recorded along the trap axis (APD  $\parallel$ ) and radially (APD  $\perp$ ) during the same experiment. In the low atom number regime, the cloud is well modeled by the Optical Bloch Equations (OBEs, dashed line) and the response is isotropic. In the large atom number regime, one observes collective Rabi oscillations only along the cloud main axis. In this regime, data are compared with ab-initio MF2 simulations (solid line).

where  $\mathbf{R}_m$  is the position of atom  $m$ ,  $\hat{e}_n = |e_n\rangle\langle e_n|$  and  $\hat{\sigma}_n^- = |g_n\rangle\langle e_n|$ .

The first term of equation (1.1) is proportional to the population inversion of each atom. This term thus represents the spontaneous emission of independent atoms. The second term is responsible for superradiance.

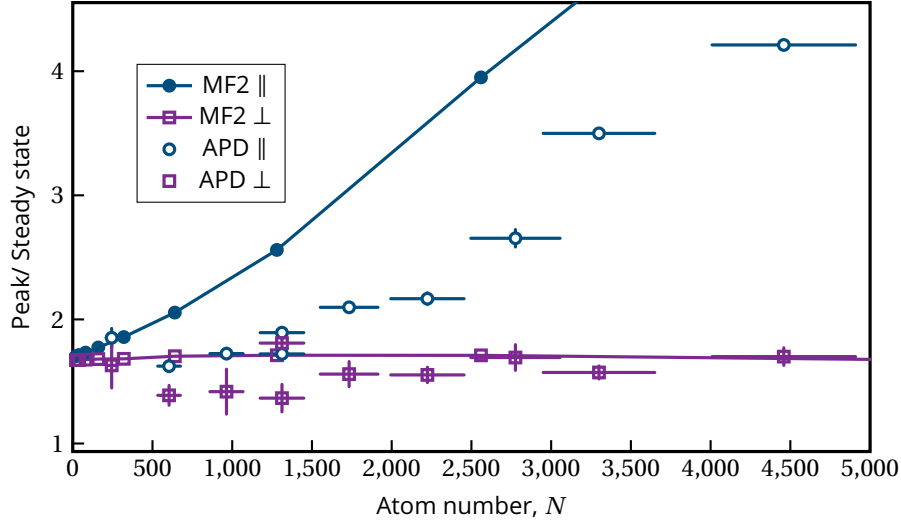


Figure 7.2: Peak over steady state as a function of the atom number, along the two observation directions. Data (empty points) are compared with ab-initio MF2 simulations (filled points). The vertical error bars represent the standard error in the estimation of the steady state (smaller than symbols).

Indeed, let us assume that (as in the Dicke regime),  $|\mathbf{R}_m - \mathbf{R}_n| \ll \lambda$ . In that case, the phase factor of the second term of equation (1.1) is equal to 1. If the two-atoms correlations are different from zero at a time  $t_0$ , let us assume that  $\langle \hat{\sigma}_m^+ \hat{\sigma}_n^- \rangle(t_0) = K$  for all atoms  $n$  and  $m$  to get an intuition,  $K$  being a constant. Since all atoms are indistinguishable in the Dicke regime, this is a good assumption. The photon rate becomes

$$\bar{\gamma}(t_0, \mathbf{k}) = \frac{1}{N} \sum_n [\langle \hat{e}_n \rangle(t_0) + (N^2 - N)K] \quad (1.2)$$

One thus recovers the  $N^2$  scaling. Note that in this case the emission is isotropic.

It is clear from figure 7.2 that the peak over steady-state value cannot be explained by the first term of equation (1.1). This indicates the presence of correlations along the main axis of the cloud. Interestingly, the coherence is not imposed by the driving laser, since the direction of superradiance is perpendicular to it. Ignoring spontaneous emission (assuming  $\Omega \gg \Gamma$ ), the laser creates the state

$$|\psi_{\text{las}}\rangle = \bigotimes_n (\cos\theta |g_n\rangle + e^{i\mathbf{k}_{\text{las}} \cdot \mathbf{R}_n} \sin\theta |e_n\rangle)$$

for which the second term of equation (1.1) averages to 0. The phase relation responsible for superradiance thus emerges during emission, and is imposed by the cloud geometry.

As explained in the previous chapter (section 1.2), the condition to observe superradiance can be expressed in terms of the Fresnel number  $F$ . In our cloud,

$$F_{ax} = \frac{\pi \sigma_r^2}{\lambda_0 \sigma_z} = 0.05 \ll 1$$

using  $\sigma_z = 15\lambda_0$  and  $\sigma_r = 0.5\lambda_0$  (see figure 1). There exists thus one spatial mode that is coupled to all atoms (that is the gaussian mode with  $z_R \sim \sigma_z$ ). In the radial direction however,  $F >$

1, so the second term of equation (1.1) averages to zero and we observe a single atom-like behavior.

## 2 Collective properties of the driven system

In this section, we characterize experimentally the collective properties of the density matrix that we prepare during the pulse and we demonstrate the presence of superradiant states. For this, we measure several observables: the Rabi frequency of the oscillations, the rate of photon emission after the end of the excitation and the decay time of the excitation. The underlying (highly non-trivial) question is whether one can deduce the atomic correlations leading to superradiance from the study of the properties of the light scattered by the cloud.

### 2.1 Decay time

The first observable we use is the decay time of the excitation after the end of the pulse. Indeed, this allows us to determine the superradiant character of the produced state.

A crucial improvement of our experimental setup is the precise control of the driving pulse duration. Indeed, by tuning the parameters of the delay generator controlling the electro-optical modulator (see chapter 6, section 2.1), one can realize short pulses of controllable duration with an extinction of about 1/100 in less than 1 ns. There is of course a limit on the shortest pulse that we can send (about 5 ns), as explained section 2.1 for optimizing of the  $\pi$ -pulse.

With this, one can stop the driving pulse at a precise time  $t_0$  during the Rabi oscillations and then measure the fluorescence emitted by the cloud after the end of the pulse. The superradiant decay time is then extracted by fitting with a single exponential decay the temporal traces in a time window of 50 ns that starts 5 ns after the end of the pulse (to avoid any parasite effect due to the superradiant burst described in the previous chapter). In the low atom number regime ( $N = 120$  in figure 7.3), one sees that the decay is always compatible with that of a single atom.

In the large atom number however ( $N = 4500$  in figure 7.3), we observe a superradiant decay, faster than  $1/\Gamma$ . Moreover,  $\tau_s$  oscillates with the same frequency as the Rabi oscillation but in quadrature with respect to it. To highlight this behavior, we report in Fig. 7.3 also a temporal trace acquired in the low atom number regime which, properly normalized, represents the population of the excited state. This observation suggests that the superradiant properties of the systems depends mostly on the population of the excited state, thus the superradiance is stronger when the population is largely inverted and vice-versa.

This conclusion is supported by the fact that a states with a population inversion such that half of the atoms are excited but prepared driving the system for a time shorter than  $1/\Gamma$  so that the coherence is still preserved, decays in the same way as the incoherent mixture achieved in the steady state (pulse  $\geq 100$  ns). This behavior is consistent with Dicke's picture, according to which the coherence is built up during the spontaneous emission, independently from the exact initial state in which the system is cast.

In the low atom number regime, one can fit the data by the solutions of the optical Bloch equations (OBE). They allow to obtain the population  $\rho_{ee}$  as a function of time, as shown in panel a) of figure 7.4. We therefore plot the superradiant decay time in the large atom number regime as a function of the population of the excited state at  $t_0$ , in figure 7.4 b). Note that it is assumed here that the time evolution of the population does not depend on the number

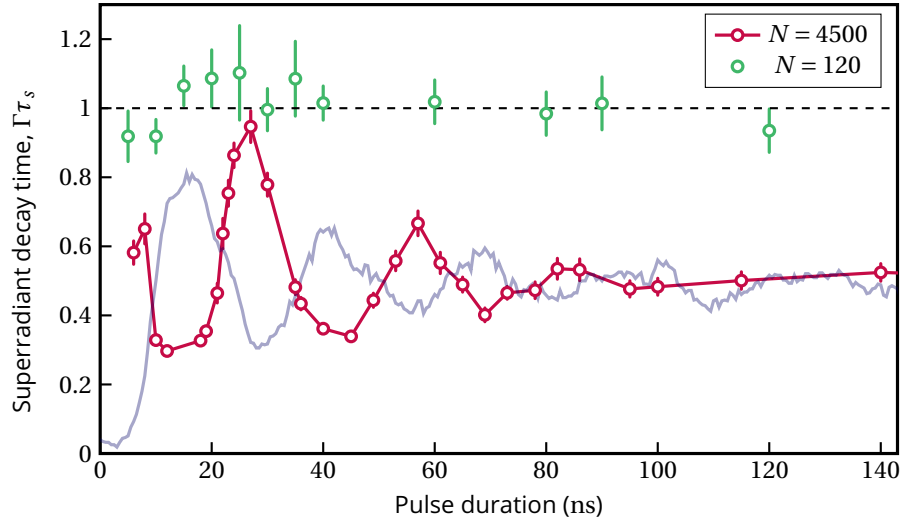


Figure 7.3: Superradiant decay time as a function of the pulse duration for  $N = 120$  atoms (green dots) and  $N = 4500$  atoms (red dots). The fluorescence collected as a function of the time (for  $N = 120$ ) is plotted with an arbitrary scale in transparency of the red dots to show the phase opposition between the two. The horizontal dashed line corresponds to the decay time of a single atom,  $1/\Gamma$  by definition. The vertical error bars are from the fit of the exponential decay of the fluorescence (see text).

of atoms. This assumption is justified by the fact that in the large atom number regime, we have observed both with APD  $\perp$  a response that matches that of a single atom and with APD  $\parallel$  collective oscillations (see figure 7.1). This suggests that the Rabi frequency does not depend on the regime studied, and is therefore independent of the atom number. We will verify this in the next section.

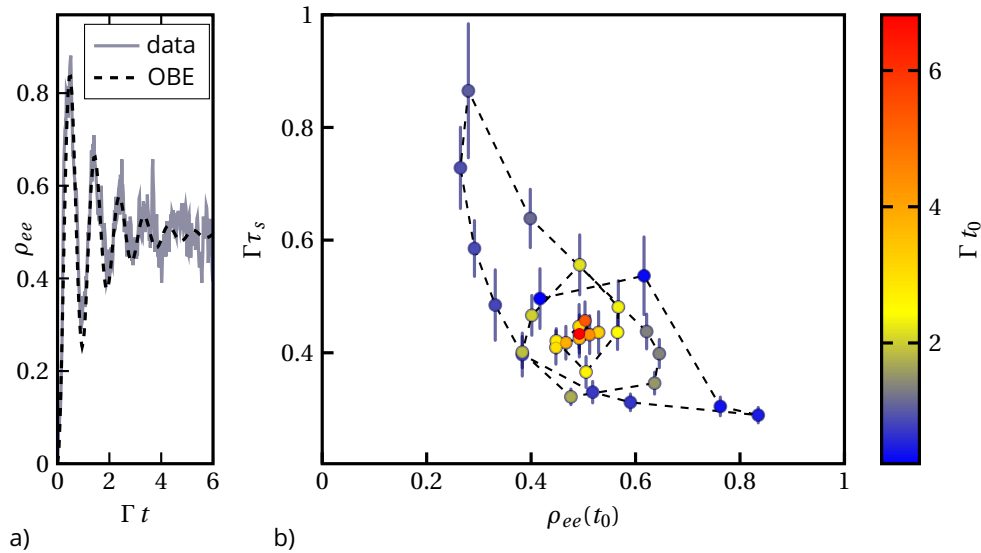


Figure 7.4: a) Fit of the ( $N = 120$ ) trace by the OBE to extract the excited state population  $\rho_{ee}(t_0)$ . b) Superradiant decay time as a function of  $\rho_{ee}$  (for  $N = 4500$ ). The time  $t_0$  is represented by the color.

In figure 7.4, we see that  $\tau_s$  and  $\rho_{ee}$  are correlated, but the data not collapse perfectly. It seems that the decay is faster when the driving stops during a downward slope of the Rabi oscillations than if it stops during an upward slope. In particular,  $\tau_s$  is identical for two equal values of  $\rho_{ee}$  separated by one period of the Rabi oscillations .

## 2.2 Rabi frequency

The next observable we consider is the Rabi frequency  $\Omega$  of the signal measured along the cloud's main axis (where superradiance is observed). Along the radial direction, we recall that the cloud's response is that of a single atom, independently of the atom number. The Rabi frequency is determined by calculating the Fourier transform of the experimental traces during the oscillations, and fitting the obtained peak by a Gaussian function. The results are shown figure 7.5.

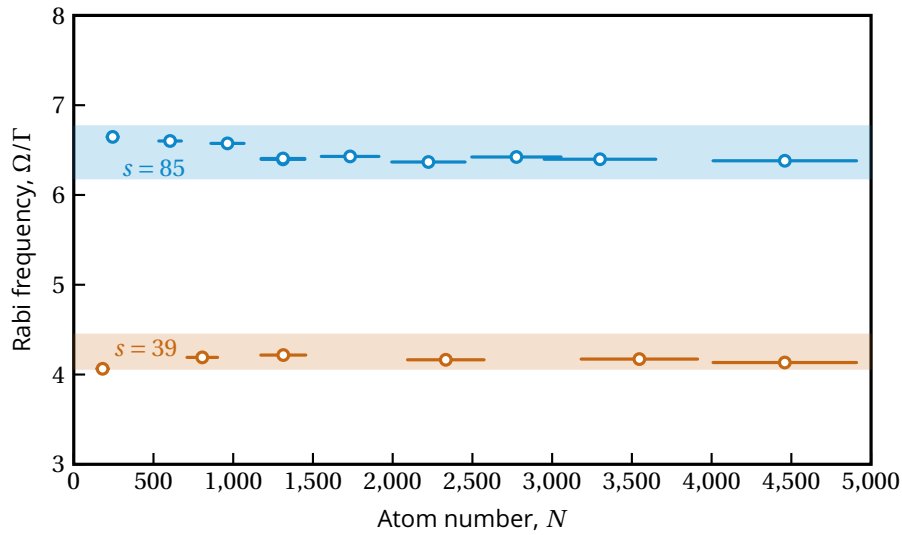


Figure 7.5: Rabi frequency as a function of the atom number, for two driving intensities. The error bars from the fit of the Fourier transform of the data (see text) are smaller than the dots. The shaded area represents the expected value for the single atom Rabi frequency, including the experimental error on the intensity of the excitation beam.

Although we observe a strong enhancement of the amount of light emitted in the axial direction, one sees in figure 7.5 that the measured Rabi frequency is independent of  $N$  within the experimental uncertainty on the excitation intensity. The fact that we also observe unchanged Rabi oscillations in the radial direction seems to indicate that, in our regime, superradiance very weakly modifies the population dynamics. This dynamics is controlled by the timescales hierarchy in our system :  $\Omega \geq \tau_s^{-1} > \Gamma$ , where  $\tau_s$  is the typical superradiance time. As shown in figure 7.5, we did the same measurement at a lower probe intensity ( $s = 39$ ), giving the same result. As we will see later in this chapter, reducing  $s$  here increases  $\tau_s$  (less superradiance), so we have still the timescale hierarchy  $\Omega \geq \tau_s$  even in this case.

In order to explain our observations, we recall that the Dicke model is qualitatively equivalent to imposing a spontaneous decay rate that depends on the population of the excited state:

$$\Gamma_D = \Gamma [1 - a\rho_{ee}(\rho_{ee} - 1)] \quad (2.1)$$

where  $a$  is a parameter related to the strength of superradiance (which dominates if  $a \gg 1$ ). OBEs can be solved with this decay rates.

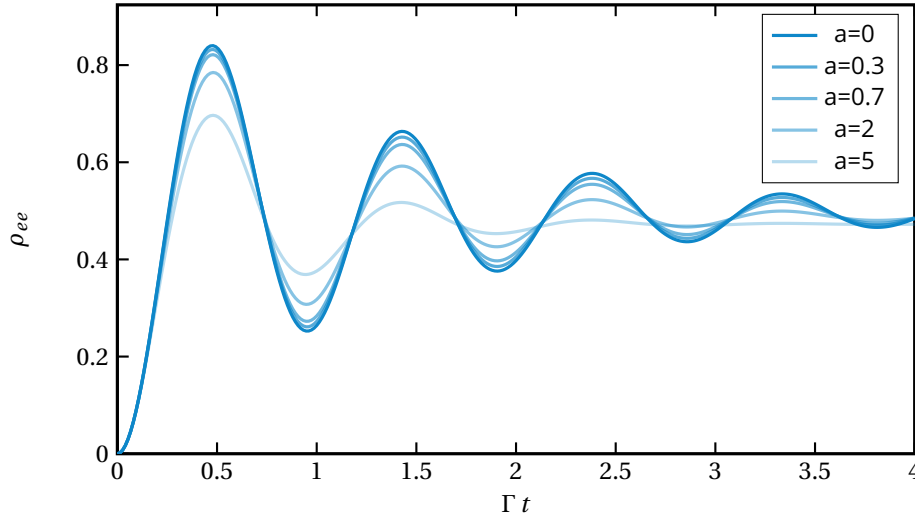


Figure 7.6: Solution of the OBE using the heuristic decay rate  $\Gamma_D$  (equation (2.1)) for various values of  $a$ .

In figure 7.6, one sees that the oscillations are damped when  $a$  increases, but that the Rabi frequency does not change. The argument is that superradiance only affects decay, not driving.

### 2.3 Photon rate in the early decay

The presence of superradiant states should lead to a modification of the photon emission rate just after the end of the driving pulse. To measure the number of excitations stored in the superradiant states, we consider the number of photons collected in the first  $26.4 \text{ ns} = 1/\Gamma$  after the end of the pulse (early decay), as shown figure 7.7.

One sees that the emission rate per atom is strongly enhanced in the large atom number regime, where superradiance occurs. The data of figure 7.7 have been measured along the long axis of the cloud. The enhancement of the photon emission rate in this direction could be related to a diminution in another. To answer this question, F. Robicheaux has performed numerical calculations of the total emission rate (in  $4\pi$ ), using (Robicheaux and Suresh 2021), as reported in figure 7.8. It shows that the scattering rate is effectively enhanced, not redistributed over the space.

Thus, superradiance indeed leads to stronger emission even when driven. However in our case, this effect occurs only in one direction so that the enhancement is weak. It explains why we do not observe a modification of the population dynamics.

### 2.4 Influence of the internal structure

In chapter 5 (section 3.2), we have shown that isolating a two-level system allows us to obtain a good contrast in the Rabi oscillations, which means to have a good control of the internal state of the atoms. We are now interested in the importance of isolating these levels to observe collective oscillations (in the high atomic number regime, where superradiance plays a

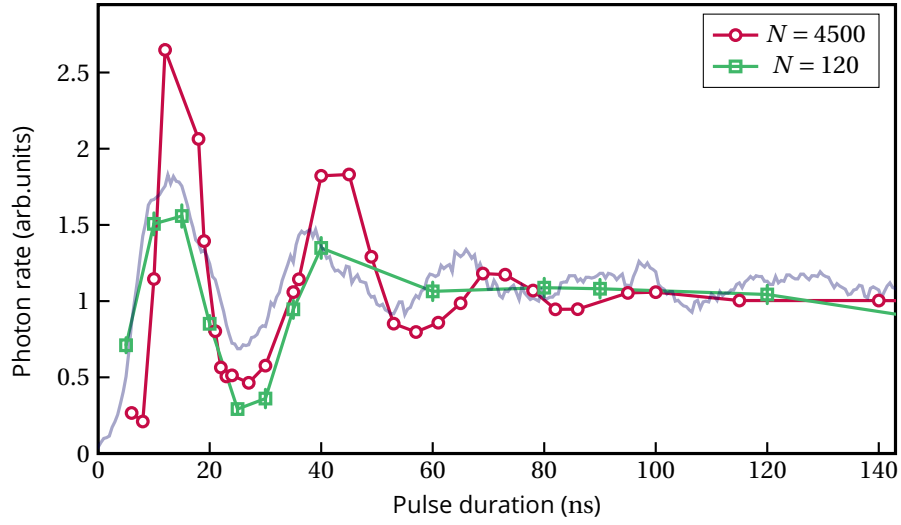


Figure 7.7: Photon number collected along the main ( $\parallel$ ) axis between the end to the pulse and  $1/\Gamma = 26.4\text{ ns}$  after, for  $N = 4500$  and  $N = 120$ . The vertical error bars correspond to the standard errors. Fluorescence during driving ( $N = 120$ ) is shown in transparency with an arbitrary scale.

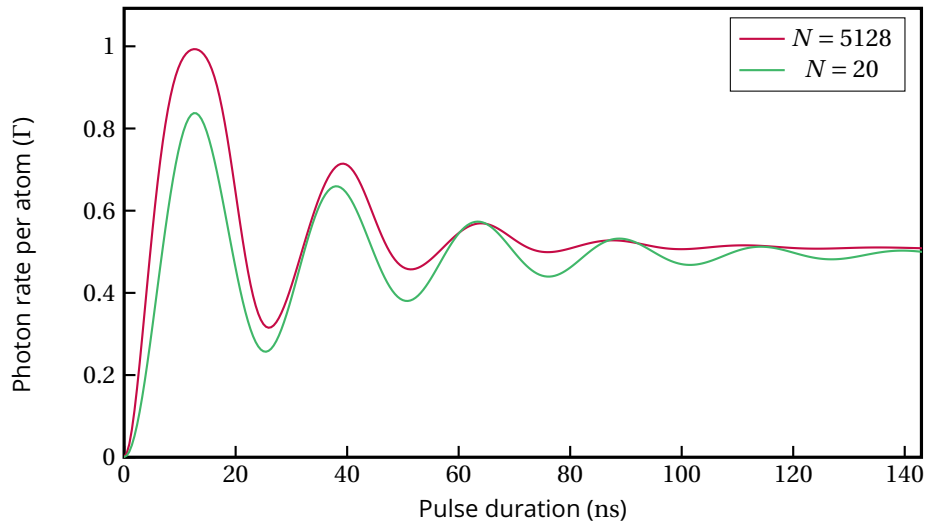


Figure 7.8: Total photon emission rate (in a  $4\pi$  solid angle) per atom, calculated with MF2, for small and large  $N$ .

role). We shine a resonant pulse of light for  $200\text{ ns}$  in the presence or in absence of the  $50\text{ G}$  magnetic field (section 3.2) and we collect the fluorescence emitted by the atoms along the main direction of the cloud. In both situations, we perform optical pumping and the atom number is roughly the same ( $N \sim 6000$ ). In the first case, shown in figure 7.9, the system undergoes Rabi oscillations that are visible for more than  $50\text{ ns} > 1/\Gamma$ . In the second case however, the photons emitted by an excited atom can drive transition to other internal levels. Thus the system possesses different Rabi frequencies and the fluorescence emitted by the cloud is the result of the beat note between them, washing out the oscillations.

The coherence does not seem to depend on the internal structure, as the two curves in

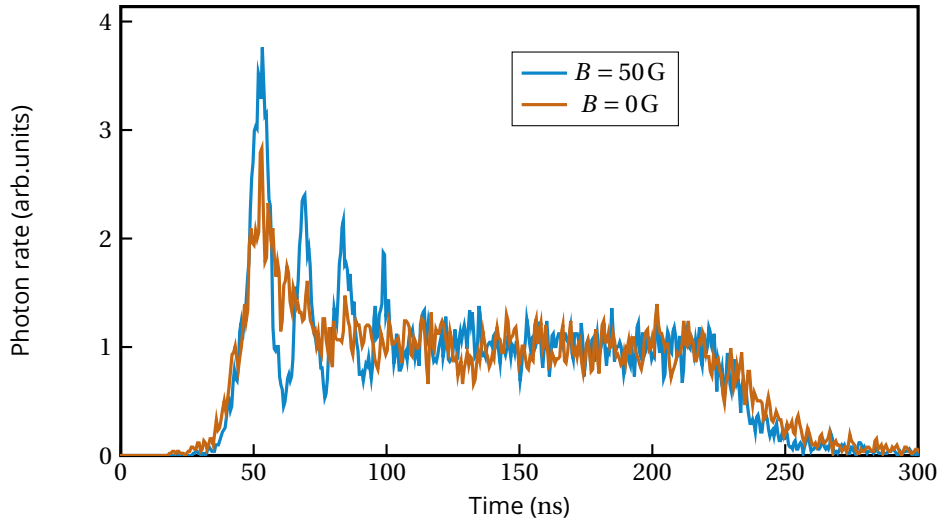


Figure 7.9: Effect of the internal structure on the collective oscillations.

figure 7.9 are damped over the same time scale.

## Conclusion

The observation of the collective oscillations, the decay and the emission rate shows that superradiance takes place in our driven atomic cloud. The resonant drive is strong enough to impose a population inversion, which seems to be the key criterion to generate superradiance during the decay of the excitation, independently of the exact state generated and without any initial coherence in the system. As shown in figure 7.3, superradiance is still observed when the steady state is reached. In the next section, we will characterize more precisely the superradiance in this regime.

## 3 Superradiance in steady-state

### 3.1 Observation of the steady-state superradiance

In the experiments described in this section, the atomic cloud is excited by a 200 ns pulse, which is long enough to reach the steady state of the driven-dissipative regime. Under the approximation that the interactions have no effect ( $\hbar\Omega \gg V_{dd}$ ), we prepare an incoherent mixture described by its density matrix

$$\hat{\rho}_N = \frac{1}{2^N} \bigotimes_i^N (|g_i\rangle\langle g_i| + |e_i\rangle\langle e_i|).$$

After the end of the pulse, we observe that the fluorescence decreases with time. In particular, there is no flash. As shown figure 7.10, we measure the superradiant decay time  $\tau_s$  by fitting the collected photon rate during the first  $26.4 \text{ ns} = 1/\Gamma$  of the decay by an exponential function, where  $\Gamma$  is the single-atom lifetime. The decay is well fitted by a single exponential function over this range. At larger times, the decay is no longer exponential, a signature of subradiance studied in the next chapter.



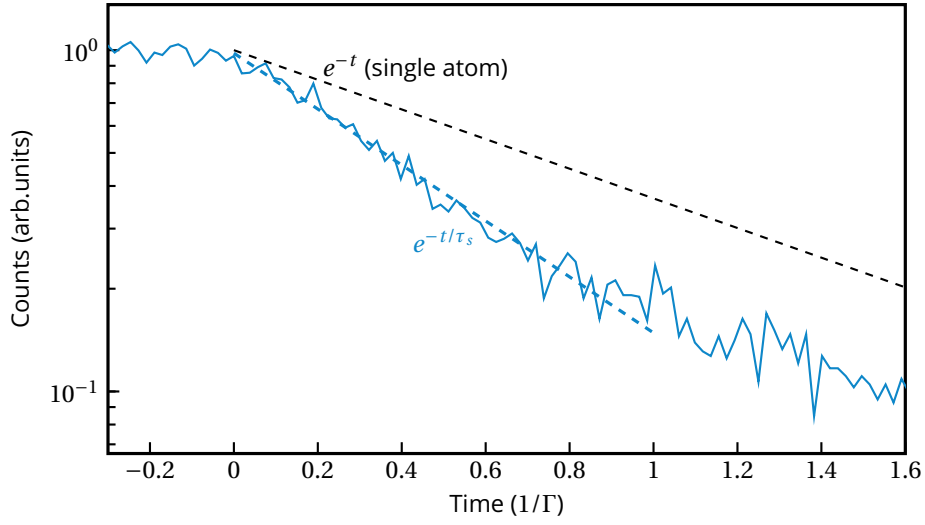


Figure 7.10: Observation of steady-state superradiance and fitting of the superradiant decay time  $\tau_s$ . The atom number is  $N = 4500$  and the origin of times is at the end of the driving pulse.

### 3.2 Directionality

We first study the evolution of the superradiant behavior as a function of the atom number, as shown figure 7.11. As done in section 1.1, we compare the data collected along the cloud's main axis (APD  $\parallel$ ) and perpendicularly to it (APD  $\perp$ ).

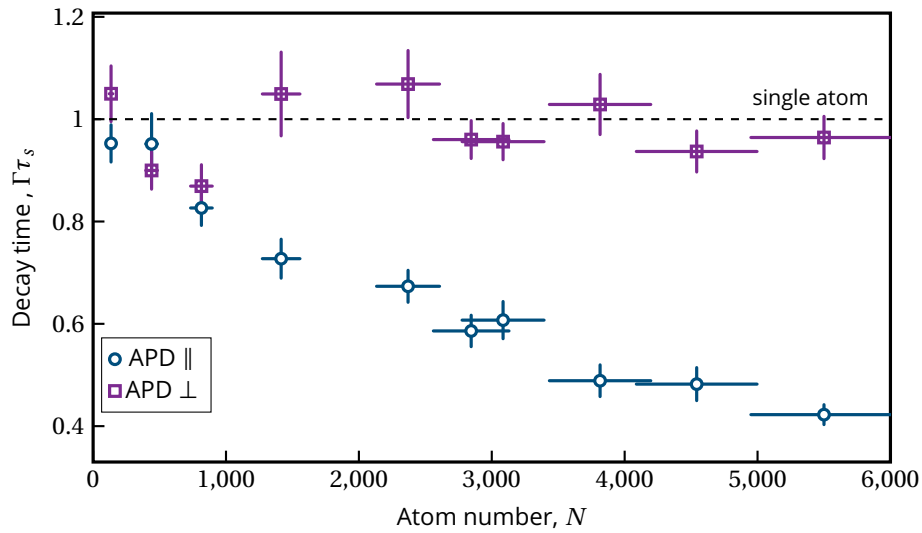


Figure 7.11: Superradiant decay time as a function of the atom number, along the cloud's axis (APD  $\parallel$ ) and perpendicularly to it (APD  $\perp$ ).

As observed before, the cloud behaves as an ensemble of independent atoms when looking radially, but shows superradiance along its axis. The fluorescence decay becomes faster as  $N$  increases.

Let us compare these measurements with those in Figure 6.11, of the decay time after a  $\pi$

pulse. The first thing we see is that in the steady-state case, there is no threshold : superradiance is observed even with a small number of atoms. At first sight, this is surprising because as explained section 1.2, the threshold comes from the geometry of the cloud, which is the same in both cases.

Our observation can be explained by the fact that we have directly populated the superradiant states with the pulse. Indeed, the density matrix  $\hat{\rho}$  can be decomposed in a superradiant and subradiant states. For example, for  $N = 2$ , we have

$$\hat{\rho}_2 = (|gg\rangle\langle gg| + |+\rangle\langle +| + |-\rangle\langle -| + |ee\rangle\langle ee|) / 2$$

where  $|\pm\rangle = \frac{1}{\sqrt{2}}(|ge\rangle \pm |eg\rangle)$  are the 2-atom super and subradiant state.

If we consider the decay time at  $1/e$  of the excitation (as for figure 6.11), we obtain that this time is shorter when starting from the steady-state than when starting from the fully excited state, because in the latter case, the photon rate first increases (flash) before decaying. To illustrate this, we calculate the populations  $\Pi_M$  in the Dicke Ladder (as in chapter 6, section 1.2):

$$\dot{\Pi}_M = \begin{cases} \Gamma_{M+1}\Pi_{M+1} - \Gamma_M\Pi_M & \text{if } -\frac{N}{2} < M < \frac{N}{2} \\ -\Gamma_M\Pi_M & \text{if } M = \frac{N}{2} \\ \Gamma_{M+1}\Pi_{M+1} & \text{if } M = -\frac{N}{2} \end{cases}$$

where  $\Gamma_M = \Gamma \left( \frac{N}{2} + M \right) \left( \frac{N}{2} - M \right)$  is the photon emission rate from the state  $|J = N/2, M\rangle$ . Figure 7.12, we show the total rate of emission

$$W_N = \frac{1}{N} \sum \Gamma_M \Pi_M$$

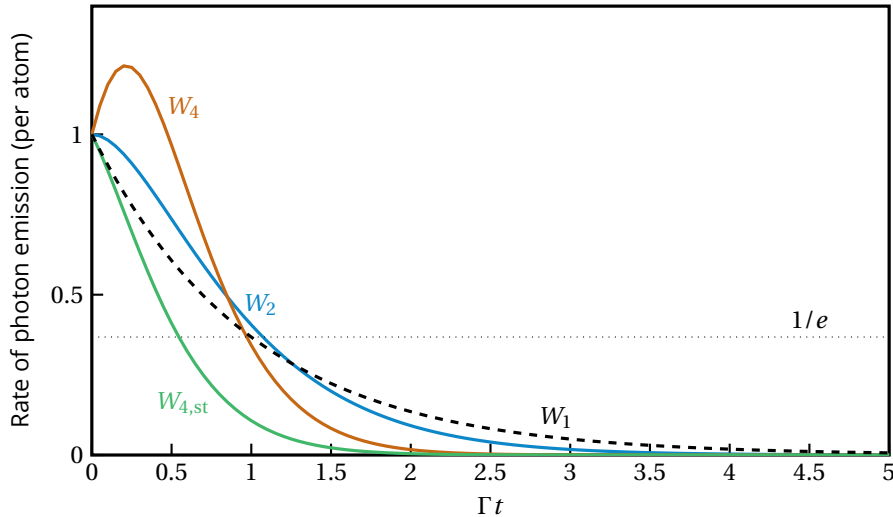


Figure 7.12: Photon emission rate per atom as a function of the time for two-atom superradiance ( $W_2$ ), four atom superradiance ( $W_4$ ), four atom in steady-state ( $W_{4,st}$ ) and for independent atoms ( $W_1$ , dashed line).

for  $N = 4$  starting from a fully excited state ( $W_4$ ) and where all states are equally populated initially ( $W_{4,st}$ ). As shown figure 7.12, the  $1/e$  decay time are close to  $1/\Gamma$  for  $W_4$  and  $W_2$ , but it

is much smaller for  $W_{4,\text{st}}$ . For the steady-state case, as the fluorescence is only exponentially decaying, there is no difference between the 1/2 decay time and the superradiant decay time  $\tau_s$ .

The decay time is also longer than the ones observed in 6.11 at high atom number. This is due to the fact that superradiance depends on the number of excited atoms, and not on the number of atoms present in the trap, as observed in figure 7.3.

### 3.3 Cooperativity parameter

The cooperativity parameter  $C$  is defined as the ratio between the atom number  $N$  and the number of modes efficiently coupled to the system  $M$ . In a sample of finite size  $R$  radiating in free space (in 3D),  $M \propto (kR)^2$  (Guerin, Rouabah, et al. 2017). In an extended cloud, the cooperativity parameter is thus proportional to the on-resonance optical depth  $b_0 = \frac{3N}{(kR)^2}$ . In the Dicke limit,  $R \ll \lambda_0$ ,  $M = 1$  so the cooperativity parameter should be the atom number.

Up to now, we have always considered that the parameter that governs the cooperativity is indeed the atom number. However, our clouds have a finite size and one could suggest that the governing parameter is rather the cloud density

$$n_0 = \frac{N}{(2\pi)^{3/2} \sigma_z \sigma_r^2}$$

as it will be for example in an infinite medium. However, one could notice that the density is a local density and thus cannot render the long-range character of the dipole-dipole interaction. Another possibility could be to define as cooperativity parameter the optical depth

$$b_0 = n_0 \sigma_z \sqrt{2\pi} \sigma_{\text{sc}}$$

as it is in the dilute systems (Guerin, Araújo, et al. 2016), where  $\sigma_{\text{sc}} = \frac{2\lambda_0^2}{2\pi}$  is the resonant scattering cross-section. To determine experimentally what is the cooperativity parameter for our conditions, we acquire three sets of data in three different trapping geometries. We use the same protocol as the one used in section 3.1 to extract the superradiant decay time.

#### Trapping geometries

The three trapping geometries are represented in figure 7.13: the first one has dimensions ( $\sigma_r \simeq 0.7\lambda_0, \sigma_z \simeq 7.7\lambda_0$ ). In the second one, we increase the power of the trapping beam by about 60% to gain a factor 2 in density without losing atoms ( $\sigma_r \simeq 0.5\lambda_0, \sigma_z \simeq 6\lambda_0$ ). To create the third one, we compress the trap using the OptoTelescope (see section 1.4) to obtain a waist  $w_0 = 1.8\mu\text{m}$ . The atom number is reduced ( $N \leq 1500$ ) but the density is large due to the reduced trapping volume ( $\sigma_r \simeq 0.4\lambda_0, \sigma_z \simeq 2.9\lambda_0$ ).

#### As a function of the density

We first show in figure 7.14 the data taken in the three traps, plotted as a function of the peak density  $n_0$ . From trap 1 to trap 3, it is clear that we increase the density for a given atom number (because the volume is reduced).

In the figure above, we see that the density is not a good parameter to describe the superradiance in our system, as the decay can be very different for the same density.

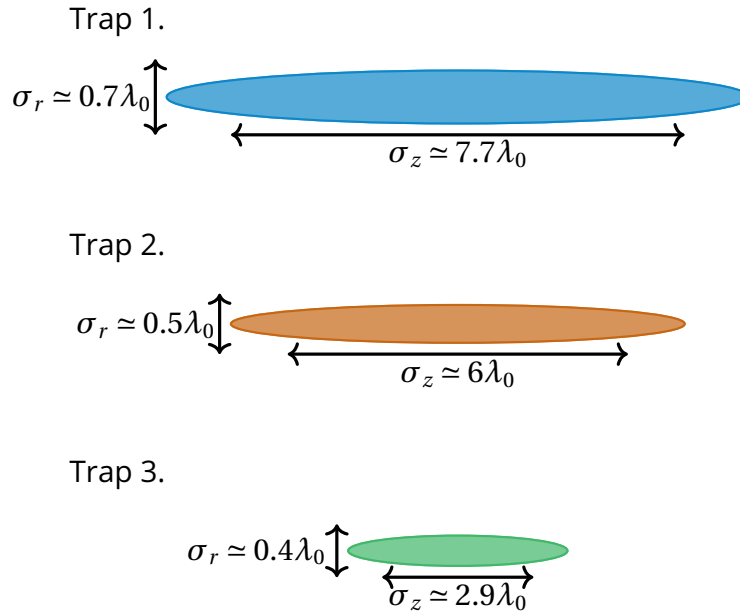


Figure 7.13: Trapping geometries used to determine the cooperativity parameter.

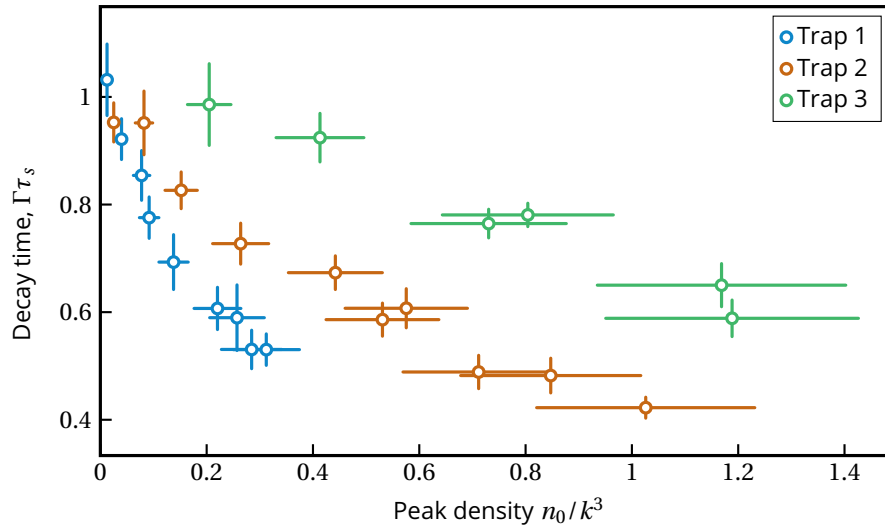


Figure 7.14: Superradiant decay time as a function of the peak density, for the three trapping geometries.

### As a function of the optical depth

We then plot the same data but now as a function of the optical depth, which is the relevant quantity in extended dilute clouds (Araújo, Krešić, et al. 2016). In figure 7.15, one can see that the optical depth is not the good parameter either.

### As a function of the atom number

As shown in 7.16, the data nearly collapse when plotted as a function of the atom number, which is thus the parameter governing the collective properties.

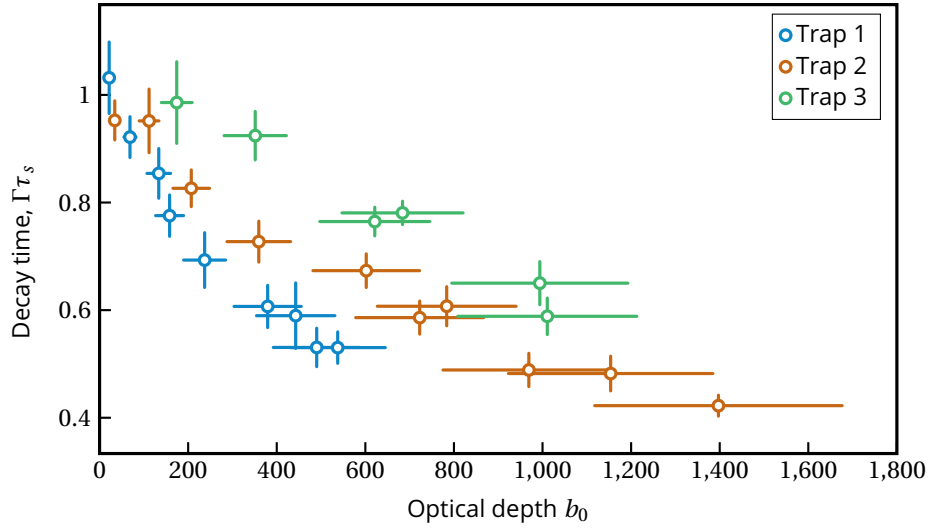


Figure 7.15: Superradiant decay time as a function of the optical depth, for the three trapping geometries.

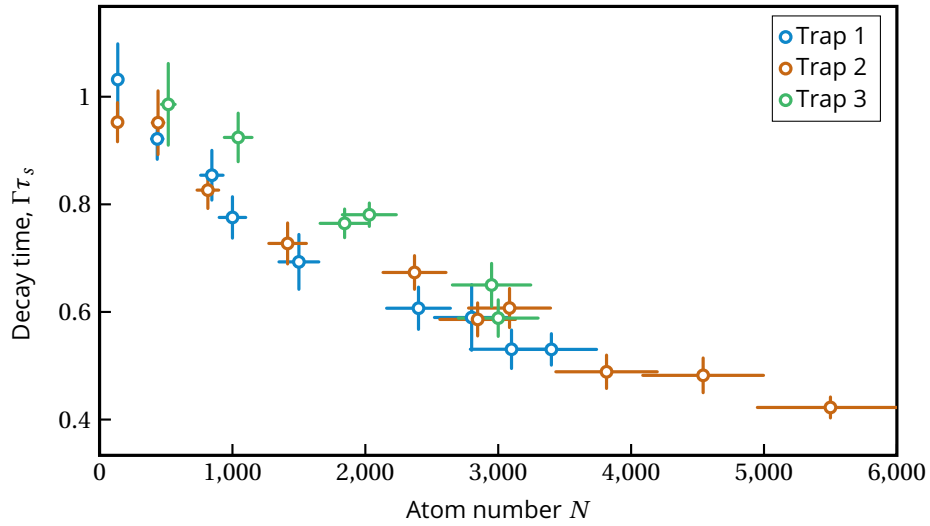


Figure 7.16: Superradiant decay time as a function of the atom number, for the three trapping geometries.

This validates the fact that our system approaches the Dicke limit. The imperfect collapse of the experimental data in figure 7.16 might be due to the fact that our system is still larger than  $\lambda_0$ .

We have performed the same analysis for the peak over steady-state value (peak amplitude of the Rabi oscillation divided by the steady-state value of the fluorescence) with the same result, as shown figure 7.17. It indicates that the collective driven regime is also governed by the atom number in the cloud. Moreover, there is no visible threshold, in agreement with the discussion section 3.1.

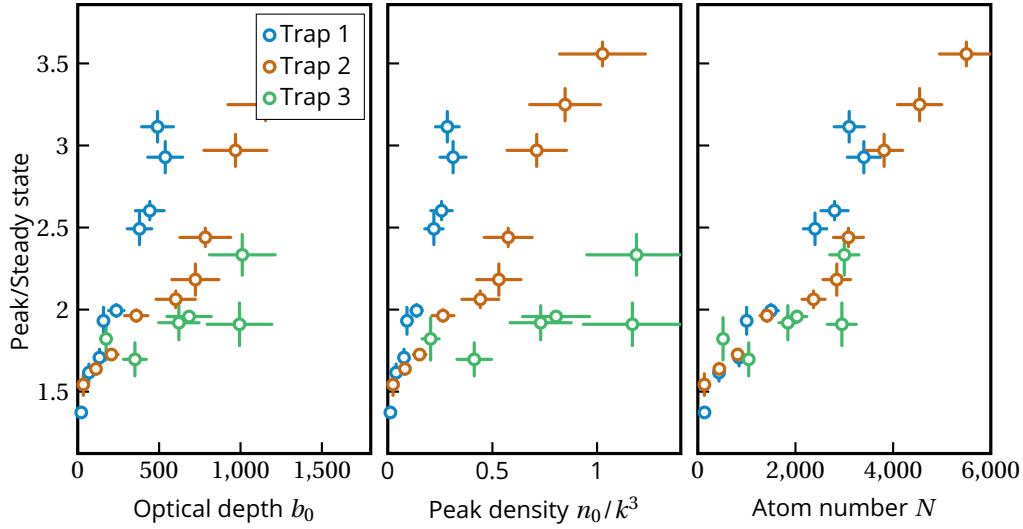


Figure 7.17: Peak over steady-state as a function of  $b_0$ ,  $n_0$  and  $N$ , for the three trapping geometries. The vertical error bars represent the standard error in the estimation of the steady state.

## 4 Superradiance as a function of the probe intensity

In this section, we investigate the influence of the probe intensity on the coherent dynamics. For this study, we use the trap number 2 (see figure 7.13), containing 6000 atoms. We scan the saturation parameter  $s = \frac{I}{I_{\text{sat}}}$  between  $s \approx 0.1$  and  $s \approx 200$  with a 10% shot-to-shot uncertainty (which gives the horizontal error bars in figures 7.18). For all the measurements below (as before), the cloud is excited using a resonant probe with polarization  $\sigma_-$  and the fluorescence is collected with the APD  $\parallel$  along the cloud's main axis, as presented in figure 1. We now use a 200 ns pulse, which is long enough to reach the steady state.

### 4.1 Peak over steady-state

The first observable for the system dynamics is the peak over steady-state value. As shown before, this value measured along the axial direction is related to the interplay between superradiance and driving. For  $s \leq 5$ , the system does not show any oscillation and the peak over steady-state ratio is thus equal to 1.

When the intensity increases, the ratio becomes very different from that expected for a single atom (solution of the Optical Bloch Equations), which is shown with a dashed line in figure 7.18. The observed behavior could be explained by the fact that the collective response depends on the atom number  $N$  (as shown figure 7.2) and more precisely on the number of excited atoms in the system (figure 7.3). In the low intensity regime, the fraction of atoms in the excited state is negligible and thus the system does not manifest any superradiant flash. Conversely, as the driving strength increases, the number of atoms in the excited state grows and the system enters in the superradiant regime, showing a large enhancement in the photon emission rate.

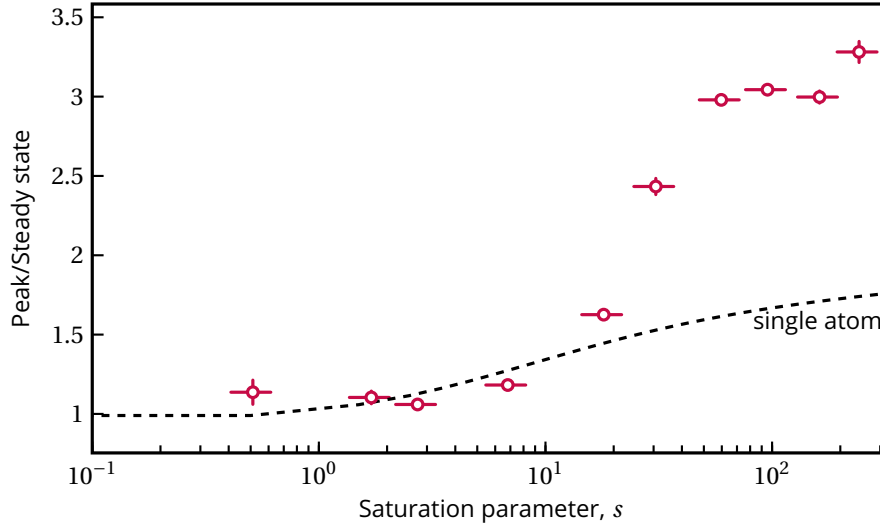


Figure 7.18: Peak over steady-state as a function of the saturation parameter  $s = \frac{I}{I_{\text{sat}}}$ . The vertical error bars are the standard error in the estimation of the steady state. The dashed line is the solution of the OBE (for a single atom).

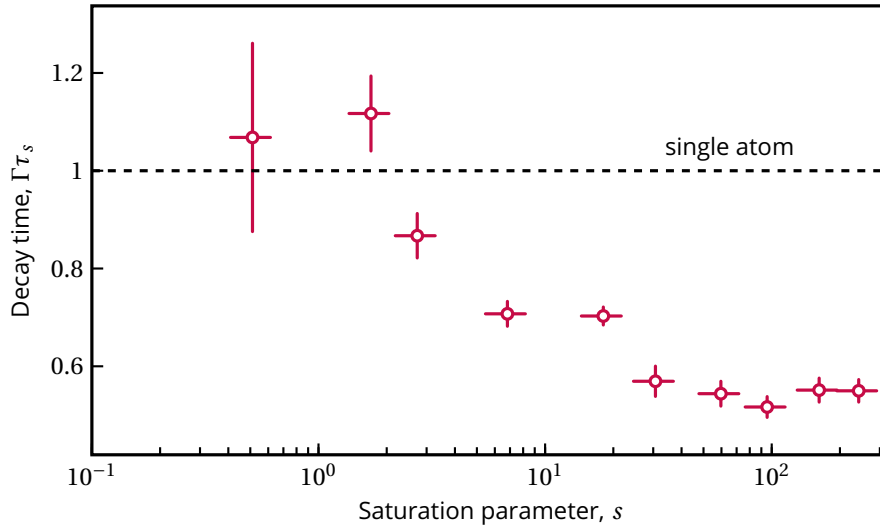


Figure 7.19: Decay time as a function of the saturation parameter  $s = \frac{I}{I_{\text{sat}}}$ , after steady-state. The dashed line is the solution of the OBE (for a single atom).

## 4.2 Decay time

A direct signature of superradiance is in the decay time, after the end of the pulse. As we have observed in section 3.1, the superradiant states are populated when the system has reached its steady state. When increasing the number of excitations, one expects to populate more superradiant states so for the decay time to become shorter. We use the same analysis protocol than in section 3.1, with an exponential fit of the decay after the end of the pulse.

In figure 7.19, we indeed observe that the superradiant behavior increases (the decay time decreases) when increasing the probe intensity. In this figure, we cannot determine if the superradiance has a threshold, that is if a minimum number of excitation is needed.

However, one can see a saturation at high intensity, which indicates that the population of the superradiant states saturates.

### 4.3 Steady-state fluorescence

In order to study more precisely the saturation, we plot in figure 7.20 the steady-state fluorescence averaged over 50 ns for different saturation parameters.

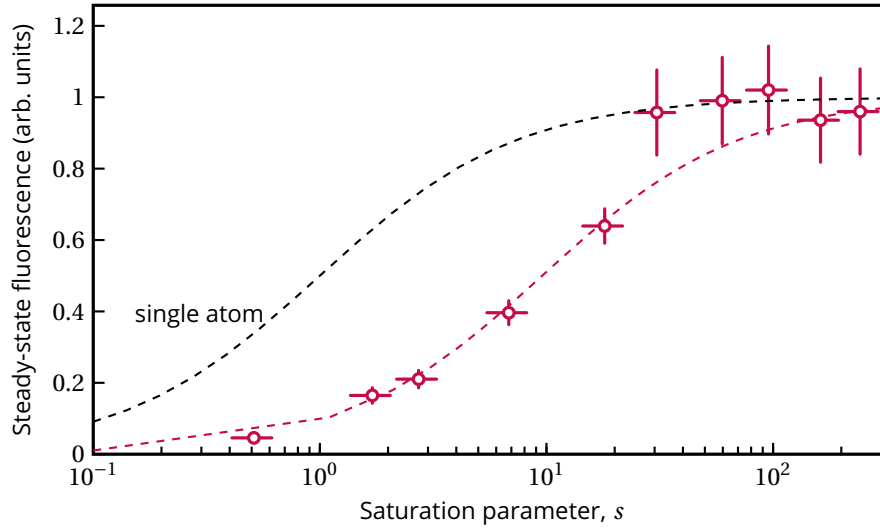


Figure 7.20: Steady-state fluorescence as a function of the saturation parameter  $s = \frac{I}{I_{\text{sat}}}$ . The black dashed line is the single atom behavior, the red dashed line is a phenomenological fit of the data.

In general, the excited state cannot be expressed as a superposition of single-atom excited states. However, a phenomenological fit with the function  $\alpha s / (1 + \alpha s)$  gives an acceptable agreement.  $\alpha = 1$  is the single-atom case, represented with a black dashed line in figure 7.20. We observe that the system saturates at larger intensity,  $\alpha = 0.19 \pm 4 < 1$ , showing that the single atom transition is broadened by superradiance. Indeed,  $\alpha < 1$  means that the saturation intensity is larger than that of a single atom,  $I_{\text{sat}}^s > I_{\text{sat}}^s$ . This implies that  $\Gamma_s \Gamma$ . This conclusion is in agreement with the observation (fig. 7.7) and the simulation (fig. 7.8) that superradiance allows to emit more photons than independent atoms.

## 5 Conclusion

In this chapter, we have observed laser driven collective oscillations and their properties of directionality, enhanced photon emission rate, Rabi frequency and the influence of the internal structure. We have shown that superradiance takes place in our system and is revealed by the light emitted along the axis. In the second part of this chapter, we have explored the steady-state regime. The presence of superradiance also in this case, parametrized by the atom number, suggests that it is based on the population of the excited state rather than on the precise state in which the system is cast. The last part of the chapter was devoted to the effect of the driving intensity, confirming that the number of excitation in the system is the parameter that governs the superradiant dynamics.



# Storage and Release of subradiant excitations

\*\*\*

In the previous chapters, we have studied superradiance in our dense cloud, i.e the decay of excitations at a rate faster than the single-atom one. This chapter is devoted to the study of its counterpart, the subradiance. Most of the results are published in (Ferioli, Glicenstein, Henriët, et al. 2021).

Subradiance has been much less observed than superradiance because of the weak coupling of the subradiant states to the environment, but direct observations were reported in a pair of ions (Devoe and Brewer 1996), in molecular systems (Takasu et al. 2012; McGuyer et al. 2015), in dilute atomic cloud (Guerin, Araújo, et al. 2016) and as a line-narrowing in an ordered 2D layer of atoms (Rui et al. 2020). Recently, the subject has regained interest in the context of quantum technologies. Indeed, it has been proposed for example to use sub-radiant states as a storage medium (Facchinetti, Jenkins, et al. 2016; H. H. Jen et al. 2020; Asenjo-Garcia et al. 2017) or as a tool for quantum information processing (Shahmoon et al. 2017) and for metrology (Plankensteiner, Ostermann, et al. 2015; Krämer, Ostermann, et al. 2016).

In this chapter, we observe subradiance in a steady-state cloud operating near Dicke's regime. Varying the number of excitations in the system, we will then characterize the multiply-excited subradiant states, with a slower decay rate than the single atom one, but with more than one photon stored. Motivated by the possibility of using subradiant states as a light storage medium, we will then demonstrate a protocol for storing and on demand releasing subradiant excitation. Finally, we will study how the long-lived states are populated, exploring the Dicke ladder.

As in chapters 6 and 7, unless explicitly stated, each measurement presented in this chapter was performed using the configuration shown in Figure 1.

## Contents

<b>1</b>	<b>Observation of subradiance</b>	<b>143</b>
1.1	Directionality	143
1.2	Nonlinear coupled dipoles (NLCD) simulations	144
1.3	Detuning	144
1.4	Polarization and internal structure	146
<b>2</b>	<b>Subradiance near Dicke's regime</b>	<b>146</b>
2.1	Tail ratio	146

2.2	Cooperativity parameter . . . . .	147
2.3	Fitting procedure . . . . .	148
2.4	Subradiant lifetime . . . . .	149
<b>3</b>	<b>Study of multiply-excited subradiant states . . . . .</b>	<b>150</b>
3.1	Single mode approximation . . . . .	150
3.2	Limits of NLCD . . . . .	152
<b>4</b>	<b>Release of subradiant excitations . . . . .</b>	<b>154</b>
4.1	Release of light stored in subradiant excitations . . . . .	154
4.2	Two dipoles toy model . . . . .	154
4.3	Experimental demonstration . . . . .	155
4.4	Analysis using eigenmodes and NLCD simulations . . . . .	156
4.5	Role of internal structure and magnetic field . . . . .	157
<b>5</b>	<b>Exploring the Dicke ladder : population of the long lived-states from the superradiant states . . . . .</b>	<b>159</b>
5.1	Decay time . . . . .	160
5.2	Photon in the late decay . . . . .	160
5.3	Master equation . . . . .	162
<b>6</b>	<b>Conclusion . . . . .</b>	<b>164</b>

---

## 1 Observation of subradiance

For all the measurements presented in this chapter, we use the configuration represented in figure 1. A high-intensity 200 ns pulse of resonant light is sent on the cloud, reaching the steady-state ( $I/I_{\text{sat}} \sim 27$ ). The main difference with the experiments described in the previous chapters is that the experimental signal we now consider is very small. Indeed, as we will see later in this chapter, only about 10% of the excitations remain in the long-lived states. Even with the largest atom number and at high intensity, given that we collect typically 0.01 photon per pulse in a 1 ns bin in steady-state, we need to repeat many times the sequences to obtain sufficient signal. We repeat the same sequence up to 20 times on the same cloud (with less than 10% of atom losses), repeating the experiment from 3000 to 10000 clouds depending on the atom number. The experimental rate is 2 Hz, it therefore takes about an hour to acquire each trace shown in this chapter.

We now consider the fluorescence emitted by the cloud after the end of the pulse. In figure 8.1, we plot the counts recorded by the APD along the cloud's main axis (APD  $\parallel$ ).

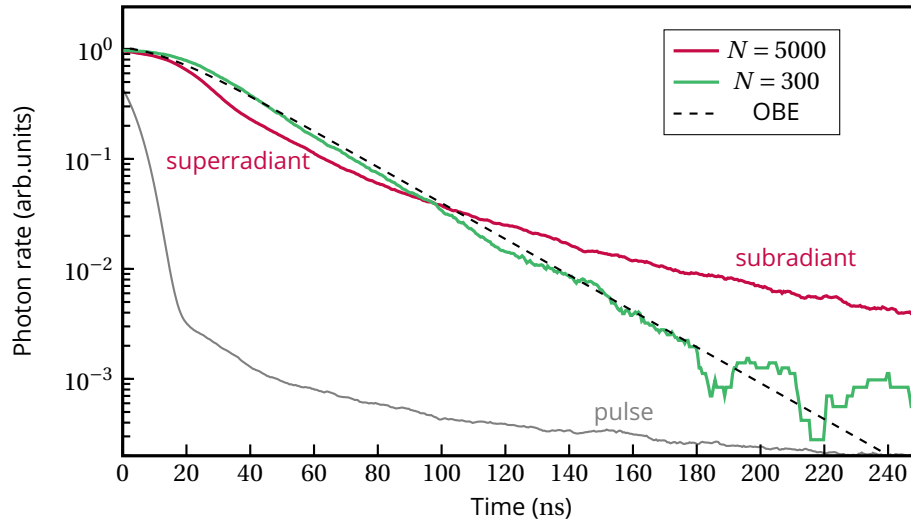


Figure 8.1: Photon rate as a function of time, recorded along the trap axis (APD  $\parallel$ ). In the low atom number regime, the cloud is well modeled by the optical Bloch equations (OBEs, dashed line). In the large atom number regime, one observes first a superradiant behavior and then a subradiant behavior. All curves have been normalized to their steady-state value (before the end of the pulse).

We have shown in chapter 7 (section 1.1) that in this case, if the atom number is large enough, we observe superradiance, that is a decay faster than that of a single atom (given by the Optical Bloch Equations). At later time, we observe a subradiant regime, where the decay is slower than that of a single atom. To show that the long-lived decay is not due to some residual driving, we plot the pulse used and the solution of the optical Bloch equations (OBE) for this pulse in the same figure.

### 1.1 Directionality

As for superradiance (section 1.1), we study the directionality of the subradiant emission in our system exploiting the two high-resolution imaging axes. In the case of superradiance, it

had been observed that it took place only in the main (long) direction of the cloud, imposed by its geometry. In figure 8.2, we see that subradiance is observed in both directions.

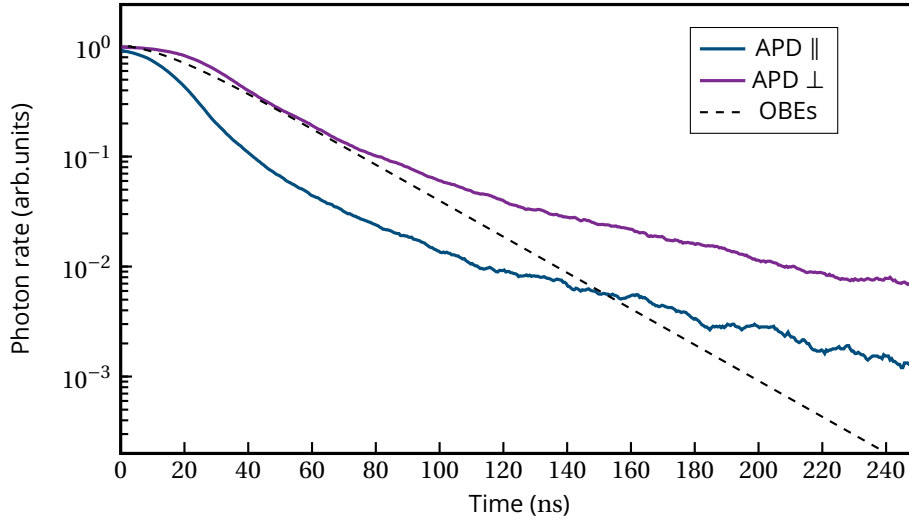


Figure 8.2: Time traces collected using APD  $\parallel$  (along the cloud's axis) and perpendicularly (APD  $\perp$ ). The dashed line shows the solution of the OBE. All curves have been normalized to their steady-state value (before the end of the pulse).

Moreover, the subradiant decay is isotropic (the slopes during the late decay are the same along the two observation directions). This shows that superradiance and subradiance are by nature different phenomena.

## 1.2 Nonlinear coupled dipoles (NLCD) simulations

In chapter 6, we have seen that superradiance results from the correlations between the dipoles. In particular, a classical simulation of nonlinear coupled dipoles (NLCD) as presented in section 2.2 (we are interested here in the strong driving regime so we must take into account the saturation of the atoms) does not show superradiance. However, this model qualitatively reproduces our experimental data on subradiance.

To illustrate this, we show in figure 8.3 a NLCD simulation in an ensemble of 200 atoms with density  $n_0 = 0.3k^3$ , under a resonant excitation of intensity  $s = I/I_{\text{sat}} \simeq 27$ , after the end of the driving pulse (which is long enough to reach the steady state). This situation reproduces our experimental conditions. The result is close to the one observed in figure 8.2, when observing radially (APD  $\perp$ ). At short time, we observe a bit of superradiance (because  $s$  is not much larger than 1), but the behavior is mostly compatible with OBEs. At later time, we observe a slow decay.

## 1.3 Detuning

The slow decay of the excitation might be due to radiation trapping rather than subradiance. In this phenomenon, photons are absorbed and then re-emitted spontaneously a large number of times by the medium in random directions, which results in a diffusion of photons following a random walk (Labeyrie et al. 2003). Contrarily to subradiance, this multiple-scattering effect depends strongly on the detuning (Guerin, Araújo, et al. 2016). We have thus acquired

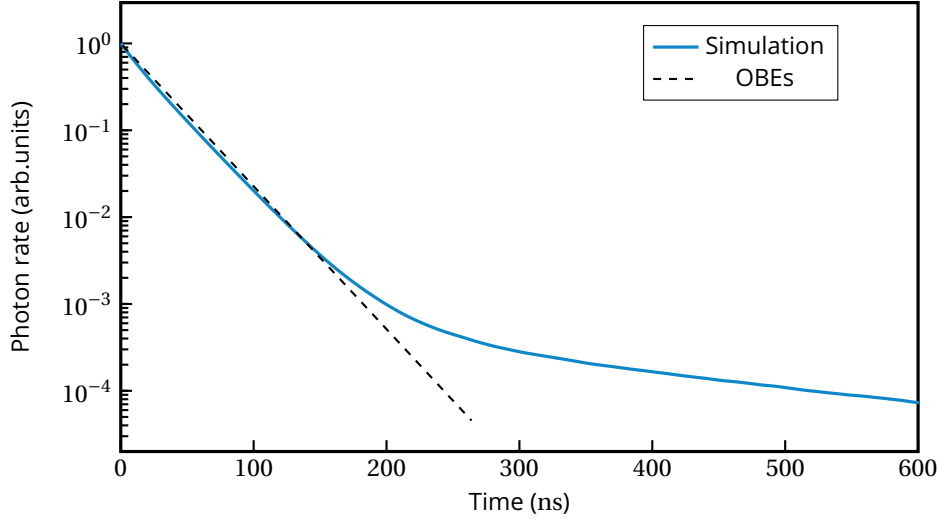


Figure 8.3: NLCD simulation of an ensemble of 200 atoms with density  $n_0 = 0.3k^3$ , under a resonant excitation of intensity  $s = I/I_{\text{sat}} \simeq 27$ , after the end of the driving pulse. Black dashed line : solution of the OBE.

sets of data for various detuning of the excitation laser. In figure 8.4, we report these measurements at resonance ( $\Delta = 0$ ) and for detunings of  $\Delta = +\Gamma$  and  $\Delta = +3\Gamma$ .

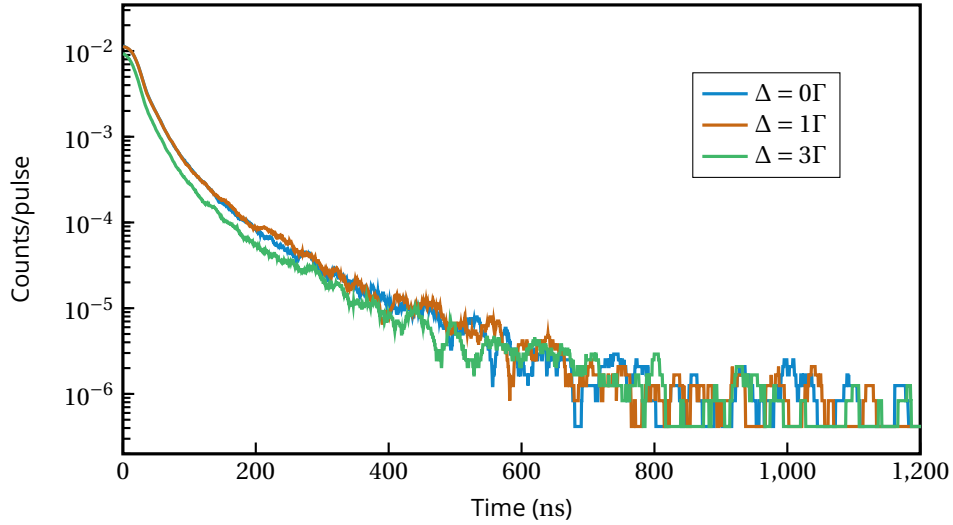


Figure 8.4: Photon count traces as a function of the driving frequency for  $\Delta = 0$ ,  $\Delta = \Gamma$  and  $\Delta = 3\Gamma$ .

As the detuning increases, a reduction in fluorescence is observed, but the slope of the decay does not depend on frequency. This demonstrates experimentally that we observe subradiance and not radiation trapping.

Note that the radiation trapping hypothesis was not really plausible in our conditions anyway: considering the scattering mean-free path  $l_{\text{sc}} = 1/(n_0\sigma_{\text{sc}})$ , with  $n_0$  the peak density and  $\sigma_{\text{sc}} = \frac{3\lambda_0^2}{2\pi}$  the resonant cross-section. In our dense clouds,  $n_0/k^3 \sim 1$  so  $l_{\text{sc}}$  is much smaller than the average interatomic distance  $\bar{l} = \frac{\lambda_0}{2\pi}$ , so the picture of photons scattering randomly

from atom to atom therefore does not hold.

In the rest of this chapter, we have performed all measurements on resonance.

## 1.4 Polarization and internal structure

Unless otherwise specified, subradiance measurements have been performed with a linearly polarized light and without any optical pumping. One may wonder how the polarization and multi-level structure impacts subradiance. We compare the case where the polarization is linear with the case where we isolated a two-level transition by applying a magnetic field of 20G and using a  $\sigma_-$  polarization. As seen in chapter 2 (section 3.2), this allows us to isolate a closed two-level transition, the other transitions being detuned by more than  $5\Gamma$ .

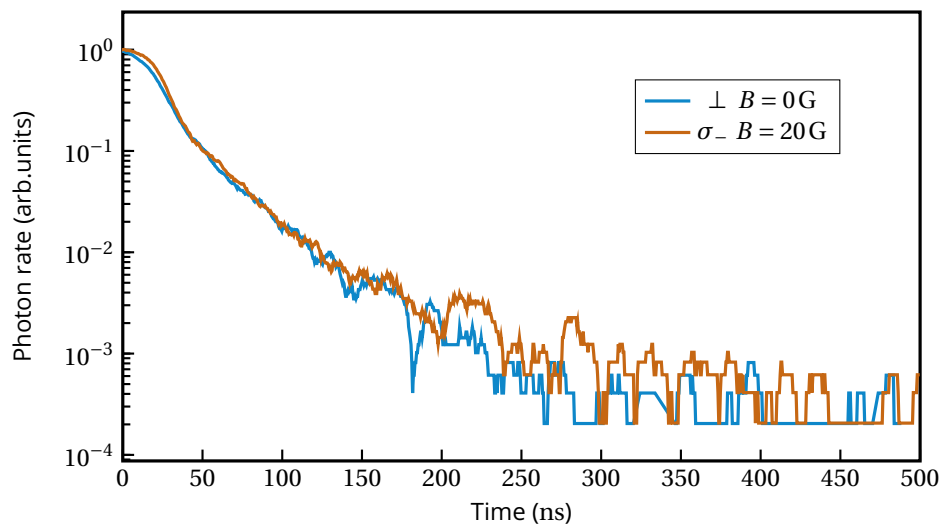


Figure 8.5: Photon count decay with : linear polarization, no magnetic field (multi-level) in blue. In orange :  $\sigma_-$  polarization and 20G magnetic field (two-level). The traces have been normalized to the steady-state value, at  $t=0$ .

In figure 8.5, we observe that the traces are very similar in the late decay (this is not the case in the early superradiant decay). We conclude that the internal structure does not play a role within our dynamic range of observation.

## 2 Subradiance near Dicke's regime

In this part, we characterize the subradiance observed in our clouds. These clouds have a prolate shape, with a radial dimension smaller than the wavelength ( $\sim 0.5\lambda$ ) and an rms axial dimension of about  $5\lambda$ . We thus approach Dicke's regime, in which many emitters are trapped in a volume comparable to the wavelength of the transition. Our observations thus amount to the first observation of subradiance near Dicke's regime.

### 2.1 Tail ratio

To quantify subradiance, we first introduce the *tail ratio* as a relative fluorescence observed in the long-lived tail relative to the total fluorescence recorded after the end of the pulse:

$$TR = \frac{\int_{4/\Gamma}^{\infty} I(t) dt}{\int_0^{\infty} I(t) dt}$$

where  $I(t)$  is the time-resolved fluorescence emitted after the end of the pulse ( $t = 0$ ). This parameter estimates the fraction of excitation hosted in the cloud  $4/\Gamma \simeq 100$  ns after the switching off. For a single atom, the tail ratio would be equal to  $e^{-4} \simeq 2\%$ .

## 2.2 Cooperativity parameter

In the same way as in section 3.3 for the study of superradiance, we determine the parameter that governs the collective effects during the late decay. For this purpose, we use the three trap geometries presented in section 3.3 and figure 7.13. We vary the number of atoms (which is the cooperativity parameter for superradiance, see previous chapter) for these three geometries. In figure 8.6, we show the tail ratio as a function of the atom number. The inset recalls the trapping geometries.

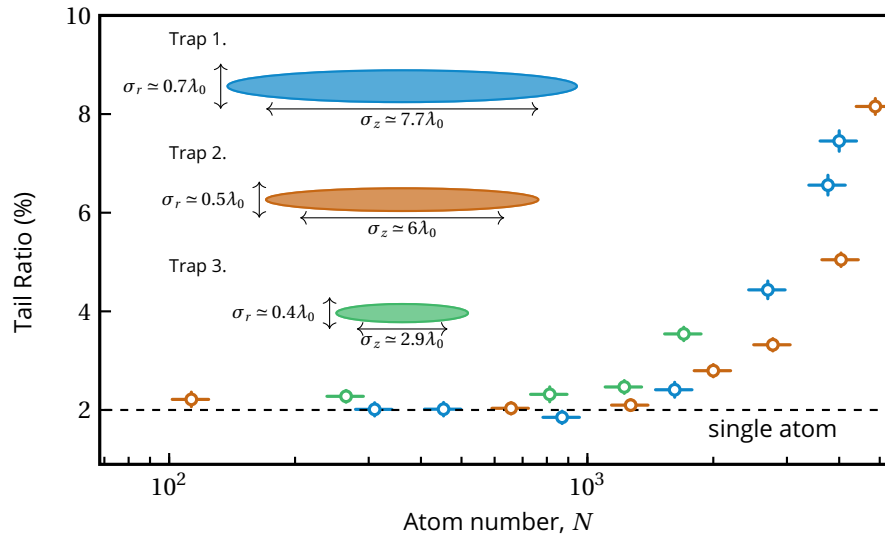


Figure 8.6: Tail ratio as a function of the atom number for the three trapping geometries represented in the inset. The single atom TR value is shown with the dashed line. Colors correspond to the trapping geometries.

In figure 8.6, we see that the data collapse as a function of the atom number, which means that  $N$  seems to be the governing parameter. The agreement is not perfect probably due to the fact that the clouds are larger than  $\lambda$  in the axial direction. We are thus not perfectly in Dicke's regime, as observed for superradiance (section 3.3). However, the fact that subradiance is nearly governed by the atom number shows that we approach Dicke's regime.

As we did for superradiance (figures 7.14 and 7.15), we then plot the same data as a function of the peak density  $n_0 = \frac{N}{(2\pi)^{3/2} \sigma_z \sigma_r^2}$  and of the optical depth  $b_0 = n_0 \sigma_z \sqrt{2\pi} \sigma_{sc}$ . We see in figure 8.7 that the data do not collapse as a function of  $n_0$  or  $b_0$ , indicating that  $N$  is indeed the cooperativity parameter. Looking at figure 8.6, it appears that subradiance is observed when the number of atoms is large enough, similarly to superradiance in inverted system described in previous chapters.

One also observes that up to 10% of the excitations are stored in the long-lived states. For

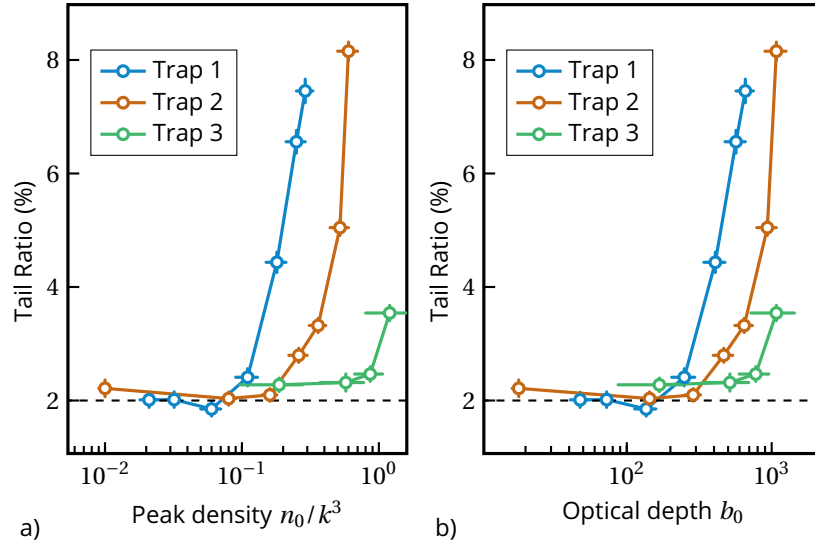


Figure 8.7: Tail ratio as a function of a) peak density  $n_0$  b) optical depth  $b_0$  for the three trapping geometries. The single atom TR value is shown with the dashed line.

$N = 5000$  and a fully-saturated cloud (1/2 excitation per atom). This corresponds to several hundreds of excitations.

In order to study subradiance quantitatively, we will now detail the procedure we used to extract the subradiant lifetime  $\tau_{\text{sub}}$ .

### 2.3 Fitting procedure

In this section we provide more details about the fitting procedure used to analyze the experimental data. Two regimes of decay can be distinguished. When the number of atoms is smaller than the threshold, the decay is qualitatively exponential. Above the threshold, we fit the decay by the sum of two exponential functions. As an example, we show in figure 8.8, panel a) an example of decay in the regime of low atom number (under the threshold, here  $N \sim 300$ ) fitted by a single exponential. On panel b), we show an example in the regime of the large number of atoms. The decay is obviously not exponential. We use the two-exponential model, which gives the characteristic times of superradiance and subradiance.

In order to discriminate the fitting regime, we calculate the mean square distance to a single exponential fit:

$$\chi^2 = \frac{1}{K_{\text{bin}}} \sum_i \frac{(N_{\text{fit}}(t_i) - N_i)^2}{N_{\text{fit}}(t_i)}$$

where  $K_{\text{bin}}$  is the number of time bins in the data set,  $N_i$  is the number of counts recorded during the bin centered on time  $t_i$  and  $N_{\text{fit}}(t_i)$  is the value of the fitting function at this time. This definition assumes a poissonian distribution of the counts in each bin. We take as a criterion that if  $\chi^2 > 1$ , the fit no longer corresponds to the model and we must use the sum of the two exponential functions to reproduce the dynamics.

Figure 8.9, we plot  $\chi^2$  as a function of the number of atoms. For the geometry of the trap used here, we see that subradiance appears for a number of atoms higher than about 1500.



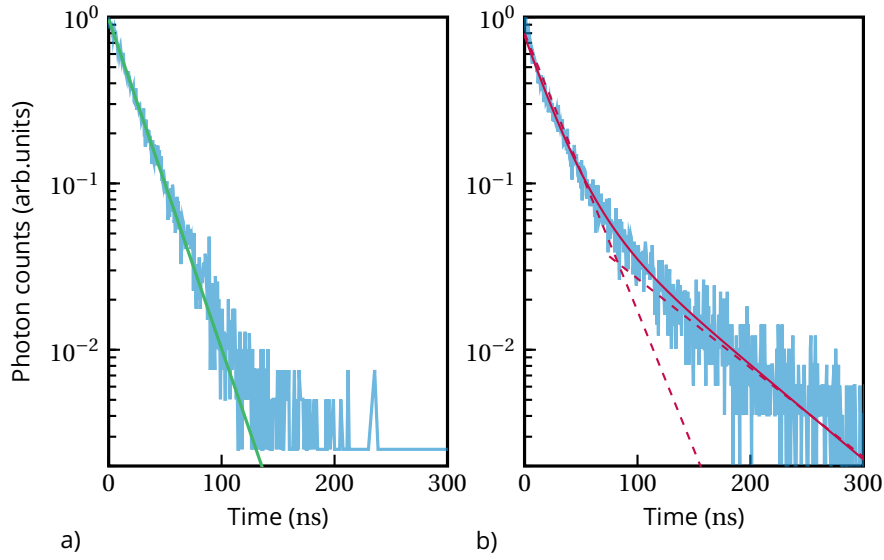


Figure 8.8: a) Example of decay in the small atom number regime ( $N \approx 300$ ) fitted by a single exponential decay. b) Example of decay in the large atom number regime ( $N \approx 4500$ ) showing superradiance and subradiance. The solid line is the phenomenological fit with the sum of two exponential functions, and the dashed lines are the extreme regimes.

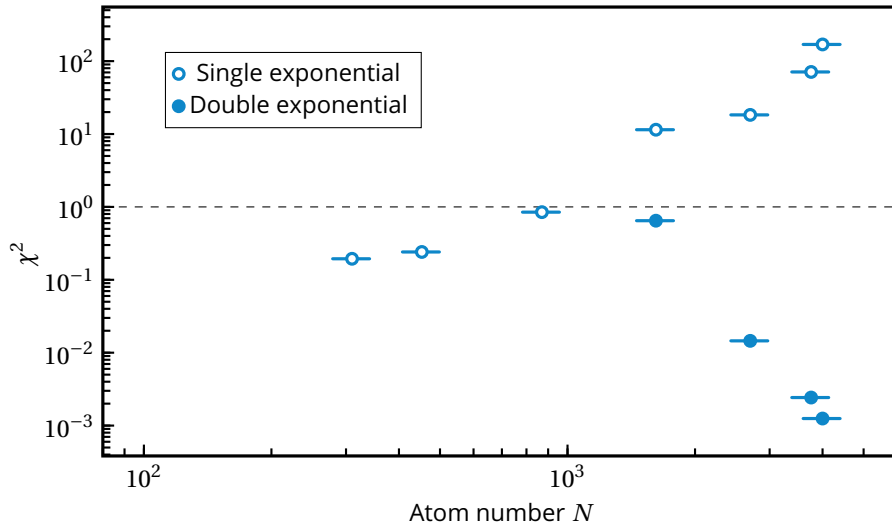


Figure 8.9:  $\chi^2$  as a function of the atom number. When  $\chi^2 > 1$  using a single exponential function, we use a sum of two exponential decays to account for the dynamics.

Thanks to this procedure, it is possible to discriminate the presence or not of subradiance. Above the threshold, it allows to determine the lifetime of the long-lived states.

## 2.4 Subradiant lifetime

The lifetime obtained by the method described above is an average lifetime. Indeed, there is a priori a great number of states which intervene, each one having its own lifetime. We showed in section 2.2 that the parameter that characterizes the subradiance is the number

of atoms in the trap. We now study the subradiant lifetime as a function of the number of atoms. For this, we use once again the three trap geometries shown in the inset of figure 8.6. The results are shown figure 8.10.

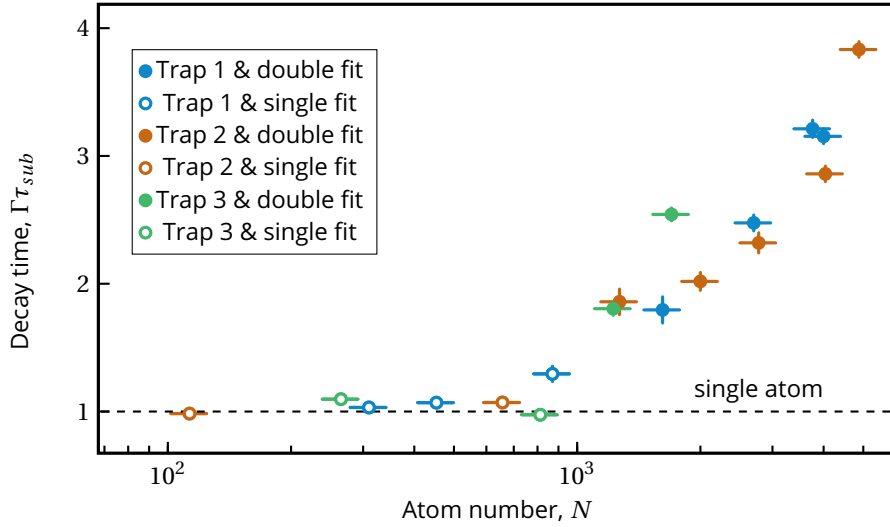


Figure 8.10: Subradiant decay times as a function of the atom number, obtained with the fitting procedure presented in section 2.3. Error bars on the decay time are standard errors from the fits. The colors refer to trap geometries given in section 3.3.

In figure 8.10, we observe once again that the curves collapse if they are plotted as a function of the number of trapped atoms. Similarly as for the tail ratio, the cloud acts as an assembly of independent atoms if the atom number is low, leading to a single-atom-like behaviour. When the atom number increases above the threshold, one sees that the subradiant lifetime increases.

When we increase the number of atoms, we increase the number of excitations stored in the subradiant states. This is a prerequisite for the application of multiple excitation storage. In the following part, we will focus on these long-lived multiply excited states.

### 3 Study of multiply-excited subradiant states

In this section, we investigate the multiply-excited subradiant states experimentally by varying the intensity of the excitation laser.

#### 3.1 Single mode approximation

For  $N \approx 4500$  atoms in a cloud, we vary the intensity of the driving pulse. The duration is still 200 ns. We vary the intensity  $s = I/I_{\text{sat}}$  between  $s \approx 0.01$  and  $s \approx 30$ . For each trace, the subradiant lifetime is extracted using the procedure described in the previous sections. In addition, we calculate the tail fluorescence as the number of detected photons for times larger than  $4/\Gamma$  after the end of the pulse.

In figure 8.11, we observe that the subradiant decay time is constant over three orders of magnitude of the excitation intensity. This constant lifetime suggests a first naive description

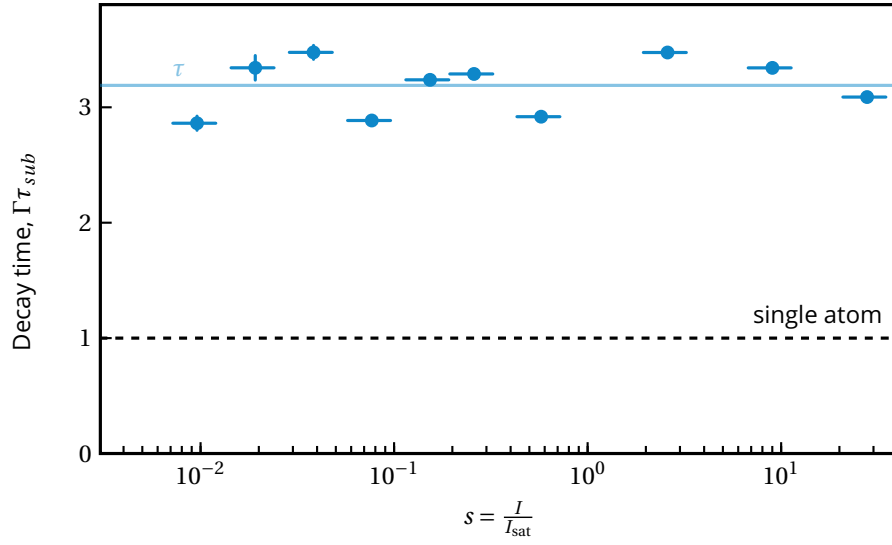


Figure 8.11: Subradiant decay times as a function of the saturation parameter of the excitation laser, obtained with the fitting procedure presented in section 2.3. Error bars on the decay time are standard errors from the fits. Black dashed line: single atom decay time.

of the data as the excitation of a single mode. The tail fluorescence (figure 8.12) increases with  $s$  before saturating at an intensity smaller than  $I_{sat}$ .

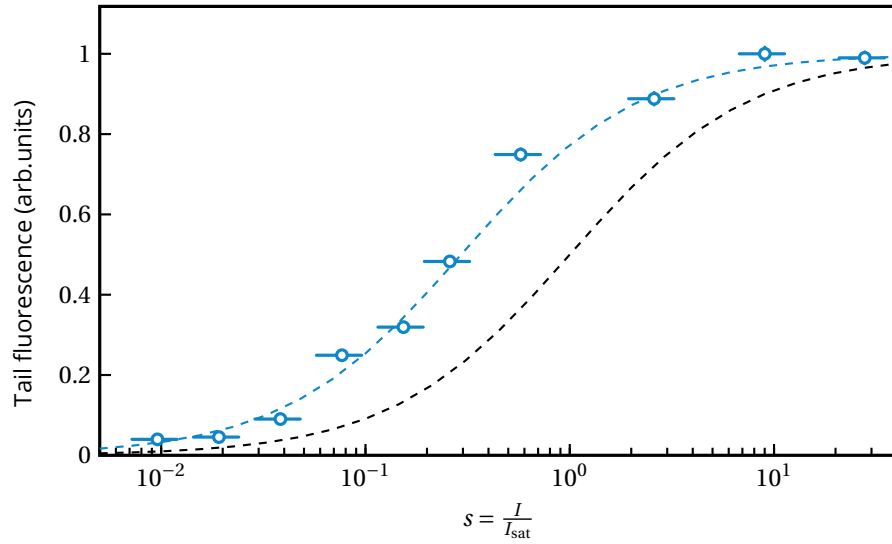


Figure 8.12: Total number of counts recorded in the subradiant tail (normalized to the maximum value). The blue dashed line is a fit by a phenomenological function, the black dashed line is the single atom response.

We use a single mode approximation to describe the population of the subradiant states  $p_{sub}$  as a function of the saturation parameter:

$$p_{sub} \propto \frac{\alpha s}{1 + \alpha s}.$$

For a single atom,  $\alpha = 1$ . By fitting the data of figure 8.12, one obtains  $\alpha = 3.4 \pm 5$ . If we assume that the lifetime  $\tau$  of a given mode dictates its saturation intensity ( $\frac{1}{\tau} \propto I_{\text{sat}}$  as for a single atom), we obtain

$$I_{\text{sat,sub}} = I_{\text{sat}}/\alpha$$

hence

$$\tau_{\text{sub}} = \alpha\tau = 3.4/\Gamma.$$

This time, represented by a solid line in figure 8.11, matches well the lifetime measured directly, confirming that a single-mode approximation seems to encompass well our observations.

However, we have shown before (figure 8.6) that about 10% of the total excitations are hosted in the long-lived states. For a fully saturated cloud of 5000 atoms (1/2 excitation per atom), it corresponds to several hundreds of excitations. A large number of modes are actually excited. Despite this large number of excitations, the decay rate remains the same demonstrating that, in the subradiant tail, the rate at which excitations decay is independent of the density of excitations in the system. This finding is consistent with multiply-excited states constructed from a large population of singly-excited subradiant states with similar decay time which decay independently.

In the case of ordered 1D array, it has been shown that subradiant states containing  $n_{\text{exc}} > 1$  excitations are built from a superposition of subradiant states of single excitation manifold which decay independently (Asenjo-Garcia et al. 2017; Henriët et al. 2019). The decay of an  $n_{\text{exc}}$  state is thus

$$R_{\text{exc}} \propto \sum_{n=1}^{n_{\text{exc}}} c_n e^{-\Gamma_n^{(1)} t}$$

where  $\Gamma_n^{(1)}$  is the lifetime of a superadiant state in the single excitation manifold. The interest of this ansatz is that the  $\Gamma_n^{(1)}$  can be calculated from the classical coupled dipole model (chapter 1, section 2.1). Our experimental discovery is that this simple picture is also valid in our disordered clouds (Ferioli, Glicenstein, Henriët, et al. 2021).

### 3.2 Limits of NLCD

Up to now, we have used non-linear coupled dipole simulations to describe subradiance. NLCD simulations are based on a mean-field approximation : it assumes that the density matrix is factorizable and that the coupling between atoms is due to their dipole moment (proportional to the coherence  $\rho_{eg}$ ). However, as shown in chapter 1 (figure 1.8), the coherence goes to zero at high intensity and the dipole vanishes. The mean-field model thus predicts that the atoms decouple from each other. When  $s$  increases, NLCD simulations should therefore recover the behavior of an assembly of independent atoms (lifetime  $1/\Gamma$ ).

In figure 8.13, we show NLCD simulations for various saturation parameters (using 100 atoms in a gaussian cloud with a peak density  $n_0/k^3 = 0.3$ ). Each trace is the result of 10 realizations of the same numerical experiment. One sees that subradiance is indeed predicted by the NLCD to disappear as the excitation strength is increased.

In figure 8.14, we report the data acquired for driving intensities reaching  $s \simeq 250$ , with  $N \sim 6000$ . Experimentally, the system still host subradiant excitations at a very large intensity. This shows that the density matrix of the system cannot be factorized throughout the decay, although it can be factorized initially. Indeed, as seen in chapter 7, we prepare in steady-state the state described by the density matrix

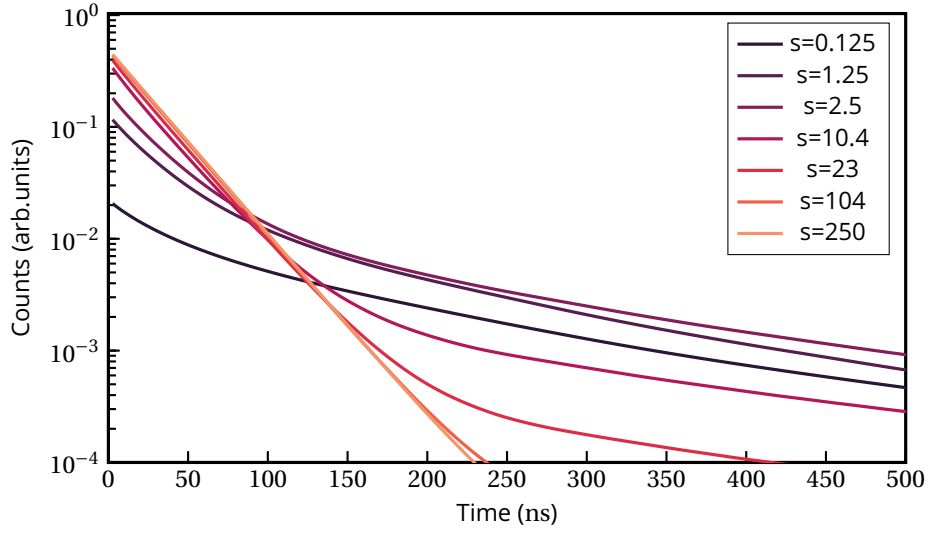


Figure 8.13: NLCD simulations, using 100 atoms at density  $n_0/k^3 = 0.3$ , normalized to the steady state value of the measurement at the largest intensity.

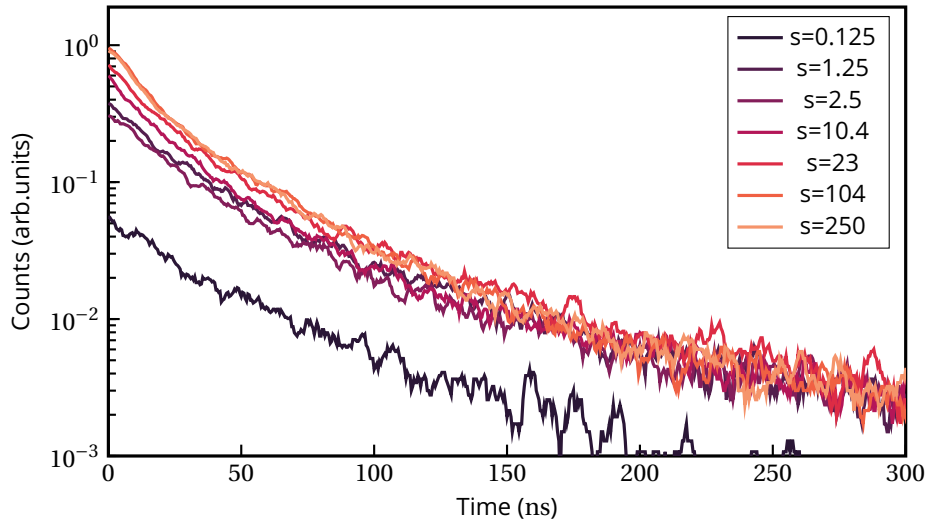


Figure 8.14: Photon count decays, for various excitation intensities. Data are shown with a moving average in a 10ns window.

$$\hat{\rho}_N = \frac{1}{2^N} \bigotimes_i^N (|g_i\rangle\langle g_i| + |e_i\rangle\langle e_i|).$$

The NLCD model is thus not sufficient to describe subradiance when the driving pulse is intense. One must therefore use methods including (at-least) two-atoms correlations, such as MF2 described in chapters 1 and 6. This has not been performed yet and could be an interesting perspective for a future study.

## 4 Release of subradiant excitations

### 4.1 Release of light stored in subradiant excitations

In this section, inspired by theoretical proposals (Facchinetti, Jenkins, et al. 2016; Asenjo-Garcia et al. 2017; Manzoni et al. 2018), we demonstrate the on-demand release of light stored in subradiant excitation. The principle is to apply a position-dependent detuning. The resulting inhomogeneous broadening makes the interaction between atoms no longer resonant: the ensemble now consists of independent atoms efficiently radiating, thus releasing the subradiant excitation.

### 4.2 Two dipoles toy model

Following (Ferioli, Glicenstein, Henriët, et al. 2021), one obtains an intuition with the following toy-model. We consider two classical dipoles  $d_1$  and  $d_2$  at distance  $r_{12}$  with a decay rate  $\Gamma$ . The time evolution of the system is (setting  $\hbar = 1$ ):

$$\begin{pmatrix} \dot{d}_1 \\ \dot{d}_2 \end{pmatrix} = \begin{pmatrix} -\frac{\Gamma}{2} & iV(r_{12}) \\ iV(r_{12}) & i\Delta - \frac{\Gamma}{2} \end{pmatrix} \begin{pmatrix} d_1 \\ d_2 \end{pmatrix} \quad (4.1)$$

where  $\Delta$  is the difference between the transition frequencies of the two atoms and  $V(r_{12})$  is the dipole-dipole interaction potential (see chapter 1, section 1.1). As shown in the first chapter, this system for  $\Delta = 0$  has two eigenmodes  $\mathbf{v}_{\pm} \propto (1, \pm 1)$  with decay rates  $\Gamma_{\pm} = \Gamma \pm 2\text{Im}[V(r_{12})]$ . These modes are the super- and subradiant modes.

Let us assume that  $\Delta = 0$  (no-inhomogeneous broadening) and that we prepare the dipoles in  $\mathbf{v}_-$  at  $t = 0$ . The system then decays with the subradiant lifetime  $\Gamma_-$ . At a time  $t_0$ , we turn on the inhomogeneous broadening,  $\Delta \neq 0$ . The projection on the superradiant mode becomes different from zero and the dipoles are now expressed as the eigenstates of the matrix in equation (4.1)  $\mathbf{v}_1 = (1, 0)$  and  $\mathbf{v}_2 = (0, 1)$ .

The evolution of the two-atom dipole is given by

$$\mathbf{v}(t) \propto e^{-\Gamma t/2} \left( \mathbf{v}_1 - e^{i\Delta t} \mathbf{v}_2 \right). \quad (4.2)$$

In the limit  $\Delta \gg |V(r_{12})|$ , we recover the single atom decay rate of the radiated power

$$\mathbf{v}^2(t) \propto e^{-\Gamma t}.$$

To illustrate this, we calculate the dipoles  $d_{1,2}$  as a function of time with  $\Gamma_+ = 1.9\Gamma$  (or  $\Gamma_- = 0.1\Gamma$ ). In the example shown figure 8.15 a), before  $t_0 = 3/\Gamma$ ,  $d_+ = 0$  and the system decays with the rate  $\Gamma_-$ . At  $t = t_0$ , we apply  $\Delta = 10\Gamma$ . We see that  $d_{\pm}$  are coupled and exchange energy. The system is now better expressed with  $d_{1,2}$ . In panel b), we show the two-atom dipole computed with equation (4.2). Before  $t_0$ , the slope is given by  $\Gamma_-$ . For  $t > t_0$ , we recover (on average) the single atom decay rate  $\Gamma$ . The residual oscillation is due to the fact that  $\Delta$  is not infinitely larger than  $|V(r_{12})|$  in this case.

This two-dipole toy model thus shows that applying a atom-dependent detuning places the atoms out of resonance and makes the system radiate as an assembly of independent emitters.

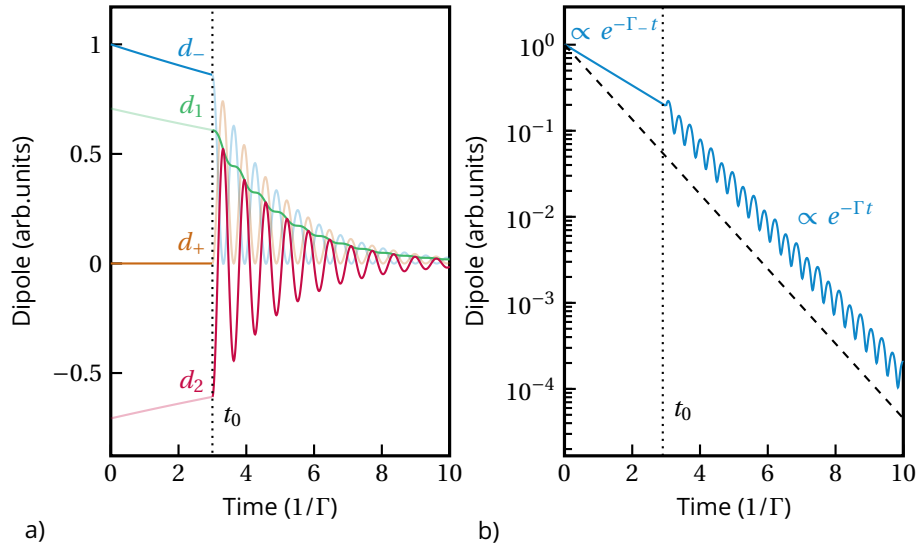


Figure 8.15: a) Time evolution of two dipoles prepared in  $d_-$  at  $t=0$  when brutally applying an inhomogeneous broadening  $\Delta = 10\Gamma$  at  $t_0 = 3\Gamma$ . b) Time evolution of the two-atom dipole (equation (4.2)), compared to a single dipole (dashed line).

### 4.3 Experimental demonstration

To apply the inhomogeneous broadening experimentally, we turn on the trap light at different times after the extinction of the excitation laser (represented with vertical arrows in figure 8.16). The far off-resonant light induces a position dependent detuning given by

$$\Delta_i(x_i, y_i, z_i) = \frac{\Delta_0}{1 + (\frac{z_i}{z_R})^2} \exp \left[ -\frac{2(x_i^2 + y_i^2)}{w_0^2(1 + (\frac{z_i}{z_R})^2)} \right]$$

where  $\Delta_0 \approx 32\Gamma$  is the light-shift induced by the trap light at the center,  $w_0 = 2.5\mu\text{m}$  is the waist and  $z_R = \frac{\pi w_0^2}{\lambda_{\text{trap}}}$  is the Rayleigh range. The standard deviation of the trap induced detuning is thus about  $4\Gamma$ . In our clouds,  $|V_{dd}| \sim \hbar\Gamma$  (for the nearest-neighbour atoms), so  $\Delta_0 \gg |V_{dd}|$ .

As shown figure 8.16, a pulse of light is observed when we apply the inhomogeneous broadening. This can be understood using the toy model: when the broadening is applied, the atoms start to radiate at a rate faster than the subradiant decay rate. The intensity emitted thus increases (before decaying). We observe that, after the release of the subradiant excitations, the decay rate is close to that of a single atom (a decay rate of  $1.3 \pm 1\Gamma$  is obtained by fitting all the data sets). The measurement figure 8.16 have been performed with  $N = 5000$  atoms. We have verified that in the low atom number regime no pulse is observed.

Moreover, it is interesting to note that the release is obtained with a light-shift that varies slowly in space. This indicates that subradiant excitations are not stored in pairs of close atoms but rather delocalized over all the atoms of the cloud (Schilder et al. 2016). This is expected for a near-resonant excitation of the cloud, as delocalized excitations corresponds to states with small interaction frequency shift  $\text{Re}[V_{dd}]$  (see chapter 1, section 2.1) and localized ones with a high  $V_{dd}$  are not excited.

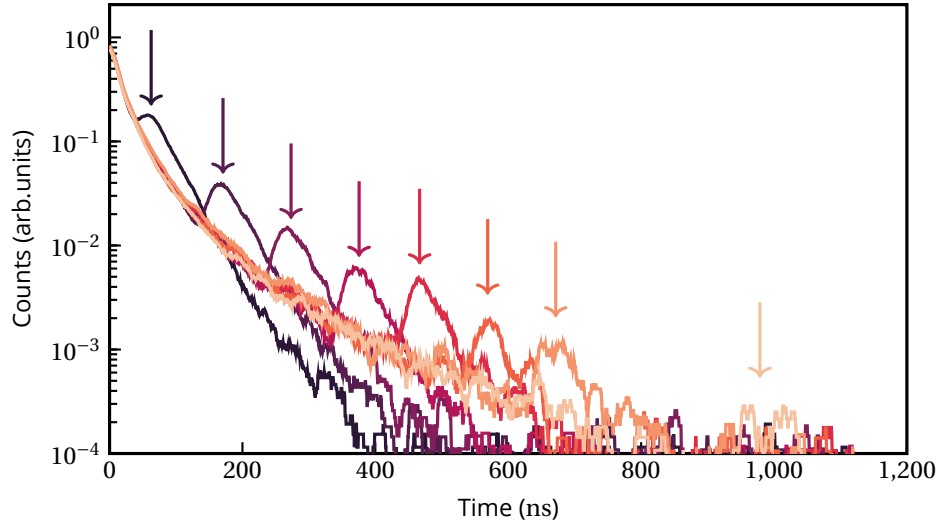


Figure 8.16: Experimental realization of release of the light stored in subradiant excitations.

#### 4.4 Analysis using eigenmodes and NLCD simulations

As discussed in Section 3, the multiply-excited subradiant modes are fabricated as superpositions of independently decaying modes containing one excitation. The study of these modes therefore allows a qualitative description of the situation. We calculate these modes and their decay rate by evaluating the eigenvalues of the interaction matrix for  $N = 5000$  classical dipoles using the inhomogeneous broadening  $\Delta_i(x_i, y_i, z_i)$ . Results are shown figure 8.17. They indicate that in the presence of the inhomogeneous broadening, the distribution of decay rates is much narrower than in free space. In particular, a significant fraction of the subradiant modes is suppressed. This confirms that subradiance is suppressed.

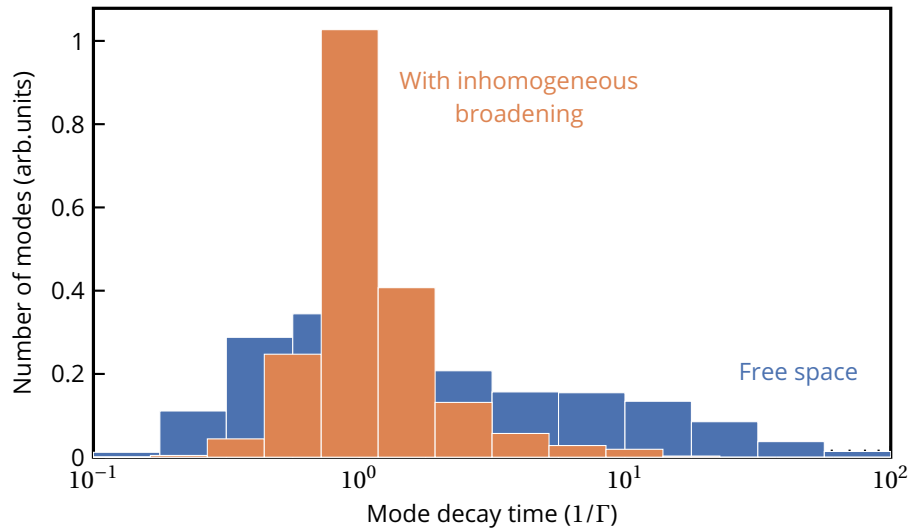


Figure 8.17: Histogram of the eigenmodes decay times, for  $N = 5000$  and the experimental density distribution in free space and with inhomogeneous broadening. Average over 10 realizations to take into account the randomness of the atomic positions.



We now perform NLCD simulations of the dynamics. Figure 8.18, we present results of simulations computed by I. Ferrier-Barbut for a cloud containing  $N = 200$  atoms with a peak density  $n_0 = 0.3k^3$ . The trap is turned on during the decay at  $t_0 = 12.5/\Gamma$  with a finite rising time of 25 ns to match our experimental parameters. In figure 8.18, we show the time evolution of the population of the excited state  $p(t) = \sum_{i=1}^N \rho_{ee}^{(i)}(t)$  (dashed lines) and the evolution of the intensity in a  $4\pi$  solid angle, which is the quantity measured experimentally and is proportional to  $-\frac{dp(t)}{dt}$  (solid lines).

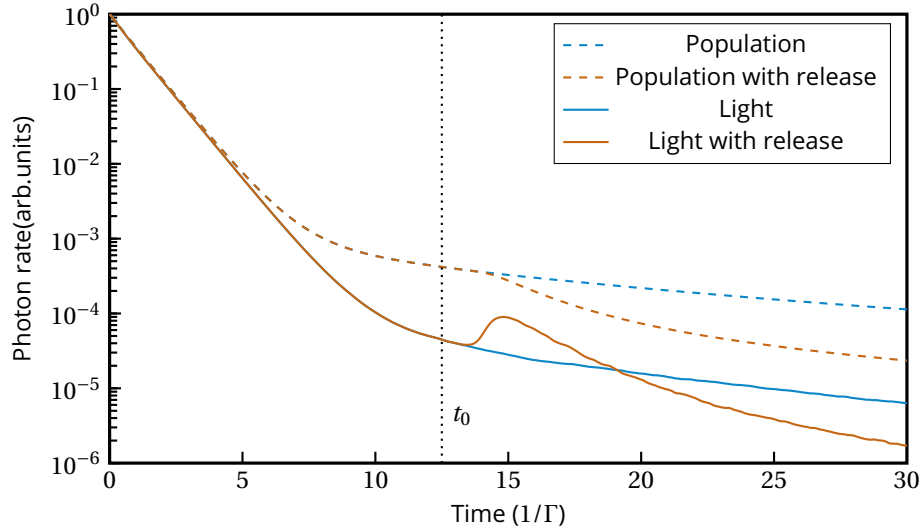


Figure 8.18: Results of NLCD simulations. The evolution of the excited state population  $p(t)$  is shown with dashed lines with and without the release (applied at  $t = t_0$ ). The resulting intensity in  $4\pi$  is shown with solid lines.

We see that when the inhomogeneous broadening is applied, the population presents a change of slope corresponding to an intensity peak. These simulations confirm our interpretations of the experimental observations.

#### 4.5 Role of internal structure and magnetic field

Finally, we investigated the directionality of the pulse emitted by the release sequence and the effect of the internal atomic structure (two- or multi-level) and of the polarization of the excitation light. We have already shown that they do not modify significantly the subradiant properties (section 1.4).

As shown in figure 8.19, we observed that the enhancement of the emission is stronger along the cloud axis, possibly due to the coupling to superradiant states in this direction. This could lead to a better control of the photons retrieved after the release. As in section 1.4, changing polarization and the internal structure of atoms does not lead to significant difference in the released pulse.

In this section, a protocol for the release of subradiant excitations stored in a cloud has been demonstrated. We have observed that in the best case, about 10% of the excitations brought into the system are stored in the long-lived states when the system is prepared in the driven steady-state (figure 8.6). In the following section, we focus on the population of subradiant states during driving. Understanding how subradiant states are populated is a

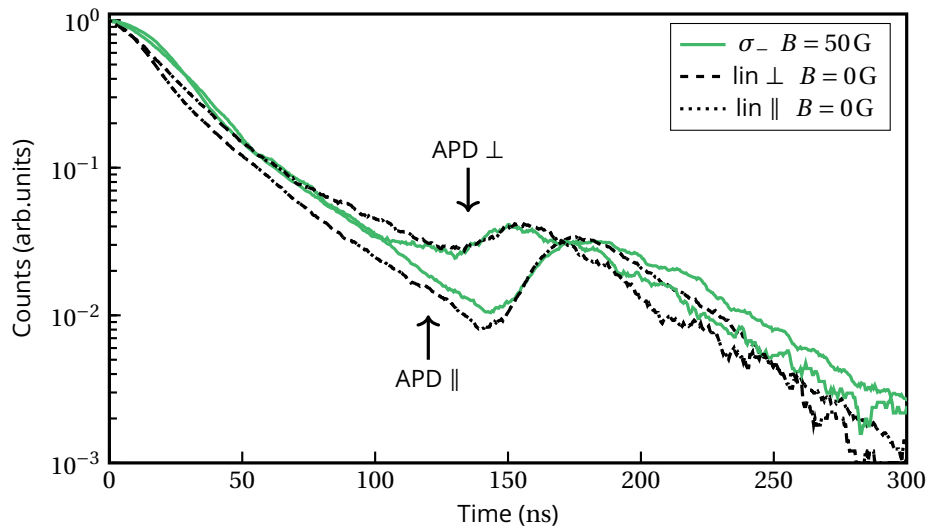


Figure 8.19: Directionality of the released pulse, observed with APD  $\perp$  and APD  $\parallel$ . We compare experiment done with a linear polarization, either parallel or perpendicular to the cloud and with a circular polarization in presence of magnetic field (two-level).

prerequisite for storage applications, for entanglement generation...

## 5 Exploring the Dicke ladder : population of the long lived-states from the superradiant states

In Chapter 7, we have studied how superradiant states are populated and evolve when the system is driven. In particular, we have shown that population inversion (the number of excitations in the system) is the main parameter that governs superradiance. In this chapter, we have reported subradiance observed when the driven steady-state is reached. Under the approximation that there is no effect of interactions ( $\hbar\Omega \gg V_{dd}$ ), the system is in an incoherent mixture described by its density matrix

$$\hat{\rho}_N = \frac{1}{2^N} \bigotimes_i^N (|g_i\rangle\langle g_i| + |e_i\rangle\langle e_i|). \quad (5.1)$$

which contains superradiant and subradiant terms. For example, for  $N = 2$ , we have

$$\hat{\rho}_2 = \frac{1}{4} (|gg\rangle\langle gg| + |++\rangle\langle ++| + |--\rangle\langle --| + |ee\rangle\langle ee|)$$

where  $|\pm\rangle = \frac{1}{\sqrt{2}} (|ge\rangle \pm |eg\rangle)$  are the 2-atom super and subradiant state.

The question is now to determine experimentally if subradiance is also observed during the Rabi oscillations. Assuming  $\Omega \gg \Gamma$ , the system is then prepared in the coherent superposition

$$|\psi_{\text{las}}\rangle = \prod_n (\cos(\Omega t) |g_n\rangle + e^{i\mathbf{k}_{\text{las}} \cdot \mathbf{R}_n} \sin(\Omega t) |e_n\rangle). \quad (5.2)$$

In the Dicke limit ( $k_{\text{las}} \cdot R_n \ll 1$ ), this state is only coupled to superradiant states since it is invariant under exchange of two atoms (see chapter 6, section 1.2).

However, our system is not perfectly in the Dicke regime because the length of our clouds is a few wavelength. Superradiance and subradiance are hence not perfect anymore. For example for  $N = 2$ ,  $\Gamma_- \neq 0$  so the subradiant state is coupled to the ground and excited states and so this state can be driven by the laser (see inset figure 8.20). Moreover, the presence of interactions between the dipoles leads to a coupling between the states. In the many-atoms case, it is possible for the superradiant states to decay through the subradiant states. There are thus several possible ways to populate the subradiant states, as represented in figure 8.20. We will now study experimentally which ones play a role in our system.

As shown in previous chapters, a crucial improvement of our experimental setup is the precise control of the driving pulse duration. We use a fiber electro-optical modulator (EOM) and two acousto-optical modulators (AOM) in series. The EOM has a rising and falling time shorter than 1 ns and an extinction of the order of  $10^{-2}$ . Using the AOMs, we obtain an extinction of  $10^{-4}$  in about 25 ns, which allows us to observe subradiance.

Resonant light is sent with an intensity  $s = \frac{I}{I_{\text{sat}}} \simeq 75$ , corresponding to a Rabi frequency  $\Omega \simeq 6.5\Gamma$ ). We then stop the driving pulse at a precise time  $t_0$  during the Rabi oscillations and then measure the fluorescence emitted by the cloud after the end of the pulse. We characterize subradiance by measuring the decay rate and the rate of photon emission in the late decay.

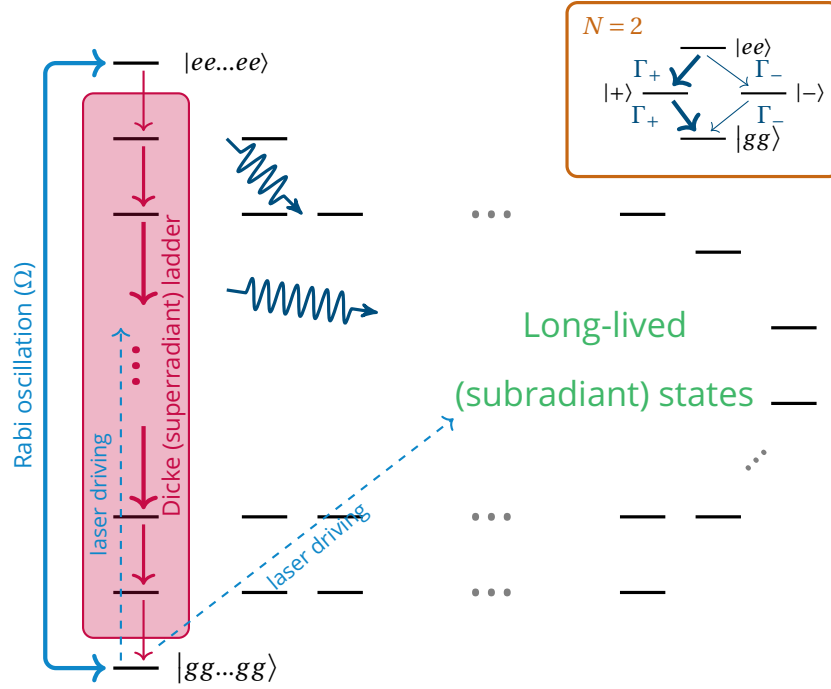


Figure 8.20: Schematic representation of the various ways to populate the subradiant states : direct laser driving or decay from superradiant states. Inset : Dicke states for  $N = 2$  near Dicke's regime ( $\Gamma_- \neq 0$ ).

## 5.1 Decay time

To analyze how subradiance emerges during the driving, we first extract the subradiant decay time  $\tau_{\text{sub}}$  using an exponential fit for  $t \geq t_0 + 4/\Gamma$ . The results are plotted figure 8.21 a).

Contrarily to superradiance (figure 7.3), the decay time does not vary with the population of the excited state. We show it by plotting in the same figure the fluorescence acquired during the Rabi oscillations in the low atom number regime, which is proportional to the population of the excited state (it is well fitted by the solutions of the optical Bloch equations, see for example 7.4 a)). The characteristic decay time is similar to the one measured in steady state for the same atom number (figure 8.10). The same dataset was used for Figure 8.21 as for determining the superradiant decay time  $\tau_s$  in Figure 7.3. Thus,  $\tau_{\text{sub}}$  can be plotted as a function of  $\tau_s$ . As shown in figure 8.21 b), the two decay times seem uncorrelated. This goes in the direction of saying that the super- and subradiant states are independent. To further investigate, we now consider the photon emission rate.

## 5.2 Photon in the late decay

We now estimate the population in the long-lived states summing the photons recorded after  $t_0 + 4\Gamma$ , as shown figure 8.22.

We see that the population of the subradiant states increases with time during Rabi oscillations, saturating when the system reaches the steady state. Several Rabi cycles are needed to reach the maximum population of subradiant states. The subradiant states are slowly populated by direct laser driving or with an optical pumping mechanism via the superradiant states (Masson et al. 2020). This mechanism has been suggested in dilute clouds of cold

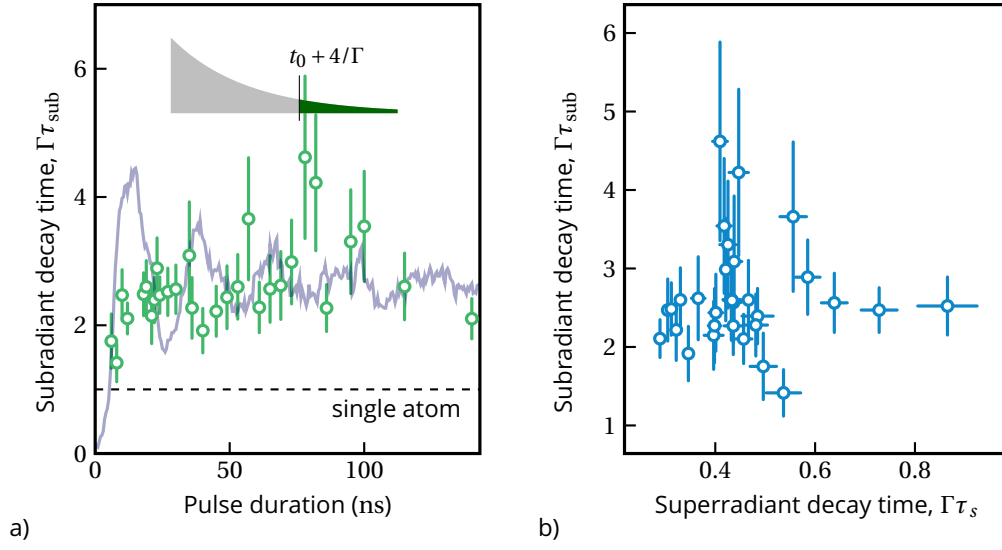


Figure 8.21: a) subradiant decay time  $\tau_{\text{sub}}$  as a function of the pulse duration. The fluorescence collected as a function of the time during the driving is plotted with an arbitrary scale as a background. The horizontal dashed line corresponds to the decay time of a single atom,  $1/\Gamma$  by definition. The vertical error bars are from the fit of the exponential decay of the fluorescence. b)  $\tau_{\text{sub}}$  as a function of the superradiant decay time  $\tau_s$  (figure 7.3), showing no correlation.

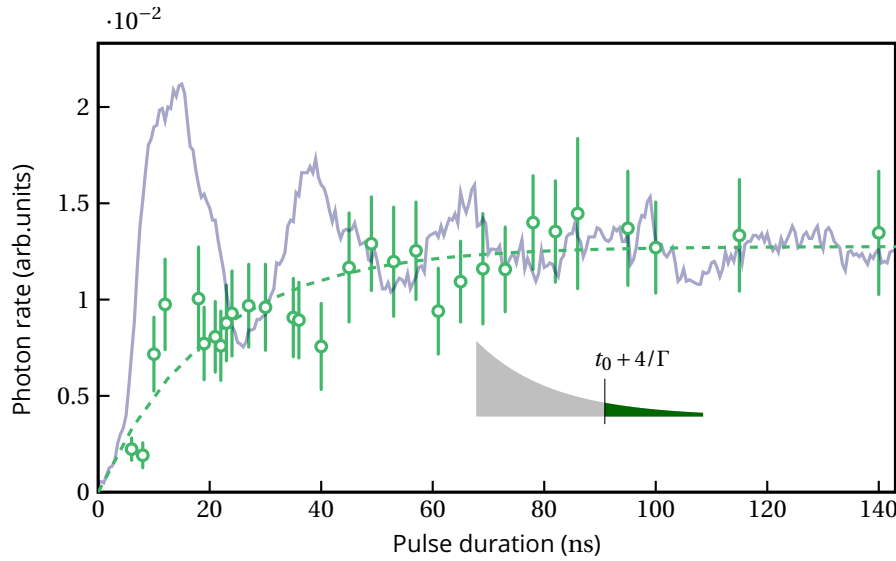


Figure 8.22: Photon collected in the late decay ( $t \geq t_0 + 4\Gamma$ ) as a function of the pulse duration. The vertical errorbar is calculated taking  $t \geq t_0 + 5\Gamma$  instead.

atoms (Cipris et al. 2020). In a two atom systems, the rate of both mechanisms is  $\Gamma_-$  (see inset figure 8.20).

We fit the experimental data with a phenomenological function  $\propto (1 - \exp[-t/\tau])$  to extract the timescale within which subradiance is build, as shown with a dashed line in figure 8.22. It gives a time constant of about 20 ns, which is similar to the damping time of the Rabi

oscillations.

To conclude, there are several processes that populate the subradiant states. The highest population of subradiant states is obtained when the system is prepared in an incoherent mixture, with a long pulse that allows the system to reach the driven steady-state.

### 5.3 Master equation

To gain a better intuition on the above observations, we solve the master equation for  $N = 2$  (section 1.2). We consider two dipoles separated by a distance  $\langle r \rangle = \lambda/3$ , which is the mean nearest neighbour interatomic distance in our experiment. As represented in the inset figure 8.23, we vary the relative angle  $\theta$  between the dipoles, keeping the distance constant. Dipoles are driven by a coherent field with Rabi frequency  $\Omega = 6.5\Gamma$  and with polarization  $\mathbf{z}$ . This field has a wavevector  $\mathbf{k}_{\text{las}} = \frac{2\pi}{\lambda}\mathbf{y}$ . The effect on the populations of the different angles can thus be observed.

For different times, we evaluate the excited state population  $\langle ee|\rho(t)|ee\rangle$  and the populations of the sub- and superadiant states  $\langle \pm|\rho(t)|\pm\rangle$  where  $|\pm\rangle = \frac{1}{\sqrt{2}}(|eg\rangle \pm |ge\rangle)$ . Results are shown figure 8.23.

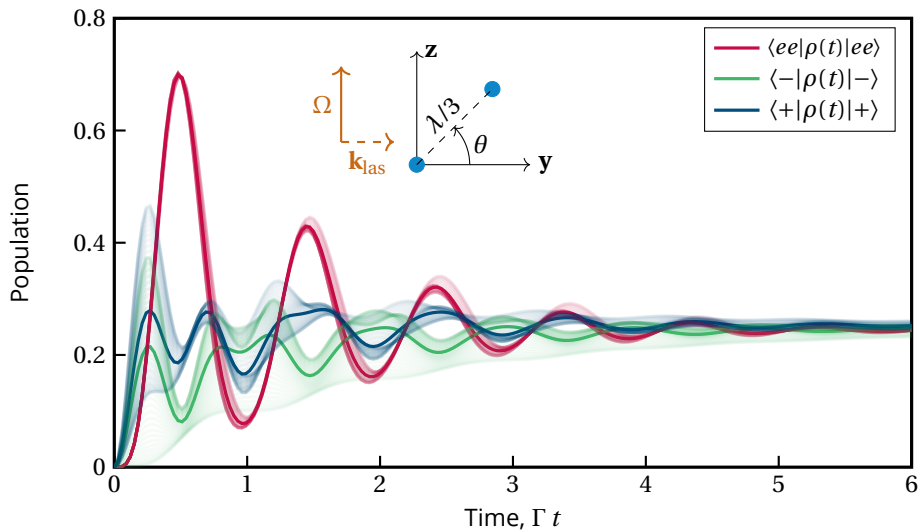


Figure 8.23: Population of the states as a function of time calculated with the master equation for  $N = 2, \Omega = 6.5\Gamma$  and  $R_{12} = \lambda/3$ . The relative angle  $\theta$  is averaged over 1000 realizations, giving the solid lines.

By varying  $\theta$ , we see that the populations of  $|\pm\rangle$  depends strongly on  $\theta$ . This was expected as we prepare (according to equation (5.2))

$$|\psi\rangle = \frac{1}{\sqrt{2}} \left( \cos(\Omega t) |g\rangle + \sin(\Omega t) e^{i\phi} |e\rangle \right)$$

with  $\phi = \mathbf{k}_{\text{las}} \cdot \langle \mathbf{r} \rangle = \frac{2\pi}{3} \cos(\theta)$ . This state is close to  $|-\rangle$  or  $|+\rangle$  depending the value of  $\theta$ . As a function of time (for a well chosen  $\theta$ ), we also see that the laser can drive selectively  $|+\rangle$  or  $|-\rangle$ . The simulations shown in figure 8.23 reproduce qualitatively well our experimental observations of subradiance.

In figure 8.23, we see that the subradiant state is slowly populated during the Rabi oscillations. At certain times (for a given  $\theta$ ), we see that  $|-\rangle$  is directly driven by the excitation laser, leading to large peaks in the population. We see it for example before the first peak of the Rabi oscillation. We also see the optical pumping mechanism from  $|+\rangle$ : the excitation is pumped to  $|-\rangle$  via the state  $|ee\rangle$  and a decay with rate  $\Gamma_-$ . As observed experimentally, the simulations using two atoms show that the population of the subradiant state is maximal when the steady state is reached, that is when the system is prepared in a mixed state.

Another possibility to populate the long-lived states is to decay from the other states. To better understand the processes at play, we calculate the populations of the states when we perform a  $\pi$  pulse, as shown figure 8.24. We turn off the pulse at a time  $t_0$  for which  $\langle ee|\rho(t_0)|ee\rangle$  is maximum.

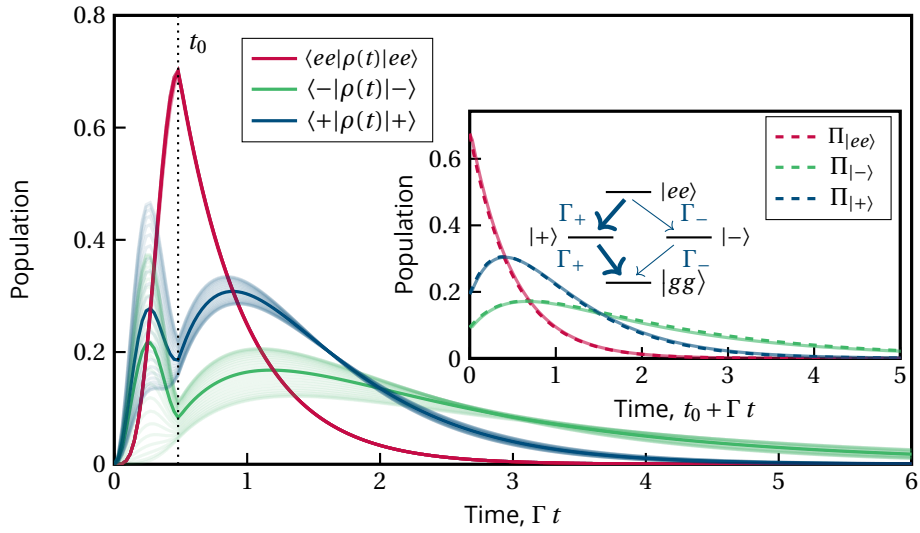


Figure 8.24: Population of the states as a function of time calculated with the master equation when realizing a  $\pi$ -pulse for  $N=2, \Omega=6.5\Gamma$  and  $R_{12}=\lambda/3$ . Driving is switched off at  $t=t_0$ . The relative angle  $\theta$  is averaged over 1000 realizations, giving the solid lines. Inset : comparison with the decay using rates equations.

We switch off the driving,  $\Omega(t \geq t_0) = 0$  and we observe that the populations of  $|+\rangle$  and  $|-\rangle$  increase before they decay. As in the two atom case,  $|+\rangle$  and  $|-\rangle$  are not coupled, the decay is obtained by solving the rates equations

$$\dot{\Pi}_m = \begin{cases} -\Gamma_+ \Pi_{ee} - \Gamma_- \Pi_{ee} & \text{if } m = |ee\rangle \\ \Gamma_+ \Pi_{ee} - \Gamma_+ \Pi_+ & \text{if } m = |+\rangle \\ \Gamma_- \Pi_{ee} - \Gamma_- \Pi_- & \text{if } m = |-\rangle \\ \Gamma_+ \Pi_+ + \Gamma_- \Pi_- & \text{if } m = |gg\rangle. \end{cases}$$

The results of these equations during the decay is shown in inset figure 8.24 and overlap with the solutions of the master equation. They indicate that  $|-\rangle$  is populated via the decay from state  $|ee\rangle$ . For  $N \gg 2$ , it is therefore expected that the subradiant states are populated by decay from the excited state. Since no correlation between the population of superradiant and subradiant states was observed, the possible decay from superradiant to subradiant states is not very efficient to populate the subradiant states.

## 6 Conclusion

In this chapter, we have observed subradiance in a steady-state cloud operating near Dicke's regime. We have characterized the multi-excited subradiant states and shown that the cooperativity parameter is the atom number. In a second part, we have demonstrated a protocol for storing and releasing subradiant excitations. Finally, we have studied the population of the subradiant states in the driven regime and explored the interplay with the superradiant states. We thus have shown that subradiant states are better populated when the system is prepared in an incoherent mixture.



# Conclusion and perspectives

\*\*\*

After having presented the work done during my thesis, I present here a summary of it and then focus on possible future works and perspectives of studies, also based on preliminary data.

In the first part of this manuscript, I gave a description of the tools we have developed and used during my work. the basic theoretical notions necessary to understand the rest of the manuscript, as well as the different types of numerical simulations used to understand the physics involved are presented. The framework and the limits of each type of simulation is summarized in figure 1.

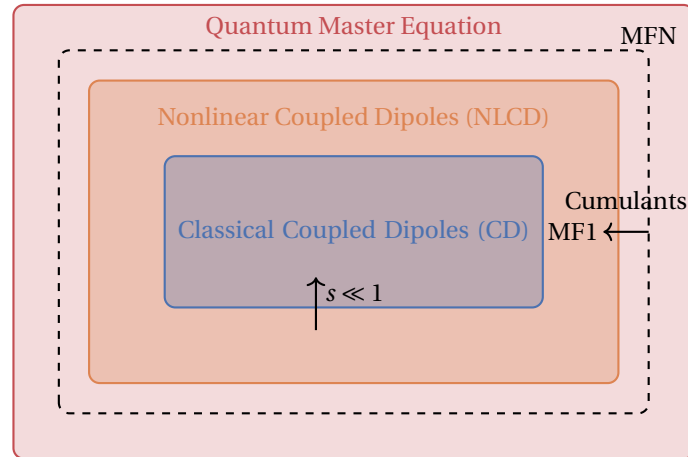


Figure 1: Schematic of the framework of the simulations. The approximations used to go from one to the other are represented by arrows.

The most general method is the direct solution of the master equation (section 1.2), but it is very expensive in computation time because the size of the Hilbert space to consider is  $2^N$ , where  $N$  is the atom number. It is however useful to perform complete simulations without approximation on a small atom number  $N$  to gain intuition. For example, it was used in chapter 8, section 5.3, for the study of the population of subradiant and superradiant states.

In order to reduce the calculation time, approximations are used. The cumulants approximation MFN (section 2.3), consists in truncating the correlations between the operators at a certain order while keeping all orders up to  $N$  amounts to a complete solution of the master equation. This method has been used at order 2 (MF2, i.e. keeping only the two-operators

correlations) to study superradiance in chapters 6 and 7 (for example section 3.1) by our collaborators F. Robicheaux and R.T. Sutherland. Neglecting all correlations between operators (MF1), one obtains a model often called "mean field" consisting in treating all the dipoles as quantum dipoles coupled via the mean field radiated by the other dipoles. This model is equivalent to the non-linear coupled dipoles (NLCD, section 2.2). It has been used for example in the study of subradiance in chapter 8 (for example figure 8.3). By reducing the intensity of the excitation laser,  $s = \frac{I}{I_{\text{sat}}} \ll 1$ , one can neglect the saturation of the dipoles. Their amplitude is therefore proportional to  $s$ . The dipoles are in this case well modeled by classical coupled dipoles simulations (section 2.1). We have used these simulations for example in the study of the 1D chain in chapter 4.

I then described the experimental system (chapter 2). This system was designed and assembled during the thesis of L. Brossard (Brossard 2019) for its vacuum part and the aspherical lenses. However, the elements presented in this chapter were realized during my thesis, in particular the trapping and observation of single atoms along the two axes as well as the control of the internal state of the atoms (sections 1.3 and 3.2). An important part was also dedicated to the preparation and characterization of the 1D chain of atoms whose collective properties are studied in chapter 4. I devoted a special chapter (3) to a particularly important improvement of the setup, which required a long work. Indeed, the implementation of  $\Lambda$ -gray molasses (GM), initially with the aim of improving the loading of single optical tweezers or the chain (section 3.2), has allowed us to load a large number of atoms in microscopic traps (section 3.3). The last chapter of the first part, chapter 4 was about the study of the collective scattering of light in a 1D atomic chain. In particular, it showed that this geometry allows us to obtain large collective effects with a small number of atoms. This study was made possible by the two high resolution axes and by the use of GM to efficiently load the chain, and demonstrated the possibilities of the experimental system.

## Perspectives of experimental improvements

The great advances made during my PhD were mainly due to an increase in  $N$  and a decrease of the interatomic distance  $\langle r \rangle$ . This opens interesting perspectives for future, as represented figure 2. The first direction of study is to load a chain with a smaller spacing than in chapter 4, for which there are two possibilities. Either we improve the loading efficiency ( $\eta = 0.5$  for the moment using GM) or we change the wavelength of the trapping beam. Indeed, the distance between two sites is  $\lambda_{\text{trap}}/2$ , so the distance between two atoms is  $\frac{\lambda_{\text{trap}}}{2\eta}$ . The other way, to which we give our favor, is to use a laser of wavelength  $\lambda_{\text{trap}} = 532 \text{ nm}$  (which creates a repulsive trap, so the infrared laser is still needed to create an attractive trapping potential, as shown figure 2 a) ) or a laser of wavelength  $\lambda_{\text{trap}} = 420 \text{ nm}$ . The second one (figure 2 b)) is more interesting because it allows to obtain a smaller inter-site spacing.

Another direction of study is to realize a chain of controllable spacing, as represented figure 2 c). With the use of an acousto-optical deflector (AOD), one can vary the distance  $a$  between atoms in individual tweezers by changing the RF frequencies seeded in the AOD. It has been shown that this allows to prepare selectively superradiant or subradiant states when  $a$  varies around a multiple of  $\lambda/2$  (Masson et al. 2020; Sutherland and Robicheaux 2016). The experimental challenge will be then to reduce the distance, for instance by loading an

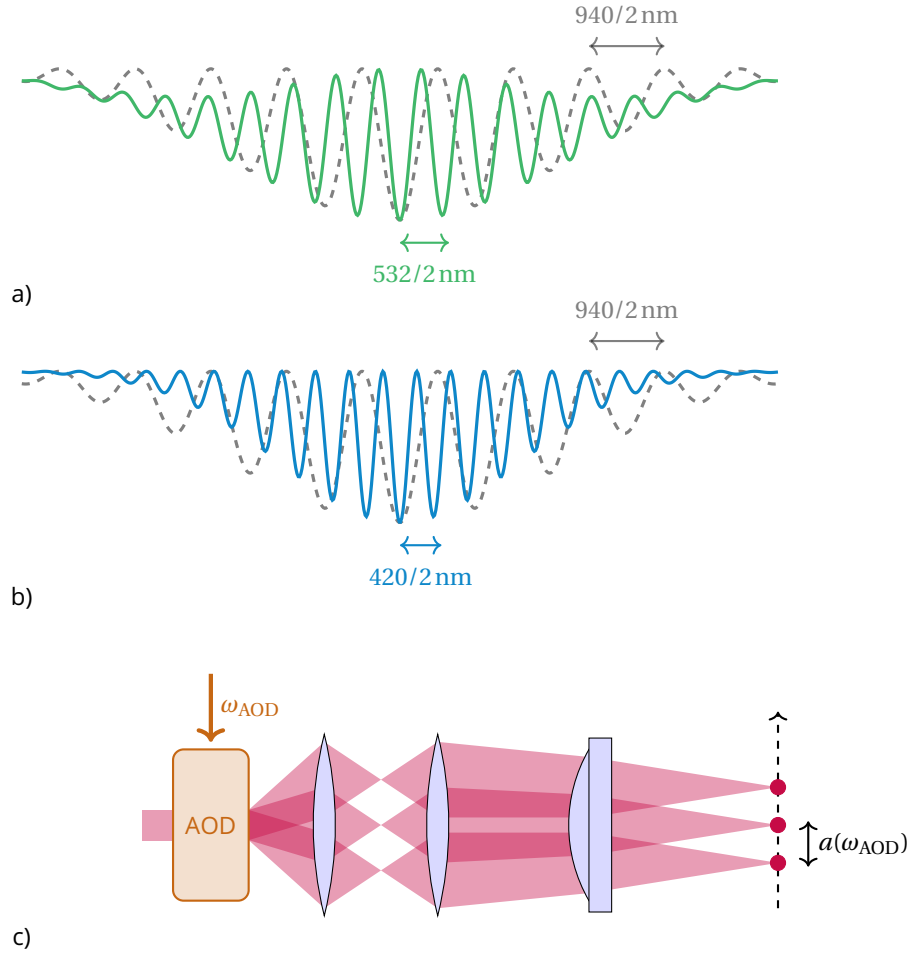


Figure 2: Perspectives of future studies of the 1D chain a) Using a green laser and the infrared laser b) Using a blue laser c) Controllable spacing using several beams displaced by an AOD.

accordion lattice (Ville et al. 2017).

## Collective light-matter interaction in dense atomic clouds

The second part of this manuscript was dedicated to the study of collective effects in dense microscopic clouds approaching Dicke regime, where the cloud's dimensions are smaller than the wavelength. I have first explained (chapter 5) how we prepare and characterize dense clouds of atoms, reaching a peak density  $n_0/k^3 \sim 1$ . The prepared cloud contains several thousands of atoms, exploiting the efficient GM loading. This is a crucial improvement compared to the previous generations of the experiments, where the atom number was limited to a few hundreds in the same traps. This allowed us to observe for the first time in the group the phenomena of superradiance and subradiance, which we found to be governed by the number of atoms in the cloud. We have compared our experimental data on Dicke superradiance to ab-initio MF2 simulations, showing good agreement. In chapter 7, we have observed laser driven collective oscillations and explored the steady state-regime and we have found that superradiance is based in the population of the excited state, rather than on the precise state in which the system is prepared. In the last chapter of this part, chapter 8, we reported the first observation of subradiance near Dicke's regime and demonstrated a protocol to store and on-demand releasing subradiant excitations. Finally, we have studied the population of the long-lived states in the driven regime and explored their interplay with the superradiant states.

### Population of super- and subradiant states

A large part of this work was devoted to the experimental study of the population of super- and subradiant states in a dense cloud approaching Dicke's regime. The following figures summarize the obtained results. Figures 3 a) and b) represent the different states of the Hilbert space, the superradiant *Dicke ladder* and the *long-lived states* for which the decay rate is smaller than that of a single atom  $\Gamma$ . In panel a) and b), we represent the different possible ways to populate the superradiant and subradiant states. Superradiant states may be driven directly by the laser (dashed blue arrow), or by decay from the fully excited state  $|ee...ee\rangle$ . We have shown that the superradiant behavior is mainly given by the number of excitations in the system, in other words the population of the excited state (obtained during Rabi oscillations). Superradiant states are thus populated mostly by the decay from the fully excited state (figure 3 a)), as predicted in Dicke's scenario.

Subradiant states may be populated either directly (dashed blue arrow), or by spontaneous decay from the superradiant states (figure 3 b). Moreover, we have shown that subradiant states are better populated when the system has reached its driven steady-state, that is when it is prepared in an incoherent mixture.

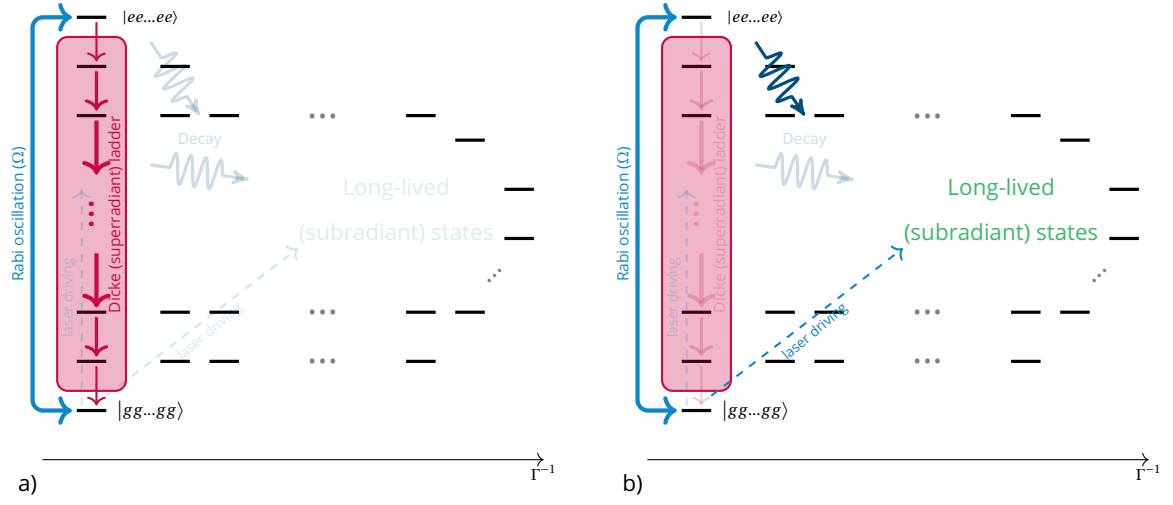


Figure 3: a) Superradiant states are populated mostly by decay from the fully-excited state. b) Long-lived (subradiant) states are populated by direct driving and decay from  $|ee...ee\rangle$ .

## Future work

During my thesis, we started to address another aspect of collective effects in dense clouds: the generation of non-classical states of light. Indeed, there are proposals that suggest to use atomic ensembles as non-linear medium (Chang, Vuletić, et al. 2014; Prasad et al. 2019). The principle is represented in figure 4 using  $N = 2$  atoms. The resonant dipole-dipole interaction  $V_{dd}$  leads to a shift of the energy levels by  $\delta = \pm \text{Re}[V_{dd}]$ . If one addresses the superradiant state  $|+\rangle$  by setting the laser frequency to  $\omega_0 + \delta$  (where  $\omega_0$  is the single atom resonance frequency), the frequency shift prevents one to populate  $|ee\rangle$ . Thus, if a first photon of the laser is absorbed by the medium, the medium will be transparent for a second photon with the same frequency (Cidrim et al. 2020).

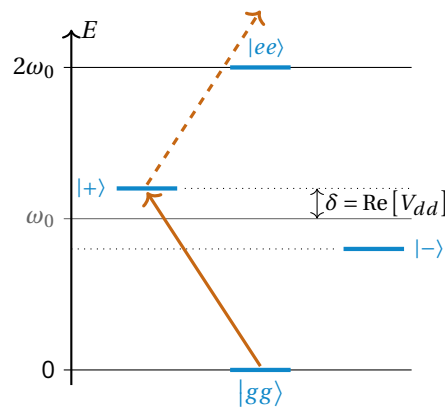


Figure 4: Non-linearity induced by the dipole-dipole interaction. If one photon of frequency  $\omega_0 + \delta$  is absorbed by the system, the system becomes transparent for other photons with the same frequency.

We therefore started to measure correlation functions of the fluorescence emitted by the

cloud. The intensity correlation function

$$g^{(2)}(\tau) = \frac{\langle \mathbf{E}(\mathbf{r}, t) \mathbf{E}(\mathbf{r}, t + \tau) \mathbf{E}^\dagger(\mathbf{r}, t + \tau) \mathbf{E}^\dagger(\mathbf{r}, t) \rangle}{\langle I(\mathbf{r}, t) \rangle \langle I(\mathbf{r}, t + \tau) \rangle}$$

where  $I(\mathbf{r}, t) = \mathbf{E}(\mathbf{r}, t) \mathbf{E}^\dagger(\mathbf{r}, t)$  allows one to identify the quantum nature of light. Indeed,  $g^{(2)}(0) < 1$  (*antibunching*) is a signature of non-classical light.

We have first measured  $g^{(2)}$  of light emitted by a dilute system containing  $N = 4000$  atoms with a peak density  $n_0 \simeq 0.04 k^3$ . In this case,  $g^{(2)}(\tau)$  is given by the Siegert relation (Ferreira et al. 2020)

$$g^{(2)}(\tau, N) = \frac{1}{N} [g^{(2)}(\tau, 1) + (N - 1)(1 + |g^{(1)}(\tau, 1)|^2)] \quad (6.1)$$

where  $g^{(2)}(\tau, 1)$  and  $g^{(1)}(\tau, 1)$  are the intensity and field correlation functions of a single atom. Expressions for these functions in steady-state and on resonance can be found in (Loudon 1983) or (Scully and Zubairy 1997).

Figure 5 shows our measurements of  $g^{(2)}$  for several saturation parameter  $s = \frac{I}{I_{\text{sat}}}$ . To obtain these data, we split the collected fluorescence into two parts using a 50/50 beamsplitter. We then record the arrival time of the photons on each path, allowing us to reconstruct the intensity correlation function  $g^2(t_1 - t_2)$  for every  $t_1, t_2$ . We then select only the times corresponding to the steady-state regime and obtain  $g^2(\tau = t_1 - t_2)$ .

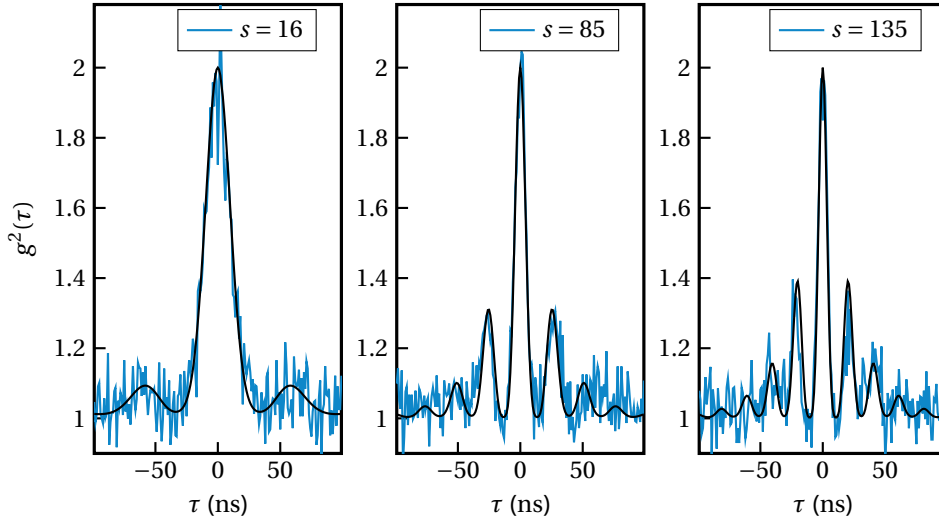


Figure 5: Intensity correlation  $g^{(2)}(\tau)$  for various values of  $s$ , with  $N = 4000$  atoms but low atomic density. Data are compared with theoretical values obtained from equation (6.1) (solid line).

In figure 5, we compare the experimental data to the theoretical prediction using equation (6.1) (solid line) for several values of the saturation parameter. We obtain a very good agreement without any free parameters (we only assume  $N \gg 1$ ).

We then perform the same measurement in a dense cloud ( $n_0 \sim k^3$ ) with  $s \simeq 50$ . Results are shown in figure 6. With the largest atom number, we see a violation of Siegert relation. We observe some “antibunching” ( $g(\tau) < 1$ ) in the minima of the oscillations. Moreover,  $g^{(2)}(0, N)$  decreases with  $N$ . In the low atom number, we recover a reasonable agreement between

the theory and the experiment, except for  $g^{(2)}(0)$  which is smaller than 2 also for the smallest atom number. We do not have an explanation for these results at this time but they allow us to hope for interesting results on the generation of non-classical states of light using dense clouds of atoms.

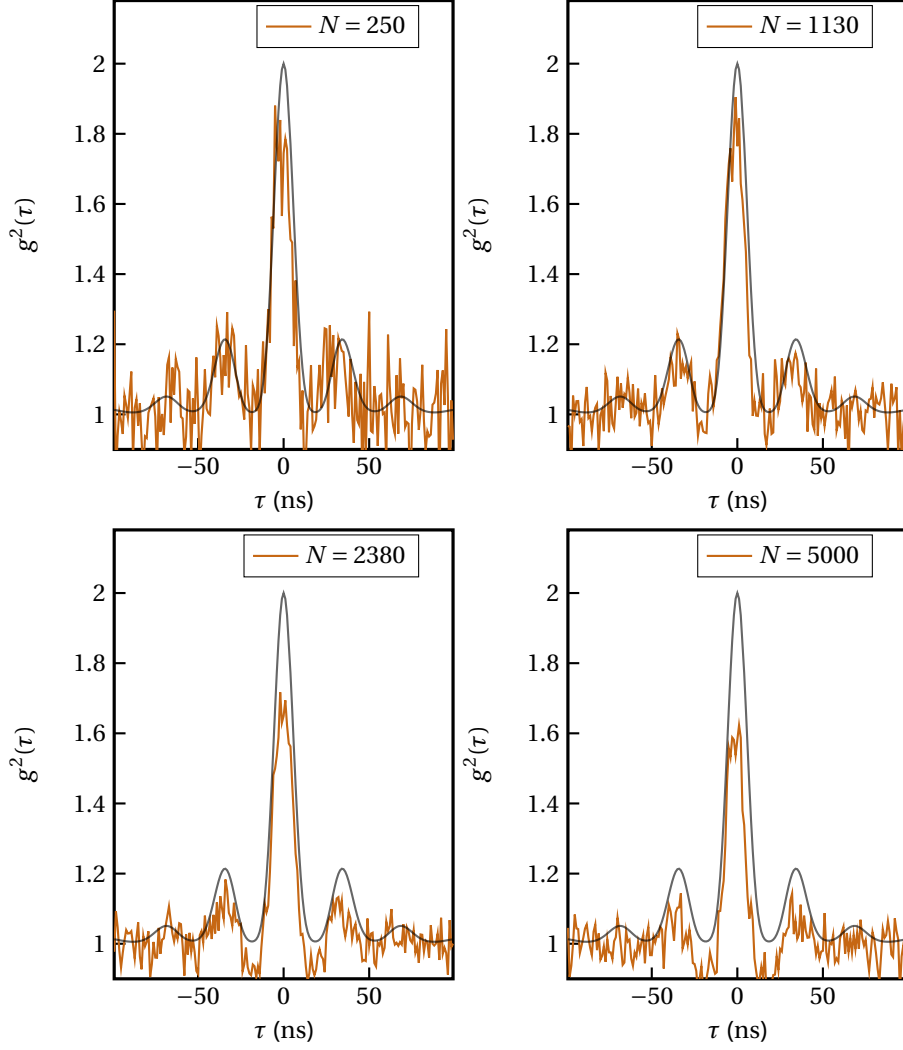


Figure 6: Intensity correlation  $g^{(2)}(\tau)$  for various values of  $N$ , with  $s \approx 50$ . Data are compared with theoretical values obtained from equation (6.1) (solid line).

To conclude, we have observed many interesting collective effects in our dense clouds of cold atoms. However, this system is far from having shown all its facets, and the perspectives of future work are many.





# Bibliography

\*\*\*

- Abanin, D. A. et al. *Colloquium: Many-body localization, thermalization, and entanglement*. In: *Reviews of Modern Physics* 91.2 (2019), p. 21001 (cited on page 1).
- Alet, F. and N. Laflorencie. *Many-body localization: An introduction and selected topics*. In: *Comptes Rendus Physique* 19.6 (2018), pp. 498–525 (cited on page 1).
- Aljunid, S. A. et al. *Phase shift of a weak coherent beam induced by a single atom*. In: *Physical Review Letters* 103.15 (2009), pp. 1–4 (cited on page 74).
- Allen, L. and J. H. Eberly. *Optical Resonance and Two-level Atoms*. Dover books on physics and chemistry. Dover, 1987 (cited on pages 18, 118, 124).
- Amico, L. et al. *Entanglement in many-body systems*. In: *Reviews of Modern Physics* 80.2 (2008), pp. 517–576 (cited on page 1).
- Ang'ong'a, J. et al. *Gray molasses cooling of  $^{39}\text{K}$  atoms in optical tweezers*. In: *ArXiv* 10.1088 51 (2021) (cited on page 68).
- Angerer, A. et al. *Superradiant emission from colour centres in diamond*. In: *Nature Physics* 14.12 (2018), pp. 1168–1172 (cited on pages 21, 87).
- Araújo, M. O., W. Guerin, et al. *Decay dynamics in the coupled-dipole model*. In: *Journal of Modern Optics* 65.11 (2018), pp. 1345–1354 (cited on pages 25, 26).
- Araújo, M. O., I. Krešić, et al. *Superradiance in a Large and Dilute Cloud of Cold Atoms in the Linear-Optics Regime*. In: *Physical Review Letters* 117.7, 073002 (2016), p. 073002 (cited on page 136).
- Asenjo-Garcia, A. et al. *Exponential improvement in photon storage fidelities using subradiance & "selective radiance" in atomic arrays*. In: *Physical Review X* 7.3 (2017), p. 31024 (cited on pages 2, 21, 73, 87, 141, 152, 154).
- Awschalom, D. et al. *Semiconductor Spintronics and Quantum Computation*. Springer Berlin Heidelberg, 2002 (cited on page 2).
- Béguin, L. *Measurement of the van der Waals interaction between two Rydberg atoms*. PhD thesis. 2014 (cited on page 36).
- Bettles, R. J. et al. *Cooperative eigenmodes and scattering in one-dimensional atomic arrays*. In: *Physical Review A* 94.4 (2016), pp. 1–15 (cited on page 22).
- *Enhanced Optical Cross Section via Collective Coupling of Atomic Dipoles in a 2D Array*. In: *Physical Review Letters* 116.10 (2016), pp. 1–5 (cited on pages 2, 73).
- Bevington, P. R. et al. *Data Reduction and Error Analysis for the Physical Sciences*. In: *Computers in Physics* 7.4 (1993), p. 415 (cited on page 67).
- Bienaimé, T. et al. *Atom and photon measurement in cooperative scattering by cold atoms*. In: *Journal of Modern Optics* 58.21 (2011), pp. 1942–1950 (cited on page 22).
- Bloch, I. et al. *Many-body physics with ultracold gases*. In: *Reviews of Modern Physics* 80.3 (2008), pp. 885–964 (cited on page 1).

- Boiron, D. et al. *Three-dimensional cooling of cesium atoms in four-beam gray optical molasses*. In: *Physical Review A* 52.5 (1995), R3425–R3428 (cited on page 61).
- Bourgain, R. et al. *Evaporative cooling of a small number of atoms in a single-beam microscopic dipole trap*. In: *Physical Review A* 88.2 (2013) (cited on pages 61, 71, 91).
- Brito, R. et al. *Superradiance*. In: *Lecture Notes in Physics* (2020) (cited on page 87).
- Bromley, S. L. et al. *Collective atomic scattering and motional effects in a dense coherent medium*. In: *Nature Communications* 7 (2016), pp. 1–7 (cited on pages 2, 22).
- Brossard, L. *Study of light-induced dipolar interactions in cold atoms assemblies*. PhD thesis. 2019 (cited on pages 3, 32, 35, 36, 43, 45, 58, 74, 95, 166).
- Browaeys, A., S. Jennewein, et al. *Coherent Scattering of Near-Resonant Light by a Dense Microscopic Cold Atomic Cloud*. In: *Physical Review Letters* 116.23 (2016) (cited on pages 3, 26).
- Browaeys, A., D. Barredo, et al. *Experimental investigations of dipole-dipole interactions between a few Rydberg atoms*. In: *Journal of Physics B* 49.15, 152001 (2016), p. 152001 (cited on page 3).
- Browaeys, A. and T. Lahaye. *Many-body physics with individually controlled Rydberg atoms*. In: *Nature Physics* 16.2 (2020), pp. 132–142 (cited on pages 3, 61).
- Brown, M. O. et al. *Gray-Molasses Optical-Tweezer Loading: Controlling Collisions for Scaling Atom-Array Assembly*. In: *Physical Review X* 9.2 (2019), pp. 1–6 (cited on pages 61, 65, 68, 71).
- Bruno, N. et al. *Maltese cross coupling to individual cold atoms in free space*. In: *Optics Express* 27.21 (2019), p. 31042 (cited on page 35).
- Buggle, C. et al. *Interferometric determination of the s and d-wave scattering amplitudes in  $^{87}\text{Rb}$* . In: *Physical Review Letters* 93.17 (2004) (cited on pages 38, 97).
- Burt, E. A. et al. *Coherence, correlations, and collisions: What one learns about Bose-Einstein condensates from their decay*. In: *Collected Papers of Carl Wieman* (2008), pp. 497–500 (cited on pages 96, 97).
- Campbell, S. L. et al. *A Fermi-degenerate three-dimensional optical lattice clock*. In: *Science* 358.6359 (2017), pp. 90–94 (cited on page 2).
- Carmichael, H. *An Open Systems Approach to Quantum Optics*. An Open Systems Approach to Quantum Optics: Lectures Presented at the Université Libre de Bruxelles, October 28 to November 4, 1991 vol.18. Springer Berlin Heidelberg, 1993 (cited on page 27).
- Chabé, J. et al. *Coherent and incoherent multiple scattering*. In: *Physical Review A* 89.4 (2014) (cited on page 22).
- Chalony, M. et al. *Coherent flash of light emitted by a cold atomic cloud*. In: *Physical Review A* 84.1 (2011) (cited on page 2).
- Chang, D. E., J. Ye, et al. *Controlling dipole-dipole frequency shifts in a lattice-based optical atomic clock*. In: *Physical Review A* 69.2 (2004), p. 23810 (cited on page 2).
- Chang, D. E., V. Vuletić, et al. *Quantum nonlinear optics - Photon by photon*. In: *Nature Photonics* 8.9 (2014), pp. 685–694 (cited on page 169).
- Chui, S.-T. et al. *Subwavelength transportation of light with atomic resonances*. In: *Physical Review A* 92.5, 053826 (2015), p. 53826 (cited on page 73).
- Cidrim, A. et al. *Photon Blockade with Ground-State Neutral Atoms*. In: *Physical Review Letters* 125.7 (2020), p. 73601 (cited on page 169).
- Cipris, A. et al. *Subradiance with saturated atoms: Population enhancement of the long-lived states*. In: *arXiv* 126.10 (2020), p. 103604 (cited on page 161).
- Citron, M. L. et al. *Experimental study of power broadening in a two-level atom*. In: *Physical Review A* 16.4 (1977), pp. 1507–1512 (cited on page 19).

- Cohen-Tannoudji, C. et al. *Mécanique quantique*. [2e]. Enseignement des sciences. Paris: Hermann, 2012 (cited on pages 38, 109).
- Colaço, L. R. et al. *Gravitational lens time-delay as a probe of a possible time variation of the fine-structure constant*. In: *European Physical Journal C* 81.6 (2021), pp. 1–9 (cited on page 2).
- Corman, L. et al. *Transmission of near-resonant light through a dense slab of cold atoms*. In: *Physical Review A* 96.5 (2017) (cited on page 79).
- Corzo, N. V. et al. *Waveguide-coupled single collective excitation of atomic arrays*. In: *Nature* 566.7744 (2019), pp. 359–362 (cited on page 73).
- Courteille, P. W. et al. *Modification of radiation pressure due to cooperative scattering of light*. In: *European Physical Journal D* 58.1 (2010) (cited on pages 22, 111).
- Daley, A. J. *Quantum trajectories and open many-body quantum systems*. In: *Advances in Physics* 63.2 (2014), pp. 77–149 (cited on page 27).
- Devoe, R. G. and R. G. Brewer. *Observation of Superradiant and Subradiant Spontaneous Emission of Two Trapped Ions*. In: *Physical Review Letters* 76.12 (1996), pp. 2049–2052 (cited on pages 21, 141).
- Dicke, R. H. *Coherence in Spontaneous Radiation Processes*. In: *Physical Review* 93.1 (1954), pp. 99–110 (cited on pages 87, 107, 109).
- Do Espirito Santo, T. S. et al. *Collective Excitation Dynamics of a Cold Atom Cloud*. In: *Physical Review A* 101.1 (2019), pp. 1–11 (cited on pages 21, 22, 27).
- Dobbertin, H. et al. *Collective dipole-dipole interactions in planar nanocavities*. In: *Physical Review A* 102.3 (2020), pp. 1–6 (cited on page 22).
- Eismann, U. et al. *Universal Loss Dynamics in a Unitary Bose Gas*. In: *Physical Review X* 6.2 (2016), p. 21025 (cited on page 97).
- Esslinger, T. et al. *Purely optical dark lattice*. In: *Optics Letters* 21.13 (1996), pp. 991–993 (cited on page 61).
- Facchinetti, G., S. D. Jenkins, et al. *Storing Light with Subradiant Correlations in Arrays of Atoms*. In: *Physical Review Letters* 117.24 (2016), p. 243601 (cited on pages 2, 87, 141, 154).
- Facchinetti, G. and J. Ruostekoski. *Interaction of light with planar lattices of atoms: Reflection, transmission, and cooperative magnetometry*. In: *Physical Review A* 97.2 (2018), p. 23833 (cited on page 73).
- Feroli, G., A. Glicenstein, F. Robicheaux, et al. *Laser driven superradiant ensembles of two-level atoms near Dicke's regime*. In: *ArXiv2107.13392* (2021), pp. 1–6 (cited on pages 117, 124).
- Feroli, G., A. Glicenstein, L. Henriët, et al. *Storage and Release of Subradiant Excitations in a Dense Atomic Cloud*. In: *Physical Review X* 11.2 (2021), p. 21031 (cited on pages 141, 152, 154).
- Ferreira, D. et al. *Connecting field and intensity correlations: the Siegert relation and how to test it*. In: *American Journal of Physics* 88.10 (2020), pp. 831–837 (cited on page 170).
- Foot, C. J. *Atomic Physics*. Oxford Master Series in Physics. OUP Oxford, 2005 (cited on pages 2, 35, 52, 58, 59, 64).
- Friedberg, R. et al. *Frequency shifts in emission and absorption by resonant systems of two-level atoms*. In: *Physics Reports* 7.3 (1973), pp. 101–179 (cited on page 20).
- Fuhrmanek, A. *From Single To Many Atoms in a*. PhD thesis. 2011 (cited on pages 32, 36, 38).
- Fung, Y. et al. *Single Atoms Preparation Using Light-Assisted Collisions*. In: *Technologies* 4.1 (2016), p. 4 (cited on pages 38, 64).
- Gallagher, A. and D. E. Pritchard. *Exoergic collisions of cold Na-Na*. In: *Physical Review Letters* 63.9 (1989), pp. 957–960 (cited on page 38).

- Gensemer, S. D. et al. *Trap-loss collisions of  $^{85}\text{Rb}$  and  $^{87}\text{Rb}$ : Dependence on trap parameters*. In: *Physical Review A* 56.5 (1997), pp. 4055–4063 (cited on page 96).
- Glicenstein, A., G. Ferioli, L. Brossard, et al. *Preparation of one-dimensional chains and dense cold atomic clouds with a high numerical aperture four-lens system*. In: *Physical Review A* 103.4 (2021), p. 43301 (cited on pages 35, 43, 45, 73, 91).
- Glicenstein, A., G. Ferioli, N. Šibalić, et al. *Collective Shift in Resonant Light Scattering by a One-Dimensional Atomic Chain*. In: *Physical Review Letters* 124.25 (2020), pp. 1–6 (cited on pages 26, 73).
- Goetschy, A. and S. E. Skipetrov. *Non-Hermitian Euclidean random matrix theory*. In: *Physical Review E* 84.1 (2011) (cited on page 23).
- Grier, A. T. et al.  *$\Lambda$ -enhanced sub-Doppler cooling of lithium atoms in D1 gray molasses*. In: *Physical Review A* 87.6 (2013), pp. 1–8 (cited on pages 62, 63).
- Grimm, R. et al. *Optical Dipole Traps for Neutral Atoms*. In: *Advances in Atomic, Molecular and Optical Physics* 42.C (2000), pp. 95–170 (cited on page 34).
- Gross, M. *phénomène de superradiance HAL Id : tel-00011834*. PhD thesis. 2006 (cited on pages 108, 111).
- Gross, M. and S. Haroche. *Superradiance: An essay on the theory of collective spontaneous emission*. In: *Physics reports* 93.5 (1982), pp. 301–396 (cited on pages 87, 110, 112).
- Grünzweig, T. et al. *Near-deterministic preparation of a single atom in an optical microtrap*. In: *Nature Physics* 6.12 (2010), pp. 951–954 (cited on page 64).
- Grynberg, G. and J.-Y. Courtois. *Proposal for a Magneto-Optical Lattice for Trapping Atoms in Nearly-Dark States*. In: *Europhysics Letters* 27.1 (1994), pp. 41–46 (cited on page 61).
- Grynberg, G., A. Aspect, et al. *Introduction to Quantum Optics*. Cambridge University Press, 2010 (cited on pages 18, 27, 62).
- Guerin, W., M. T. Rouabah, et al. *Light interacting with atomic ensembles: collective, cooperative and mesoscopic effects*. In: *Journal of Modern Optics* 64.9 (2017), pp. 895–907 (cited on pages 3, 135).
- Guerin, W., M. O. Araújo, et al. *Subradiance in a Large Cloud of Cold Atoms*. In: *Physical Review Letters* 116.8 (2016), pp. 1–5 (cited on pages 2, 21, 25, 87, 135, 141, 144).
- Guo, B. et al. *Ultrafast dynamics observation during femtosecond laser-material interaction*. Vol. 1. 3. IOP Publishing, Sept. 2019 (cited on page 1).
- Helmerson, K. et al. *Laser cooling of magnetically trapped neutral atoms*. In: *Journal of the Optical Society of America B* 9.11 (1992), p. 1988 (cited on page 34).
- Henriet, L. et al. *Critical open-system dynamics in a one-dimensional optical-lattice clock*. In: *Physical Review A* 99.2 (2019), pp. 1–20 (cited on page 152).
- Hettich, C. et al. *Nanometer resolution and coherent optical dipole coupling of two individual molecules*. In: *Science* 298.5592 (2002), pp. 385–389 (cited on pages 21, 87).
- Huang, J.-S. et al. *Mode Imaging and Selection in Strongly Coupled Nanoantennas*. In: *Nano Letters* 10.6 (2010), pp. 2105–2110 (cited on page 2).
- Jackson, J. D. *Classical Electrodynamics, 3rd ed.* Wiley, 1999 (cited on pages 1, 14, 15, 17, 25).
- Jen, H. H. et al. *Subradiance dynamics in a singly-excited chiral-coupled atomic chain*. In: *Physical Review A* 101.2, 023830 (2020), p. 023830 (cited on pages 87, 141).
- Jen, H.-H. *Collective light emission : many quantum emitters*. Bristol: IOP Publishing, 2020 (cited on page 110).
- Jenkins, S. D. et al. *Collective resonance fluorescence in small and dense atom clouds: Comparison between theory and experiment*. In: *Physical Review A* 94.2 (2016), pp. 1–15 (cited on pages 3, 41).

- Jennewein, S., Y. R. P. Sortais, et al. *Propagation of light through small clouds of cold interacting atoms*. In: *Physical Review A* 94.5 (2016), pp. 1–6 (cited on pages 3, 26, 79).
- Jennewein, S. *Reponse optique de nuage Rb87 dense*. PhD thesis. 2017 (cited on page 58).
- Jennewein, S., L. Brossard, et al. *Coherent scattering of near-resonant light by a dense, microscopic cloud of cold two-level atoms: Experiment versus theory*. In: *Physical Review A* 97.5 (2018), pp. 1–5 (cited on pages 3, 26).
- Jiang, Y. et al. *Matter-wave Atomic Gradiometer Interferometric Sensor (MAGIS-100)*. In: *Quantum Science and Technology* 6.4 (2021) (cited on page 2).
- Joffe, M. A. et al. *Transverse cooling and deflection of an atomic beam inside a Zeeman slower*. In: *Journal of the Optical Society of America B* 10.12 (1993), p. 2257 (cited on page 34).
- Johansson, J. R. et al. *QuTiP: An open-source Python framework for the dynamics of open quantum systems*. In: *Computer Physics Communications* 183.8 (2012), pp. 1760–1772 (cited on page 27).
- Julienne, P. S. et al. *Collisional stability of double bose condensates*. In: *Physical Review Letters* 78.10 (1997) (cited on page 96).
- Keaveney, J. et al. *Cooperative Lamb shift in an atomic vapor layer of nanometer thickness*. In: *Physical Review Letters* 108.17 (2012), pp. 1–5 (cited on page 3).
- Kinoshita, T. et al. *All-optical Bose-Einstein condensation using a compressible crossed dipole trap*. In: *Physical Review A* 71.1 (2005), pp. 1–4 (cited on page 90).
- Krämer, S., L. Ostermann, et al. *Optimized geometries for future generation optical lattice clocks*. In: *Europhysics Letters* 114.1 (2016), p. 14003 (cited on pages 87, 141).
- Krämer, S. and H. Ritsch. *Generalized mean-field approach to simulate the dynamics of large open spin ensembles with long range interactions*. In: *European Physical Journal D* 69.12 (2015) (cited on pages 21, 28, 29).
- Kubo, R. *Generated cumulant expansion method*. In: *Journal of the Physical Society of Japan* 17.7 (1962), pp. 1100–1120 (cited on pages 28, 118).
- Kuppens, S. J. M. et al. *Loading an optical dipole trap*. In: *Physical Review A* 62.1 (2000), p. 13 (cited on page 34).
- Kwong, C. C. et al. *Coherent light propagation through cold atomic clouds beyond the independent scattering approximation*. In: *Physical Review A* 99.4 (2019), pp. 1–15 (cited on page 22).
- Labeyrie, G. et al. *Slow diffusion of light in a cold atomic cloud*. In: *Physical Review Letters* 91.22 (2003), pp. 1–4 (cited on page 144).
- Lawlor, D. *Introduction to Light Microscopy*. Springer, Cham, 2019 (cited on page 1).
- Lenef, A. and S. C. Rand. *Electronic structure of the N-V center in diamond: Theory*. In: *Physical Review B* 53.20 (1996), pp. 13441–13455 (cited on page 2).
- Léonard, J. et al. *Optical transport and manipulation of an ultracold atomic cloud using focus-tunable lenses*. In: *New Journal of Physics* 16 (2014) (cited on page 43).
- Lett, P. D. et al. *Observation of atoms laser cooled below the doppler limit*. In: *Physical Review Letters* 61.2 (1988), pp. 169–172 (cited on page 34).
- Lichtman, J. W. and J. A. Conchello. *Fluorescence microscopy*. In: *Nature Methods* 2.12 (2005), pp. 910–919 (cited on page 1).
- Lin, K.-T. et al. *Scalable collective Lamb shift of a 1D superconducting qubit array in front of a mirror*. In: *Scientific Reports* 9.1 (2019) (cited on page 22).
- Loudon, R. *The Quantum Theory of Light*. Second. Oxford: Clarendon Press, 1983 (cited on page 170).
- Ludlow, A. D. et al. *Optical atomic clocks*. In: *Reviews of Modern Physics* 87.2 (2015) (cited on page 2).

- Luiten, O. J. et al. *Kinetic theory of the evaporative cooling of a trapped gas*. In: *Physical Review A* 53.1 (1996), pp. 381–389 (cited on page 97).
- Mandel, L. and E. Wolf. *Collective atomic interactions*. Cambridge University Press, 1995 (cited on page 111).
- Manzoni, M. et al. *Optimization of photon storage fidelity in ordered atomic arrays*. In: *New Journal of Physics* 20.8 (2018), p. 083048 (cited on page 154).
- Marti, G. E. et al. *Imaging Optical Frequencies with 100  $\mu$ Hz Precision and 1.1  $\mu$ m Resolution*. In: *Physical Review Letters* 120.10 (2018), p. 103201 (cited on page 2).
- Masson, S. J. et al. *Many-Body Signatures of Collective Decay in Atomic Chains*. In: *Physical Review Letters* 125.26 (2020), p. 263601 (cited on pages 160, 166).
- McGuyer, B. H. et al. *Precise study of asymptotic physics with subradiant ultracold molecules*. In: *Nature Physics* 11.1 (2015), pp. 32–36 (cited on pages 21, 87, 141).
- Mehlstäubler, T. E. et al. *Atomic clocks for geodesy*. In: *Reports on Progress in Physics* 81.6 (2018) (cited on page 2).
- Meir, Z. et al. *Cooperative lamb shift in a mesoscopic atomic array*. In: *Physical Review Letters* 113.19 (2014), pp. 1–5 (cited on pages 22, 73).
- Mlynek, J. A. et al. *Observation of Dicke superradiance for two artificial atoms in a cavity with high decay rate*. In: *Nature Communications* 5 (2014), pp. 1–6 (cited on page 87).
- Needham, J. A. et al. *Subradiance-protected excitation transport*. In: *New Journal of Physics* 21.7 (2019), p. 73061 (cited on page 73).
- Norcia, M. A. et al. *Superradiance on the millihertz linewidth strontium clock transition*. In: *Science Advances* 2.10 (2016) (cited on page 120).
- Okaba, S. et al. *Superradiance from lattice-confined atoms inside hollow core fibre*. In: *Communications Physics* 2.1 (2019), pp. 1–10 (cited on pages 21, 87).
- Pavolini, D. et al. *Experimental evidence for subradiance*. In: *Physical Review Letters* 54.17 (1985), pp. 1917–1920 (cited on pages 21, 87).
- Pellegrino, J. et al. *Observation of suppression of light scattering induced by dipole-dipole interactions in a cold-atom ensemble*. In: *Physical Review Letters* 113.3 (2014), pp. 1–5 (cited on pages 3, 41, 82, 91).
- Perczel, J. et al. *Topological Quantum Optics in Two-Dimensional Atomic Arrays*. In: *Physical Review Letters* 119.2 (2017), p. 23603 (cited on page 2).
- Peyrot, T., N. Šibalić, et al. *Measurement of the atom-surface van der Waals interaction by transmission spectroscopy in a wedged nanocell*. In: *Physical Review A* 100.2 (2019) (cited on page 3).
- Peyrot, T., Y. R. Sortais, A. Browaeys, et al. *Collective Lamb Shift of a Nanoscale Atomic Vapor Layer within a Sapphire Cavity*. In: *Physical Review Letters* 120.24 (2018) (cited on page 3).
- Peyrot, T., Y. R. Sortais, J. J. Greffet, et al. *Optical Transmission of an Atomic Vapor in the Mesoscopic Regime*. In: *Physical Review Letters* 122.11 (2019) (cited on page 3).
- Phillips, W. D. and H. Metcalf. *Laser Deceleration of an Atomic Beam*. In: *Physical Review Letters* 48.9 (1982), pp. 596–599 (cited on page 34).
- Plankensteiner, D., L. Ostermann, et al. *Selective protected state preparation of coupled dissipative quantum emitters*. In: *Scientific Reports* 5 (2015), pp. 1–12 (cited on pages 73, 87, 141).
- Plankensteiner, D., C. Hotter, et al. *QuantumCumulants.jl: A Julia framework for generalized mean-field equations in open quantum systems*. In: *ArXiv210501657 Quant-Ph* (2021), pp. 1–16 (cited on pages 28, 29).
- Prasad, A. S. et al. *Correlating photons using the collective nonlinear response of atoms weakly coupled to an optical mode*. In: *ArXiv1911.09701* (2019), pp. 1–9 (cited on pages 73, 169).

- Riehle, F. *Caesium Atomic Clocks*. In: *Frequency Standards* (2005), pp. 203–227 (cited on page 2).
- Rio Fernandes, D. et al. *Sub-Doppler laser cooling of fermionic 40K atoms in three-dimensional gray optical molasses*. In: *Europhysics Letters* 100.6 (2012), p. 63001 (cited on page 63).
- Robicheaux, F. and D. A. Suresh. *Beyond lowest order mean field theory for light interacting with atom arrays*. In: *Physical Review A* 104.2, 023702 (2021), pp. 1–14 (cited on pages 29, 118, 130).
- Roof, S. J. et al. *Observation of Single-Photon Superradiance and the Cooperative Lamb Shift in an Extended Sample of Cold Atoms*. In: *Physical Review Letters* 117.7 (2016), pp. 1–5 (cited on pages 2, 87).
- Rosi, S. et al.  *$\Lambda$ -enhanced grey molasses on the D 2 transition of Rubidium-87 atoms*. In: *Scientific Reports* 8.1 (2018), pp. 1–9 (cited on page 65).
- Rui, J. et al. *A subradiant optical mirror formed by a single structured atomic layer*. In: *Nature* 583.7816 (2020), pp. 369–374 (cited on pages 2, 73, 141).
- Ruostekoski, J. and J. Javanainen. *Arrays of strongly coupled atoms in a one-dimensional waveguide*. In: *Physical Review A* 96.3 (2017), pp. 1–13 (cited on page 23).
- Schilder, N. J. et al. *Polaritonic modes in a dense cloud of cold atoms*. In: *Physical Review A* 93.6 (2016), pp. 1–8 (cited on pages 23, 155).
- Schlosser, N. et al. *Sub-poissonian loading of single atoms in a microscopic dipole trap*. In: *Nature* 411.6841 (2001), pp. 1024–1027 (cited on pages 37, 38).
- Schymik, K. N. et al. *Enhanced atom-by-atom assembly of arbitrary tweezer arrays*. In: *Physical Review A* 102.6 (2020), p. 63107 (cited on page 61).
- Schymik, K.-N. et al. *Single atoms in optical tweezers arrays at cryogenic temperatures*. In: *Physical Review Applied* 16 (2021), pp. 1–7 (cited on page 36).
- Scully, M. O. and A. A. Svidzinsky. *The super of superradiance*. In: *Science* 325.5947 (2009), pp. 1510–1511 (cited on page 87).
- Scully, M. O., E. S. Fry, et al. *Directed spontaneous emission from an extended ensemble of N atoms: Timing is everything*. In: *Physical Review Letters* 96.1 (2006), pp. 1–4 (cited on page 87).
- Scully, M. O. and M. S. Zubairy. *Quantum Optics*. Cambridge University Press, 1997 (cited on page 170).
- Shahmoon, E. et al. *Cooperative Resonances in Light Scattering from Two-Dimensional Atomic Arrays*. In: *Physical Review Letters* 118.11 (2017), pp. 1–6 (cited on pages 2, 73, 87, 141).
- Skipetrov, S. E. and A. Goetschy. *Eigenvalue distributions of large Euclidean random matrices for waves in random media*. In: *Journal of Physics A* 44.6 (2011) (cited on page 23).
- Söding, J. et al. *Three-body decay of a rubidium Bose-Einstein condensate*. In: *Applied Physics B* 69.4 (1999), pp. 257–261 (cited on pages 96, 97).
- Sokolov, I. M. and W. Guerin. *Comparison of three approaches to light scattering by dilute cold atomic ensembles*. In: *Journal of the Optical Society of America B* 36.8 (2019), p. 2030 (cited on page 22).
- Solano, P. et al. *Super-radiance reveals infinite-range dipole interactions through a nanofiber*. In: *Nature Communications* 8.1 (2017), pp. 1–7 (cited on pages 21, 73, 87).
- Solomon, G. S. et al. *Single-mode Spontaneous Emission from a Single Quantum Dot in a Three-Dimensional Microcavity*. In: *Physical Review Letters* 86.17 (2001), pp. 3903–3906 (cited on page 2).
- Sortais, Y. R. P., A. Fuhrmanek, et al. *Sub-Poissonian atom-number fluctuations using light-assisted collisions*. In: *Physical Review A* 85.3 (2012), pp. 1–4 (cited on pages 38, 39).
- Sortais, Y. R. P., H. Marion, et al. *Diffraction-limited optics for single-atom manipulation*. In: *Physical Review A* 75.1 (2007), pp. 1–7 (cited on pages 3, 35, 37).

- Steane, A. M. et al. *Radiation force in the magneto-optical trap*. In: *Journal of the Optical Society of America B* 9.12 (1992), pp. 2142–2158 (cited on page 92).
- Steck, D. A. *Rubidium 87-Line Data*. In: 75.2 (2001), pp. 463–468 (cited on page 53).
- Sutherland, R. T. and F. Robicheaux. *Collective dipole-dipole interactions in an atomic array*. In: *Physical Review A* 94.1 (2016) (cited on pages 74, 75, 77, 84, 166).
- *Superradiance in inverted multilevel atomic clouds*. In: *Physical Review A* 95.3 (2017), pp. 1–13 (cited on page 29).
- Takasu, Y. et al. *Controlled production of subradiant states of a diatomic molecule in an optical lattice*. In: *Physical Review Letters* 108.17 (2012), pp. 3–7 (cited on page 141).
- Tan, S. M. *Computational toolbox for quantum and atomic optics*. In: *Journal of Optics B* 1.4 (1999), pp. 424–432 (cited on page 27).
- Thijssen, R. et al. *Plasmon Nanomechanical Coupling for Nanoscale Transduction*. In: *Nano Letters* 13.7 (2013), pp. 3293–3297 (cited on page 2).
- Tuchendler, C. et al. *Energy distribution and cooling of a single atom in an optical tweezer*. In: *Physical Review A* 78.3 (2008), pp. 1–9 (cited on pages 37, 65).
- Vetsch, E. et al. *Optical interface created by laser-cooled atoms trapped in the evanescent field surrounding an optical nanofiber*. In: *Physical Review Letters* 104.20 (2010) (cited on page 73).
- Ville, J. L. et al. *Loading and compression of a single two-dimensional Bose gas in an optical accordion*. In: *Physical Review A* 95.1 (2017), pp. 1–7 (cited on page 167).
- Walker, T. G. and M. Saffman. *Entanglement of Two Atoms Using Rydberg Blockade*. In: *Advances in Atomic, Molecular and Optical Physics* 61. November 2018 (2012), pp. 81–115 (cited on page 57).
- Wang, T. et al. *Superradiance in ultracold Rydberg gases*. In: *Physical Review A* 75.3 (2007), pp. 3–6 (cited on pages 21, 87).
- Waseda, Y. et al. *X-Ray Diffraction Crystallography*. Vol. 33. 3. Springer Berlin Heidelberg, 2011 (cited on page 1).
- Weidemüller, M. et al. *A Novel Scheme for Efficient Cooling below the Photon Recoil Limit*. In: *Europhysics Letters* 27.2 (1994), pp. 109–114 (cited on page 61).
- Yu, S. P. et al. *Nanowire photonic crystal waveguides for single-atom trapping and strong light-matter interactions*. In: *Applied Physics Letters* 104.11 (2014) (cited on page 73).
- Zhu, B. et al. *Light scattering from dense cold atomic media*. In: *Physical Review A* 94.2 (2016), pp. 1–13 (cited on pages 22, 25).



**Résumé:** Ce manuscrit est divisé en deux parties. La première partie porte sur les outils théoriques et expérimentaux développés et utilisés pour cette thèse. Dans cette partie sont d'abord détaillés les modèles théoriques et les méthodes numériques nécessaires à l'étude de la diffusion de la lumière dans des ensembles atomiques. Ensuite est présenté le dispositif expérimental développé par l'équipe pour cette étude, utilisant des nuages d'atomes froids de Rubidium dans des pièges optiques. Une attention particulière est donnée à la préparation d'ensembles d'atomes à deux niveaux, réalisés grâce à un fort champ magnétique et au pompage optique dans les sous-niveaux Zeeman. Un chapitre est ensuite dédié à une technique expérimentale, les mélasses grises, dont la mise en place a été un travail important de cette thèse. Le résultat est significatif car ces mélasses ont permis d'augmenter le nombre d'atomes piégés d'un facteur dix, ce qui a ensuite permis d'observer les effets collectifs décrits dans la seconde partie du manuscrit. Le dernier chapitre de la première partie présente des résultats obtenus dans le régime classique avec une chaîne d'atomes. Un décalage de la résonance atomique est observé en raison de l'interaction collective entre les atomes de la chaîne. Dans ce chapitre, nous démontrons l'intérêt de structurer les ensembles d'atomes dans l'espace pour renforcer les interactions entre les dipôles induits par la lumière et modéliser la réponse collective de l'ensemble.

La deuxième partie de ce manuscrit aborde les propriétés d'émission collective d'ensembles denses d'atomes froids dans un régime proche du régime de Dicke, pour lequel un grand nombre d'atomes est contenu dans un volume dont les dimensions sont plus petites que la longueur d'onde de la transition atomique,  $\lambda$ . Nous étudions l'émission spontanée de ces systèmes lorsqu'ils sont soumis à de la lumière laser résonante, pendant et après l'excitation. On observe ainsi les désexcitations superradiantes (plus rapides que celle d'un atome unique) et sous-radiantes (plus lentes que celle d'un atome unique). Dans le premier chapitre de cette partie est présentée la préparation et la caractérisation des nuages d'atomes. Le grand nombre d'atomes piégés (environ 6000), associé aux dimensions microscopiques des ensembles (de l'ordre de la longueur d'onde) permettent d'obtenir des densités de l'ordre de  $k^3$ , où  $k = \frac{2\pi}{\lambda}$ . Une telle densité rend importantes les interactions entre les dipôles en champ proche. Les deux chapitres suivants sont dédiés à l'étude de la superradiance. En mesurant l'émission de fluorescence lors de la désexcitation d'un ensemble totalement excité, nous retrouvons les lois d'échelles prédites par le modèle de Dicke. Nous caractérisons la superradiance dans nos ensembles, au-delà du modèle idéal de Dicke, et on montre qu'elle est gouvernée par le nombre d'atomes mais aussi par la géométrie du nuage. Nous étudions ensuite la superradiance dans le régime « piloté », pendant l'excitation résonante, et on observe une émission collective de lumière. Dans le dernier chapitre, nous caractérisons la sous-radiance dans nos ensembles, et on montre qu'elle est gouvernée par le nombre d'atomes. La dynamique de la population des états sous-radiants est étudiée grâce à des mesures résolues en temps. Enfin, nous démontrons un protocole pour relâcher à la demande des excitations stockées dans ces états sous-radiants, ce qui est un prérequis pour des applications de stockage de la lumière.

En conclusion, nous donnons des perspectives pour des recherches futures, en incluant des résultats préliminaires sur les corrélations d'intensité de la lumière diffusée. Ces mesures ont pour but de démontrer la génération d'états non-classiques de la lumière par des nuages denses d'atomes froids.

